UNIVERSITE NICE-SOPHIA ANTIPOLIS – UFR Sciences
Ecole Doctorale de Sciences Fondamentales et Appliquées

THESE

pour obtenir le titre de
Docteur en Sciences
de l'UNIVERSITE de Nice-Sophia Antipolis

Discipline : Physique

présentée et soutenue par
Michel Khoury

Croissance de GaN Semipolaire par Epitaxie en Phase Vapeur aux Organométalliques sur Substrats de Si Structurés

Metal Organic Vapor Phase Epitaxy of Semipolar GaN on Patterned Silicon Substrates

Thèse dirigée par Philippe Vennéguès & Jesus Zúñiga-Pérez
et co-dirigée par Guy Feuillet

Soutenue le : 22-02-2016

Jury

I. Sagnes	Directeur de Recherche CNRS – LPN, Marcoussis, France	Rapporteur
F. Scholz	Professeur, Institut für Optoelektronik - Ulm, Germany	Rapporteur
I. Berbezier	Directeur de Recherche CNRS - IM2NP, Marseille, France	Examinateur
M. Charles	Ingénieur CEA – LETI, Grenoble, France	Examinateur
J. Zúñiga-Pérez	Chargé de Recherche CNRS – CRHEA, Valbonne, France	Examinateur
G. Feuillet	Directeur de Recherche CEA – LETI, Grenoble, France	Co-directeur de Thèse
P. Vennéguès	Ingénieur de Recherche CNRS – CRHEA, Valbonne, France	Directeur de Thèse

Centre de Recherche sur l'Hétéroépitaxie et ses Applications, CNRS, Valbonne
Laboratoire d'électronique et de technologie de l'information, CEA, Grenoble

Résumé

Jusqu'a présent, les dispositifs optoélectroniques commerciauxs à base de GaN sont épitaxiés selon la direction c, qui souffre de deux limitations intrinsèques. D'une part, les fortes discontinuités de polarisation aux interfaces, qui sont responsables de l'effet Stark quantique confiné. Ceci mène, dans le cas des dispositifs optiques GaN, à une séparation de la fonction d'onde des électrons et des trous dans les puits quantiques. La combinaison d'une longue durée de vie excitonique et la présence de défauts non-radiatives se traduit par une diminution des performances du dispositif. D'une autre part, l'incorporation d'indium sur les plans polaires (000+1) est plus difficile que sur d'autres orientations cristallographiques. Ces effets néfastes peuvent être partiellement dépassés en réalisant la croissance du GaN sur des plans cristallographiques autre que le plan (000+1). Ces plans semi polaires ou nonpolaires conduisent éventuellement à l'amélioration des performances des dispositifs. En fait, la seule solution disponible pour l'instant pour la croissance de dispositifs à base de GaN semipolaire est l'homoépitaxie, ce qui a ses limitations puisque les substrats sont de petite taille et leur prix est élevé. Cela justifie la croissance du GaN semi-polaire sur d'autres types de substrats, spécialement sur silicium. Néanmoins, les couches de GaN semi-polaires hétéro-épitaxiées sur des substrats de Si sont caractérisées par une forte densité de défauts structuraux. Afin qu'elles puissent concurrencer efficacement les performances offertes par les substrats GaN massifs, la densité de ces défauts doit être fortement réduite, ce qui est l'objectif principal de ces travaux de thèse. Dans cette étude, la croissance de couches de GaN semi-polaire $(10\bar{1}1)$ et $(20\bar{2}1)$ par MOVPE sur des substrats de silicium structurés sera évaluée. La stratégie générale de fabrication consiste a structurer l'orientation adaptée du substrat silicium de façon a révéler des facettes Si(111). La croissance sélective du GaN selon l'axe c sera réalisée sur ces substrats préparés, où les cristaux orientés selon l'axe c seront amenés à coalescer pour atteindre enfin la couche semi-polaire.

Le deuxième chapitre de cette thèse est dédié à introduire les propriétés basiques du GaN. Les avantages offerts par le GaN semi-polaire seront présentés et on décrira brièvement l'état de l'art des techniques de réduction de défauts. Les éléments nécessaires pour comprendre les techniques

de caractérisations utilisées (*i.e.* diffraction des rayons X, microscopie électronique à transmission, microscopie à force atomique et photoluminescence) seront développés afin de permettre une meilleure compréhension des résultats présentés dans les chapitres suivants.

Le troisième chapitre discute les résultats obtenus sur le GaN $(10\bar{1}1)$ semi-polaire épitaxié sur des substrats Si(001) désorientés de 7° et structurés. Tout d'abord, le procédé de fabrication des substrats est décrit, et la relation d'épitaxie entre l'orientation semi-polaire désirée et l'orientation du silicium choisie est expliquée. Ensuite, la croissance inclinée de l'AlN et du GaN sur les substrats traités est étudiée. On a changé les conditions de croissance pour mieux comprendre l'effet de ces changements sur la morphologie du GaN épitaxié. Les résultats indiquent que la technique efficace d'annuler les défauts in-situ pour l'orientation $(11\bar{2}2)$ n'est pas valable dans notre cas pour l'orientation $(10\bar{1}1)$. Des caractérisations optiques et structurales ont été menées sur les couches GaN $(10\bar{1}1)$ épitaxiées par une seule étape "single-step". Les résultats montrent que l'approche de croissance classique, adapté à notre orientation cristallographique, donne des résultats à l'état de l'art tels que publiés dans littérature pour l'orientation $(10\bar{1}1)$. Néanmoins, ces résultats ne sont surement pas suffisants pour la fabrication de dispositifs optoélectroniques performants. Pour y remédier, on a introduit pour la première fois une technique de traitement de surface qui sert à arrêter la propagation des défauts. Les résultats des caractérisations structurales et optiques indiquent une amélioration remarquable par rapport à la croissance classique "single-step", et a dépassé sans doute l'état de l'art publié à propos de l'orientation $(10\bar{1}1)$. Malgré le fait que la compréhension complète de cette méthode de blocage de défauts n'est pas pour l'instant complète, et que la poursuite de l'amélioration doit être poursuivie, la méthode introduite peut être le point de départ pour atteindre un procédé complètement in-situ qui empêche les défauts structuraux d'atteindre la surface.

Dans le quatrième chapitre la croissance de GaN $(20\bar{2}1)$ semi-polaire sur des substrats Si(001) désorientés de 1° et structurés a été réalisé. L'objectif étant de démontrer la faisabilité, pour la première fois, de la croissance de l'orientation $(20\bar{2}1)$ sur silicium. Plusieurs conditions de croissance ont été testées. Tous les résultats confirment que la formation de la surface inclinée $(10\bar{1}1)$ dans la phase de croissance initiale est inévitable. La formation inévitable de cette surface $(10\bar{1}1)$ inclinée de 13° par rapport au plan horizontal impose un alignement géométrique où la hauteur des ailes c du Ga polaire reste toujours en dessous des ailes c de polarité N, très défectueuses. Une telle géométrie ne permet pas d'appliquer les stratégies de réduction de défauts qui conduit à la surcroissance des régions défectueuses d'un cristal par les zone sans défauts du cristal adjacent. Cependant, on a réussi à coalescer des cristaux adjacents grâce au procédé de croissance d'une seule étape. Les couches coalescées montrent l'alternance d'une surface micro-facettée dominée par des plans cristallographiques semi-polaires et non-polaires qui sont favorables énergétiquement. Si on vise la fabrication de dispositifs, ces surfaces demandent une étape de polissage mécanique pour rendre la surface lisse. Les caractérisations structurales et optiques indiquent que la qualité des couches épi-

taxiées sur silicium est comparable à celle des couches épitaxiées sur saphir. On peut prédire que la réduction de la densité des défauts pour l'orientation $(20\bar{2}1)$ peut être aussi obtenue en introduisant l'inter-couche introduite dans le chapitre précédent et qui empêche la propagation des défauts.
Dans le cinquième chapitre on introduit ce qu'on appelle la gravure face arrière (meltback etching en anglais) et nous discutons ses possibles origines. Les substrats endommagés sont caractérisés optiquement et chimiquement, et un modèle sur les étapes d'évolution de la gravure face arrière est proposé. L'étude de la gravure face arrière ne tombe pas dans les objectives de ces travaux de thèse, mais afin d'éliminer sa présence qui endommage les couches épitaxiées, différentes voies tentant de le supprimer sont présentées. Les résultats indiquent que les conditions de croissance ont un effet important, favorisant ou empêchant la gravure face arrière. La croissance d'une couche d'AlN à basse température et l'introduction d'une fraction de N2 dans le gaz porteur, durant la croissance de GaN, ont montré que c'est possible d'arrêter la gravure face arrière. Malheureusement, les deux méthodes proposées dans les conditions de croissance qu'on utilise influent sur la qualité de la couche, soit par la création d'une morphologie rugueuse, soit par une augmentationde la densité des défauts structuraux. Par conséquent, la gravure face arrière reste un obstacle majeur, spécialement sur les substrats structurés. De plus, sa présence réduit la palette de conditions de croissances possibles Par conséquence, il est encore nécessaire de trouver une couche qui arrête la gravure face arrière sans compromettre la qualité des couches.
Ces travaux de thèse ont été réalisés en collaboration entre deux laboratoires, CNRS-CRHEA (Valbonne, France) et le CEA-LETI (Grenoble, France) dans le cadre du projet Labex-GaNex. Les travaux comportent, de façon générale deux étapes: la première est la fabrication des substrats silicium structurés, qui été réalisée dans les salles blanches du CEA-LETI, et la deuxième se base sur la croissance MOVPE et les caractérisations correspondantes qui ont eu lieu au CNRS-CRHEA.

Mots-clefs: GaN, Silicium, Semipolaire, Croissance Selectif

Contents

List of Acronyms

AFM	Atomic Force Microscopy
BOE	Buffered Oxide Etch
BSF	Basal Stacking Fault
BF	Bright Field
CL	Cathodolumenisence
CCD	Charge Coupled Device
D^0X	Donor Bound Exciton
DF	Dark Field
EDX	Energy Dispersive X-Ray
EELS	Electron Energy Loss Spectroscopy
EL	Electro Lumenisence
ELO	Epitaxial Lateral Overgrowth
EQE	External Quantum Efficiency
FWHM	Full Width Half Maximum
HAADF	High Angle Annular Dark Field
HVPE	Hydride Vapor Phase Epitaxy
IBS	Ion Beam Sputtering
IQE	Internal Quantum Efficiency
LD	Laser Diode
LED	Light Emitting Diode
MD	Misfit Dislocation
MO	Metal Organic
MOVPE	Metal Organic Vapor Phase Epitaxy
NBE	Near Band Edge
PD	Partial Dislocation
PL	Photolumenisence
PSF	Prismatic Stacking Fault
RIE	Reactive Ion Etching
SEM	Scanning Electron Microscopy
STEM	Scanning Transmission Electron Microscopy
TD	Threading Dislocation
TEM	Transmission Electron Microscopy
QCSE	Quantum Confined Stark Effect
QW	Quantum Well
XRD	X-Ray Diffraction

1 Introduction

1.1 General overview

Group-III nitride semiconductors, comprised by GaN, AlN and InN, and their ternary and quaternary alloys permit direct band gap emission from 0.7 eV to 6.2 eV, spanning from the infrared through the entire visible spectrum and deep into the UV [1]. GaN was first investigated as a potential material for LEDs in the late 1960s when single crystalline GaN was first reported by H.P. Maruska and J.J Tietjen at RCA Laboratories [2]. After multiple years of research, significant achievements were made in GaN epitaxial growth and effective p-type doping. These breakthroughs permitted the invention of efficient blue LEDs that enabled bright and energy-saving white light sources and paved the way to a multitude of other applications. The blue LED pioneers, Hiroshi Amano [3], Isamu Akasaki [4] and Shuji Nakamura [5], later received and shared the 2014 Nobel Prize in Physics [6] for their seminal contributions.

Since the first demonstration of a high-power InGaN-based LED [7, 8], blue LEDs have reached record external quantum efficiencies (EQE) exceeding 80% [9]. However, for longer wavelengths, which require higher indium contents, the efficiency of InGaN-based LEDs significantly drops as the wavelength increases beyond 500 nm. This phenomenon is known as the *green-gap*. Current commercial optoelectronic devices (*i.e.* LEDs and LDs) based on GaN heterostructures are grown along the *c*-direction, which intrinsically suffers two main limitations that are likely to contribute to this reduction in efficiency. The first is the strong polarization discontinuities across nitride hetero-interfaces that are responsible for the quantum confined Stark effect, leading in the case of GaN-based optical devices to electron-hole wave function separation within the quantum wells, and thus, a decrease in the oscillator strength [10]. The associated longer exciton lifetime together with the occurrence of non-radiative defects, result in decreasing the device's efficiency. The second is the indium incorporation on the polar plane, which appears to be relatively limited when compared with its incorporation on other crystallographic orientations.

Partially overcoming these deleterious effects can be attained by growing GaN on alternative planes, such as semipolar ones [11]. Currently, demonstrated LEDs and LDs on semipolar films showing remarkable results are grown homoepitaxially on virtually defect-free bulk GaN substrates [12, 13, 14]. However, such substrates are currently only available in small sizes (typically 10 mm × 20 mm) and are highly priced, which sets them short for meeting industrial needs. At this point, the epitaxy of semipolar GaN layers on foreign substrates becomes appealing, especially on silicon. However, the current semipolar GaN films grown heteroepitaxially on silicon are still plagued with high densities of structural defects, so for them to effectively compete with the quality that bulk GaN substrates offer, these densities must be substantially reduced.

1.2 Objectives & contributions

The main motivation of the thesis is therefore devoted to improve the quality of semipolar GaN on patterned silicon substrates. The process adopted consists of patterning the appropriate silicon wafer orientation in order to reveal Si (111) facets, over which the selective growth of GaN along the +*c*-direction will be carried out. The *c*-oriented crystals will be brought to coalescence such that a continuous semipolar layer is achieved. Indeed, the overall approach to selectively grow semipolar GaN on patterned substrates has been previously demonstrated. However, no major advancement has been reported for producing universal methods that reduce the density of defects in these layers.

The contribution of this thesis encompasses four main aspects: (1) since a previous study on semipolar GaN-on-Si in our laboratory was lacking before this work, the first target was to establish the know-how of substrate fabrication, over which the hetereoepitaxial growth of GaN is then carried out. (2) the presentation of a novel method whose purpose is the efficient defect blocking that may pave the way towards high-quality heteroepitaxially grown semipolar layers. (3) the demonstration of the $(20\bar{2}1)$ semipolar orientation, which has not been previously reported on silicon substrates. (4) a study towards a better understanding of the so-called meltback etching effect and the presentation of methods that lead to its prevention. Further contributions of this PhD have been included in two filed patents, which will not be addressed in this manuscript.

This PhD has been conducted between two labs, CNRS - CRHEA (Valbonne, France) and CEA - LETI (Grenoble, France) in the framework of the Labex-GaNeX network. The work consisted of two stages: first, the silicon substrate fabrication, which was carried out in the cleanrooms of CEA - LETI, and second, the MOVPE growth and characterization that took place in CNRS - CRHEA.

1.3 Manuscript preview

The thesis is divided into six chapters (including this one), and is structured as follows:

- **Chapter 2:** introduces the fundamental physical concepts underlying this work. The discussion covers the necessary background on GaN properties, and justifies the interest in the growth of semipolar orientations. The method used in this work to obtain semipolar GaN layers will then be described, and the state-of-the-art approaches to reduce defect densities using the same approach will be shown. The necessary background of the used characterization techniques will also be presented to set the stage for understanding the characterization carried out in the subsequent chapters.

- **Chapter 3:** covers the results obtained on the semipolar GaN $(10\bar{1}1)$ grown on patterned silicon (001)7°off substrates. The work has been carried out with the objective of achieving layers having the lowest possible defect density. Different growth approaches to achieve this aim will be presented, and the obtained layers will be characterized and compared with previously reported state-of-the-art.

- **Chapter 4:** demonstrates the growth of semipolar GaN $(20\bar{2}1)$ on patterned silicon (114)1°off substrates. The crystals' behavior under different growth conditions will be described, and the subsequent optical/structural characterization will be investigated.

- **Chapter 5:** addresses a major problem encountered during the course of this PhD, which is the so-called *meltback etching*. The objective of this chapter is to introduce the observed phenomenon and to present the investigated attempts for its prevention.

- **Chapter 6:** summarizes and concludes the results presented in this thesis and gives an outlook beyond this work.

- **Appendix:** includes the substrate patterning process details specific to the cleanroom apparatus' utilized in this work. This may be a useful guide for anyone seeking to reproduce the presented results.

Introduction (Français)

Introduction générale

Les semi-conducteurs du groupe III-nitrure composés de GaN, AlN et InN ainsi que de leurs alliages ternaires et quaternaires autorisent l'émission de rayonnement infrarouge à ultraviolet en couvrant tout le spectre visible, soit les largeurs de bande directe allant de 0,7 eV à 6,2 eV. Le GaN a suscité de l'intérêt dès la fin des années 1960 pour les applications de type DEL lorsque les premières couches monocristallines ont été obtenues par H. P. Maruska et J. J. Tietjen du Laboratoire RCA. Après des années de recherche, la croissance épitaxiale du GaN et de son dopage de type p ont été significativement améliorés. Ces progrès ont permis l'invention des DELs bleues à haut rendement et ainsi au développement de sources de lumière blanche intenses, économes en énergie, et ont ouvert la route à d'autres types d'applications. Les pionniers des DELs bleues, Hiroshi Amano, Isamu Akasaki et Shuji Nakamura, ont obtenu le prix Nobel en 2014 pour leurs contributions. Depuis leur première démonstration, les DELs bleues à base d'InGaN ont atteint des records de rendement quantique externe, dépassant les 80%. Cependant, pour les longueurs d'onde plus longues (typiquement $\geq$ 500 nm) nécessitant une concentration d'indium plus élevée, l'efficacité des DELs chute drastiquement. Ce phénomène est connu sous le nom de *"green-gap"*. Les dispositifs optoélectroniques commerciaux reposent sur des couches de GaN épitaxiées selon l'axe c, une orientation qui possède deux limitations intrinsèques pouvant contribuer à la réduction de l'efficacité. La première limitation est la forte discontinuité de polarisation à l'hétéro-interface des nitrures. Dans le cas de double hétérostructures comme les puits quantiques, ces discontinuités de polarisation sont responsables de l'effet Stark confiné quantiquement etmènent à une séparation de la fonction d'onde électron-trou. L'association d'une longue durée de vie excitonique combinée à l'apparition de défauts non-radiatifs se traduisent par une diminution de la force optique de l'oscillateur ce qui a pour conséquence de réduire les performances du dispositif. La deuxième limitation concerne l'incorporation d'indium qui se trouve être moins importante sur les surfaces polaires que sur les surfaces ayant d'autres orientations cristallographiques. La croissance de GaN d'orientations cristallines alternatives, comme par exemple sur des surfaces semi-polaires, peut partiellement aider à surmonter ces effets néfastes. Les résultats récents concernant les DELs et LDs homo-épitaxiés sur des substrats de GaN semi-polaires sans

défaut sont remarquables. De tels substrats ne sont cependant disponibles qu'en petites tailles (typiquement de l'ordre de 10 mm × 20 mm), et leur prix reste élevé, les rendant incompatibles avec les besoins industriels. L'épitaxie du GaN sur des substrats différents, en particulier le silicium, devient ainsi de plus en plus attrayant. Néanmoins, les couches semi-polaires de GaN hétéro-épitaxié sur des substrats de Si se caractérisent par une haute densité de défauts structuraux. Afin que les DELs sur Si puissent concurrencer les performances obtenues sur substrats de GaN massifs, la densité de ces défauts doit être substantiellement réduite.

Objectifs et contributions

La motivation essentielle de ma thèse est l'amélioration de la qualité des couches de GaN semi-polaire sur des substrats de silicium structuré. La procédure adoptée consiste à structurer un substrat de silicium ayant l'orientation adéquate afin d'y faire apparaitre des facettes orientées [111] sur lesquelles une croissance sélective du GaN orienté cest réalisée. Les cristaux orientés selon l'axe c sont ensuite amenés à se coalescer afin d'obtenir une couche continue de GaN semi-polaire. Cette approche a été déjà démontrée mais peu de progrès ont été accomplis jusqu'ici afin de réduire la densité des défauts des couches de GaN semi-polaire sur silicium

Cette thèse présente quatre directions principales: (1) Puisque la croissance de GaN semi-polaire sur silicium n'avait jamais été réalisée dans notre laboratoire, le premier objectif fut l'élaboration d'une méthode de fabrication des substrats. (2) Le développement d'une nouvelle méthode ayant pour but de bloquer les défauts cristallins et ouvrant ainsi la porte à l'obtention de couches semi-polaire de GaN de haute qualité. (3) La réalisation pour la toute première fois de GaN orienté $(20\bar{2}1)$ sur silicium. (4) L'analyse des conséquences de la gravure face arrière *(meltback etching)* et la présentation des méthodes aidant à la prévention de ses effets indésirables. Des travaux supplémentaires de ce travail de thèse ont été inclus dans deux brevets déposés et ne seront pas abordés dans ce manuscrit.

Les travaux de cette thèse ont été conduits entre deux laboratoires, le CNRS-CRHEA (Valbonne, France) et le CEA-LETI (Grenoble, France) dans le cadre du projet Labex-GaNeX. Les travaux se divisent en deux parties: d'une part la fabrication des substrats silicium, réalisée dans les salles blanches du CEA-LETI, et d'autre part est la croissance par MOVPE ainsi que les caractérisations correspondantes au CNRS-CRHEA.

Aperçu du manuscrit

Le manuscrit est divisé en six chapitres (y compris celui ci) et est structuré de la manière suivant:

- **Chapitre 2:** introduit les principes physiques fondamentaux de nos travaux. Les discussions couvrent les propriétés essentielles du GaN et justifient l'intérêt de la croissance le long d'orientations semi-polaires. La méthode utilisée pour l'obtention des couches de GaN semi-polaires y est décrite et l'état de l'art des approches utilisées pour la réduction de la densité des défauts y est présenté. Les techniques de caractérisations utilisées sont également brièvement introduites dans ce chapitre afin de faciliter la compréhension des chapitres ultérieurs.

- **Chapitre 3:** présente les résultats obtenus pour le GaN $(10\bar{1}1)$ semi-polaire épitaxié sur des substrats Si(001) désorientés de 7° et structurés. Les travaux ont été menés avec pour objectifla minimisation de ladensité des défauts cristallins.Les différentes approches de croissance utilisées sont présentées et les couches obtenues sont caractérisées et comparées avec celles de l'état de l'art.

- **Chapitre 4:** démontre la croissance de GaN $(20\bar{2}1)$ semi-polaire sur des substrats Si(114) désorientés de 1° et structurés. Le comportement du cristal y est décrit selon les conditions de croissance et les caractérisations optiques/structurales y sont étudiées.

- **Chapitre 5:** répond à un problème majeur rencontré lors de cette thèse: la gravure face arrière (*"meltback etching"* en anglais). L'objectif de ce chapitre est d'introduire le phénomène observé et de présenter les tentatives effectuées pour sa prévention.

- **Chapitre 6:** résume et conclut les résultats présentés dans cette thèse et donne une perspective au delà de ce travail.

- **Annexe:** décrit le procédé utilisé pour la structuration des substrats de silicium en salle blanche.

2 Fundamentals

This first chapter will introduce the crystalline structure and other important properties of III-nitride semiconductors that are necessary for understanding the nature of these materials. The topics discussed in this chapter are intended to provide an insight into some fundamentals which are of importance for understanding the subsequent work. Semipolar GaN particularities will be emphasized.

2.1 Background on GaN properties

Group III-nitride materials (AlN, GaN, InN) and their alloys can crystallize in two common crystal structures: either cubic zinc-blende or hexagonal wurtzite structure. In this work, only the wurtzite crystal structure will be addressed.

2.1.1 Crystal structure and orientations

The wurtzitic GaN phase has a hexagonal unit cell and belongs to the $P6_3mc$ space group. The unit cell of a hexagonal lattice is defined by two equal and co-planar vectors $\vec{a}_1$, $\vec{a}_2$ at 120° to one another, and a third axis $\vec{c}$ at right angles (Figure 2.1). The complete lattice is constructed by repeated translations of the points at the unit cell corners by the vectors $\vec{a}_1$, $\vec{a}_2$ and $\vec{c}$. A third axis, $\vec{a}_3$, can be naturally introduced in the basal plane in order to reflect the symmetry of this plane: $\vec{a}_3 = -(\vec{a}_1 + \vec{a}_2)$. The wurtzite structure exhibits a slight deviation from the ideal structure. Therefore, besides the two basis vectors a and c, another value that characterizes this deviation is the internal parameter u, which is defined by the product uc being the length of the group-III to group-V (cation-anion) bond in the c-direction.

The lattice points of the hexagonal lattice are usually indexed with four indices (*h k i l*), known as the Miller-Bravais indices. The third index, *i*, is defined by the subtraction of the *h* and *k* indices *i* = -(*h* + *k*) [15].

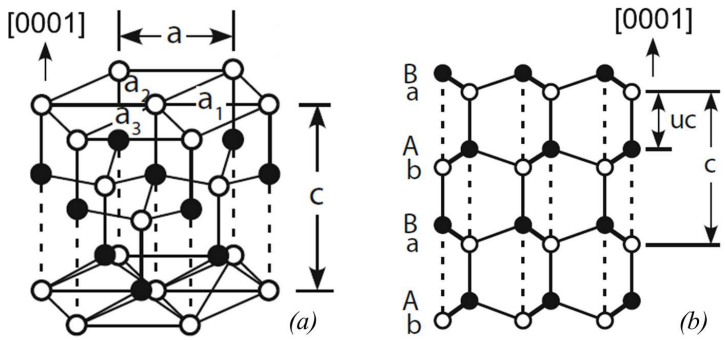

*Figure 2.1 – Atomic structure of III-nitride wurtzite crystal structure in (a) bird's-eye view and (b) projection along the [11$\bar{2}$0] zone-axis. Closed circles represent Ga (Al, In) and open circles represent the nitrogen atoms. The lattice constants: **a** and **c** as well as the cation-anion (group-III to group-V) bond spacing **uc** are marked.*

Epitaxial layers are labeled according to the crystal plane which is parallel to the substrate. When the growth direction is parallel or perpendicular to the polar *c*-axis, the orientations are denoted as polar and nonpolar, respectively. Planes oriented at an intermediate angle between a nonpolar and polar plane are referred to as semipolar, which will be the center of attention throughout this thesis (Figure 2.2).

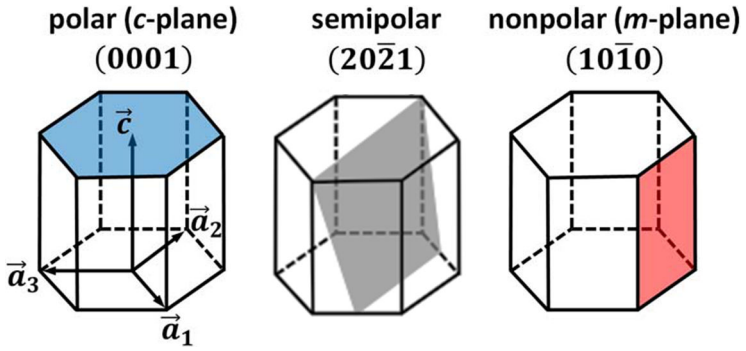

Figure 2.2 – Examples of different GaN orientations including polar (blue), semipolar (20$\bar{2}$1) (grey) and nonpolar (10$\bar{1}$0) (red).

Furthermore, for polar growth, the [0001] and [000$\bar{1}$] directions are not equivalent (see figure 2.3). Considering the bonds between Ga and N along the <0001> direction, the vector pointing from Ga to N is identified as [0001], and the layer grown along this direction is referred to as *gallium*-polar (*Ga*-polar), whereas the layer grown in the opposite direction (*i.e.* [000$\bar{1}$]) is referred to as *nitrogen*-polar (*N*-polar) [16] (Figure 2.3). Moreover, besides influencing the electrical properties at heterointerfaces, the surface properties in terms of morphology and chemical/thermal stability, are strongly affected by the polarity [17].

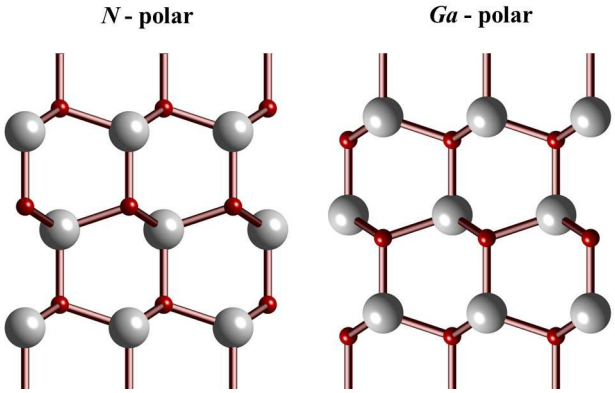

Figure 2.3 – Schematic representation of the two polarities in GaN: N-polar (left) and Ga-polar (right). White and red atoms correspond to gallium and nitrogen, respectively.

2.1.2 Structural defects

The structural quality of epitaxial films is very critical for optoelectronic device applications. The presence of elevated densities of structural defects significantly reduces carrier lifetimes and, consequently, devices' efficiency. Since this thesis will be largely dedicated to the investigation of the defects in the grown semipolar layers, two possible classes of defects formed in a GaN crystal will first be introduced.

2.1.2.1 Dislocations

Heteroepitaxially grown materials are accompanied by the formation of a large number of dislocations, which are line defects, and can be divided into two groups: misfit dislocations (MD) and threading dislocations (TD). Dislocations are defined by the plane they lie in and the *Burgers vector*, **b**, which is a translation lattice vector constructed by considering the positions of atoms after completing a closed loop of an arbitrary size around the dislocation. The Burgers vector therefore describes the lattice displacement introduced within the crystal by the dislocation. As such, three dislocation types in GaN are distinguished: *a*-type with $\mathbf{b} = \frac{1}{3}\langle 11\bar{2}0\rangle$, *c*-type with $\mathbf{b} = \langle 0001\rangle$ and *a*+*c*-type with $\mathbf{b} = \frac{1}{3}\langle 11\bar{2}3\rangle$ (Figure 2.4) [18]. TDs, as their nomenclature indicates, "thread" through the material, mainly following the growth direction. On the other hand, MDs mainly lie in heteroepitaxial interfaces to partially or fully accommodate misfit strain originating from the lattice mismatch between the grown layer and the foreign substrate.

Dislocations cannot simply end in the crystal. They can either make a closed loop, or interact with other defects, or terminate at a free crystal surface. Dislocations are non-radiative recombination

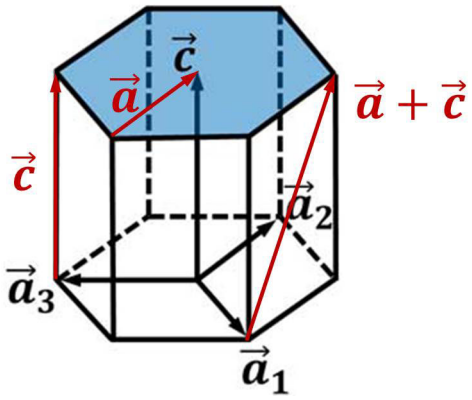

Figure 2.4 – Schematic of wurtzite structure with red arrows indicating the different types of dislocations.

centers acting as "sinks" for charge carriers and are therefore inimical for the fabrication of optoelectronic devices. Besides, device lifetimes are inversely proportional to the TD density [19] that also cause thermal complications and consequently require intricate heat management designs [20].

For as-grown heteroepitaxial polar GaN as is (*i.e.* films grown on planar substrates without any pre/post-processing), state-of-the-art TD densities are in the order of 3.0×10^8 cm^{-2} [21] on Si (111) and 4.0×10^7 cm^{-2} on Al_2O_3 (0001) [22]. Indeed, lower TD densities, in the mid-10^6 cm^{-2} have been demonstrated, but come at the expense of additional complex fabrication steps [23]. On the other hand, TD densities of heteroepitaxial semipolar GaN range between $3.0 \times 10^7 cm^{-2}$ [24] and 2.0×10^{10} cm^{-2} [25] for patterned and planar substrates, respectively.

2.1.2.2 Basal stacking faults

Besides TDs, the most prominent structural defects in semipolar and nonpolar GaN are basal stacking faults. BSFs are planar defects locally forming an ABC cubic structure within the usual ...*ABABAB*... hexagonal stacking sequence. Three types of BSFs are distinguished in literature [26] (Figure 2.5):

- Intrinsic (I_1) BSFs: contain *one* cubic violation of the hexagonal wurtzite stacking and have a stacking sequence of: *ABABCBCBC*...
- Intrinsic (I_2) BSFs: involve *two* cubic violations of the hexagonal wurtzite stacking and have a stacking sequence of: *ABABCACAC*...
- Extrinsic (E) BSFs: contain *three* cubic violations of the hexagonal wurtzite stacking and have a stacking sequence of: *ABABCABAB*...

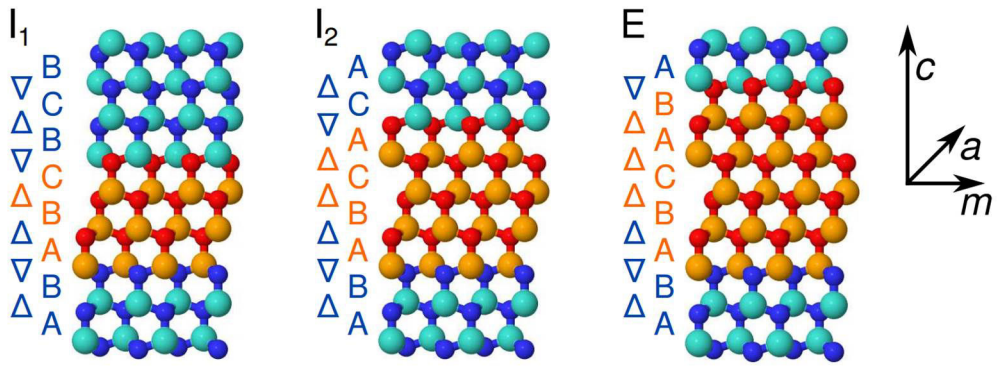

Figure 2.5 – Stacking sequences for intrinsic I_1, I_2 and extrinsic stacking faults, E. The successions $A \rightarrow B$, $B \rightarrow C$ or $C \rightarrow A$ are marked by $\triangle$, while their opposites are marked by ∇. The wurtzite stacking is an alternation $\triangle\ \nabla$, while the cubic stacking is represented by a sequence of the same operator (Image source: [27]).

When ending within a crystal, BSFs are terminated by partial dislocations (PD). PDs have a Burgers vector $\mathbf{b} = \frac{1}{6}[20\bar{2}3]$ in the case of I_1-type BSFs, $\mathbf{b} = \frac{1}{3}[10\bar{1}0]$ in the case of I_2-type BSFs, and $\mathbf{b} = \frac{1}{2}[0001]$ for E-type BSFs [28, 29]. Moreover, a BSF may be connected to another BSF through a prismatic stacking fault (PSF) situated in a prismatic $(11\bar{2}0)$ plane [30].

For c-plane GaN, BSFs are parallel to the growth surface and are rarely observed, except when low-temperature buffer layers are used [31]. In contrast, for nonpolar and semipolar layers, BSFs are aligned perpendicular and at an inclined angle with respect to the wafer plane, respectively. Formation energies of BSFs increase with the increasing number of cubic violations in the wurtzite stacking: $E > I_2 > I_1$ [29]. Having the lowest formation energy, I_1 BSFs are therefore the most common type observed.

Several BSF formation mechanisms are proposed in literature. One is a result from growth errors [32] that occur when adatoms on the growth surface bond on a wrong site (C in a stacking of ABAB). This is mainly a result of growth conditions that do not favor sufficient ad-atom surface diffusion (*i.e.* far below optimum growth temperatures) that consequently increases the formation probability of BSFs [33]. Another proposed BSF formation mechanism in heteroepitaxially grown planar nonpolar films (eventually also valid for semipolar) is a result of coalescence of nuclei at very early growth stages when a 3D nucleation is adapted. In other words, the structural and chemical differences between wurtzite materials and foreign substrates result in the high differences of interfacial energies ensuing a Volmer-Weber growth mode (*i.e.* island formation) regardless of the orientation. At early growth stages, the epilayer is not continuous and is formed along islands of nuclei of different sizes. This results in the formation of MDs nucleating independently in the different islands, hence creating lattice plane translations. The compensation of such translations leads to the formation of intrinsic

BSFs (and perfect dislocations) when the coalescence of neighboring islands occurs. This can be reduced by tuning growth conditions to shift from 3D to 2D (*i.e.* no island formation) growth modes and eventually obtain flat films from the earliest growth stages [34].

Furthermore, BSFs can also be created when the growth is performed in the N-polar, -*c*-direction [35, 36]. This has been observed in epitaxial lateral overgrowth (ELO), and is related to the growth rate of the -*c*-wing, which is slower than the +*c*-wing. As investigated by Zywietz *et al.* [37], this has been associated to the differences of adatoms diffusion on both kinds of surfaces, which results in the trapping of adatoms in the face centered cubic (*fcc*) position, hence forming BSFs in the -*c*-wings. Sun *et al.* [38] alternatively suggested an elevated impurity incorporation in -*c*-facets than in the +*c* ones eventually aiding in nucleating BSFs.

In principle the presence of BSFs is unfavorable for proper device functioning. It has been shown on highly faulted nonpolar GaN LEDs that the output power is significantly influenced by the presence of BSFs, which induce carrier scattering and laterally hamper the carrier transport in the n-GaN layers [39]. Structural identification of BSFs can be performed using TEM. Alternatively, and because BSFs are optically active defects, their presence can be detected by luminescence spectroscopy (*i.e.* photoluminescence and cathodoluminescence).

2.1.3 Polarization and the quantum confined Stark effect

Heterostructures grown along the polar orientation exhibit polarization induced electric fields that impact optoelectronic device performance and have two different origins: one which is the intrinsic spontaneous polarization, and the strain-induced piezoelectric polarization. For wurtzite crystals, the total polarization $P = P_{sp} + P_{pz}$.

2.1.3.1 Spontaneous polarization

Wurtzite structures, unlike cubic semiconductors, possess a unique polar axis (*i.e.* [0001]). As a result of the crystal polarity named in the previous section, and the electro-negativity difference between the Ga-atom and N-atom, negative charges at the (0001) surface and positive charges at the $(000\bar{1})$ surface accumulate, hence creating electric dipoles along this axis [40]. This leads to a spontaneous polarization field pointing towards the $[000\bar{1}]$ axis as shown in figure 2.6 *i.e.* from Ga-terminating surface to N-terminating one; thus $P_{sp} < 0$ [41]. The spontaneous polarization of relaxed alloys for a given composition also depends linearly on the average u parameter, which indicates that spontaneous polarization differences are mainly due to the varying the cation-anion bond length [42].

2.1.3.2 Piezoelectric polarization

The second origin of electrical polarization in heterostructures, referred to as piezoelectric, is strain-induced and depends on the strain sign [43]. The crystal deformation is induced by external deformation of the lattice constants (*a, c*) in addition to the change of the internal displacement parameter *u*. In the case of a hexagonal crystal structure, an example of strain is a thin epitaxial layer with the lattice constant a_l, grown in the polar *c*-direction on a lattice mismatched substrate with the lattice constant a_s. Initially, only the thin film will be strained (*i.e.* pseudomorphic growth). When $a_l > a_s$, the result is an in-plane negative compressive strain. When $a_s > a_l$, the layer will then be under tensile strain.

In the most general case, the piezoelectric polarization is a vector $\vec{P_{pz}}$ being related to the strain tensor σ_j via the piezoelectric tensor e_{ij} [40]:

$$P_{pz} = e_{ij}\sigma_j \tag{2.1}$$

2.1.3.3 Polarization-induced surface charges

The displacement of the cation and anion induces a dipole moment. In a crystal, the dipole moments are aligned, and successive dipoles in the polarized direction will cancel each other out. However, a discontinuity of the polarization at surfaces or at interfaces leads to a charge density at the surface/interface:

$$\sigma = (\vec{P}_1 - \vec{P}_2) \cdot \hat{n} \tag{2.2}$$

where $\vec{P}_1$ and $\vec{P}_2$ are the net polarizations at the two sides of the interface and $\hat{n}$ the unit vector normal to the heterointerface plane. It can be deduced from the above equation that the interfacial charge density is related to the orientation of this interface, and is maximal in *c*-plane oriented films. The charges at the interface consequently induce a large built-in electric field.

Figure 2.6 depicts the different directions of piezoelectric polarizations and electric fields as a function of the grown epilayers. For instance, in the compressive strain case of InGaN/GaN, the epitaxial layer is laterally compressed in the wafer plane (lattice parameters InGaN > GaN), leading to a piezo-

electric component anti-parallel to the spontaneous component. Conversely, in the tensile strain case of AlGaN/GaN, the layer is expanded along the lateral direction (lattice parameters AlGaN < GaN), and the piezoelectric component is aligned parallel to the spontaneous one [44].

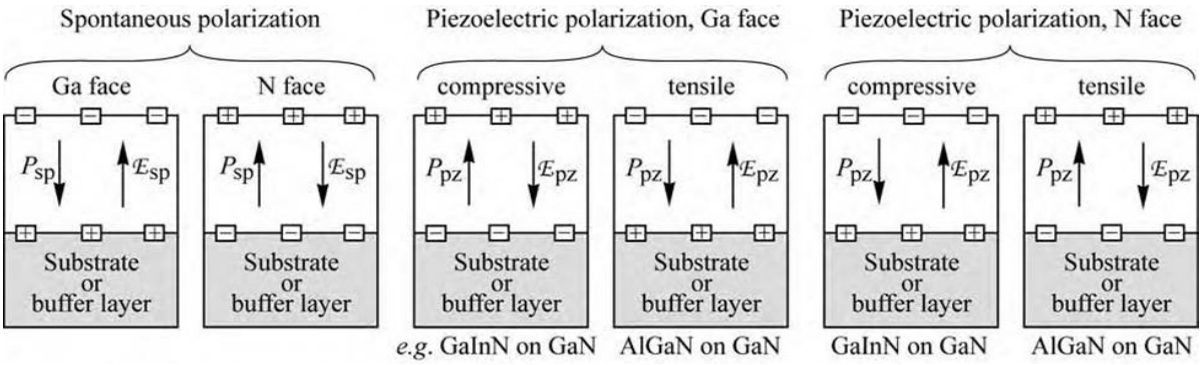

Figure 2.6 – Schematic representation of the surface charges and direction of the electric field and polarization field for spontaneous and piezoelectric polarization in III-nitrides for Ga and N faces (Image source: [1])

One experimental manifestation of polarization in heterostructures is the quantum-confined Stark effect (QCSE). In LEDs, this results in two major consequences: the spatial separation (*i.e.* reduced wavefunction overlap) of electrons in the conduction band and holes in the valence band (Figure 2.7), hence reducing the overall radiative recombination probability, in addition to the decrease in the transition energy (*i.e.* red shift) [45, 46].

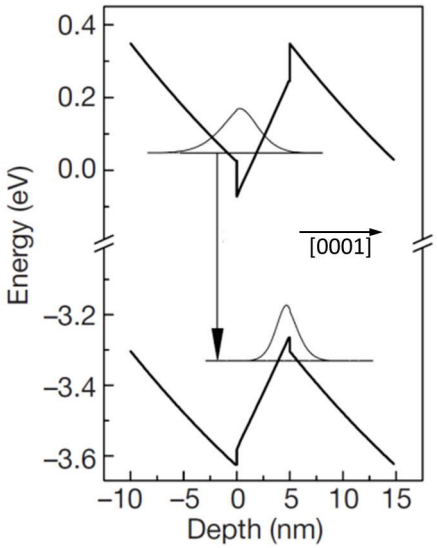

Figure 2.7 – The electrostatic fields present in [0001] heterostructures result in a QCSE and in particular in poorer electron–hole wavefunction overlap (Image source: [10]).

Although advantageous for some devices (*i.e.* transistors) [47], the QCSE has a deleterious effect on defected GaN-based optoelectronic devices grown along the *c*-axis. More particularly, this phe-

nomenon is partially responsible for the reduced efficiency of LEDs aimed to operate in the longer-wavelength portion of the visible spectrum (*i.e.* green/yellow) due to the necessity of higher InN concentrations, which consequently induce larger polarization fields [48].

2.2 Semipolar growth orientations

Having introduced some general notions on elementary crystallography and polarization, this section will focus on particularities of semipolar orientations, and eventually argue their benefits. Moreover, different approaches that permit obtaining semipolar GaN will be introduced, and two different foreign substrates for the heteroepitaxial growth will be compared.

2.2.1 Why semipolar GaN?

Despite the well-mastered *c*-plane III-N epitaxy, there are several undesirable properties that may ultimately limit the efficiency of nitride-based devices. Therefore, the growth of semipolar oriented GaN layers has become a research topic of interest especially in the last decade, and that for several major reasons. First, the reduction of polarization fields resulting in QCSE, and second, the possibility of enhanced indium incorporation.

2.2.1.1 Reduced polarization and QCSE

The primary undesired property of *c*-plane GaN for optoelectronics is the strong spontaneous and piezoelectric polarization fields that act along the growth direction. Early theoretical studies suggested that polarization effects in GaN optical devices could be mitigated by rotating the polar axis away from the polarization discontinuity interface. Orienting layers on different planes permits the reduction of polarization induced charges by changing the angle between the heterointerface and the polar axis. In 2000, Waltereit *et al.* [10] experimentally demonstrated the first polarization-free III-N structures in $(1\bar{1}00)$ GaN grown on (100) $LiAlO_2$ substrates.

A comprehensive polarization analysis published by Romanov *et al.* [11] incorporating strain and stress components and elastic anisotropy, shows the dependence of the total polarization discontinuity on θ (*i.e.* inclination angle of the *c*-axis) for InGaN/GaN layers (Figure 2.8). The total polarization discontinuity projected perpendicular to the interface is maximum for *c*-plane (0001), crosses zero at $\theta \simeq 45°$, switches sign, and again becomes zero for nonpolar $(10\bar{1}0)$. For orientations beyond 90°, the total polarization discontinuity exhibits a reverse sign. For instance, the polarization discontinuity on semipolar $(20\bar{2}\,\bar{1})$ is positive, while the polarization discontinuity on semipolar $(20\bar{2}1)$ is negative,

but exhibit the same magnitude. Also from figure 2.8, both $(20\bar{2}\,\bar{1})$ and $(20\bar{2}1)$ oriented InGaN QWs exhibit about a quarter of the polarizaton discontinuity obtained on *c*-plane, suggesting a greatly reduced QCSE.

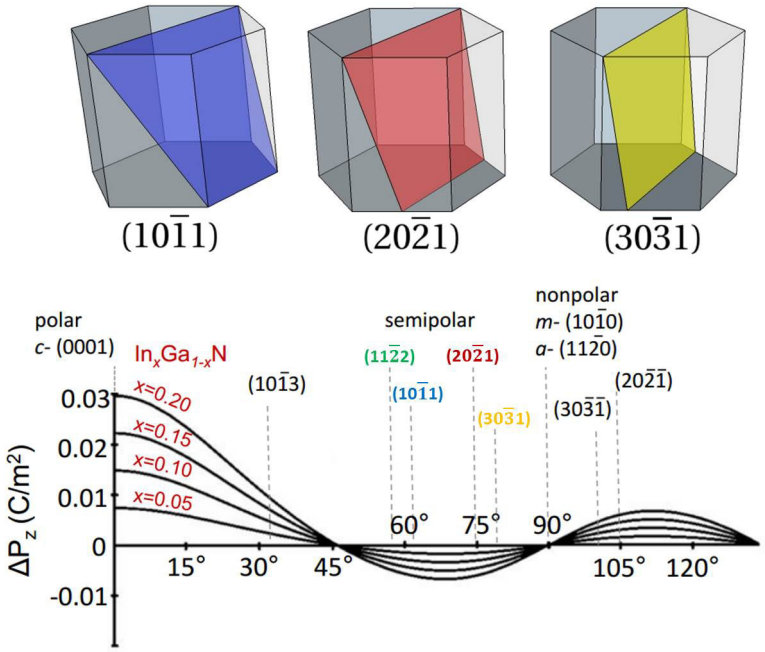

Figure 2.8 – Polarisation variation as a function of the semipolar plane inclination (Image source: [11]).

Thus, by decreasing the influence of the polarization fields, the electron-hole wavefunction overlap is enhanced, resulting in an improvement in the radiative emission rates. The effect of fixed interfacial or surface polarization charges can be nullified or reduced by performing growths along nonpolar or semipolar orientations. Semipolar oriented layers exhibit finite (eventually nullified for some particular orientations), but reduced spontaneous and piezoelectric polarization fields compared to those on *c*-plane. This is illustrated in figure 2.9.

2.2.1.2 Possibility of enhanced indium incorporation

Since semipolar surfaces are expected to alleviate the problem of polarization discontinuity at interfaces between layers with different indium compositions, examining properties of different growth planes and their behavior regarding the incorporation of indium, dopants and impurities is necessary if the mastering of QW growth is to be developed. It is likely that these features are impacted by factors such as the density of dangling bonds, step edges and surface nature.

Theoretically, it has been shown by Northrup and Neugebauer [50] that semipolar surfaces such as $(11\bar{2}2)$ and $(10\bar{1}1)$ expose binding sites for Ga and In atoms that may accommodate the relatively larger In atoms more easily than sites available on the polar (0001) and nonpolar $(10\bar{1}0)$. It has also

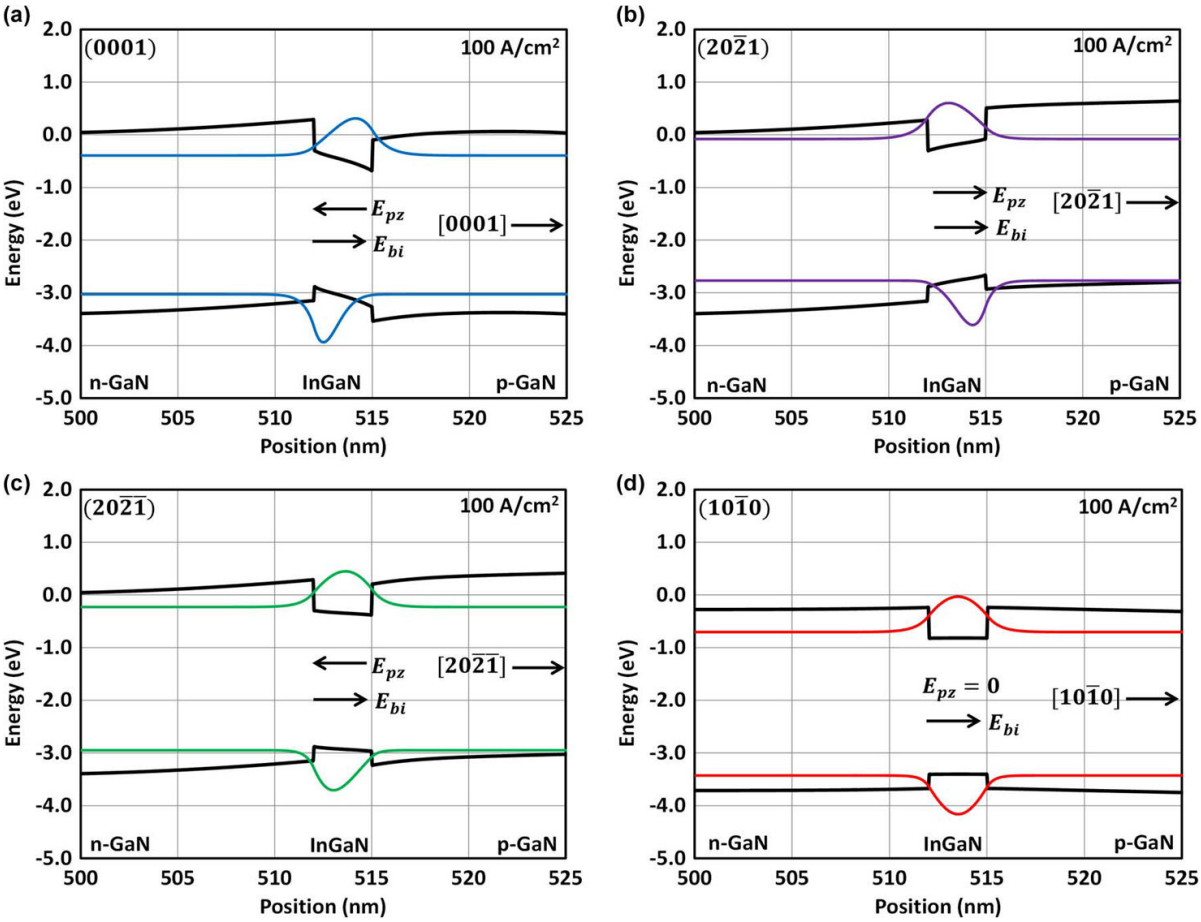

Figure 2.9 – Simulated energy band diagrams for (a) polar (0001), (b) semipolar (20$\bar{2}$1) (c) semipolar (20$\bar{2}\,\bar{1}$) and (d) nonpolar (10$\bar{1}$0). (Image source: [49])

been demonstrated that indium will, over a large range of growth conditions, incorporate in higher concentrations on the (11$\bar{2}$2) than on the (10$\bar{1}$0) as a result of the significantly lower In chemical potential [51]. Moreover, a repulsive interaction between In and Ga atoms has been noted to be higher in In-rich (0001) surfaces [52] than on semipolar surfaces. This smaller effective interaction in semipolar surfaces partially cancels the repulsion arising from the strain and becomes an attractive interaction arising from in-plane bonding between neighboring indium atoms.

Experimentally, Zhao *et al.* [53] compared the indium incorporation on nonpolar and several semipolar planes. They showed that (11$\bar{2}$2) and (20$\bar{2}\,\bar{1}$) exhibit the highest indium incorporation, and that they can be grown at higher temperatures than their (11$\bar{2}\,\bar{2}$) and (20$\bar{2}$1) counterparts for the same emission wavelength. Wernicke *et al.* [54] showed that photoluminescence and electroluminescence emission energies for QWs grown on different crystal orientations show large variations reaching up to 600 meV (Figure 2.10). The emission energy was investigated throughout a wide range of growth temperatures and indicated that the (10$\bar{1}$1) plane shows the highest indium incorporation

efficiency compared to the (0001) plane and other semipolar planes (*i.e.* $(11\bar{2}2)$ and $(20\bar{2}1)$). So, for the same indium concentration, higher growth temperatures can be enabled because of a higher incorporation.

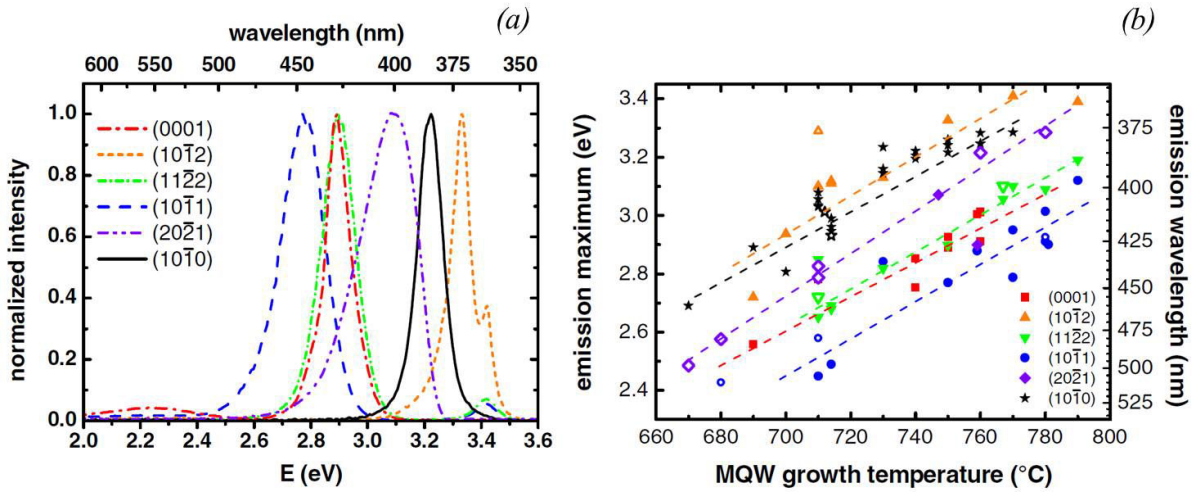

Figure 2.10 – (a) Normalized room-temperature PL and EL emission spectra for c-plane, semipolar and nonpolar InGaN QWs grown at 750°C. (EL for $(20\bar{2}1)$, PL for all other orientations. (b) Room-temperature PL and EL emission energies for c-plane, semipolar and nonpolar InGaN QWs as a function of the growth temperature. Filled symbols denote MQWs and open symbols denote SQW. (Image source: [54])

In terms of device fabrication, it appears that these higher indium concentrations can be achieved on semipolar GaN, as shown on the $(11\bar{2}2)$ semipolar orientation that resulted in LEDs with wavelengths from 527 to 568 nm and improved EQE [55]. 531 nm [56], 530 nm [57] and 520 nm [58] green lasing of InGaN Based LDs on semipolar $(20\bar{2}1)$ free-standing GaN substrates have also been demonstrated.

Indeed, different semipolar planes have shown more or less similar efficiencies, and this may be a result of the different growth properties between these crystallographic orientations. However, experimental demonstrations remain, to-date, controversial in determining the "best" semipolar plane for largest indium incorporation [59]. Moreover, whether or not indium incorporation on semipolar GaN is enough to give a significant edge over polar GaN remains highly disputed.

2.2.1.3 Efficiency droop

Another significant and enduring challenge faced by GaN-based LEDs is the loss of efficiency at high operating current densities (*i.e.* beyond the point where the efficiency peaks), also known as *efficiency droop* (Figure 2.11). Droop is also a reason behind the elevated cost of LED bulbs. For example, instead of generating, say 100 W output with a single 1 mm^2 chip, manufacturers need to use ten chips driven at 10 times lower currents. The physical cause of the efficiency droop is highly controversial and to-date remains a topic of active research. Plenty of conflicting results have

been reported on the origin of the droop, and the LED community has not yet reached a consensus to answer the question. There are several proposed mechanisms brought forward to explain this phenomenon, among them are: Auger recombination and electron leakage.

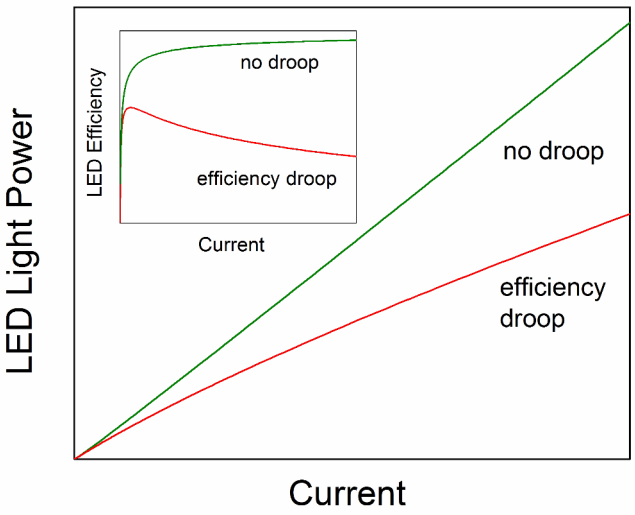

Figure 2.11 – Illustration of LED efficiency droop. (Image source: [60]).

- **Auger recombination:** In the Auger process, an electron recombines with a hole, transferring the released energy for exciting a third carrier instead of emitting a photon. Auger scales as the third power of carrier density, and thus, its importance increases for larger injection currents [61], meaning that there is a higher proportion of electron-hole interactions that don't lead to radiative recombination [62].

- **Electron leakage:** Generally refers to the escape of electrons from the active region to the p-type region. The leaked electrons may then recombine with holes either in the p-type region or at the contacts thereby reducing the hole injection into the QWs.

  In GaN-based LEDs, electron leakage from the active region is enhanced at high injection currents by sheet charges at heterointerfaces that result from the polarization induced electric fields. The positive sheet charges which are attractive to electrons cause the conduction band to be pulled down. As a result, the effective barrier height for electrons is reduced resulting in a large electron leakage [63].

The Auger effect, a priori, can be minimized when thick QWs are used. Thick QWs increase the recombination volume, which in turn reduce carrier density, and make three-carrier interactions required for Auger recombination less probable. However, achieving this in *c*-plane GaN is difficult

as increasing the InGaN QW thickness leads to a further decrease in the electron-hole wave-function overlap. On the other hand, one way electron leakage can be reduced is by reducing the piezoelectric fields in the structures hence minimizing the band structure deformation. Therefore, using semipolar oriented layers reduces the piezoelectric field, enables thicker QWs and thus minimizes the droop.

Having listed the potential, yet controversial advantages of semipolar over polar GaN, the issue of determining the ultimate substrate and eventual most adapted growth technique remains a highly debated issue.

2.2.2 How: Semipolar GaN? Homoepitaxy

Efficient and long lifetime GaN based optical devices emitting in the long wavelength regime require high crystalline quality. Ultimately, and of course depending on the intended application (*i.e.* LDs or LEDs: the former necessitates lower defect densities whereas the latter is more tolerant.), TD densities in the $10^5 cm^{-2}$ range and BSF-free layers are highly desirable [39].

Several methods are currently employed for the fabrication of high-quality semipolar GaN substrates (Figure 2.12). In 2008, Kenji *et al.* [12] demonstrated that by growing a few centimeter thick *c*-plane "boules" by HVPE [1] and subsequently slicing them at particular angles, the desired nonpolar (90°) or semipolar (inclined) planes can be obtained (Figure 2.13). This technique achieves TD densities in the order of $10^5 cm^{-2}$. GaN single crystals with TD densities as low as $10-100 cm^{-2}$ have been also reported using high nitrogen pressure solution (HNPS) growth [14]. Furthermore, the ammonothermal method [2] has demonstrated TD densities below $10^4 cm^{-2}$. This method, for now, is the most interesting since it has the potential to be up-scaled to close the gap with large surface area substrates currently used commercially [13, 64].

All the aforementioned fabrication techniques have a common advantageous trait that is the drastically low TD densities that can be achieved which remains, to-date, several orders of magnitude lower than typically reported for semipolar layers grown heteroepitaxially.

Besides drastically reducing TD densities, these methods lead to nominally BSF-free material. These substrates are therefore valuable for the fundamental understanding of semipolar GaN behavior experimentally and for demonstrating the ultimate device performance. However, their current size (typically 10 mm × 20 mm), price and production volume fall short of the industrial needs. At this point, foreign substrate usage, namely silicon and/or sapphire becomes inevitable.

[1] Mitsubishi Chemical Corporation (Japan)
[2] Ammono (Poland)

Figure 2.12 – (a) Ammonothermal pure GaN crystal (Ammono, Poland) (b) As grown HVPE GaN (Mitsubishi Chemical, Japan) (c) High Pressure Solution Growth. (Image source: Yole Développement.)

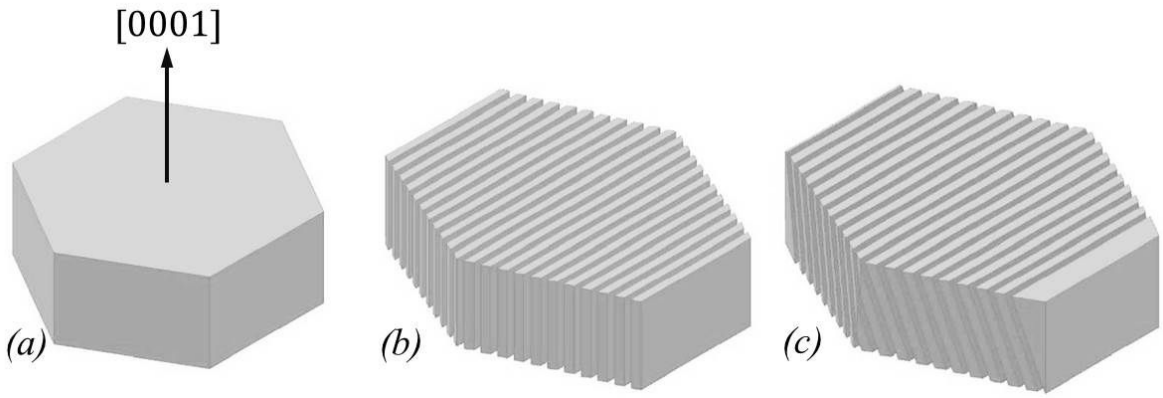

Figure 2.13 – Schematic illustration of (a) c-plane as-grown HVPE boules that are sliced at (b) 90° *for nonpolar and (c) at intermediate angles for semipolar.*

2.2.3 How: Semipolar GaN? Heteroepitaxy

Several approaches are available for the growth of semipolar GaN on foreign substrates. One of them, and virtually the simplest one, is the direct growth of GaN on a planar foreign substrate. A more complex approach involves substrate pre-patterning. Both approaches will be discussed below.

2.2.3.1 Planar growth

Several attempts on the direct growth of semipolar GaN on a planar foreign substrate have been published such as the growth of $(11\bar{2}2)$ and $(10\bar{1}3)$ [65, 25] GaN on *m*-plane sapphire. Ravash *et al.* [66] also demonstrated the growth of single component semipolar GaN on planar high index Si $(11h)$ substrates. Planar growth of semipolar GaN on flat spinel (*i.e.* $MgAl_2O_4$) substrates was also attempted [67]. However, the common feature between all reported layers remains their low film qualities, which is insufficient for device fabrication. Typically, semipolar GaN films grown on planar sapphire substrates exhibit a BSF density of $2.0 \times 10^5\ cm^{-1}$ and TD density of $2.0 \times 10^{10}\ cm^{-2}$ [25].

Defect reduction routes have therefore been applied in order to reduce the elevated defect densities. For example, *in-situ* LT-AlN interlayers have shown to be effective in blocking BSFs from propagating to the surface [68], however such interlayers have shown to be only effective with low inclination ($\sim 20°$) semipolar orientations. Additionally, the classical ELO has been implemented for BSF and TD blocking [69], but this technique is effective in blocking the defects from the "wing" regions whereas defects generated in the openings eventually terminate at the surface and keep large areas on the top surface with elevated densities of defects.

Therefore, the direct planar growth provides simplicity and straightforwardness over any other process. However, the approach comes at an in-affordable price as the layers remain plagued with BSFs despite the attempts for their elimination. As a result, alternative approaches to grow a wider range of semipolar orientations on foreign substrates must be adapted if low-defect films, and eventually devices, have to be realized.

2.2.3.2 Semipolar GaN on inclined *c*-facets

The growth of III-nitrides along the polar *c*-direction is now well mastered and high quality crystalline heteroepitaxial films are obtained. Taking advantage of that feature, Honda *et al.* [70] proposed to use a method involving the patterning of substrates with the objective of exposing inclined facets on which inclined GaN polar growth along [0001] would take place. Further coalescence of consecutive GaN bands allows the formation of a continuous semipolar layer. This approach is equally applicable for both, silicon [71] and sapphire [72, 73, 74].

This method presents a rather simple pre-growth processing approach, and is described in the following list and depicted in figure 2.14 [3]:

- Substrate processing is initiated by depositing a dielectric mask (*e.g.* SiO_2 and/or SiN) that prevents GaN nucleation on the horizontal substrate surface.

- Then, using conventional photolithography, the substrate is patterned with a striped mask to form bands (stripe directions and orientations vary as a function of the substrate and the wanted nucleation facets. Details will be given for each orientation in the subsequent chapters).

[3] It is to be noted here that the displayed schematics solely serve to clarify the concept and relationship between the substrate orientation, nucleation facet inclination and eventual obtained semipolar layer. The schematics do not comply to accurate to-scale dimensions, and they may largely vary depending on the substrate and the fabrication.

- Afterwards, the substrate is anisotropically etched using either a wet (KOH or TMAH for Si and H_3PO_4/H_2SO_4 for sapphire) or dry etching (RIE applicable only in the case of sapphire) to finally obtain etched openings with inclined nucleation facets (typically two {111} facets for Si and one (0001) facet on sapphire).

- Finally, in the case of Si, in order to dictate the growth only on the adequate facet, an IBS [75] machine is necessary, permitting an inclination of the substrate with respect to the ion beam to deposit a dielectric layer therefore masking the opposite sidewall[4]. In the case of sapphire, the inclined deposition approach can be utilized, however, and since the etched facets are not equivalent, by adjusting the growth conditions, the growth can be performed solely on the desired nucleation facet.

- Inclined growth then proceeds on the adequate facet in the +*c*-direction until adjacent crystals coalesce, and a semipolar layer is obtained (Figure 2.14).

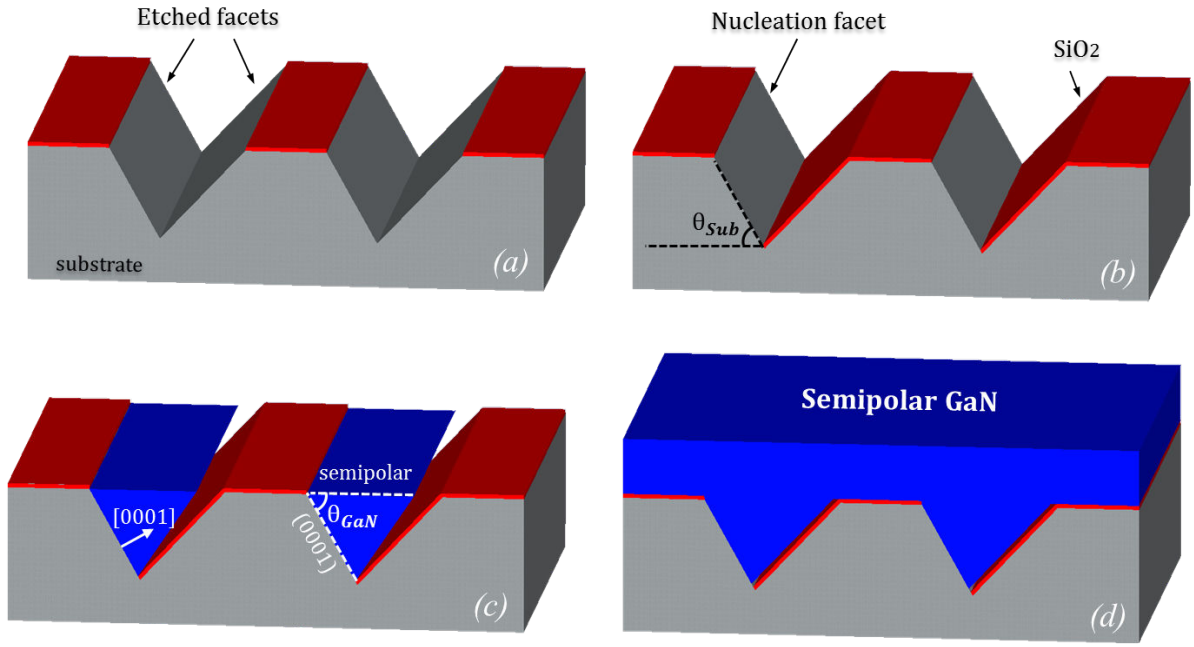

Figure 2.14 – Fabrication process and patterning depiction of the substrates and the selective area growth of c-GaN on the inclined facets to form a continuous layer of semipolar GaN when adjacent crystals coalesce.

The semipolar orientation of the resulting GaN film depends on the inclination of the facets with the substrate surface plane. In order to obtain interesting semipolar orientations parallel to the substrate's surface, the angle between the nucleation facet and the substrate surface has to be equivalent

[4]Illustration and description of the IBS mode of operation is shown in Appendix A

to the inclination between the GaN *c*-plane and the targeted semipolar plane. Table 2.1 lists the interesting GaN orientations as a function of the substrate orientation and the respective nucleation facet inclination.

Substrate	Orientation	Angle to nucleation facet	Semipolar GaN	Angle to (0001)	Ref.
Silicon	(001) 7° off	61.74°	$(10\bar{1}1)$	61.76°	[70]
Silicon	(113)	58.52°	$(11\bar{2}2)$	58.22°	[71]
Silicon	(113)	79.98°	$(30\bar{3}1)$	79.68°	[This Thesis]
Silicon	(114) 1° off	74.83°	$(20\bar{2}1)$	74.85°	[This Thesis [76]]
Silicon	(111) 4° off	74.53°	$(20\bar{2}1)$	74.85°	N/A
Sapphire	$(11\bar{2}3)$	61.76°	$(10\bar{1}1)$	61.76°	[72]
Sapphire	$(1\bar{1}02)$	58.22°	$(11\bar{2}2)$	58.22°	[73]
Sapphire	$(22\bar{4}3)$	74.85°	$(20\bar{2}1)$	74.85°	[74]

Table 2.1 – Obtainable semipolar GaN orientations as a function of the initial substrate orientation

This approach is more advantageous than the direct planar growth of GaN on a foreign substrate: *first*, because the nucleation footprint is reduced, therefore reducing the total number of generated defects; *second*, because the mastered polar growth will be exploited for growing semipolar GaN; and *third*, as will be detailed later, this inclined growth enables a significant reduction of dislocations propagating to the surface via TD bending.

The promising features this technique presents has attracted the interest of many groups working on semipolar GaN, including us. So this PhD will focus on adapting this approach on silicon substrates to address and investigate different semipolar orientations. As a result, it is here important to emphasize that all the growths in this work will take place along the +*c*-direction regardless of the final semipolar orientation, which means that the growth is always Ga-polar.

2.2.4 Heteroepitaxial semipolar GaN: Sapphire or Silicon?

Having chosen the growth method of semipolar GaN on a foreign substrate, the next step involves the substrate selection: sapphire or silicon?

Apart from the necessity of meeting industrial needs, cost is the main driver for foreign substrate usage. Besides cost, both, sapphire and silicon provide advantages over homoepitaxy in terms of abundance and large surface area availability. However, criteria such as lattice matching, thermal expansion coefficients, surface chemistry, temperature stability and conductivity are to be addressed in order to achieve high-quality GaN layers.

2.2.4.1 Sapphire

Up to date, sapphire remains the substrate on which the vast majority of GaN-based optoelectronic devices are manufactured. Sapphire is relatively low-cost compared to bulk GaN and is now available in surface area diameters reaching up to 6 in.. Moreover, despite the high lattice mismatch ($\sim 16\%$) with GaN and the higher thermal expansion coefficient ($5.45 \times 10^{-6} K^{-1}$ for GaN and $7.50 \times 10^{-6} K^{-1}$ for Al_2O_3) causing compressive strained layers [77], GaN (polar) grown on sapphire has reached very high qualities and matured technologies enabling devices meeting commercial needs. Furthermore, unlike silicon, growth of GaN on sapphire does not face two major issues: neither cracking nor meltback etching (which will be later discussed and detailed in this manuscript).

2.2.4.2 Silicon

As mentioned earlier, a major reason for the growth of GaN on silicon is the availability of large diameter substrates and with it the possible reduction of manufacturing cost. It is therefore fruitful to further examine where silicon is dominant elsewhere.

Specific advantages of silicon include the source material, silica, which is widely abundant, inexpensive, and can be refined into high-purity silicon, in addition to having a crystal perfection better than any other substrate. Large ingots of silicon are readily produced by the Czochralski method [78]; 12 in. (300 mm) diameter wafers are currently in industrial production lines (for electronic applications) and 18 in. (450 mm) diameter wafers [79] are expected in the next 2-5 years. Moreover, silicon provides a larger frame for manipulating substrates. In terms of pre-growth patterning (*i.e.* masking, wet and plasma etching). This possibility brings a new degree of freedom towards a wider framework to be tested. Silicon can also meet the requirements for conducting substrates that will potentially enable integration of optoelectronic devices with Si based electronics.

Furthermore, and besides the aforementioned advantages to adopt silicon as a substrate, the most significant feature of silicon is the possibility of using crystalline orientations that enable the growth of the interesting semipolar GaN orienations (Table 2.1). Indeed, this possibility exists also for sapphire but remains more challenging because of the inherent difficulty of slicing sapphire along "exotic" orientations.

Without any doubt, silicon does present an interesting ensemble of advantages. However, significant intrinsic crystallographic and chemical disadvantages are also present to hamper meeting industrial necessities. These disadvantages, due to their significance for this PhD will be discussed separately in section 2.2.5.2.

Nevertheless, the economic imperative, particularly the requirement to increase production and reduce costs by using larger wafers, still gives an edge for silicon over sapphire and is the primary reason capturing the interest of many research groups and industrials.

In this PhD, silicon has been chosen to be the substrate of focus, and as mentioned earlier, the growth on the inclined facets will be adapted. From now on, properties and characteristics of the growth of (0001) GaN on Si (111) will be the center of attention regardless of the final semipolar orientation.

2.2.5 Semipolar GaN on silicon

2.2.5.1 GaN (0001) - Si (111) epitaxial relationship

All the epitaxial layers investigated in the framework of this project have been grown on silicon substrates. Regardless of the initial wafer orientation, after the substrate patterning, Si (111) will be the only nucleation plane for GaN. For GaN growth on Si, Si(111) is the most frequently used orientation, regardless of the implemented growth method (*i.e.* MOVPE or MBE) because of its trigonal symmetry (Figure 2.15).

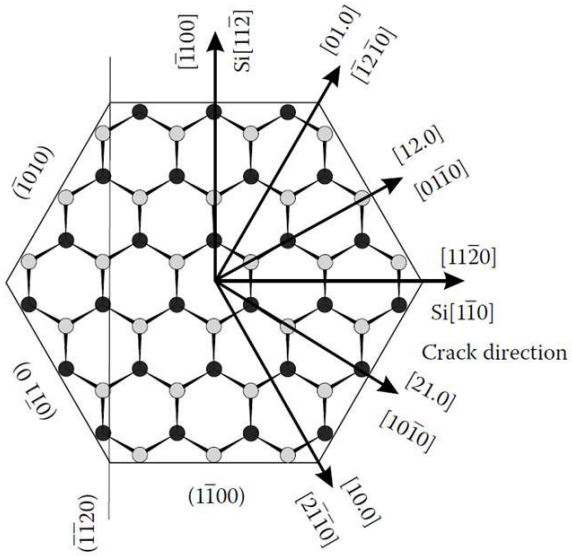

Figure 2.15 – GaN (0001)- Si (111) epitaxial relationship. (Image source: [80])

2.2.5.2 Problems associated with Si

Despite the handful advantages that silicon provides, it does come with disadvantages. In the analysis of the issues limiting the epitaxy of III-N materials on silicon substrates, investigators in the field have commonly focused on three main factors that will be subsequently detailed: (1) large lattice mismatch between GaN (0001) and Si (111); (2) cracking problem; (3) meltback etching.

Lattice mismatch: the large difference in the lattice parameters of GaN ($a_{GaN(0001)} = 0.31892nm$) and ($a_{Si(111)} = 0.38403nm$) yields a lattice parameter mismatch of −16.9% (+16% for sapphire) which is one of the reasons for high TD densities for GaN on Si (111).

Cracking: besides the lattice mismatch, indeed, the thermal expansion coefficient of GaN in comparison to that of Si is also highly mismatched. The in-plane (*i.e.* GaN (0001) and Si (111)) thermal expansion coefficient of GaN is $5.59 \times 10^{-6} K^{-1}$ and that of Si is $3.77 \times 10^{-6} K^{-1}$ [81]. This mismatch leads GaN layers to be under tensile stress (compressive in the case of sapphire) during cool-down from growth to room temperature, thus generating cracks for thicknesses exceeding 1 μm [80]. Smooth layers with low dislocation densities can be only achieved when a sufficient thickness above 2 μm is grown. This thickness is necessary for most devices since it enables defect filtering (for example 3D growth modes which require higher thicknesses to coalesce) to in turn yield enhanced quality epilayers.

The cracking problem however, can be overcome, and there are two fundamentally different methods for achieving thick crack-free GaN on Si [82]. The first method is the growth of a graded AlN-AlGaN buffer layer on top of Si whose role is to place GaN under compression and thus compensate the tensile stress whilst the cool-down takes place [83, 84] thus leading to completely crack free layers [85]. In a similar manner, the introduction of AlN interlayers (LT-AlN [86] and HT-AlN [87]) also contributes to counterbalance the tensile strain induced by the thermal mismatch. Up to 6.7 μm thick crack-free GaN layers have been grown [88] using this method. The second way is patterning the substrate to localize the growth on small areas, small enough to prevent layers from cracking [89] due to enhanced lateral strain relaxation. Using this method, completely crack free areas of 100 μm × 100 μm have been reported reaching a thickness of 3.6 μm [90, 91]. Another technique, developed by Bridgelux and previously commercialized by Toshiba [5], solves the tensile strain problem with a proprietary buffer layer that the companies claim to deliver crack-free 8 in. GaN-on-silicon wafers (No further details are accessible).

Meltback etching: One of the important challenges to epitaxial growers working on GaN-on-Si is meltback etching. First described by Ishikawa *et al.* [83], meltback etching is an alloying reaction of Si with Ga mostly pronounced at high growth temperatures. This reaction causes deterioration in the Si and leads to numerous macro-holes and voids on the surface [92]. The exact origin is not yet clarified, but the reaction once initiated, cannot be stopped and leads to a rough surface inadequate for any sort of post-processing [93]. Being a major problem, Chapter 5 will be dedicated to the investigation of means to prevent it.

[5] The company announced its exit from the white LED business in October 2015.

2.3 Defect reduction in semipolar GaN films on inclined facetted foreign substrates

Structural defects present in any heteroepitaxially grown film are related to differences between the substrate and the deposited films mostly in terms of structure, chemistry, lattice parameters and thermal expansion coefficients. Numerous foreign substrates have been tested for the growth of semipolar III-nitrides (*i.e.* $(1\bar{1}02)$ *r*-sapphire, $(1\bar{1}00)$ *m*-sapphire, Si (112) , or (100) $MgAl_2O_4$) and they all differ from III-nitrides by at least one of the aforementioned properties [94]. The microstructures of heteroepitaxially grown GaN films are therefore highly defective no matter what substrate is used.

Indeed, several defect-reduction methods have been applied in semipolar oriented layers. For instance, low-temperature AlN interlayers (inserted between two GaN layers) that have shown to be effective for BSF blocking in low-inclination semipolar orientations (*e.g.* $(1\bar{1}04)$ and $(1\bar{1}06)$)[68]. Other approaches involving in-situ surface treatments [95] by SiN [96] or ScN [97] have been investigated, in addition to other techniques that have been reviewed by P. Vennéguès [94].

The following sections will highlight the "sub-methods" of the main defect reduction philosophy investigated in this work which is the growth on inclined *c*-facets (see section 2.2.3.2). What is meant by "sub-methods" is basically the strategies that can be employed, or have been employed, to further reduce extended defect densities whilst this inclined growth; all towards attaining nominally defect-free semipolar layers. It is worthwhile noting here that the following methods are, in principle, equally applicable on sapphire and silicon.

2.3.1 Footprint reduction

The first naturally intuitive and effective approach to the problem of elevated TD densities is reducing the growth area footprint by selective area epitaxy. Reduced growth areas mean less room for defect nucleation at the interface between GaN and the foreign substrate. As a consequence, the number of initially generated TDs is reduced and therefore fewer propagate to the final film surface.

In the case of inclined growth of *c*-GaN, footprint reduction is feasible by the size reduction of the inclined nucleation facet (Si (111) or sapphire (0001)), which can be done by reducing the etching durations (see section 2.2.3.2) [98].

2.3.2 Growth modes

During selective area epitaxy, changing growth conditions (*i.e.* temperature, pressure, V/III ratio) affects how GaN crystals behave, and consequently influences the propagation mechanisms of dislocations. The following sections will point out two different growth modes that have different impacts on the TDs' behavior and consequently on their propagation towards the surface.

2.3.2.1 Dislocation bending induced by progressive pyramidal formation

This process, first demonstrated on stripe patterned *c*-plane GaN [99], consists of inducing the progressive formation of triangular GaN pyramids through an escalating trapezoidal buildup. During the growth, dislocations initially propagate vertically along the +*c* growth direction. A growth rate in the vertical direction being higher than the lateral one, leads to intermediate trapezoidal cross sectional shapes, as indicated by the white dashed lines in figure 2.16 (a). As the growth advances, the size of the topmost *c*-facet gradually decreases. The vertical dislocation lines then approach the free surface edge between the top and inclined facets, and then bend towards the new free surface, thus adopting a new direction in the basal plane [100, 101, 102]. Dislocations located in the center of the window are the last ones to bend, if at all, since the lateral facets first reach the dislocations closest to the edge of the mask.

The dislocation bending phenomenon implies that a vertically threading line is not the most favorable energetic configuration. For a given crystal, the energy of a dislocation depends on its Burgers vector and its line direction, and the dislocation propagates along the direction that minimizes its energy [103].

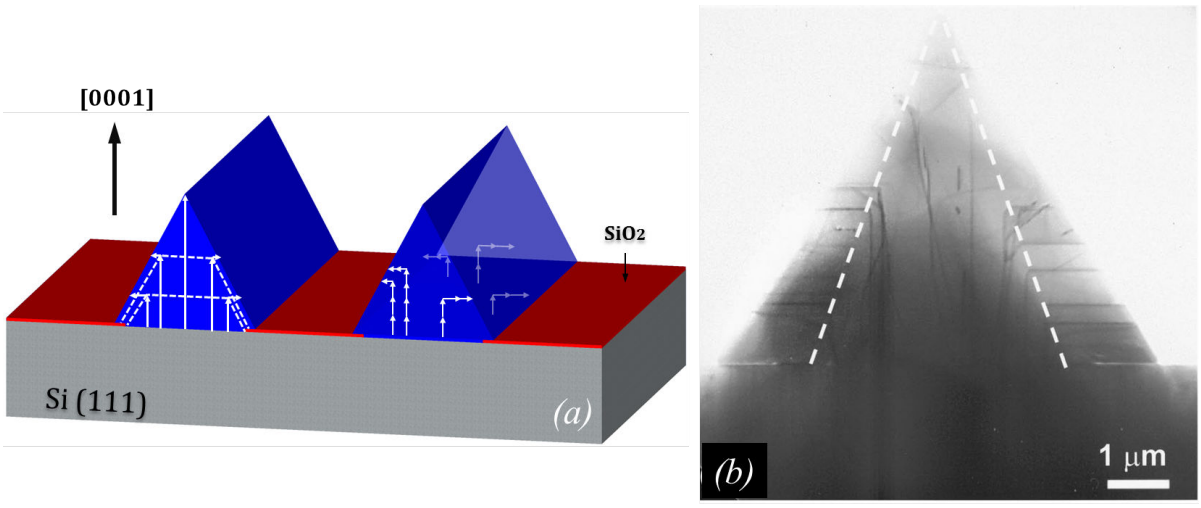

Figure 2.16 – (a) Schematic displaying TD bending upon triangular formation and (b) corresponding TEM image.

In a similar manner, the progressive formation of a triangular crystal can be applied for the inclined growth of *c*-GaN. The difference is that instead of growing *c*-plane GaN vertically (*i.e.* on a planar/horizontal Si (111) substrate), the growth of *c*-plane GaN proceeds at an inclined nucleation surface. Therefore, dislocations initially propagate parallel to the growth direction (*i.e.* inclined *c*-axis) and then bend by 90° when they intersect the pyramid limit, adapting a direction within the (0001) basal plane. After bending, TDs extend towards the surface along with the GaN from the adjacent stripe hence creating a confined area of accumulated defects (*i.e.* -*c*-wing), as shown in figure 2.17. This will be further discussed in sections 3.2.2 and 4.4, describing the defect behavior while growing $(10\bar{1}1)$ and $(20\bar{2}1)$ semipolar GaN, respectively.

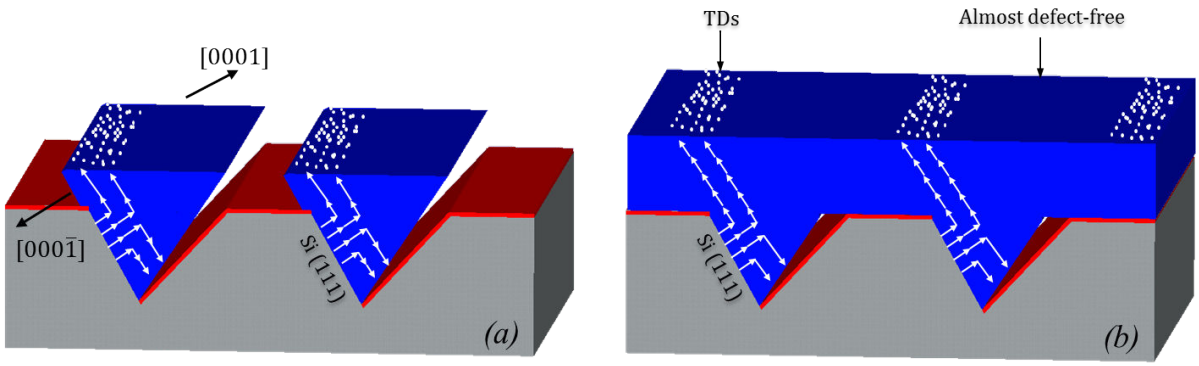

Figure 2.17 – Schematic displaying TD bending upon triangular formation for semipolar GaN (a) before and (b) after coalescence.

2.3.2.2 No pyramidal formation

In an alternative approach, growth conditions are adapted so the +*c*-direction and lateral direction grow at equivalent rates. Such a growth mode does not favor the progressive pyramidal formation discussed previously, hence no TD bending will occur. Instead, continuous propagation in the +*c*-direction will take place.

In this case, TDs emerging in the [0001] direction will be blocked by the opposite facet of the same crystal whilst coalescence occurs, thus preventing them from emerging to the surface (Figure 2.18). It is here necessary to emphasize on the importance of the created voids between adjacent crystals, since they play a key role in creating a free surface for the termination of TDs. Similarly, BSFs generated in the -*c*-direction are also terminated at the voids before they reach the surface. This approach, has been applied for the $(11\bar{2}2)$ oriented GaN layers grown on patterned Si (113) [71].

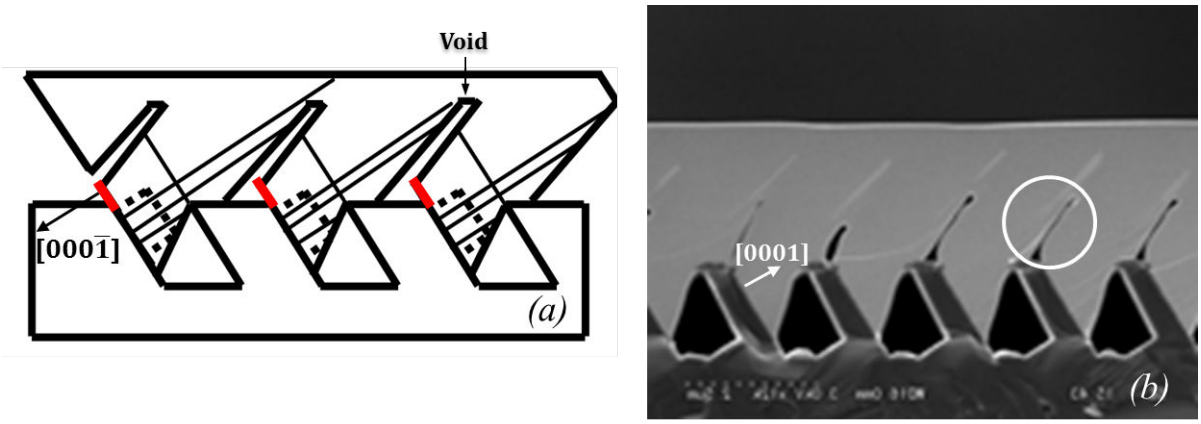

Figure 2.18 – (a) Schematic representation of TD direct propagation and their eventual blocking by the created void between adjacent crystals (red lines represent the BSFs appearing in the -c-direction) and (b) the corresponding SEM of the performed growth. (Image source: [71])

2.3.3 Voided adjacent crystal overlapping

Using a three-step growth method, planar GaN $(11\bar{2}2)$ on patterned sapphire with significant quality can be obtained. In this case, growth conditions are fine-tuned over three consecutive steps in order to overlap adjacent crystals and create "voids" that create free terminating surfaces for bent TDs and BSFs generated in the -*c*-direction and therefore inhibits their propagation towards the surface (Figure 2.19). A TD density of $5.1 \times 10^7 cm^{-2}$ and a BSF density below 30 cm^{-1} has been reported [104]. Defect blocking using voids was also demonstrated on patterned Si (113) for the same GaN semipolar orientation but by maintaining the same growth conditions throughout the entire growth process [71].

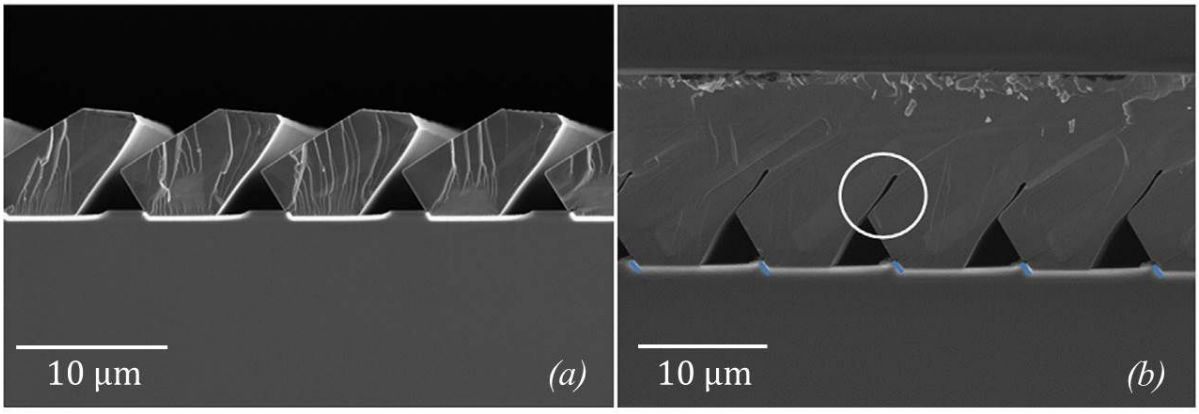

Figure 2.19 – Defect blocking mechanism by creating voids. (Image source: [104])

This technique is advantageous for several reasons: first, because it primarily solves the problem of extended defect propagation by adapting the inclined *c*-plane growth; second, layers can be achieved in a single growth run which does not come at the expense of higher complexity; third, these layers

can be a starting point for the further growth of thick HVPE layers, thereby enabling a TD reduction below $10^6\ cm^{-2}$. The growth of semipolar GaN using this method however is highly dependent on energetically favorable planes which also means that the possibility of manipulating them upon changes in growth conditions for all orientations could be difficult.

2.3.4 Dual step selective area growth

Similar to the two-step epitaxial lateral overgrowth (ELO) on polar GaN, Tanikawa *et al.* [24] demonstrated a significant reduction of the dislocation density in a semipolar $(11\bar{2}2)$ GaN stripe on a patterned Si substrate by the two-step selective growth. After depositing a SiO_2 mask on the $(11\bar{2}2)$ face of a flat coalesced GaN layer grown on a (113) Si substrate, GaN was selectively regrown only on the open windows of $(11\bar{2}2)$ face. The dislocation density estimated from the dark-spot density in a CL image reached $3.0 \times 10^7 cm^{-2}$ (Figure 2.20).

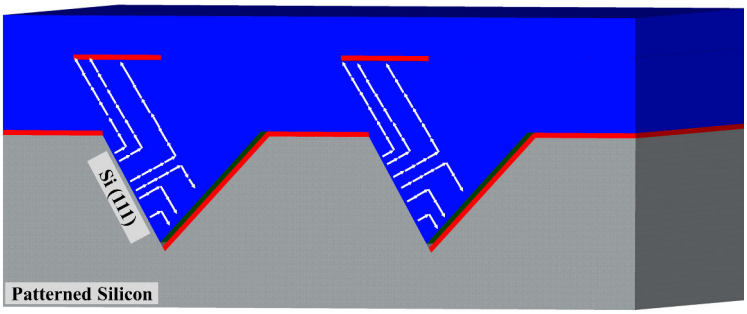

Figure 2.20 – Schematic displaying the dual step selective area growth method.

This technique is certainly effective in growing layers virtually defect-free. However, the dual growth steps adapted are undesirable. First because of the added complexity, and second because of the thermal dilation discussed earlier that may cause cracks in the first growth run, and eventually favor meltback etching in the second.

2.4 Structural and optical characterization of semipolar GaN

Before discussing the obtained results in the subsequent chapters, this section's objective is to establish a brief description of the particularities used in each characterization technique, hence, the necessary background for understanding the forthcoming results. General descriptions and detailed treatments will not be discussed here, however, the reader will be guided to selected references for further resources. The hardware/software used to acquire all the shown images and spectra will be mentioned.

2.4.1 X-ray diffraction (XRD)

Because of the fact that this thesis addresses different semipolar orientations, XRD becomes an essential tool in understanding the crystalline behavior as a function of different growth conditions and/or fabrication geometries for each orientation. HRXRD is a non-destructive technique used to explore the structural properties of the crystal. A series of structural data can be extracted from diffraction patterns, including the crystal quality (*i.e.* defect density estimations), in addition to the strain states (*i.e.* lattice parameters) of the epitaxial films. Bragg's law is the basic principle for x-ray diffraction:

$$2d_{hkl}sin\theta = n\lambda \tag{2.3}$$

where d_{hkl} is the interplanar spacing of the *(hkl)* plane, n is the diffraction order, θ is the Bragg's angle and λ the wavelength of the x-ray source pre-defined by the used apparatus. Diffraction consists of the constructive interference of x-ray waves scattered by atoms arranged periodically in a crystal that only occur if the path difference between the incident and diffracted beam is an integer multiple of the wavelength.

X-ray diffractometers generally provide six motorized movements, three translational and three rotational motions. The translational motions are represented by the orthogonal indexes X, Y, and Z that enable positioning the samples on the goniometer center. The rotational motions are represented by ω, ϕ and χ, and are illustrated in figure 2.21.

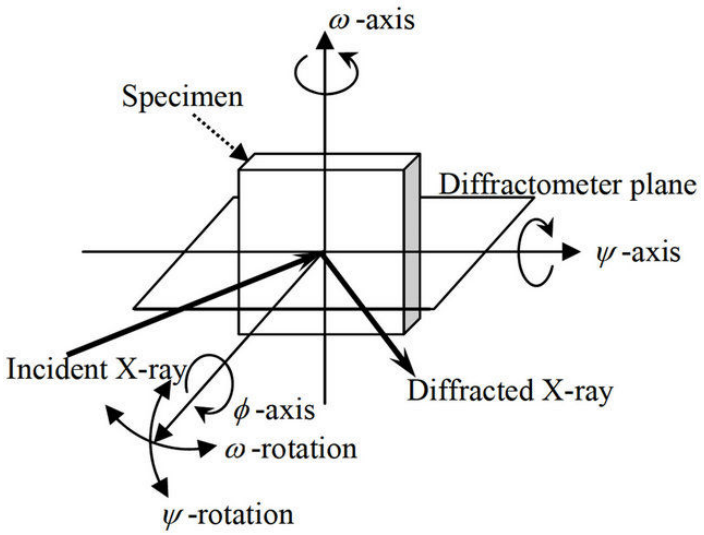

Figure 2.21 – Commonly used angles in HRXRD: ω, ψ, ϕ and χ (Image source: [105])

The following lists the most common types of XRD scans and their corresponding description:

- ω: The detector remains stationary, and the sample is rotated around the ω axis. An ω-scan is also called a "rocking curve", as it corresponds to the rocking of the sample with respect to the ω axis. ω scans are typically used to evaluate the crystal quality, as the line width of the peak is usually broadened by dislocations and wafer curvature.
- $2\theta - \omega$: The sample is rotated by ω and the detector is rotated by 2θ, with an angular ratio of 1:2. It probes the radial directions in reciprocal space, and thus, it is used to evaluate the lattice parameters.
- ϕ: Rotation of the sample around an axis perpendicular to its surface.
- χ: Rotation of the sample around an axis contained within its surface and the plane defined by the incoming beam and the detector arm.

The most common measurement used to asses the structural quality of a thin film is the FWHM of a rocking curve performed on a symmetrical reflection (*i.e.* corresponding to a crystallographic plane parallel to the sample surface). Rocking curves of the symmetrical reflection have been recorded at different azimuths, ϕ angles, as shown in figure 2.22. By varying ϕ what is effectively changed is the in-plane direction contained within the scattering plane during the measurement [106].

Unlike polar oriented GaN, in semipolar and nonpolar orientations, the rocking curve FWHM of symmetric reflections varies periodically as the sample is rotated around an axis normal to its surface [107]. Figure 2.22 shows an example from a sample grown in this PhD where the FWHM alternates with ϕ and exhibits minima and maxima when the in-plane projection of the x-ray is parallel and perpendicular to the stripes, respectively.

The source of this anisotropy in semipolar and nonpolar films remains, to-date, controversial. Several reports discuss this variation and associate it to different reasons. According to Paskova *et al.* [108], anisotropy is only visible for nonpolar layers grown on foreign substrates and is absent for bulk material. The group demonstrated that heteroepitaxially grown GaN possesses a high density of BSFs leading to anisotropic structural characteristics, while the $(11\bar{2}0)$-plane bulk GaN, sliced from boules, exhibits a low defect density and thus narrow rocking curves with isotropic in-plane character. Also, McLaurin *et al.* [109] show that BSFs are the predominant source of rocking curve width anisotropy in their investigated nonpolar m-plane films. By using the Williamson-Hall analysis, BSF densities in highly faulted films were estimated, and a linear broadening with the increase in BSF densities was detected. Roder *et al.* [110] suggested that the elastic and thermal anisotropies of the GaN and the substrate (sapphire in their case) result in an in-plane stress and a wafer curvature, both of which

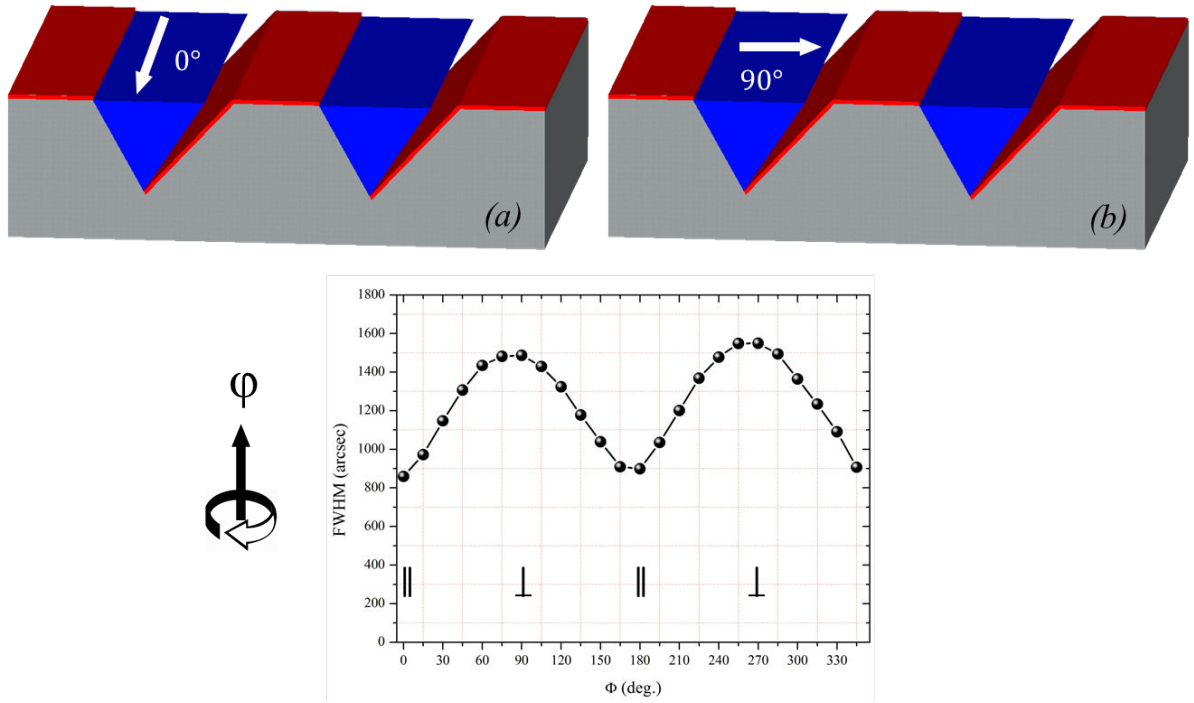

Figure 2.22 – Omega scans on the azimuthal angles parallel and perpendicular to the stripes.

are different in the two in-plane directions parallel and perpendicular to the GaN *c*-axis. Moreover, GaN $(11\bar{2}0)$ samples grown by HVPE with a thickness variation from 6.7 μm to 64.8 μm were studied, and a broadening of reflections as a function of thickness was observed and was directly associated to wafer bending. Others suggest crystal mosaicity [111] and surface roughness to be contributors to this observed anisotropy in nonpolar and semipolar GaN.

While all the above mentioned effects may contribute to this anisotropy, a study conducted by Serafińczuk *et al.* [112] investigating nominally perfect nonpolar and semipolar samples cut from the same ammonothermal grown crystal, has also shown rocking curve FWHM broadening along different in-plane directions. This study concludes that the observed anisotropy in nonpolar and semipolar GaN is an intrinsic property of these orientations.

In any case, and regardless of the origin of this anisotropy, the rocking curve FWHM is a qualitatively representative measurement and will be utilized as a reference throughout the subsequently presented results, to evaluate the improvement or degradation of the layers.

High resolution X-ray diffraction measurements were carried out in a Panalytical X-ray diffractometer using CuKα radiation (λ = 0.154056 nm).

2.4.2 Transmission electron microscopy (TEM)

TEM is the tool employed for the micro-structural characterization of the grown layers offering a broad range of characterization capabilities at high spatial and analytical resolutions. In practice, TEM focuses an electron beam on a specimen creating diffraction patterns that can be measured from microscopic regions. TEM can be used to make images of the electron intensity emerging from samples. Variations in the electron diffraction intensity across a specimen is referred to as "diffraction contrast" and is useful for creating images of defects. In the framework of this project, TEM is primarily used for in-depth evaluation of defect structures, namely TDs and BSFs and their behavior in the grown layers.

2.4.2.1 TEM operation modes

After the electron beam hits the sample situated in the object plane, electrons are scattered. Electrons scattered in the same direction are focused in the back focal plane, and as a result, a diffraction pattern is formed there, and can be projected on the visualization screen. By positioning an objective aperture at the diffraction plane (*i.e.* where the diffracted beams are focalized), an image is created in the image plane with only the electrons that have been diffracted by a specific angle [113]. This defines two imaging modes illustrated in figure 2.23:

- When the aperture is positioned to pass only the transmitted (un-diffracted) electrons, a *bright-field* (BF) image is formed. In this case, the crystalline parts in Bragg orientation (*i.e.* highly diffracting) appear dark and the less diffracting regions appear bright.
- When the aperture is positioned to pass only one diffracted beam, a *dark-field* (DF) image is formed. By tilting the incident beam, the diffracted beam becomes positioned in the center and can be selected without re-positioning the aperture.

To obtain lattice images, an atomic resolution is required, thus, high-resolution TEM (HRTEM) mode is used. In this mode, a large objective aperture is selected, which permits various beams, including the direct beam to pass. This creates an image formed by the interference of the diffracted beams with the direct beam. If the microscope resolution is sufficiently high, then HRTEM images are obtained.

Another technique used in this thesis is scanning transmission electron microscopy (STEM). Images may be acquired by focusing the electron beam into a narrow spot, which is scanned over the sample, thus producing an image. Also, by using a high-angle annular dark field (HAADF) detector, direct information on local chemistry at the atomic scale may be also obtained. This is due to the atomic-number (Z) sensitive nature of the HAADF contrast (Z-contrast).

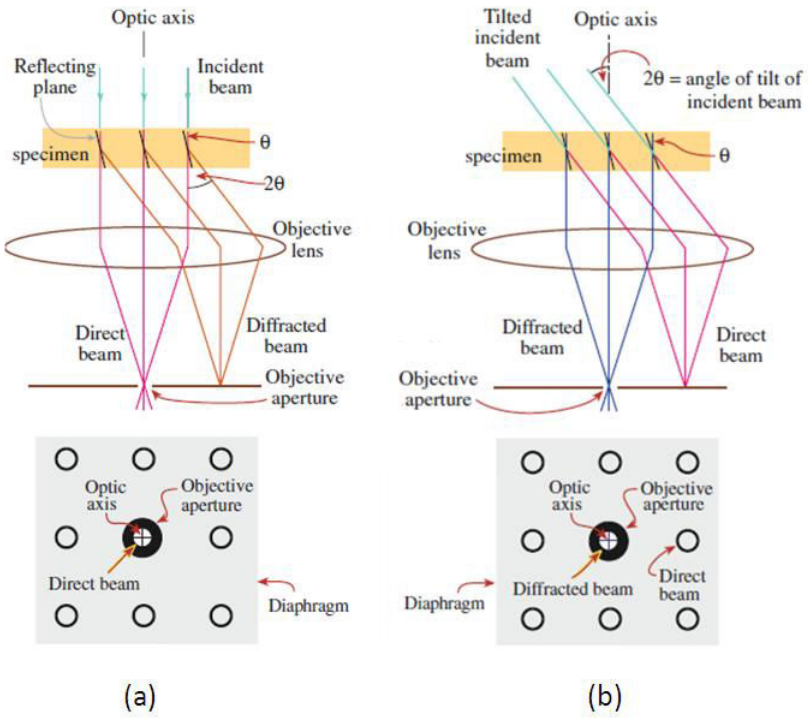

Figure 2.23 – Schematic diagram for (a) bright field and (b) dark field imaging (Image source: [113]).

2.4.2.2 Defect imaging and extinction rules

The objective of the following section is to identify the extinction rules, or in other words: under which specific conditions do particular defects appear in contrast for defect imaging as a function of the utilized diffracted beam **g**.

Threading dislocations: Given that diffracting planes are distorted in the vicinity of dislocations, TEM enables the imaging of defects through the "**g**·**b** rule" – If the Burgers vector of the dislocation is perpendicular to the active diffraction vector (*i.e.* $\mathbf{g}\cdot\mathbf{b}=0$), there will be no diffraction contrast from the dislocation, and the dislocation will therefore be invisible.

Threading dislocation	Burgers vector	$\vec{g}$ = (0002)	$\vec{g}$ = (10$\bar{1}$0)
TD *a*-type	$\frac{1}{3}$ <11$\bar{2}$0>	0	1 ($\frac{2}{3}$ in contrast)
TD *c*-type	<0001>	2	0
TD *a*+*c*-type	$\frac{1}{3}$ <11$\bar{2}$3>	2	1 ($\frac{2}{3}$ in contrast)

Table 2.2 – Scalar product values of $\mathbf{g}\cdot\mathbf{b}$ *for different values of* **g** *and* **b**. *Values correspond to whether or not a TD is visible.*

By selecting a given set of diffracted beams **g**, one can determine the Burgers vector **b** of a dislocation as a function of the $\mathbf{g}\cdot\mathbf{b}$ contrast observed by the image. Table 2.2 summarizes the scalar product

values of $\mathbf{g}\cdot\mathbf{b}$ for different values of $\mathbf{g}$ and $\mathbf{b}$. For the orientations used in this thesis, accessible diffraction vectors are $\vec{g}$ = (10$\bar{1}$0) and $\vec{g}$ = (0002). Therefore, a DF image acquired with $\vec{g}$ = (10$\bar{1}$0) permits two-third of the *a*-type and *a*+*c*-type TDs to appear in contrast. Another DF image acquired with $\vec{g}$ = (0002) permits acquiring contrast for all *c*-type and *a*+*c*-type TDs. Therefore, these combinations enable distinguishing between the different types of TDs present in the crystals.

Basal stacking faults: In a similar manner to TDs, the presence of BSFs (see section 2.1.2.2) generates a deformation in the lattice defined by a displacement vector $\mathbf{R}$. Following the $\alpha = 2\pi\mathbf{g}\cdot\mathbf{R}$ rule, a BSF of displacement vector $\mathbf{R}$ is out-of-contrast in a DF image using diffraction vector $\mathbf{g}$ if α is a multiple of 2π. Table 2.3 summarizes the displacement vectors and extinction rules of BSFs.

Defect	Displacement vector	$\vec{g}$ = (0002)	$\vec{g}$ = (10$\bar{1}$0)	$\vec{g}$ = (30$\bar{3}$1)
BSF I_1-type	$\frac{1}{6}$ <20$\bar{2}$3>	2π: No	$\frac{4\pi}{3}$: **Yes**	5π: **Yes**
BSF I_2-type	$\frac{1}{3}$ <10$\bar{1}$0>	0: No	$\frac{4\pi}{3}$: **Yes**	4π: No
BSF E-type	$\frac{1}{2}$ <0001>	2π: No	0: No	π: **Yes**

Table 2.3 – Scalar product values of $\mathbf{g}\cdot\mathbf{R}$ for different values of $\mathbf{g}$ and $\mathbf{R}$. Yes and No correspond to whether or not a BSF is in contrast.

TEM is therefore an inevitable technique for qualitative analysis of defects. However, a drawback associated to TEM, besides the necessary extensive time-consuming sample preparation, is the limited zones that can be imaged. This makes TEM inadequate for statistical analysis.

TEM images discussed in this manuscript were prepared by conventional mechanical and ion milling techniques. TEM observations were carried out in three different TEMs. A JEOL 2010 and JEOL 2100 TEMs operating at 200 kV, and a FEI TITAN ULTIMATE operating at 300 kV was also employed for STEM and chemical contrast HAADF imaging.

2.4.3 Cathodoluminescence (CL)

Electrons can be used to characterize materials in many ways. Interactions of keV electrons (in a scanning electron microscope for example) with matter lead to different signals, such as secondary electrons, backscattered electrons, x-rays and photons in a wide spectral range. This last process is called CL and can be defined as the emission of light as the result of electron - *"cathode ray"* - excitation [114].

For a CL system integrated in a SEM, an aluminium parabolic mirror is placed between the sample stage and the electron gun. Through a hole in the mirror, the sample is irradiated with electrons and the luminescence is collected. For the most efficient collection, the sample must be in the focal point of the mirror, which is 1 mm below the mirror itself (for the apparatus used in this work). Because

of the parabolic shape, the mirror reflects the light as a parallel beam into a waveguide. Afterwards, the emitted light from the sample is collected, and can be detected in two imaging modes depending on the apparatus' configuration: panchromatic and monochromatic. In panchromatic mode, the imaging sensor is sensitive to a wide range of wavelengths of light, typically collecting all emitted photons spanning a large part of the visible spectrum and/or UV. The image is then formed by individual pixels, each corresponding to the intensity of all the collected photons where the *e*-beam impinges on the region associated to that pixel. In monochromatic mode, the collected photons are guided through a monochromator, which contrary to panchromatic imaging, only allows to make an image at a single particular wavelength. Moreover, CL provides the possibility of spectral mapping. By using the beam-scanning facility within an SEM, a CL spectrum may be collected at each scanned point within the characterized material, thus creating a 2-dimensional spectral map [115].

An advantage of CL compared to other forms of luminescence, like PL (see section 2.4.4), is the high spatial resolution that can be achieved. The typical diameter of an electron beam is in the order of nanometers and the interaction volume of such a beam is in the order of 100 nm (depending on the accelerating voltage of the SEM: typically between 1 keV and 30 keV), which is at least one order of magnitude smaller than the spot of a typical UV micro-photoluminescence setup. The interaction volume of the electrons with the material determines the spatial resolution. By varying the accelerating voltage one can also obtain depth resolved information, as the penetration of the electrons increases with the increase of the beam energy. Figure 2.24 displays Monte-Carlo simulations of the electron beam penetration depth in a GaN layer as a function of different accelerating voltages [116].

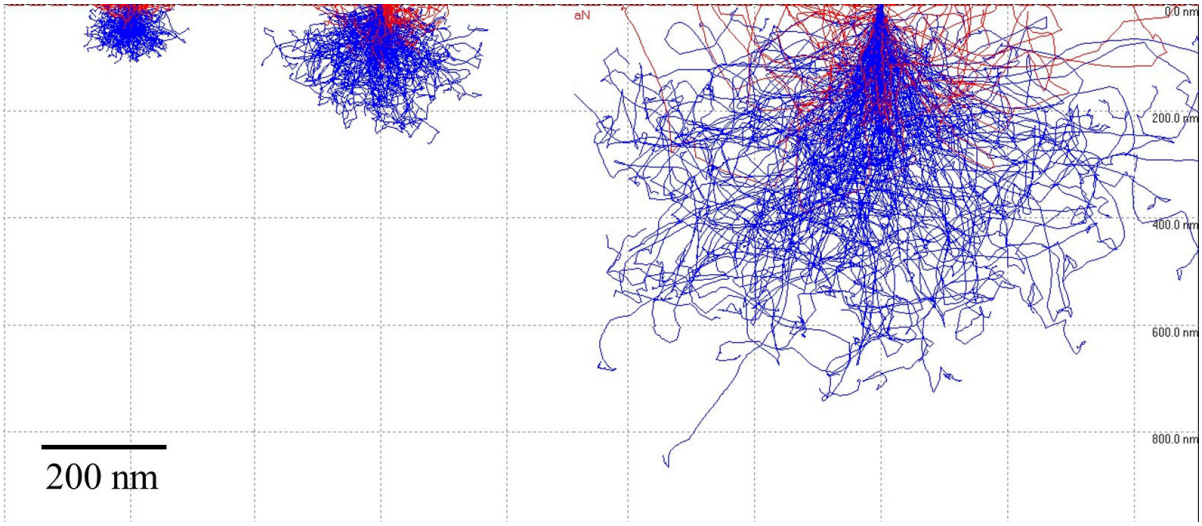

Figure 2.24 – Simulation of the electron penetration depth into a GaN layer at (a) 3 kV (b) 5 kV (c) 10 kV acceleration voltages.

CL is therefore a tool for high-resolution defect imaging and characterization [117]. In our case a high spatial resolution is desirable, given that the growth is carried out on patterned substrates, which

means that a detailed understanding of individual stripe behavior is necessary. Besides, by taking advantage of the elevated spatial resolution CL provides, acquiring spectra and analyzing their peak positions can be highly effective for locally studying material strain states, doping and impurities.

2.4.3.1 Defect imaging

In the following, CL defect imaging will be introduced, namely applied to TDs and BSFs. The objective is to familiarize the reader with the subsequent figures that will be discussed in the upcoming chapters emphasizing how defects are displayed.

Threading dislocations: One of the main reasons CL is employed in our case is to spatially study the TD distribution in the grown semipolar layers. TDs emerging to the surface are predicted to introduce deep states in the gap. TDs act as non-radiative recombination centers consequently creating a contrast in CL images. This contrast results in TDs appearing as dark spots in panchromatic CL images and reduces the intensity in acquired CL spectra.

In principle, depending of the density of TDs, no other technique as statistically adequate as CL for the quantitative characterization of TDs in semipolar layers (not the case for *c*-plane GaN [118]). Therefore, CL panchromatic imaging of TDs is the most reliable quantitative tool for this job. However, CL is only reliable for high-quality GaN layers (regardless of the orientation) with dislocation densities in the order of $10^8\ cm^{-2}$ or lower. On highly defected regions, the mean distance between spot centers is lower than the electron interaction value and/or diffusion length that results in black spots merging, making it impossible to individually distinguish closely spaced TDs and, therefore, underestimating TD densities actually present in the layers [118]. Figure 2.25 shows an SEM image of a *c*-plane GaN surface (after a particular annealing to increase TD diameter size, described in [118]) and its corresponding CL panchromatic scan showing that closely spaced multiple TDs appear as a single black spot.

Therefore, CL can be used for the understanding of defect distribution and for the determination of TD densities provided that layers have a low TD density. However, from the qualitative point of view, it is not possible to distinguish the different types of TDs if CL alone is used as a characterization technique. Figure 2.26 shows a typical panchromatic scan at low temperature (77 K) displaying TDs as black spots.

Basal stacking faults: Besides spatially studying TDs, CL is also an efficient technique to investigate BSFs quantitatively (*i.e.* with reliable statistics) and qualitatively. As mentioned earlier, BSFs are plane layers of cubic phase surrounded by wurtzite phase. They can be considered as uniaxially

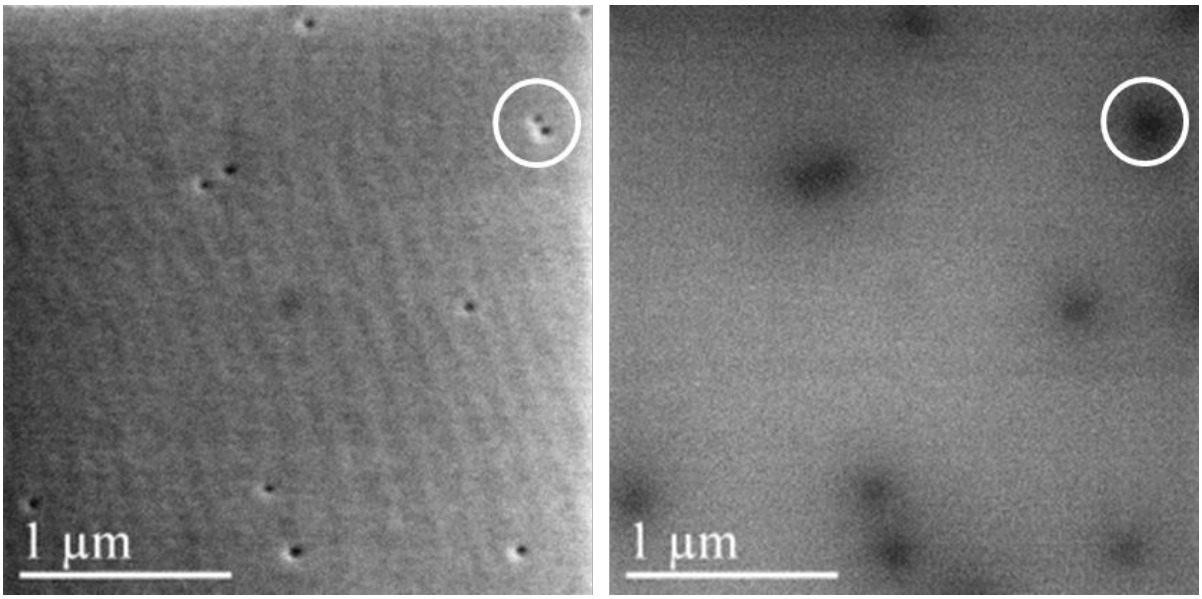

Figure 2.25 – (a) Plane-view SEM image of c-plane GaN after silane treatment and (b) its corresponding CL panchromatic image at room temperature. (Image courtesy of Florian Dubois)

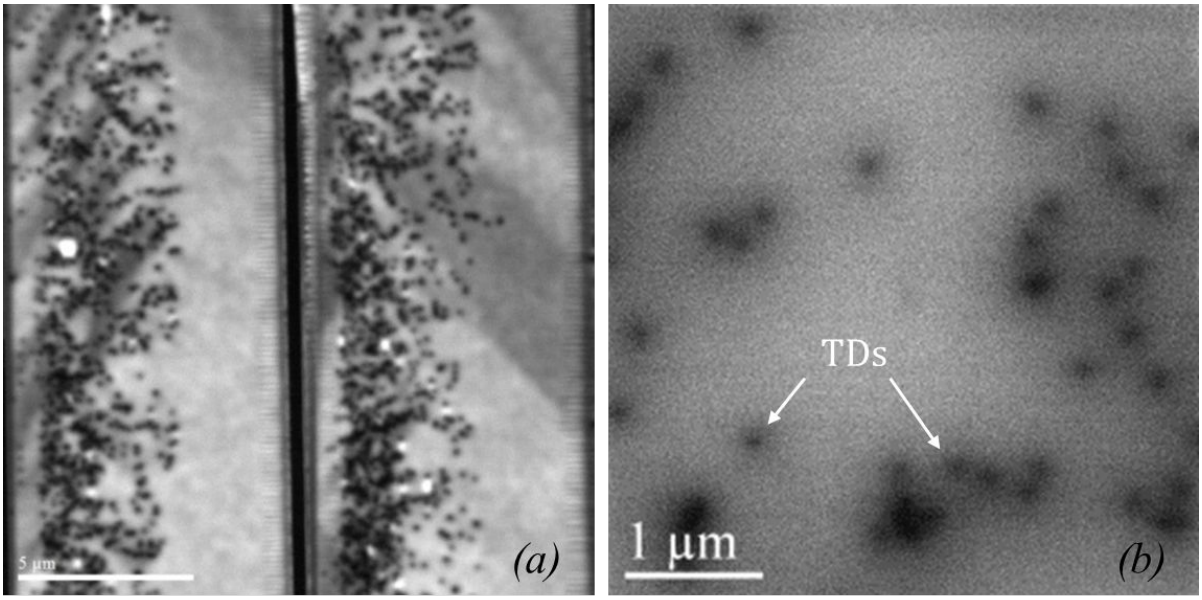

Figure 2.26 – Plane-view panchromatic CL images at different magnifications showing black spots as dislocations

compressed cubic phase forming a quantum-well-like region of zinc-blende material embedded in the wurtzite host, resulting in potential wells for electrons [119] that give rise to a luminescence line below the wurtzite band gap [29, 120]. In short, the aforementioned models presenting BSFs as quantum wells mean that contrary to TDs, BSFs are radiative defects (Partial dislocations terminating BSFs are non-radiative). In what concerns semipolar (and nonpolar) samples studied in low temperature

plane-view CL, BSFs correspond to bright white luminescent lines when panchromatic images are acquired (Figure 2.27) while images recorded at 3.42, 3.35 and 3.29 eV will display, spatially resolved, I_1, I_2 and E BSFs.

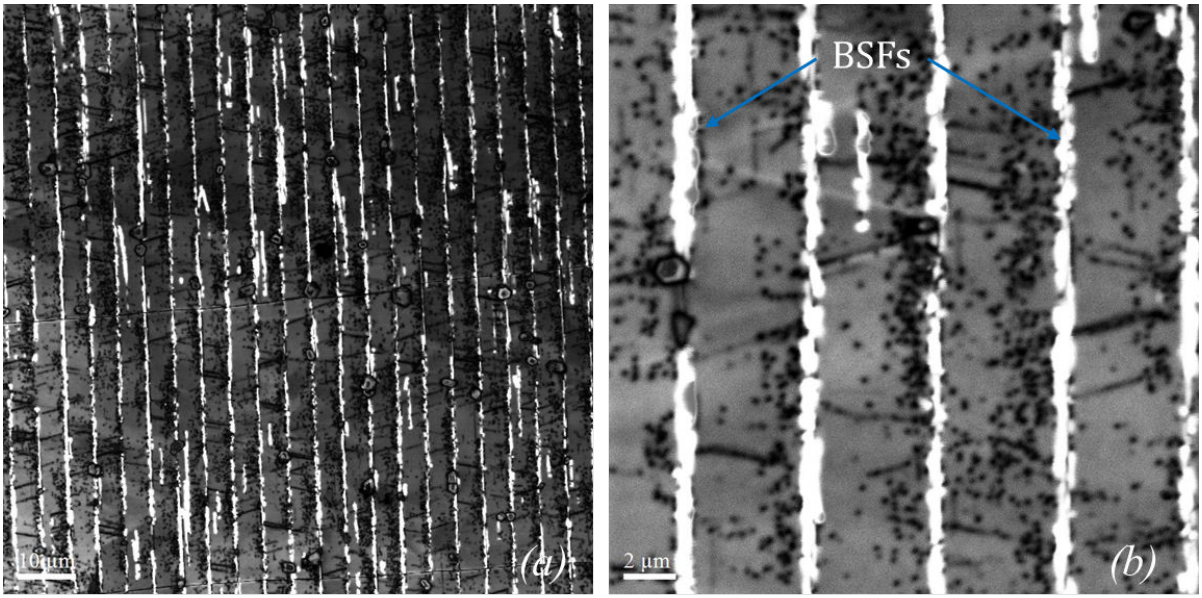

Figure 2.27 – Plane-view panchromatic CL image acquired at 77 K showing BSFs as luminescent white lines.

By measuring the length of the segments observed, and dividing over the total measured area, one can quantitatively estimate the total BSF density on the sample. However, when the luminescent lines are too close as a result of an elevated BSF density, or clustering, the density determination becomes impossible.

Cathodoluminescence images and spectra were recorded using a Gatan MonoCL4 system integrated to a JEOL 7000 SEM operating at 5 kV (unless stated otherwise) and a spectrometer equipped with a photomultiplier for monochromatic imaging and a CCD camera for spectral mappings. The monochromator contains two gratings, one blazed at 500 nm with 1200 lines/mm and one blazed at 1600 nm with 600 lines/mm. For cryogenic measurements, the samples were cooled down to 77 K using liquid nitrogen. The CL spectra presented in the subsequent chapters are all calibrated and corrected for the system responses using a mercury lamp.

2.4.4 Photoluminescence (PL)

PL is the emission of light from a material under optical excitation. In a material system like GaN, the thermal equilibrium is broken by the external optical excitation, which excites the electrons from the valence band to the conduction band, provided that the incident light source has sufficient energy (*i.e.* higher than GaN's bandgap at 3.4 eV). Eventually, these excitations relax and the system returns

to its equilibrium state through the recombination of electron-hole pairs. This process is usually achieved by either band-to-band transitions, or transitions through discrete levels in the band gap related to dopants or through nonradiative recombination at defects. The spectrum is then recorded, and peaks with different energies are related to different recombination processes. The electronic band structure of the studied material can be investigated by analyzing its PL spectrum.

Table 2.4 provides the main transitions and their corresponding energies observed in a typical semipolar GaN PL spectrum. A high crystal quality GaN layer's spectrum is nominally dominated by excitonic recombination, typically consisting of free and bound exciton recombination.

Transition Line	Energy (T = 10K)
Free Exciton (A)	3.478 eV (3.45 eV (tensile) - 3.49 eV (compressive))
Free Exciton (B)	(A) + 7 - 8 meV
Free Exciton (C)	(A) + 20 meV
A-LO	(A) - 92 meV
D^0X (neutral donor bound exciton) [6]	(A) - 6 meV
D^0X - LO	D^0X - 92 meV
BSFs ($I_1 - I_2 - E$)	3.42 - 3.35 - 3.29 eV [7]

Table 2.4 – GaN optical transitions and their corresponding energies.

PL is also an essential tool for investigating defects, essentially BSFs mainly present in semipolar layers, which as mentioned in the previous section, act as quantum wells and are radiative defects. However, in a similar manner to CL, particular measurement precautions must be taken to employ excitation densities low enough to avoid saturation of defect-related PL. Operated otherwise, excitonic emissions become favorable and the false impression of the relative strength of defect-induced transitions is given [122]. It may also be worth noting here that BSF types sometimes exhibit different transition energies or shifts. It has been suggested by Paskov *et al.* [123] that this energy variation is mainly due to the inhomogeneous spatial distribution of the BSFs where emission often occurs from a bundle of BSFs rather than from a single one. This can be regarded as a MQW having a different total width and barrier thickness and consequently transitions at shifted energies. Furthermore, PL may also be employed for the determination of strain in the epilayers [124, 125]. The presence of strain in GaN films affects the position of the near-band-edge PL lines because the resulting stresses alter the bandgap energy.

PL is a complementary and necessary technique to CL employed to evaluate the overall optical quality of materials by integrating larger surface areas, mainly depending on the diameter of the excitation source that is typically in the order of 200 μm. However, for localized PL measurements,

[6] The given energy corresponding to the D^0X is most likely a result of impurities arising from Si, given the growth is performed on Si substrates.

[7] Other reports associate this transition to partial dislocations terminating the BSFs [121].

μ-PL can be employed. μ-PL utilizes the same laser source but the sample is excited through a microscope objective reducing the spot size to ~ 2 μm enabling a more precise excitation of more localized regions of interest.

Two types of lasers were used in this work: a frequency-doubled argon ion Ar^+ laser emitting at 244 nm, and a HeCd laser operating at 325 nm. Signals were detected through a Jobin-Yvon 64 cm focal length monochromator using a cooled GaAs photo-multiplier and conventional lock-in techniques. Low temperature measurements were acquired at $\sim$ 10 K using a liquid helium cooling system. All the discussed PL spectra in the subsequent chapters are all calibrated and corrected for the system responses using a mercury lamp.

2.4.5 Atomic force microscopy (AFM)

AFM is used to resolve surface morphologies down to a nanometer resolution (*i.e.* in the z-axis normal to the surface) [126] and can be used to characterize almost any type of surface. The operating principle consists of a cantilever with a nanometric-sized tip to scan the sample surface. Surface morphologies are investigated using an AFM working in tapping mode where the cantilever oscillates by a piezoelectric element mounted in the tip holder at a frequency close to its resonant frequency. When the tip approaches the surface, the atomic forces between the tip and the sample surface (*i.e.* Van der Waals forces, dipole-dipole interactions, electrostatic forces...) may vary the amplitude of the oscillation. The feedback signal is then processed, and a surface topography map is acquired.

In principle, for c-GaN layers' surface studies, AFM is mainly employed for: first, TD quantification which emerge towards a free surface and give rise to surface depressions which are easily identified by AFM. Second, the root mean square *(rms)* roughness where the summations are performed over all the acquired image pixels, and the mean height is calculated.

In this work, contrary to c-plane GaN, AFM cannot be implemented for TD imaging on semipolar oriented layers due to the invisibility of surface depressions associated to TDs or their eventual inexistence. In a study of $(10\bar{1}1)$ semipolar GaN, pyramidal pits were observed with AFM topographies, similar to ones observed on polar-GaN. However, the observed pit density was $2.9 \times 10^5 cm^{-2}$, compared to $1.2 \times 10^8 cm^{-2}$ when measured by CL which is three orders of magnitude lower [127], confirming the technique's unreliability for TD imaging. Figure 2.28 shows two scans corresponding to polar and semipolar surfaces where TDs appear as black spots in the former and are inexistant in the latter. AFM will therefore solely be employed for the investigation of surface roughness. From the viewpoint of technological applications, *rms* roughness is an important surface parameter, whose

reduction is necessary for obtaining device-quality films, since elevated interfaces' roughness might prevent subsequent technological processing (*i.e.* metal contacts, homogeneous spin coating, etching, etc.).

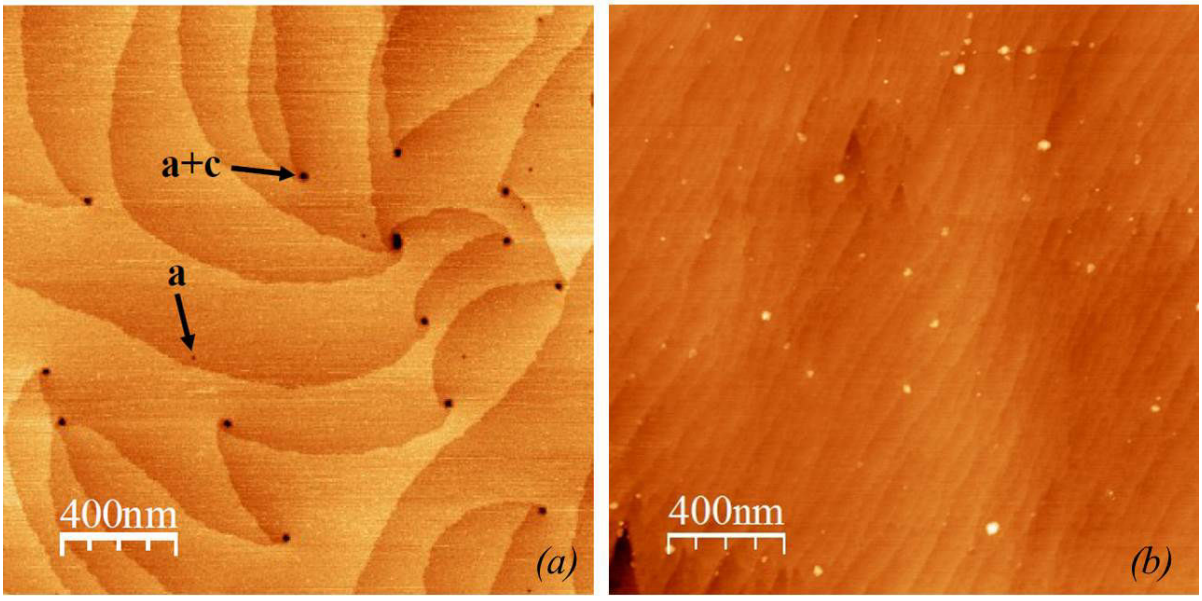

Figure 2.28 – 2 µm × 2 µm AFM scans on (a) polar and (b) semipolar surfaces (same scale).

A VEECO NanoScope IV AFM operating in tapping mode was used to acquire the images presented in this manuscript. AFM data have been analyzed using WSxM software [128].

2.5 Summary

In this chapter the basic properties of GaN material have been introduced. The major concepts related to advantageous semipolar particularities have been presented and a summary of the state-of-the-art defect reduction strategies was described. The final section introduced the necessary elements of the used characterization techniques in order to set the grounds for a better understanding of the results presented in the subsequent chapters.

3 GaN (10$\bar{1}$1) on Silicon (001)7°off

This chapter will be dedicated to the study of (10$\bar{1}$1) GaN grown on patterned (001)7°off Si substrates. The (10$\bar{1}$1) orientation is one of the most exploited on silicon substrates, and was the first demonstrated semipolar orientation on a patterned foreign substrate [70, 127]. Reports have indicated a higher indium incorporation efficiency in semipolar (10$\bar{1}$1) InGaN/GaN QWs than in polar and nonpolar ones [129]. Additionally, demonstrated devices on the (10$\bar{1}$1) orientation have shown interesting properties in terms of reduced blue-shift as compared to that found in conventional *c*-plane LEDs [130].

Since the first demonstration of (10$\bar{1}$1) GaN on patterned silicon in 2002 [70], there hasn't been a significant improvement of the layers' quality, which are still affected by important densities of structural defects. So, the objective of this work is to primarily address this issue and present the investigated methods employed for their reduction. The first part of this chapter will begin by introducing the substrate fabrication steps, and then the subsequent epitaxial growth of AlN and GaN will be described, and will be referred to as "single-step classical growth". Structural and optical characterization of grown layers will be investigated and details of the outcomes will be discussed. The second part will introduce a unique method to block extended defects from propagating towards the surface. Subsequent characterization will emphasize on the quality improvement that has been gained by this method in comparison to the classical method and previously reported state-of-the-art.

3.1 Substrate selection and fabrication

In order to select compatible Si substrates for semipolar GaN epitaxial growth on inclined facets, it is necessary to understand the crystallographic relationship between the substrate and the desired semipolar orientation. Figure 3.1 shows a stereographic projection of Si (001) exhibiting four Si

{111} facets positioned symmetrically at 54.74° from the normal [001]. It has been pointed out in section 2.2.3.2 that in order to obtain a semipolar orientation parallel to the subtrate's surface, the angle between the nucleation facet and the substrate surface has to be equivalent to the inclination between the GaN *c*-plane and the targeted semipolar plane.

Therefore, targeting the (10$\bar{1}$1) GaN orientation requires a Si (001) substrate with an off-axis tilt of 7° in order to accommodate the difference between the (001) and (111) Si, that is 54.74°, and the angle between (10$\bar{1}$1) and (0001), 61.76°. In our case, the 7° miscut is tilted towards the [$\bar{1}$ $\bar{1}$0] direction (indicated by the dashed yellow circle in figure 3.1) around [$\bar{1}$10]. The inclination angles with Si then become ≈ 61.74° (54.74° + 7°) for the Si ($\bar{1}$ $\bar{1}$1) facet and ≈ 47.74° (54.74° − 7°) for the Si (111), with Si ($\bar{1}$ $\bar{1}$1) being the nucleation facet.

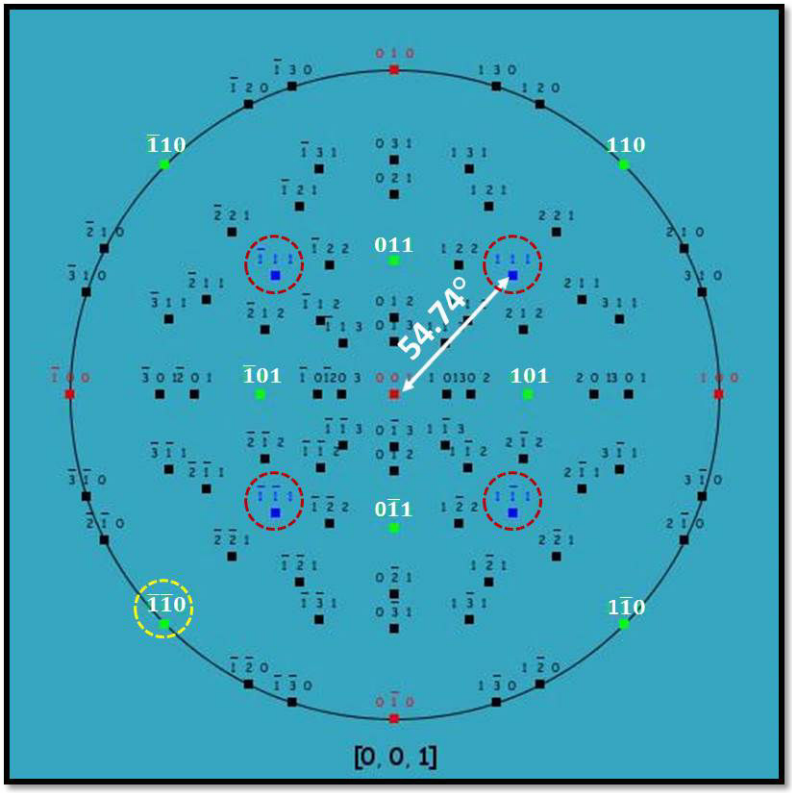

Figure 3.1 – Stereographic projection of Si (001) displaying the four {111} *facets each positioned at* 54.74° *from (001) (Image source: [131]).*

After identifying the crystallographic relationships, the pre-growth substrate fabrication is launched and consists of the following steps as illustrated in figure 3.2 [1]:

[1] Detailed processing information, and parameters used to fabricate the samples used in this work can be found in the Appendix.

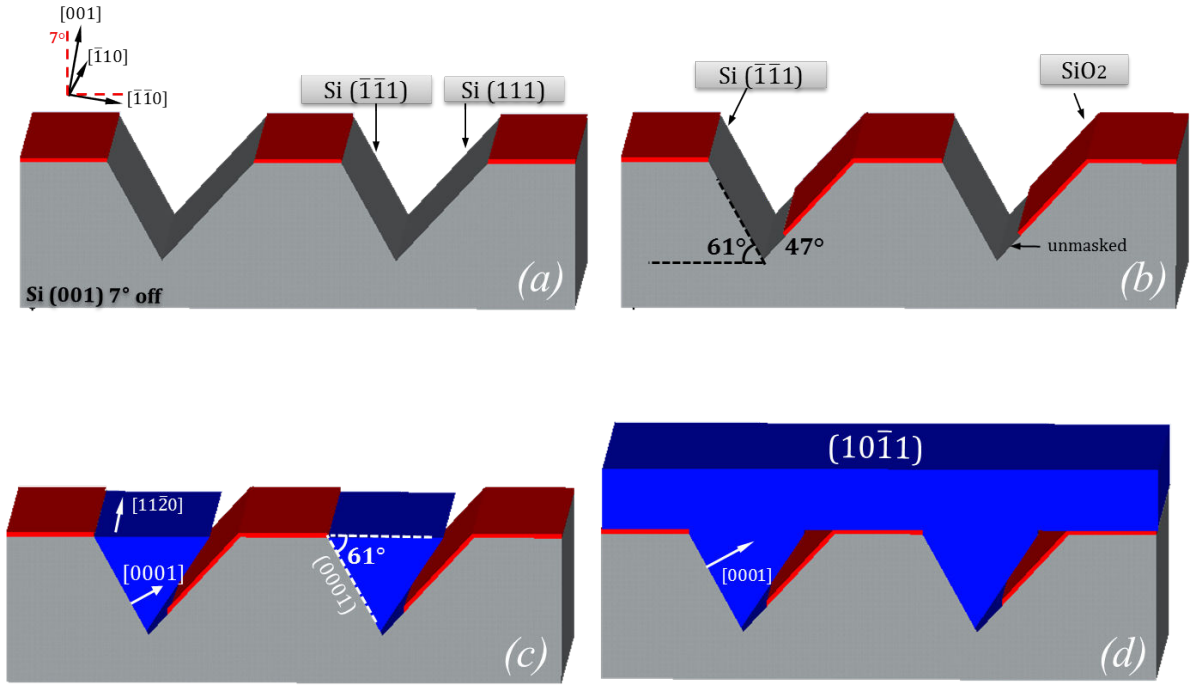

Figure 3.2 – Schematic of the Silicon (001)7° off substrate processing steps: (a) KOH anisotropic etching and (b) inclined IBS deposition. The schematic of the inclined growth of GaN (c) before and (d) after coalescence.

- Photolithography of stripes oriented parallel to the [$\bar{1}$10] Si substrate direction. Choice of dimensions may vary, but in our case an 8.5 μm period (5 μm opening and 3.5 μm mask) and 5 μm period (2.5 μm opening and 2.5 μm mask) masks have been used. The effect of the pattern design on the grown layers will be discussed in section 3.2.3.

- After defining the bands, anisotropic KOH wet etching is used to expose the {111} facets. In our case the two exposed silicon facets are the ($\bar{1}$ $\bar{1}$1) and (111) inclined at 61° and 47°, respectively. The KOH etching duration determines the etching depth of the grooves and consequently the size of the facets as shown in figure 3.3. Since KOH etching is anisotropic and selective on the Si {111} facets, the etching stops when two complete {111} facets are formed, hence creating the so-called "V-groove".

- Inclined dielectric deposition of SiO_2 on the Si (111) facet inclined at ≈ 47°. This step is performed by the IBS technique [75] that permits the inclination of the ion-beam with respect to the sample. If oriented correctly facing the beam, a deposition on one facet is possible, hence leaving only the Si ($\bar{1}$ $\bar{1}$1) facet exposed for epitaxy. This step is crucial in order to dictate the growth in a single direction. Otherwise, and since both etched {111} facets are equivalent, GaN will grow on both facets. However, due to the apparatus' limitation and the dimensions of the used patterns, a shadowing effect upon tilting results in an SiO_2 layer that does not mask the

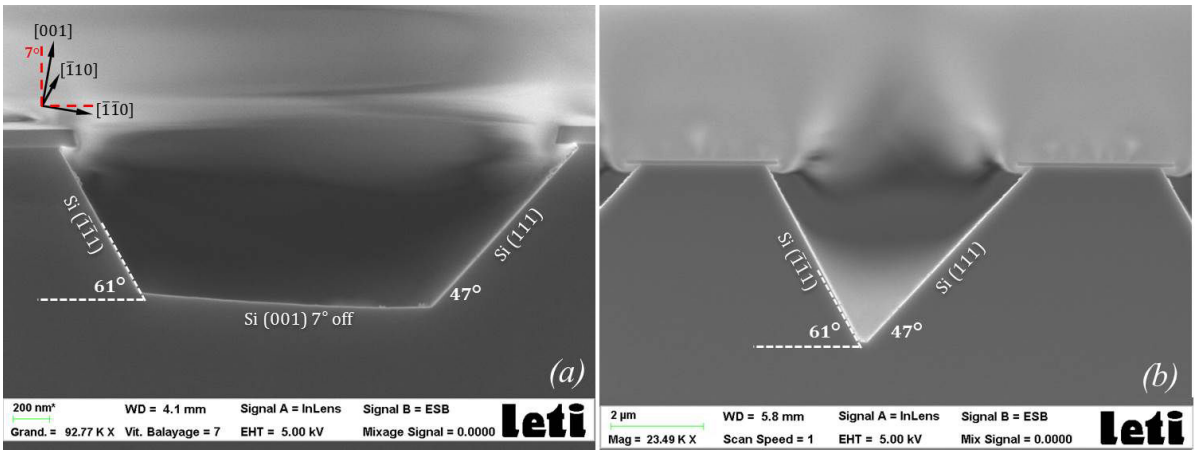

Figure 3.3 – Cross sectional SEM images of samples after (a) short KOH etching duration and (b) long KOH etching duration. The etching stops when a complete V-groove is obtained. (N.B: the displayed images have different scales.)

whole Si (111) facet, and a small portion in the bottom of the etched groove remains exposed. This is shown in figure 3.2 (b). The different consequences of this exposed opening will be elaborated in section 3.2.5 and section 3.3.2.1.

Details of the substrate processing steps are included in the appendix. The descriptions include technical details such as KOH etching rates of different silicon orientations, inclined depositon tilting angles, dry etching recipes, etc.

3.2 Classical single step growth

3.2.1 Selective area epitaxy

After the substrate processing is terminated, patterned samples are then ready for growth. A Thomas Swan Close Coupled Showerhead MOVPE reactor was used in all the performed growths in this work. The used precursors were Trimethylaluminum (TMAl), Trimethylgallium (TMGa) and Ammonia (NH_3).

Initially, an AlN buffer layer is deposited on the inclined Si ($\bar{1}\,\bar{1}$1) facets. Thereon, as shown in figure 3.2 (c), the selective inclined growth of GaN along the [0001] direction is done on the nucleation facets, forming pyramidal bands with topmost (10$\bar{1}$1) surfaces. Further growth results in the coalescence of adjacent bands, which forms a flat continuous (10$\bar{1}$1) semipolar GaN oriented film, as shown in figure 3.2 (d). In the following sections, the investigated growth conditions for AlN and GaN will be described.

3.2.1.1 AlN buffer layer

Various buffer layers have been used to grow GaN on Si (111) such as AlN, 3C-SiC, AlAs and GaAs. However AlN has shown to yield the best results and its primary advantage is that it can be grown in the same reactor as GaN [132]. The buffer layer also serves as a barrier between the silicon substrate and the GaN that blocks the reaction between silicon and gallium responsible for meltback etching.

Ideally, high temperatures are necessary for the growth of high-quality AlN on Si (111) by MOVPE [132, 133]. Different growth conditions (*i.e.* pressure, V/III ratio and temperature) have been investigated in order to grow the AlN buffer layer over which the subsequent GaN crystals will nucleate. Indeed, we have seen that AlN layers grown at 1350°C at a thickness of 100 nm do effectively yield good structural quality GaN layers grown thereon. However, GaN layers on AlN grown at 1350°C [2] at thicknesses of 100 nm exhibited highly damaged surfaces as a result of meltback etching. Growing thicker layers (*i.e.* 200 nm or more) slightly reduces the meltback etching effect, but in turn requires longer growth runs at elevated temperatures. Exploiting this possibility was limited by the MOVPE reactor that was in use, which imposed searching for alternative growth conditions for AlN.

On the contrary, low temperatures (*i.e.* 1100°C) have shown to drastically reduce meltback etching but resulted in very low structural quality GaN, coupled with a rough and irregular surface morphology [3]. A compromise between these two effects lead us to grow the AlN buffer layer at 1250°C to a thickness of 150 nm. In order to assess the effect of growth parameters on the subsequent GaN, this will constitute our buffer layer unless otherwise stated.

Besides the crystalline AlN grown on the exposed Si $(\bar{1}\,\bar{1}1)$ facet, poly-crystalline AlN was consistently deposited on the SiO_2 mask (top and inclined facets) due to the short diffusion length of aluminum, and hence a low selectivity. The parasitic poly-crystalline AlN deposited on the mask forms a continuous layer and has approximately the same thickness as the crystalline AlN grown on silicon. As will be shown in the following sections, the deposited poly-crystalline AlN on the SiO_2 mask may not be problematic, and can serve as a mask for the subsequent GaN overgrowth.

3.2.1.2 Investigated GaN growth conditions

The growth rates and the formation of equilibrium crystalline facets during the growth process depend on the growth parameters [134]. The GaN growth pressure, V/III ratio and temperature have been varied. Each parameter has been varied individually while maintaining all remaining parameters constant. The study was designed in order to determine the effect of growth conditions on the

[2] This temperature is the set point, however, the real growth temperature is ~ 250°C lower than the thermocouple temperature, and is ~ 1100°C.

[3] The effect of AlN growth temperature on meltback etching will be described in Chapter 5.

crystal morphology and to evaluate the quality thereof, establishing the optimal growth parameters. What is essentially meant here by "crystal morphology" is how the crystal shape is adjusted upon changing growth conditions in terms of favoring different facets over others in addition to enhancing growth rates in certain directions. Besides understanding the effect of the growth conditions on the morphology of the crystals, studying growth parameters is also crucial for finding the right adapted conditions as a function of the chosen substrate geometry (*i.e.* period, size of the facets/depth of the grooves) in order to minimize the generation of defects.

Growth pressure: This parameter is controlled via a pressure valve in the reactor and is typically varied between 20 mbar and 800 mbar for MOVPE. In our case, the pressure has been varied for the growth of GaN from 100 mbar to 600 mbar while maintaining other parameters constant (T = 1210°C; V/III ratio = 3100; t = 2500 s.)

The behavior of the grown crystals upon changing the pressure is shown in figure 3.4. Given that the growth time is constant, one can spot that as the pressure increases from 100 to 300 to 600 mbar, the growth rate along the +c-direction decreases from 0.13 to 0.10 to 0.04 μm/min, respectively. This indicates that the growth rate depends on the pressure, which is determined by precursors' transfer process from the reactor's gas inlets to the surface of the substrate, where the TMGa is dissociated and results in the growth of GaN. Accordingly, the growth rate from a simple boundary layer model (*i.e.* the thin layer of flowing precursor gas at the immediate vicinity of the substrate surface) can be considered, as described by the following equation:

$$r_g = (constant) p_{TMGa} \left(\frac{v_{gas}}{P_{reactor}} \right)^{\frac{1}{2}} \tag{3.1}$$

where p_{TMGa} is the partial pressure in the input gas stream; v_{gas} is the gas velocity, which depends on the difference between the pressure in the gas inlet and the reactor pressure; and $P_{reactor}$ is the total reactor pressure [135]. In terms of growth directions, at pressures of 300 and 600 mbar, the growth mainly proceeds along the +c-direction, while the growth in the direction normal to the surface is negligible. Thus, the topmost semipolar facets remain at almost the same level as the SiO_2 mask. At 100 mbar, the growth rate normal to the surface is slightly higher, but remains negligible compared to [0001]. This morphology is not favorable (*i.e.* growth only along the +c-direction), because if any further extension of the crystal occurs, the crystal and the opposite masked facet will get in contact. We have seen that this contact will result in a supplementary source of defects.

Another remarkable issue is the parasitic deposition of poly-crystalline GaN on the mask, which is clearly influenced by the growth rate. At pressures of 300 and 600 mbar, almost no parasitic

GaN was deposited on the mask. However, at 100 mbar poly-crystalline GaN excessively stuck on the topmost masked stripe (see figure 3.4 (a)). This deposition observed at low pressure may be due to the increased material transport to the surface, which increases the probability of species incorporating at random sites, and therefore increases parasitic deposition.

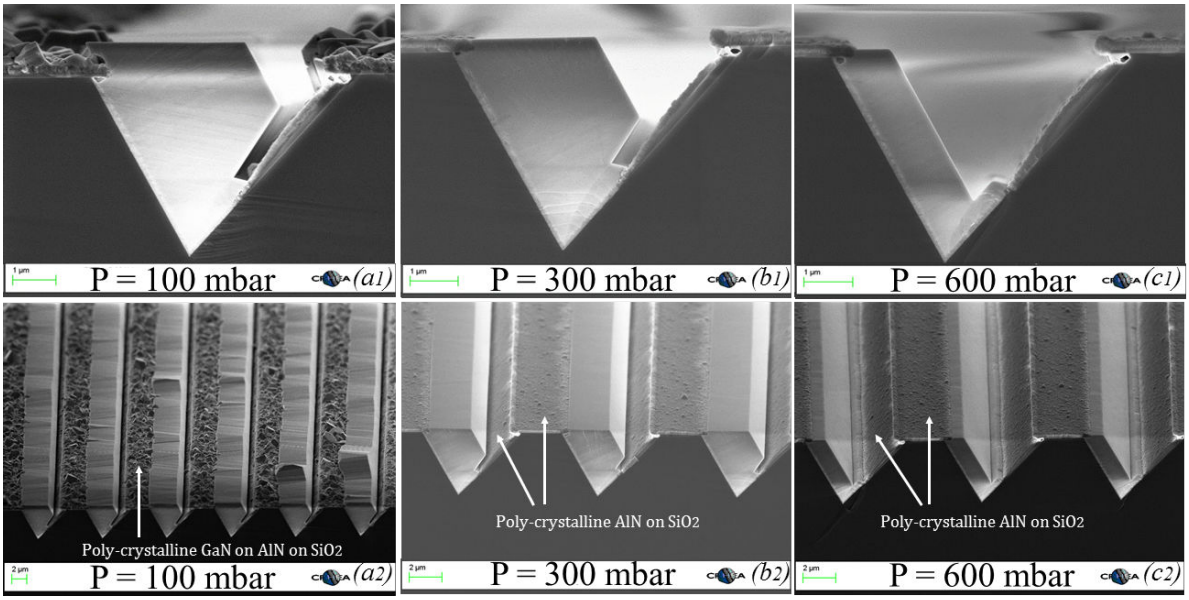

Figure 3.4 – SEM images in cross section and bird's eye view of the effect of pressure on the progress and morphology of the growth. (a) 100 mbar, (b) 300 mbar and (c) 600 mbar.

Seeing the morphology, the most reasonable choice to carry on with in the initial growth stages is 300 mbar. Lower pressures have resulted in excessive poly-crystalline GaN depositions on the mask, which is unfavorable as it may interrupt adatom migration to their correct nucleation sites, and hence disturb the overall growth. Higher pressures showed very slow growth rates, which is unfavorable in our case since longer growth runs will be required and will increase the probability of meltback etching.

GaN V-III ratio: A growth parameter strongly influencing material quality and behavior during growth is the precursor molar flow ratio, or V/III ratio for GaN. The V/III ratio has been varied for the growth of GaN from 220 to 4200 while maintaining other parameters constant (T = 1210°C; P = 300 mbar; t = 2500 s). As shown in figure 3.5, at V/III ratios of 1550 and above, the growth only proceeds in the +c-direction at a rate of ~ 0.061 μm/min, while the growth rate normal to the surface is almost null. At low V/III ratios (between 220 and 650), the growth rate normal to the surface is enhanced and reaches 0.024 μm/min in comparison to 0.138 μm/min in the +c-direction.

The growth rate enhancement in the direction normal to the surface is necessary since it permits the crystals to grow above the mask without getting in contact with the opposite masked (111) facet.

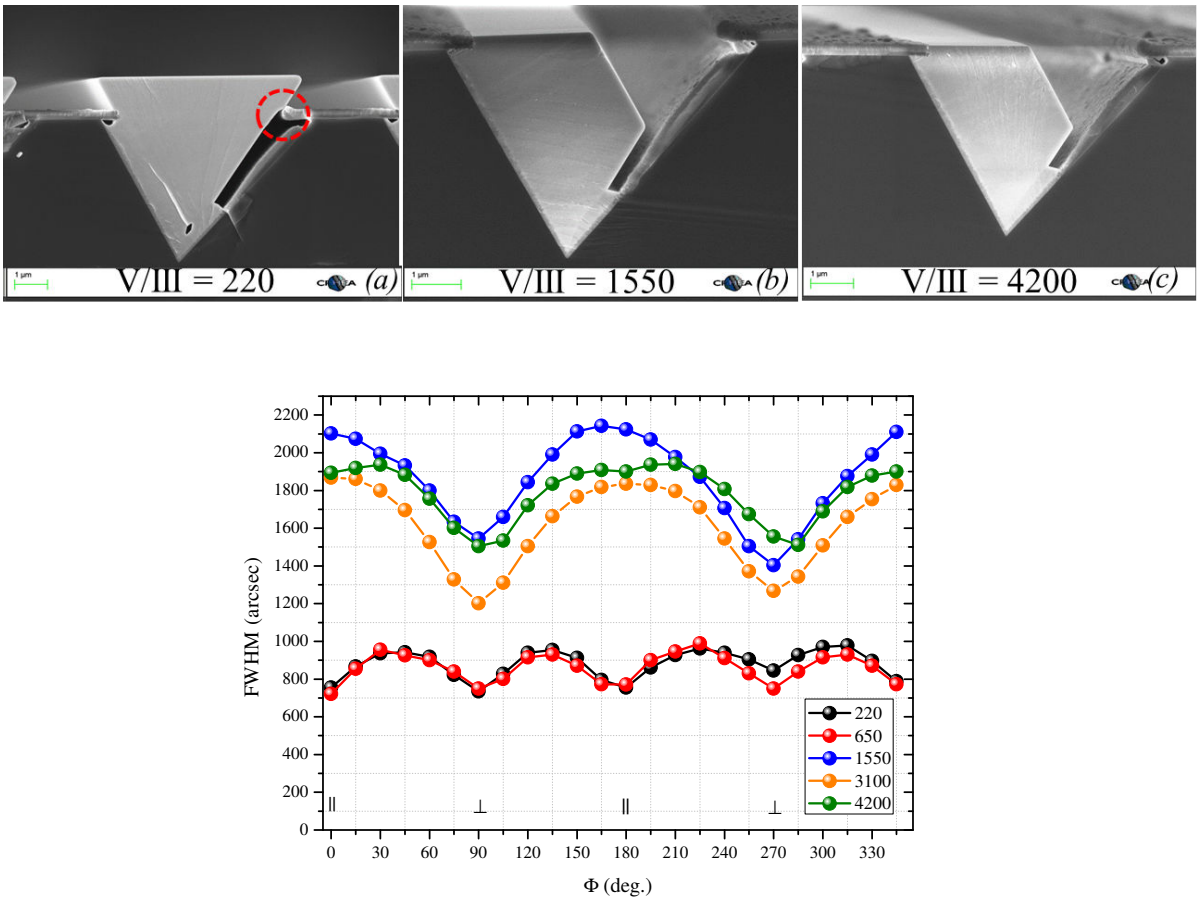

Figure 3.5 – Cross-sectional SEM images showing the effect of the V/III ratio on the progress and morphology of the growth at V/III ratios of (a) 220, (b) 1550 and (c) 4200. The plot shows the FWHM values of the acquired XRD symmetrical rocking curves on the azimuthal angles parallel and perpendicular to the stripes for each V/III ratio.

The zone where possible contact may occur is indicated by the dashed red circle in figure 3.5 (a). Section 3.2.2.2 later on shows the consequence of this contact and its effect on defect generation. Moreover, XRD symmetrical $\omega-$scans on the azimuthal angles parallel ($0° - 180°$) and perpendicular ($90° - 270°$) to the stripes indicate an improvement of the crystal quality with a decrease in V/III ratio. The average FWHM is decreased by almost a factor two (from 1700 to 900 arcsec) when growing from V/III ratios in the order of 1550 and above, to V/III ratios below 650.

GaN growth temperature: Another critical growth parameter affecting the morphology and structural quality of the grown crystals is the susceptor temperature. Temperature is controlled by modifying the output power of the tungsten heater [4]. All growth temperatures in this work are measured from a thermocouple placed inside the susceptor[5].

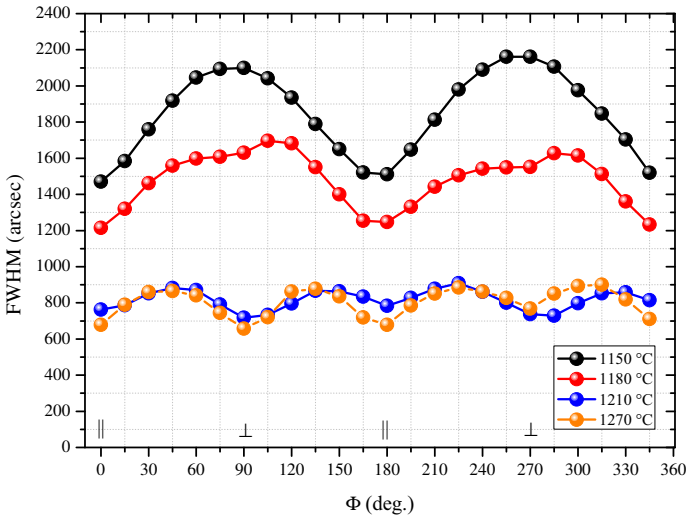

Figure 3.6 – The FWHM values of the acquired XRD symmetrical rocking curves on the azimuthal angles parallel and perpendicular to the stripes for different GaN growth temperatures.

The effect of temperature on the GaN crystals was assessed. It has been found that no variation is introduced in terms of favoring certain crystallographic facets over others. However, varying the temperature greatly influenced the roughness of the facets and the symmetrical scans' FWHM. The minimum GaN growth temperature investigated was 1150°C while the maximum growth temperature was 1270°C (The growth pressure at 300 mbar and V/III ratio at 220 were kept constant). Low temperatures were found to cause irregular shapes of the crystals and well-defined surfaces cease to exist. Higher temperatures do not noticeably improve the structural quality as seen by the symmetrical rocking curves, but instead have shown to contribute to increasing the probability of meltback etching. Figure 3.6 shows the FWHMs of the XRD symmetrical $\omega-$scans on the azimuthal angles parallel and perpendicular to the stripes as a function of the investigated temperatures. The plots show that growth temperatures of 1210°C or above are necessary for improved structural quality. The optimal temperature enabling well defined surfaces and good structural quality has been found to be 1210°C. Additionally, the growth rate showed a null dependence on the growth temperature, further indicating that the process is diffusion controlled and in our case depends on the reactor pressure and the V/III ratio.

[4] The tungsten heater has three independent concentric zones in the Thomas Swan reactor used in this thesis.

[5] Actual substrate surface temperatures are ~ 150 – 200°C lower than the thermocouple temperature and larger deviations are expected for higher temperatures.

3.2.1.3 Selected growth conditions and coalescence

Having reviewed the different tested GaN growth conditions and their effect on the morphology, the coalescence of neighboring crystals and the formation of a flat semipolar (10$\bar{1}$1) surface will be discussed. The utilized growth conditions for the samples characterized in the following sections are: 150 nm thick AlN seed layer grown at T = 1250°C, with GaN grown with P = 300 Torr, T = 1210°C and a V/III ratio of 220. This growth process is referred to as "single-step classical growth" since growth conditions have not been changed throughout the growth process.

Figure 3.7 (a) shows the crystals in the initial growth stages marked with dashed lines indicating the progress of the growth in the polar [0001] and semipolar (*i.e.* normal to the surface) directions. What is notable is the consistent formation and dominance of a flat (10$\bar{1}$1) surface. This has also been observed under a wide range of growth conditions. The (10$\bar{1}$1) surface is highly stable [136] and energetically more favorable than other semipolar surfaces. Therefore, the formation of this flat surface creates a geometry where adjacent crystals along the stripes have a common topmost facet positioned at the same height. As the growth proceeds, the progressive formation of a pyramid is observed, and coalescence occurs when neighboring crystals approach one another. After coalescence, the growth proceeds only in the direction normal to the surface. Figure 3.7 (b) shows the coalesced crystals forming a continuous and flat (10$\bar{1}$1) semipolar GaN layer.

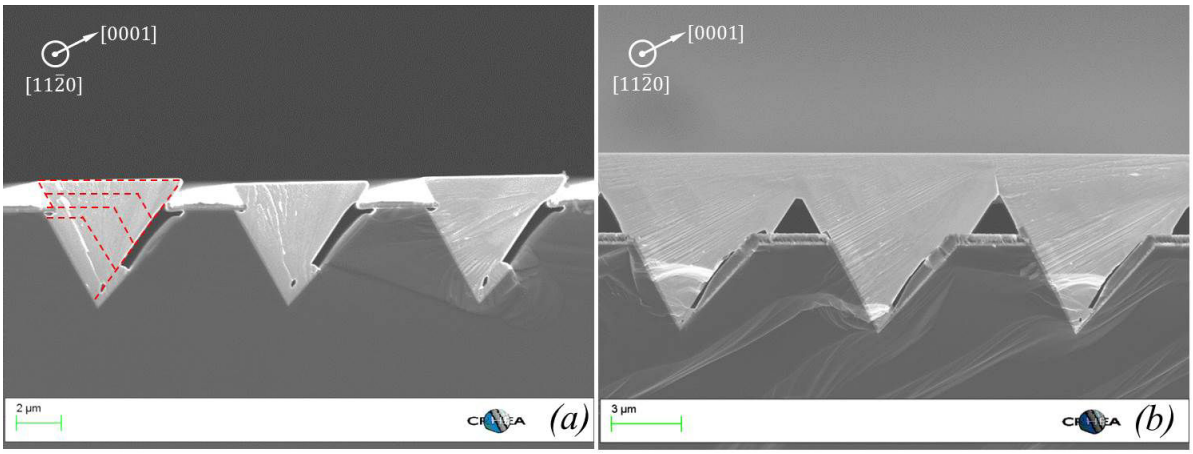

Figure 3.7 – Cross sectional SEM images of the grown crystals (a) before and (b) after coalescence.

3.2.2 Defect behavior and spatial distribution

The following section describes the behavior and spatial distribution of crystalline defects that are present in the grown semipolar (10$\bar{1}$1) GaN layers.

3.2.2.1 Threading dislocations

The TD behavior is highly affected by the crystal's morphology evolution that is primarily determined by the growth conditions and the utilized pattern dimensions. TDs' behavior in the volume of the crystal, starting from the nucleation to the TDs' spatial distribution and effect on the surface will be investigated and described below.

Transmission electron microscopy: Figure 3.8 (a) shows a cross-sectional BF multi-beam TEM image along the [11$\bar{2}$0] zone axis. TDs are initially nucleated at the Si/AlN/GaN interface at the very early growth stages. TDs initially thread along the +*c*-direction (*i.e.* growth direction) and then gradually bend at 90° within the basal plane. This is a classical behavior of dislocation bending, which occurs upon the progressive formation of a pyramidal crystal (see section 2.3.2.1). TDs bending downwards terminate on the substrate side of the crystal whereas TDs bending upwards propagate towards the surface and are distributed along a stripe corresponding to the topmost lateral facet of the pyramidal bands. This is illustrated in figure 3.8 (b).

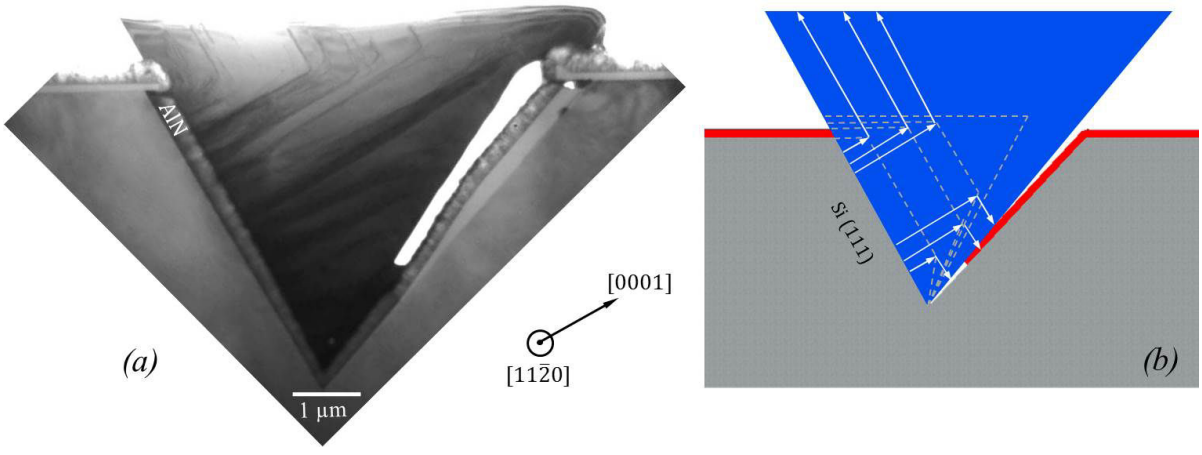

Figure 3.8 – (a) Cross-sectional BF-TEM image showing the bending of threading dislocations in the basal plane perpendicular to the growth direction. (b) shows a schematic illustrating the TDs' bending upon the progressive formation of a pyramidal crystal.

Cathodoluminescence: In order to further understand the TD bending effect on their subsequent spatial distribution and effect on luminescence, plane-view CL was performed. Figures 3.9 (a) and (b) display a bird's eye view SEM image of the crystals and the corresponding plane-view panchromatic

CL image acquired at 77 K. The TEM figure discussed earlier indicating that TD bending upwards eventually thread to the surface is translated in figure 3.9 (b) confirming the striped distribution of black spots corresponding to TDs along the topmost semipolar surface. The dashed red line shows the edge of the completion of the perfect pyramid signifying the bending of all initially generated TDs, which means that any further growth will result in an almost defect-free extension, at least before grain coalescence takes place. Figure 3.9 (c) displays a plane-view CL NBE intensity diagram acquired at 77 K of the stripes indicating the non-radiative effect of TDs by suppressing luminescence intensity in the highly defected areas. Moreover, seeing the high density of observed closely spaced TDs, quantitative assessment of TD densities is not possible since black spots corresponding to TDs cannot be individually resolved.

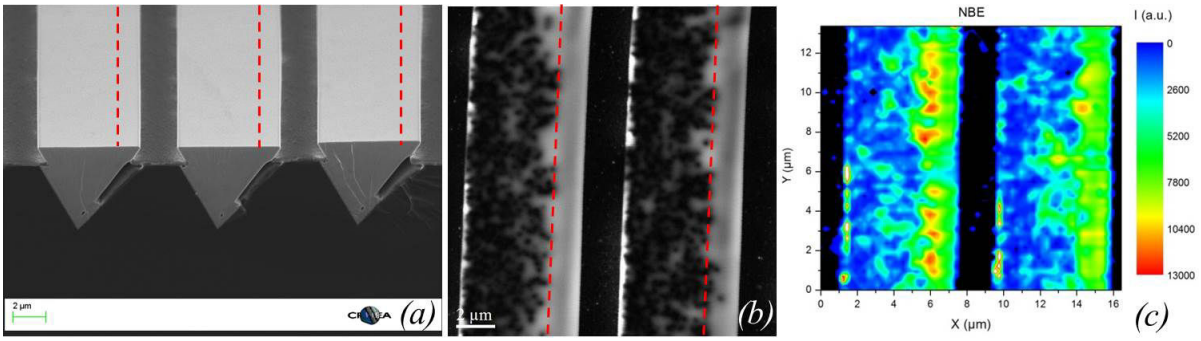

Figure 3.9 – (a) SEM bird's-eye view of pyramidal stripes and (b) their corresponding plane-view panchromatic CL image at 77 K. The dashed red line indicates the edge of the completion of the triangle signaling the bending of all initially generated TDs. (c) A NBE intensity mapping displaying the effect of TDs in inhibiting luminescence and showing the high intensity from the nominally defect-free areas.

3.2.2.2 Basal stacking faults

In this section, the formation of BSFs in our samples will be discussed: the regions where BSFs are generated and their final spatial distribution.

BSF generation: Before describing the BSF formation and their localized positioning, the crystal morphology and facet formation will be introduced. Figure 3.10 shows an SEM image of a pyramidal stripe where its growth has proceeded until its height became larger than the height of the silicon nucleation facet and the SiO_2 mask, combined. Accordingly, at this point the growth proceeds in the [000$\bar{1}$] direction (*i.e.* -*c*-direction). The formed facets are indicated on figure 3.10, and their size ratios may slightly differ (almost negligible difference) from one growth to another depending on the growth conditions.

Cross sectional TEM was performed on the grown crystals. Figure 3.11 shows a DF-TEM image acquired with diffraction vector (10$\bar{1}$0) and the corresponding HRTEM image acquired in the zone

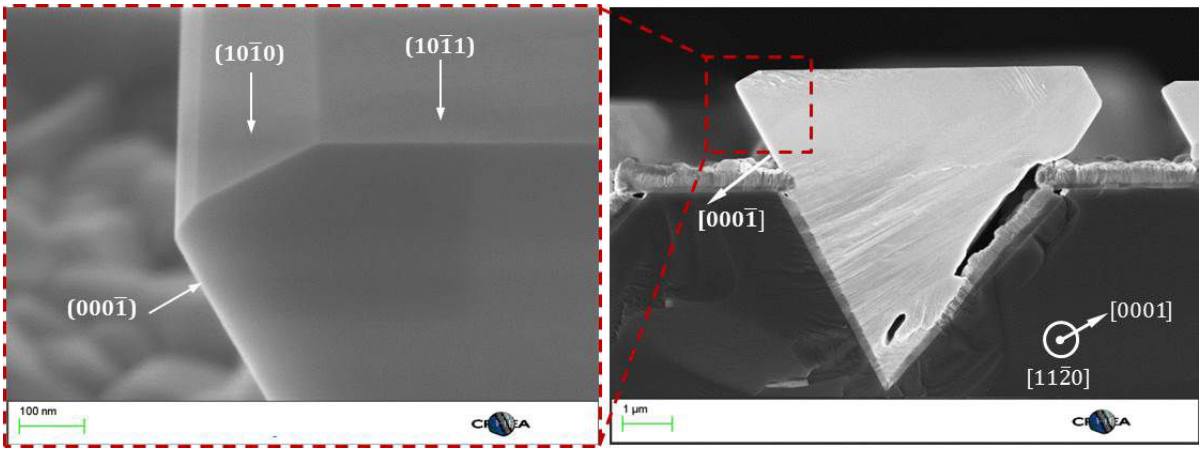

Figure 3.10 – SEM images of a crystal showing the formation of the facets when the pyramidal island's base becomes larger than the silicon nucleation facet width and grows beyond the dielectric mask.

indicated by the dashed red square shown in figure 3.10. BSFs were only observed along the –*c*-wing where the growth proceeds above the SiO_2 mask. No BSFs were observed in any other region in the crystal.

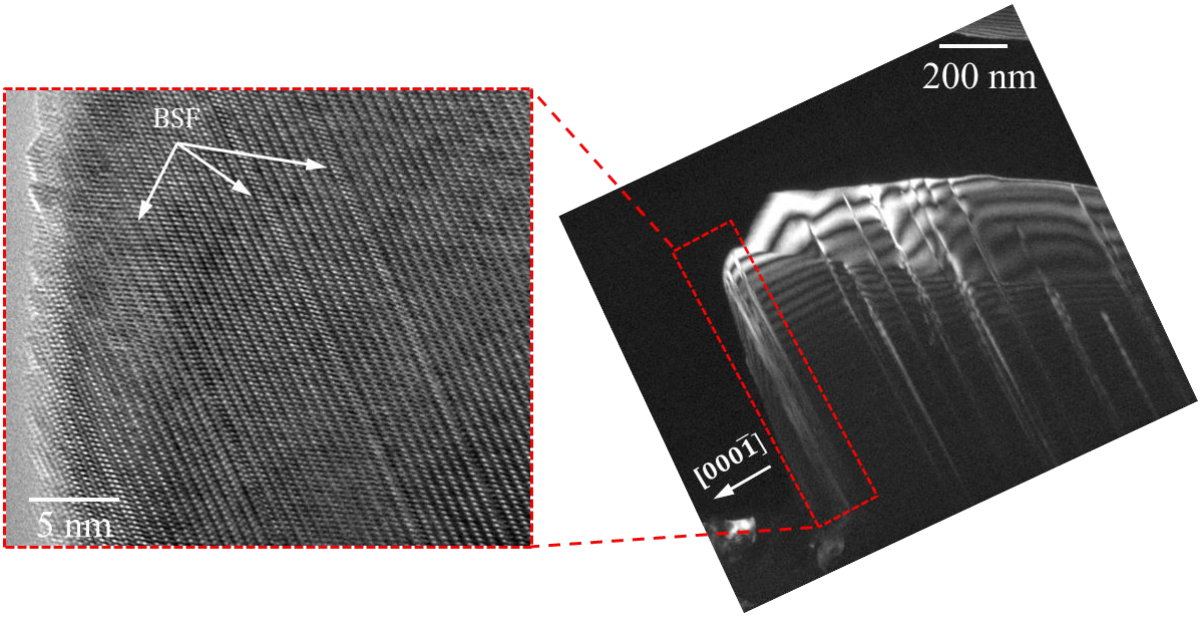

Figure 3.11 – Dark-field TEM image with [10$\bar{1}$0] diffraction vector showing BSFs created in the –c-wing (right) and the corresponding HRTEM image of the faulted region (left).

Several groups have reported on the formation of BSFs in the -*c*- wing of GaN crystals [35, 36]. BSF formation has been suggested to be related to the significantly slower growth rate in the -*c*-wing (N-polar) compared to the +*c*-wing (Ga-polar), which in our case was found to range between 1:10 and 1:20 depending on growth conditions. This slow growth rate may cause elevated impurity incorporation on the (000$\bar{1}$) plane, which could result in adatom nucleation at faulty sites hence forming

BSFs. This may be supported by the impurity incorporation investigation on polar, nonpolar and semipolar planes carried out by Cruz *et al.* [137], which identified a significant increase of impurity incorporation on the N-face side of any given plane.

Adjusting growth conditions may decrease the size of the -*c*-wing, which may slightly reduce the overall density of nucleated BSFs. However, although densities may vary, BSFs in our case were always detected in the -*c*-wings.

Spatial distribution and spectral signatures of BSFs: Figure 3.12 shows a cross-sectional SEM image of coalesced adjacent stripes with the -*c*-wing marked in red lines, and a panchromatic plane-view CL image acquired at 77 K (the SEM and CL images do not correspond to the same sample).

As mentioned earlier, the coalescence of adjacent pyramidal islands occurs while the topmost (10$\bar{1}$1) surface of all the bands is at the same height. This geometry essentially implies that all the BSFs initially generated in the -*c*-wing emerge towards the surface and remain on the surface, thereby influencing the final quality of the material. This is shown in figure 3.12 (b), where BSFs (indicated with red arrows) accumulate on the surface in the form of long elongated white lines.

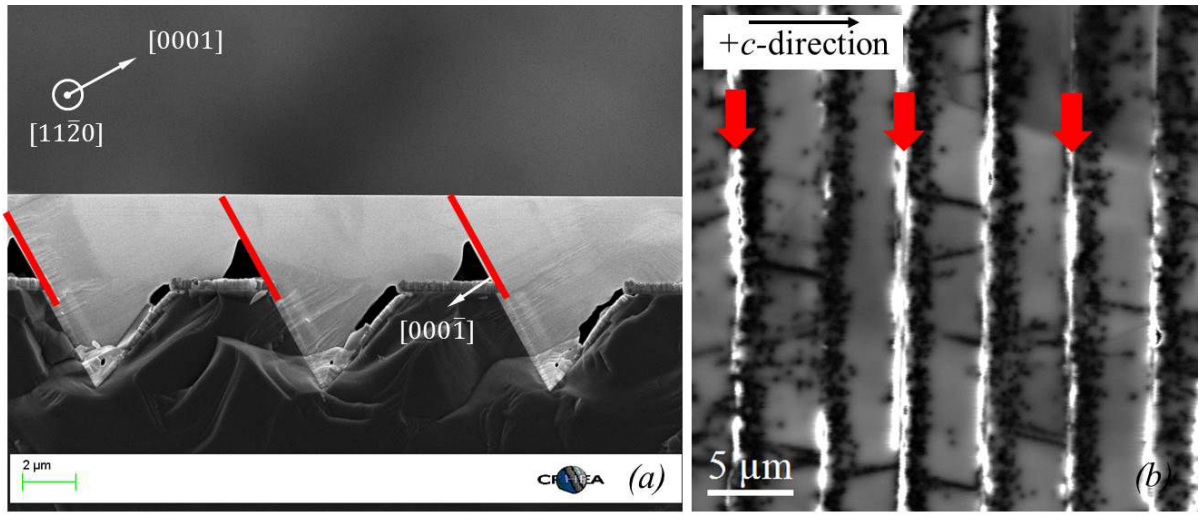

Figure 3.12 – (a) Cross-sectional SEM image of coalesced pyramidal islands showing the -c-wings as red lines and (b) a plane-view panchromatic CL image aquired at 77 K showing BSFs emerging at the surface as white luminescent regions.

Besides BSFs regularly appearing in the -*c*-wings, it has been observed that BSFs occasionally appear in the stripe itself, as indicated in figure 3.13. This is attributed to a contact between the +*c*-plane of the initial GaN pyramid and the inclined opposing facet masked with SiO_2 (which has a deposited

layer of poly-crystalline AlN). However, this contact can be eliminated by adjusting growth conditions *i.e.* Low V/III ratios [6] that enhance the growth rate normal to the final layer (*i.e.* [10$\bar{1}$1]) (see figure 3.9).

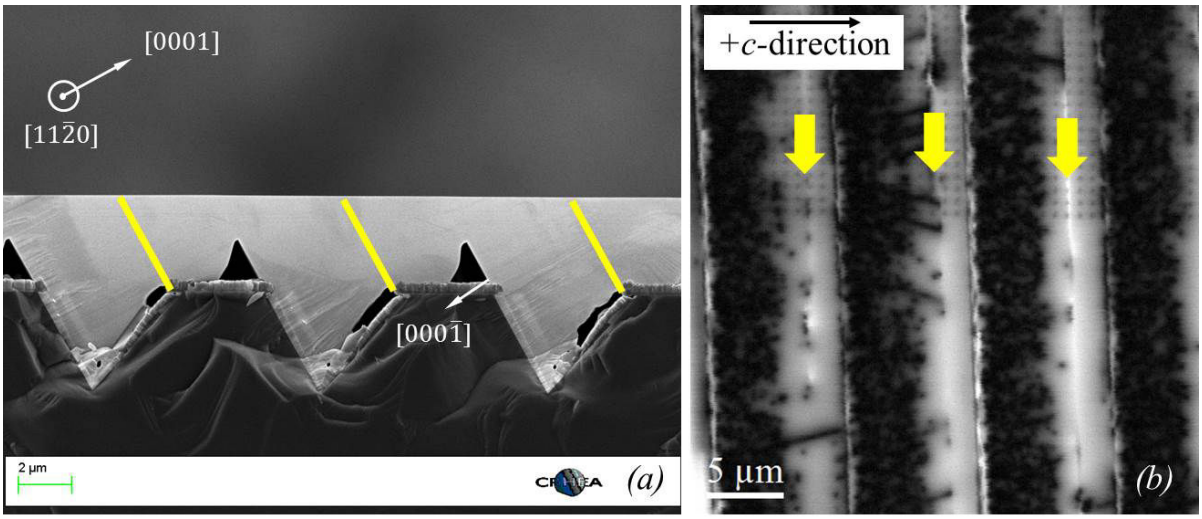

Figure 3.13 – (a) Cross-sectional SEM image of coalesced pyramidal islands showing BSFs that could be created in the stripe as a result of contact with the opposing facet as yellow lines and (b) a plane-view panchromatic CL image aquired at 77 K sowing BSFs emerging on the stripes as white luminescent lines.

Seeing that BSFs are confined in the -*c*-wings, their nature in these wings remains to be assessed. Figure 3.14 displays three plane-view monochromatic CL images acquired in the same region at 77 K at different energies associated to BSFs: 3.41 eV, 3.33 eV and 3.28 eV, and the corresponding spectrum acquired in the -*c*-wing showing transitions associated to these BSFs.

By assessing the BSF distribution in the -*c*-wings, one feature can be recognized. For the 3.41 eV emission, attributed to I_1 BSFs, it can be remarked that they are distributed in continuous regions elongated on the entirety of the bands. On the other hand, the 3.33 eV and 3.28 eV transitions, associated to I_2 and E-type BSFs respectively, show a rather "spotty" interrupted behavior. This difference may be linked to the fact that I_1 BSFs having the lowest formation energy are more likely to form, and therefore have a higher density (see section 2.1.2.2). Moreover, luminescence from I_1-type BSFs have systematically shown higher CL and PL intensities than I_2 and E-type ones.

In principle, BSFs have well-defined transition energies and luminescence peaks. However, a wide range of emission energies has been attributed to BSFs in literature: *e.g.* between 3.40 eV and 3.42 eV for I_1 and 3.32 eV to 3.36 eV for I_2. In what concerns the extrinsic BSFs, to which we attribute the 3.28 eV transition, other groups often associate it to luminescence from prismatic stacking faults. Several proposed factors may be associated to shifting BSF luminescence lines, such as closely spaced BSF

[6] also as a function of the pattern period and nucleation facet size

bundling [123], coupling with point defects [138] and strain induced shifts [139]. Given the dense clustering of BSFs and hence their high overall density, it is not possible to resolve them individually and give an overall density.

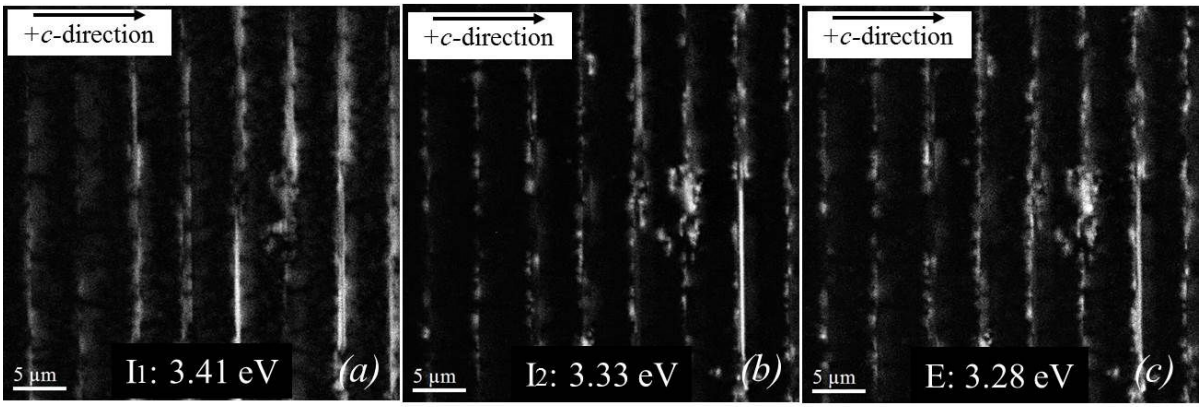

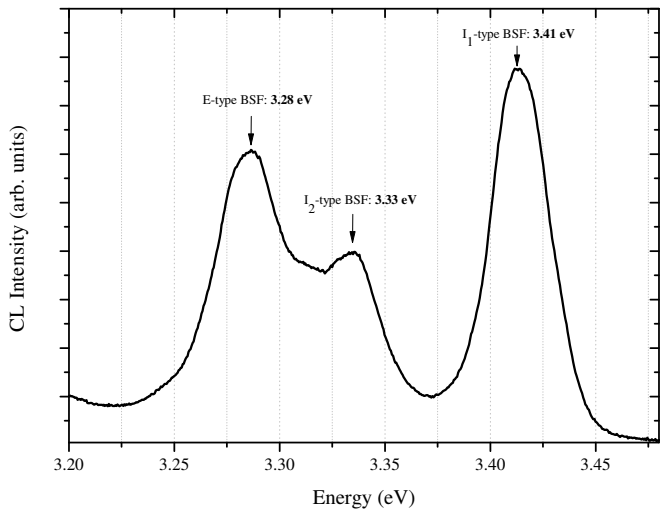

Figure 3.14 – Monochromatic CL images at 77 K acquired at (a) 3.41 eV (b) 3.33 eV and (c) 3.28 eV, nominally corresponding to I_1, I_2 and E BSFs respectively. The spectrum displays luminescence acquired from the -c-wing showing transitions corresponding to the observed BSFs.

3.2.2.3 Non-radiative line defects

Another type of defect observed in coalesced layers corresponds to non-radiative lines oriented along specific crystallographic directions (see figure 3.15). Okada *et al.* suggested that the fact that these lines are non-radiative at any wavelength, indicates that they correspond to dislocations or clusters of dislocations [140], which is what we also observe in our layers.

Figure 3.15 shows a panchromatic CL image of a coalesced (10$\bar{1}$1) semipolar layer. Two types of intersecting lines were systematically observed forming an angle of ≈ 29.5° between each other, and

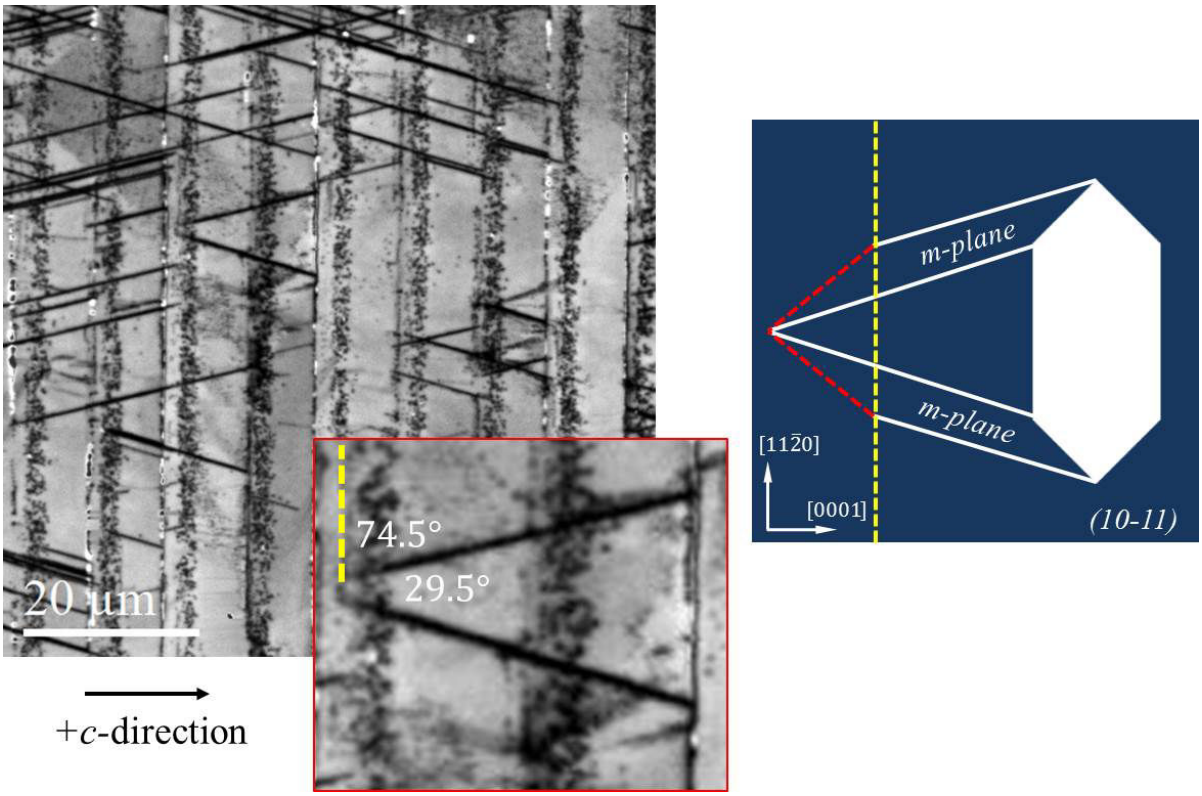

Figure 3.15 – Plane-view panchromatic CL image displaying the non-radiative lines. The reference dashed yellow line corresponds to the projection of the inclined c-plane. The figure to the right illustrates a top-view of the (10$\bar{1}$1) semipolar crystal with the yellow line resembling the c-plane, and the red lines resembling the in-plane intersection between the c-plane and the m-plane.

an angle ≈ 74.5° against the projection of the *c*-plane, as shown in figure 3.15. The in-plane angle φ corresponds to the projection of the *c*-plane and *m*-plane on the (10$\bar{1}$1) surface, and is calculated according to the following equation:

$$\varphi = sin^{-1}\left(\frac{\sqrt{a^2+c^2}}{\frac{a}{2}}\right) \tag{3.2}$$

where *a* and *c* correspond to the lattice constants of the *a*-axis and *c*-axis respectively. The numerical value of the calculated in-plane angle φ was found to be 74.8° which correlates well with the measured experimental value at ≈ 74.5°.

Moreover, figure 3.16 shows a plane-view SEM image and its corresponding panchromatic CL image of a region at the edge of the wafer where the growth has been largely perturbed showing some regions that have been coalesced whereas other bands have not. It has been remarked that these lines only appear on coalesced bands and very rarely on uncoalesced ones. In principle, uncoalesced

bands experience less tensile strain than the coalesced ones, since they can better relax via the free edges. This permits formulating the hypothesis that these non-radiative lines are created to relax the additional strain created upon coalescence. There are two *m*-planes intersecting the (10$\bar{1}$1) plane that could both contribute to relaxation, leading to dislocation cross-hatching as seen in figure 3.15.

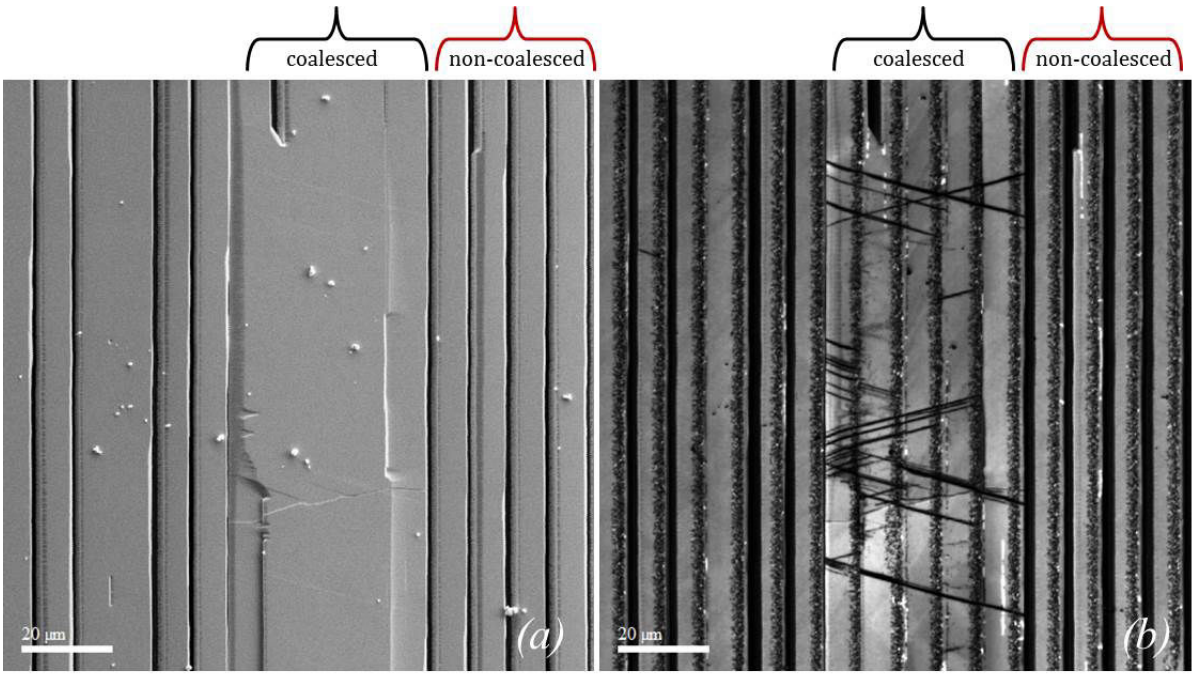

Figure 3.16 – (a) Plane-view SEM image of a perturbed surface with coalesced and non-coalesced bands and (b) its corresponding panchromatic CL image showing the inclined non-radiative lines appearing exclusively on coalesced bands.

This may be associated to the formation of misfit dislocations. In order for a MD to form where it can resolve stress, the dislocation must move through the crystal lattice, usually by a mechanism known as glide. This has been observed in cubic materials by Matthews and Blakeslee [141], where stress relaxation can occur in the two in-plane directions via misfit dislocation formation and glide on the energetically favorable (111) slip system after exceeding the film's critical thickness. For the wurtzite structure, the most favorable glide plane is the *c*-plane (basal slip). However, for films grown in polar and nonpolar planes, there is no shear stress resolved on the *c*-plane, so basal slip cannot occur [142]. In the case of semipolar epitaxy, the basal plane is inclined with respect to the surface. Therefore, stress relaxation can occur by MD glide on the (0001) plane [143]. In this case, the basal plane gliding only permits relaxation in a single direction, which is not what we observe. Alternatively, a second relaxation mechanism can be activated via slip on the prismatic planes of type $\{1\bar{1}00\}$ [144]. Therefore, given the inclination of the observed segments, which corresponds to the intersection of the prismatic *m*-planes with the topmost (10$\bar{1}$1) plane, it may be suggested that dislocation glide on the prismatic planes are the origin of these non-radiative lines.

3.2.3 Pattern's design effect on extended defects

Besides varying growth conditions in order to reduce the density of generated defects, we have investigated the effect of the substrate's striped pattern and its consequences on the generation of TDs and BSFs. The two main design parameters are the nucleation facet size and the pattern period. The facet size is determined by the KOH etching duration, while the pattern period is defined by the mask used in photo-lithography.

The number of TDs reaching the surface is highly dependent on the size of the inclined nucleation facet (*i.e.* the footprint on the substrate). It has been found that the width of the topmost defective region on the stripe is directly proportional to the width of the Si ($\bar{1}\,\bar{1}$1) facet (*i.e.* nucleation facet).

Figure 3.17 compares two panchromatic plane-view CL images of coalesced layers under similar growth conditions but with different patterning geometries: (a) with a 5 μm period and ≈ 500 nm nucleation facet size and (b) with an 5 μm period and ≈ 3000 nm nucleation facet size. The 500 nm facet results in an approximate 1.5 μm defected region, over the 5 μm stripe width, whereas the 3000 nm facet results in an approximate 3 μm defected region over the 5 μm period [7].

The reason behind this difference is explained by two observations: first, a smaller nucleation area means decreased surface contact between GaN and the foreign substrate, which is consequently translated by generating a fewer number of TDs at the Si/AlN/GaN interface and therefore fewer TDs are available to propagate towards the surface. Second, the smaller facet permits a quicker formation of a complete pyramid and therefore an earlier completion of TDs bending, which enables a better spatial confinement of the defects. In short, etching a smaller nucleation facet permits a decreased number of generated TDs at the heteroepitaxial interface and consequently a fewer number from propagating to the film surface (see further on for a discussion on the smallest facets available).

To gain further insight on the effect of nucleation footprint on the overall structural quality, symmetrical XRD on-axis (10$\bar{1}$1) $\omega-$scans were performed, and the rocking curves' FWHMs were assessed for samples having a 2.5 μm thickness [8]. Surprisingly, and in contrast to the TD density behavior, the XRD results systematically demonstrated that the crystal quality on a shallowly etched nucleation facet is inferior to that of a larger facet. The layers grown on smaller facets consistently exhibited higher FWHM average values in addition to a more significant anisotropy translated by minima and maxima much further apart than the ones of the layers grown on the larger facets (see Table 3.1).

[7] The high density of TDs in the defected zones makes determining their exact density impossible. Therefore, and in order to facilitate TD quantification, their density will be assessed based on the ratio between the defected and non-defected areas.

[8] The thickness is measured from the flat masked silicion facet to the topmost surface as indicated by the red arrow in figure 3.17

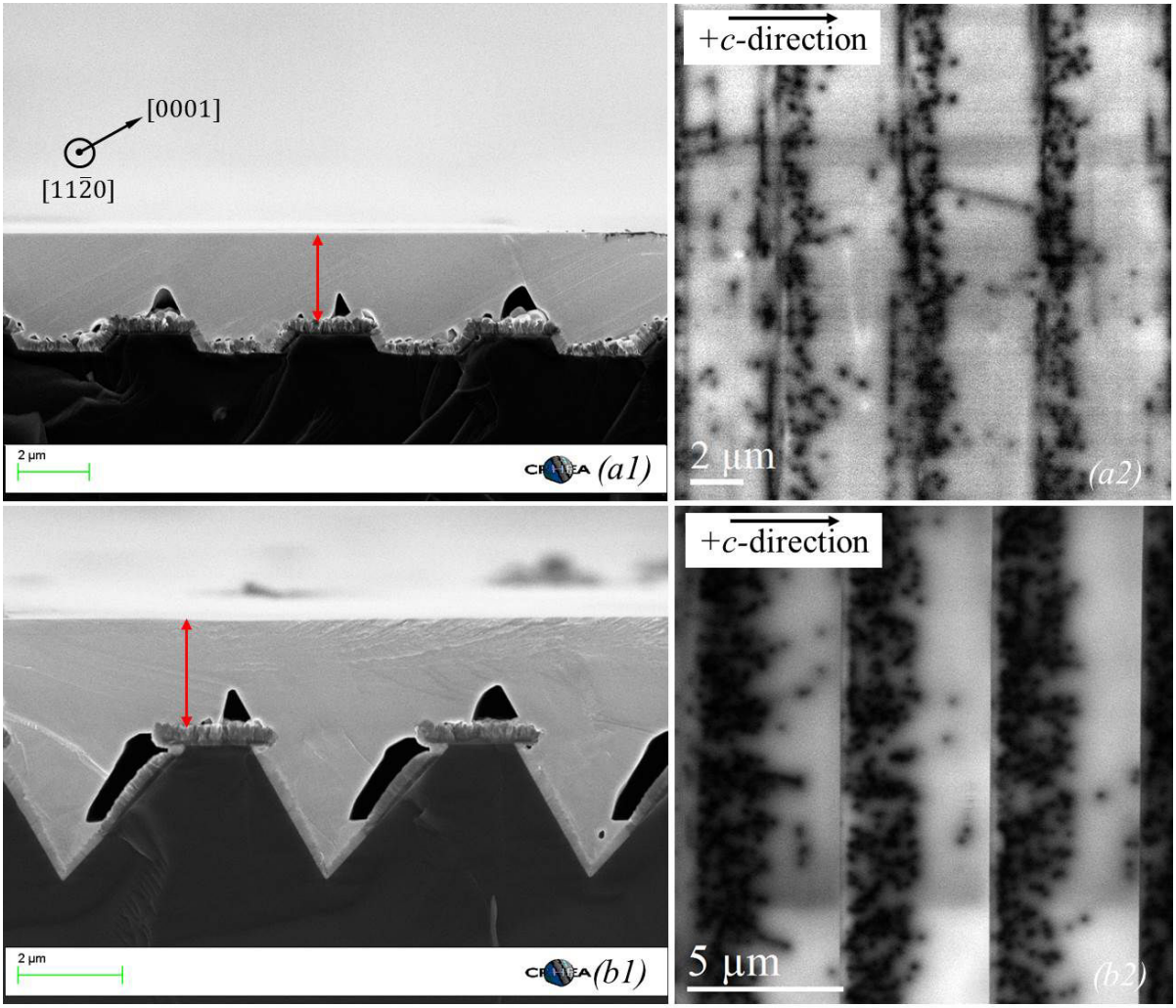

Figure 3.17 – Cross sectional SEM images (not the same scale) and their corresponding plane view panchromatic CL images of GaN layers grown on (a) substrates with a 5 µm pattern period and nucleation facet size of $\approx 500nm$ *and (b) 5 µm pattern period and nucleation facet size of* $\approx 3000nm$.

This may be explained by the increase in BSF density when the smaller facet geometry is adopted with the same pattern period. Indeed, when the growth of GaN proceeds on small facets, the formed pyramidal bands grow higher than the substrate and the mask, faster than the ones growing on larger facets. Consequently, for smaller facets, larger -*c*-wings are formed, which have shown to be typically faulted with BSFs [9].

Figure 3.18 shows a plot of the low-temperature PL intensity as a function the different nucleation facet sizes (*i.e.* 5 μm period with a 3 μm nucleation facet; and 5 μm period with a 0.5 μm nucleation facet). By comparing these two samples, the intensity of BSFs follows the same trend and as the NBE

[9] I_1 and I_2-type BSFs can contribute to the FWHM of the symmetrical (10$\bar{1}$1) scan, when measured with the projection of the x-ray beam parallel to the projection of the *c*-axis, *i.e.* perpendicular to the stripes (see BSF extinction rules in section 2.4.2.2)

Nucleation facet size	Pattern period	FWHM (∥)	FWHM (⊥)
500 nm	5 μm	826	1474
3000 nm	5 μm	838	1001

Table 3.1 – FWHM (arcsec) of symmetrical X-ray rocking curves on-axis (10$\bar{1}$1) $\omega-$scans on GaN layers grown on patterned substrates with different nucleation facet sizes. The parallel (∥) and perpendicular (⊥) notations refer to the direction of the x-ray source with respect to the stripe direction. Studied samples have been grown under identical growth conditions and have the same thickness.

emission, despite the change of the etched facet size. This suggests that smaller nucleation facets result in a higher NBE emission intensity as a result of a decreased density of TDs. However, the smaller nucleation facets also cause the formation of a larger -*c*-wing to +*c*-wing ratio, and thus a higher density of BSFs.

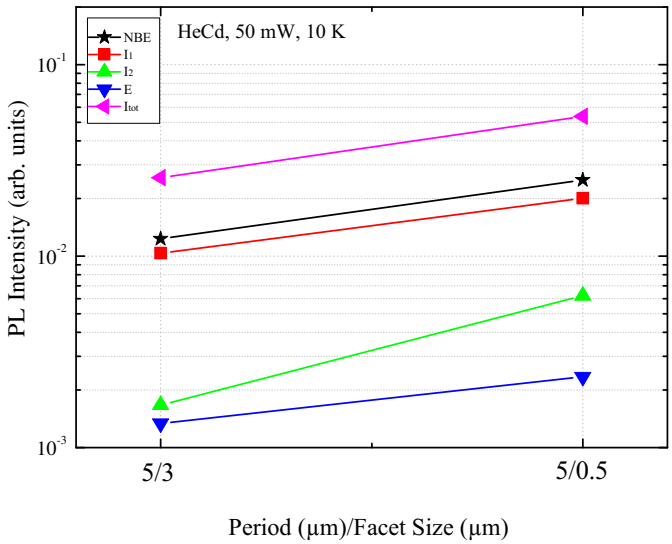

Figure 3.18 – Low temperature PL intensities of the NBE and BSF transitions as a function of the period and etched facet size. The two studied geometries are (a) 5 µm period with a 3 µm nucleation facet and (c) 5 µm period with a 0.5 µm nucleation facet. The (★) notation represents the NBE emission; the (■), (▲) and (▼) notations represent the I_1, I_2 and E-type BSFs; and the (◀) notation represents the total intensity of all signals combined.

To sum up, in order to reduce the TD density on the surface, the smallest possible facet size and largest possible period should be applied. Small facets will enable less nucleation of TDs and wider periods will permit wider terraces free of dislocations. Concerning BSFs, we have seen that for the same period: as the facet size decreases, the -*c*-wing extension increases. So, upon increasing the period size, the -*c*-wing extension will further increase. However, seeing that the growth rate for the +*c*-wing is 10 to 20 times faster than the -*c*-wing, adapting large pattern periods will result in an increase in the +*c*-wing to -*c*-wing ratio if compared to smaller pattern periods, which may

contribute to reducing the overall BSF density. However, from the fabrication/growth point of view, both extremes (*i.e.* very small facets and very large periods) display limitations that do not permit to push this idea to infinity.

On silicon, etching extremely small facets is a challenge, especially when KOH wet baths are utilized. The main problem is controlling the etching start, which is a classical problem widely addressed in literature [145, 146]. What is meant by "etching start" is when the etching effectively begins after a patterned wafer is immersed in KOH, which counter-intuitively, does not begin immediately, and requires a certain *random* duration to launch. This can be due to several reasons: the first thing that comes to mind is the formation of a native oxide on silicon after the lithography process that defines the bands. The formation of a native oxide temporarily blocks the KOH from etching the silicon before localized etching begins (generally from the center or from the edges of the substrate) and then gradually spreads towards the rest of the substrate as the oxide layer is lifted-off. Indeed, a solution to this problem is to chemically remove the formed oxide layer by BOE or highly diluted HF just before etching with KOH. However, with the considerably small pattern dimensions used in our case (*i.e.* 5 μm period with 2.5 μm openings), a significant in-homogeneity in removing the oxide layer has been observed, hence influencing the subsequent KOH etching. The inhomogeneous oxide removal can be improved by adapting longer BOE etching durations. This, indeed, removes homogeneously the native oxide from the whole substrate surface, but on the other hand destroys the deposited dielectric mask used to define the stripes. Any imperfection or perturbation in defining this mask consequently influences the KOH etching of silicon, which causes inadequately defined facets and significant macro-steps on the {111} facets. Another reason causing inhomogeneous KOH etching may be temperature gradients in chemical baths, which become more severe as the bath volumes increase. It is worthwhile noting here that the aforementioned critical problem is particular for etching silicon. Etching sapphire for the same purpose of defining inclined facets is less problematic since it could be done using dry reactive ion etching, which can in principle achieve perfect homogeneity.

Therefore, fabricating very small nucleation facets on silicon requires extreme precise control of the chemical etching process, since any imperfection on the wafer will result in a difference of facet sizes on different parts of the substrate. This will affect the growth, in particular, leading to regions coalescing before others. Moreover, a variation in facet sizes on the same wafer will lead to different growth rates under identical growth conditions, primarily due to inhomogeneous adatom migration to nucleation sites.

Furthermore, the point of view suggesting large periods (hundreds of micrometers) to create larger defect free terraces is also limited by the necessary growth duration to coalesce neighboring stripes. Ideally, if an LED of size, say 200 μm × 200 μm, is to be fabricated, a period of 200 μm would be prefer-

able, leading to an array of LEDs, one on each individual stripe. This proposal however, would require long growth durations, which highly increase the probability of meltback etching, and therefore the destruction of the surface. A design trade-off has to be implemented.

Following this, two patents addressing potential solutions for inclined facet size control have been filed, but will not be discussed in this manuscript [10].

3.2.4 Roughness variation as a function of layer thickness

One of the important surface parameters from the point of view of technological applications is the *rms* roughness, whose reduction is necessary for obtaining epi-ready films. In this section, a surface study including quantitative roughness determination of the semipolar GaN growth will be presented.

It would have been interesting to begin with the analysis of the wet etched Si ($\bar{1}\,\bar{1}$1) surface onto which the GaN is grown. However, the apparatus' limitations does not permit measuring these relatively highly inclined facets at 61° as the AFM's cantilever eventually gets in contact with the topmost part of the substrate, hence inhibiting the tip from reaching the inclined surface. Consequently, we will assume that all surfaces are identical, although we are aware that some fabrication imperfections may be present: macro-steps can be easily encountered on the Si (111) nucleation facets after the wet KOH etching especially if a perfect stripe alignment is not achieved during photo-lithography[11].

The AFM images shown in figure 3.19 display surfaces having different GaN thicknesses ranging from uncoalesced stripes to coalesced films up to 4 μm thick. Such layers were achieved on identically prepared substrates by varying the growth time while maintaining constant growth conditions. The shown regions are, 2 μm × 2 μm and 5 μm × 5 μm except for the uncoalesced stripes (4 μm × 4 μm instead of 5 μm × 5 μm).

As displayed in figure 3.19, a common feature between all the acquired AFM images is the surface topography, which exhibits atomically flat terraces and atomic steps. Figure 3.20 plots the *rms* roughness as a function of different growth times (*i.e.* different thickness). The values indicate that the *rms* on 2 μm × 2 μm scans very slightly increases from 0.30 nm to 0.67 nm from uncoalesced stripes to coalesced 4 μm layers, respectively. The 5 μm × 5 μm scans follow a similar trend, and increase from 1.20 nm to 2.00 nm. In what concerns the 10 μm × 10 μm scans, which have only been measured

[10] Filed Patents:

- M. Khoury, J. Zúñiga-Pérez, P. Vennéguès and G. Feuillet. Filed Patent: **FR. 15/55582**
- G. Feuillet, M. Khoury, J. Zúñiga-Pérez and P. Vennéguès. Filed Patent: **FR. 15/61619**

[11] It is to be noted that all fabricated samples have been aligned with a Normarski microscope, relying on human eye precision.

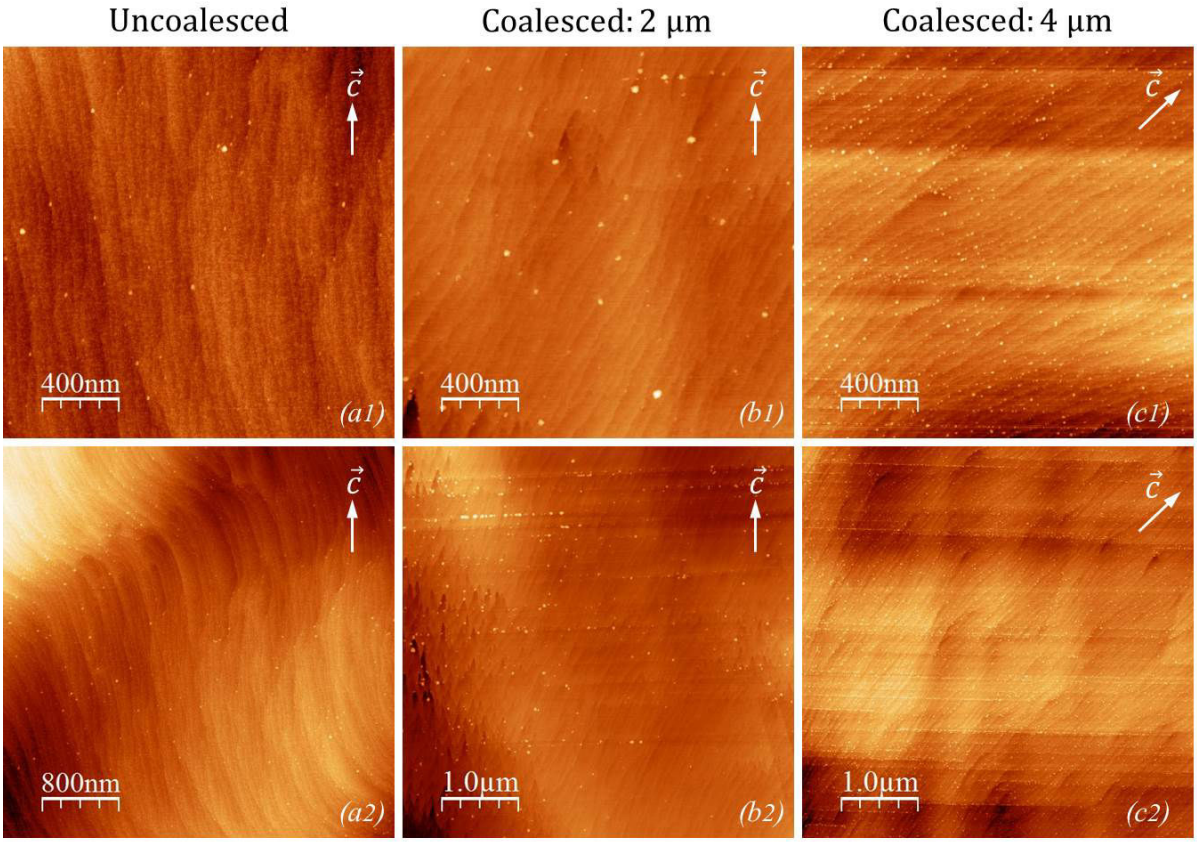

Figure 3.19 – AFM images of samples grown under similar growth conditions but with varying thickness. (a) 2 µm × 2 µm and 4 µm × 4 µm for uncoalesced bands, (b) 2 µm × 2 µm and 5 µm × 5 µm for 2 µm thick coalesced layers and (c) 2 µm × 2 µm and 5 µm × 5 µm for 4 µm thick coalesced layers. The white arrows indicate the +c-direction that is perpendicular to the bands.

on the coalesced layers, a more significant increase in the *rms* roughness can be noticed, reaching up to 7.00 nm for a 4 μm thick layer. This can be associated to surface undulation, which in our case does not correspond to a systematic particular direction. In comparison with (0001) GaN grown on Si (111), an *rms* of 0.80 nm for 10 μm × 10 μm scans on layers having the same thickness (*i.e.* 4 μm) have been reported [133]. The *rms* values for the (10$\bar{1}$1) surfaces may be enough for subsequent growth (*i.e.* active regions), which could eliminate the necessity of a post-growth chemo-mechanical polishing step to flatten the surface [147].

If a closer look is taken on the images, one can notice the presence of *surface decorations* appearing as bright dots on the surfaces, which are systematically seen to be attached to the terrace edges. What is also clearly visible is the increase in their density as the growth time increases. These decorations may be responsible in contributing to the increase of *rms* values since surface line-scans indicate that their heights can reach up to 2 nm along the *z*-axis. Their origin is not well understood, but could be associated to contamination originating from the reactor chamber walls [148].

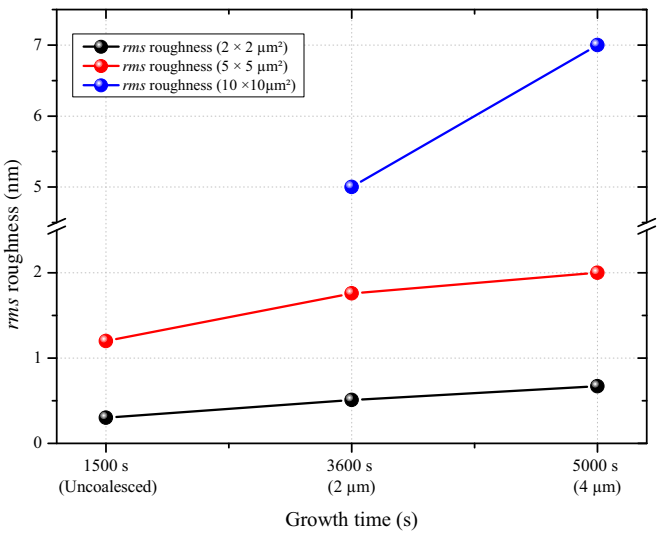

Figure 3.20 – Plot of the rms roughness evolution for different scan sizes as a function of the growth time and hence layer thickness.

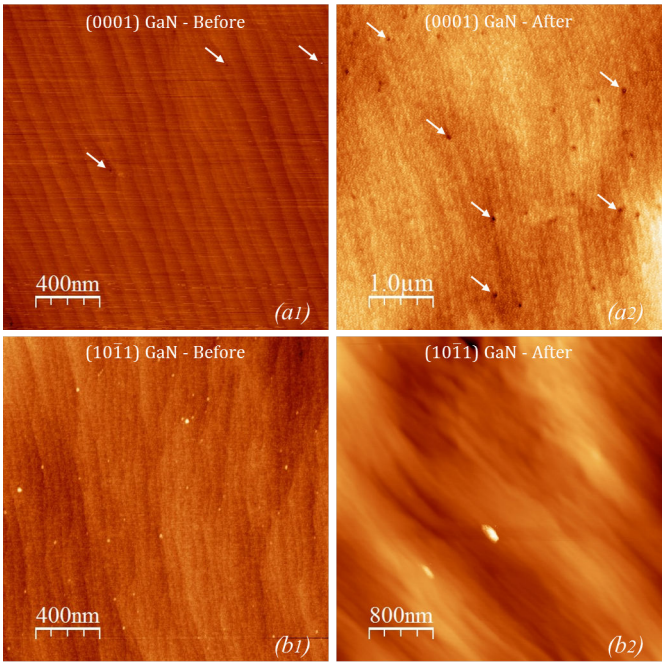

Figure 3.21 – AFM images of the surface morphology before (2 µm × 2 µm) and after (5 µm × 5 µm) the silane treatment on (a) polar and (b)semipolar (10$\bar{1}$1) surfaces. Notice the increase in pit size after the silane treatment for c-plane GaN only. The white arrows show where TDs appear.

It is also worth noting here that contrary to *c*-plane GaN, no surface pits associated to TDs have been observed. The silane (SiH_4) surface treatment used in *c*-plane GaN [118] for increasing the diameter of TD pits has also been tested for the semipolar films. However, no effect has been detected on the layers, and no observable pits came into existence. This is shown in figure 3.21.

3.2.5 Nucleation on the opposite Si (111) facet

As mentioned in the description of the fabrication process, the last step involves an IBS deposition in order to mask one facet and limit the growth on the opposite one. During the inclined deposition, a shadowing effect of the ion beam by the masked topmost flat band may exist, hence leaving a small portion of the supposedly masked (111) facet, unmasked (see section 3.1 and figure 3.2 (b)). Consequently, when the growth proceeds, crystalline GaN will be deposited on the entire Si ($\bar{1}\,\bar{1}$1) facet as well as on the small exposed part on the bottom of the Si (111) facet.

The effect of this parasitic growth on defect generation has been investigated by TEM (Figure 3.22). It was observed that the large crystal, grown on the "correct" ($\bar{1}\,\bar{1}$1) facet, over-grows the smaller one rapidly, hence inhibiting any further extension that may affect the surface. However, at the grain boundaries where both crystals get in contact, the formation of cubic GaN is observed (see figure 3.22 (c),(d)). This is consistent with a recent study dedicated to intentionally grow cubic GaN on patterned Si (001) on-axis substrates, by growing two opposing hexagonal GaN crystals [149].

3.2.6 "Classical growth" overall quality

Structural and optical characterization was performed in order to determine the overall quality of the grown layers when the classical growth process is adopted (*i.e.* single-step growth process). The following characterized semipolar GaN layer was grown on a patterned substrate having a period of 8.5 μm and a facet size ~ 5 μm.

Figure 3.23 shows low temperature PL spectra of a coalesced 2.5 μm thick (10$\bar{1}$1) semipolar layer (blue), and a high-quality 12 μm thick (0001) GaN on Si (111) (black) used for reference. The PL spectrum of the semipolar layer exhibits a D^0X transition energy at 3.457 eV indicating that the layers are under tensile strain. The semipolar layers also indicate the presence of an important density of BSFs. PL transitions at 3.402 eV, 3.320 eV and 3.279 eV correspond to I_1, I_2 and E-type BSFs, respectively. The NBE transitions have generally shown intensities higher by a factor three than transitions associated to I_1-type BSFs. For different layers coalesced under different growth conditions, the NBE to BSF peak intensity ratios have shown to systematically exhibit similar intensity values when the classical single-step growth is adapted. For comparison, (10$\bar{1}$1) semipolar layers grown on sapphire using the same patterning technique and inclined growth, display similar values, as reported by Schwaiger *et al.* [72]. Their layers also exhibit elevated densities of BSFs translated into PL spectra showing NBE:BSF intensity ratios of almost 1:1.

From the structural point of view, samples' quality has been assessed by measuring the XRD rocking curve FWHMs of the symmetrical (10$\bar{1}$1) reflections at different azimuthal angles. The FWHM of coalesced ~ 2.5 μm thick layers amounted, in the best case, to 717 and 909 arcsec when measured

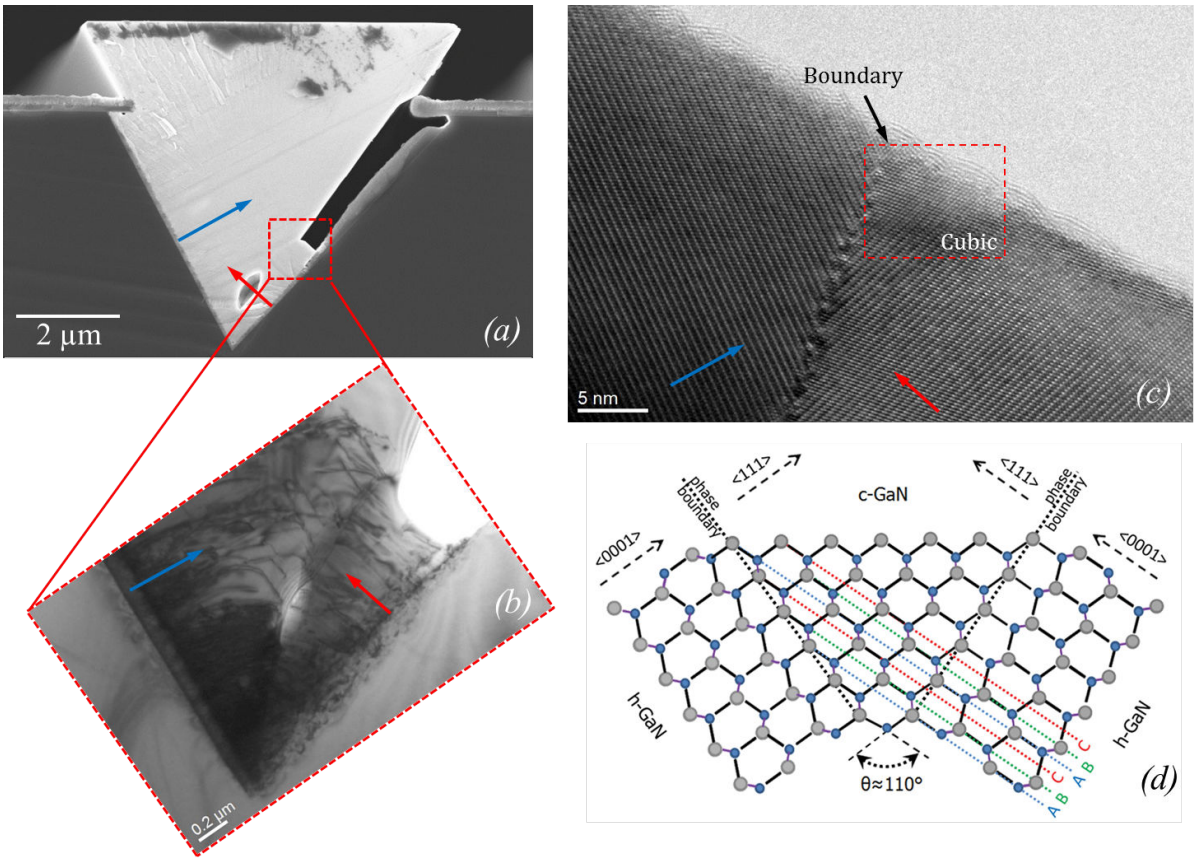

Figure 3.22 – (a) SEM image displaying crystals nucleating on the unmasked and on the partially masked Si (111) facets, and whose c-directions are indicated by the arrows (b) Bright-field TEM image at the interface between the two crystals. (c) HRTEM image at the same interface indicating the cubic phase formation at the two wurtzite interfaces and (d) the corresponding schematic of the cubic stacking between two hexagonal stacks (Image source: [149]). The blue arrows indicate the growth direction of the large crystal grown on the ($\bar{1}\,\bar{1}$1) facet and the red arrows indicate the growth direction of the small parasitic crystal grown on the unmasked part of the (111) facet.

parallel and perpendicular to the stripes, respectively. Takami *et al.* reported on ~ 4 μm thick (10$\bar{1}$1) semipolar layers grown on (11$\bar{2}$3) patterned sapphire substrates, FWHMs of 875 and 313 arcsec when parallel and perpendicular to the stripes, respectively [127].

3.2.7 Discussion on single-step growth

In principle, the objective of this PhD is to obtain coalesced semipolar GaN layers with the lowest density of structural defects. The first part of this chapter was dedicated to investigate the growth of semipolar (10$\bar{1}$1) on patterned Si (001)7°off using a classical single step epitaxial process. The results have indicated that these heteroepitaxial layers are heavily plagued with structural defects, essentially BSFs and TDs.

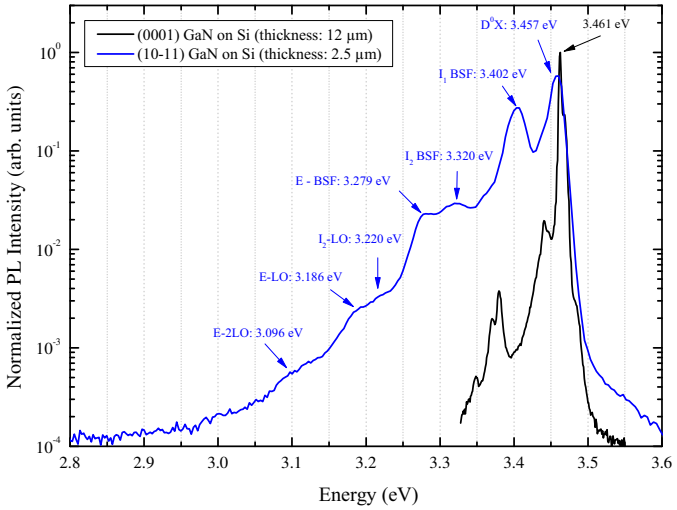

Figure 3.23 – PL spectra acquired at 10 K. The spectrum in blue corresponds to a coalesced 2.5 µm thick (10$\bar{1}$1) semipolar GaN film on patterned silicon. The spectrum shown in black corresponds to a high-quality 12 µm thick (0001) GaN grown on Si (111) by MOVPE, and is used for reference. Typically observed transitions are marked on the spectra.

In order to reduce the density of structural defects, several defect management strategies have been proposed earlier in literature, as described in section 2.3. For example, the voided adjacent crystal overlapping (see section 2.3.3), which consists in overlapping the defected -*c*-wings with the high-quality +*c*-wings by performing a three-step growth process. This approach, applied for the growth of the (11$\bar{2}$2) orientation, has shown to be the most efficient method for blocking defects from propagating towards the topmost surface [71, 104]. Consequently, this technique requires fine tuning of growth conditions that enable controlling growth rates in different directions, which is necessary to manage the geometry of the bands.

However, as shown in this chapter, the (10$\bar{1}$1) surface is highly stable under a wide rage of growth conditions (see section 3.2.1.2). The elevated stability of the (10$\bar{1}$1) surface permits its natural formation and dominance over other crystallographic facets. This, in turn, decreases the possibility of controlling the band geometry by tuning growth conditions. As a result, the topmost (10$\bar{1}$1) surfaces of adjacent bands always lie in the same plane and at the same height. This stable geometrical alignment, thus, does not permit the implementation of the aforementioned defect reduction method for the growth of (10$\bar{1}$1) GaN.

Since a *universal* method applicable for blocking defects in all semipolar orientations lacks, different strategies have been addressed.

3.3 Defect reduction by inter-layer insertion in (10$\bar{1}$1) semipolar GaN

The following sections will be dedicated to describe the different attempted approaches to reduce the density of defects propagating to the surface via in-situ interlayer insertion. First, inserting a LT-AlN interlayer between GaN layers will be investigated and the subsequent effect on structural defects will be described in section 3.3.1. Later on, another approach originally introduced in this PhD, also employed for the reduction of TDs and annihilation of BSFs in semipolar (10$\bar{1}$1) GaN, will be studied and discussed in section 3.3.2.

3.3.1 Low-Temperature AlN interlayers

Significant BSF reduction and their possible elimination in semipolar GaN films on planar Si (112) and Si (113) has been reported by inserting a LT-AlN interlayer sandwiched between two GaN layers [150]. This LT-AlN interlayer has shown to be effective in blocking defect propagation for semipolar GaN layers with (10$\bar{1}$6), (10$\bar{1}$4) [68] and (10$\bar{1}$3) [151] orientations grown on planar silicon.

To reproduce this approach, a LT-AlN layer grown at 750°C was inserted between two GaN layers, both grown under identical conditions. The growth durations of the LT-ALN interlayers were 120 s (≈ 3 nm), 300 s (≈ 7.5 nm) and 600 s (≈ 15 nm) to study the effect of the interlayer thickness [12]. In figure 3.24, it is shown that the LT-AlN interlayer follows the surface morphology of the first coalesced GaN layer, which is nearly parallel to substrate surface, indicating a smooth morphology.

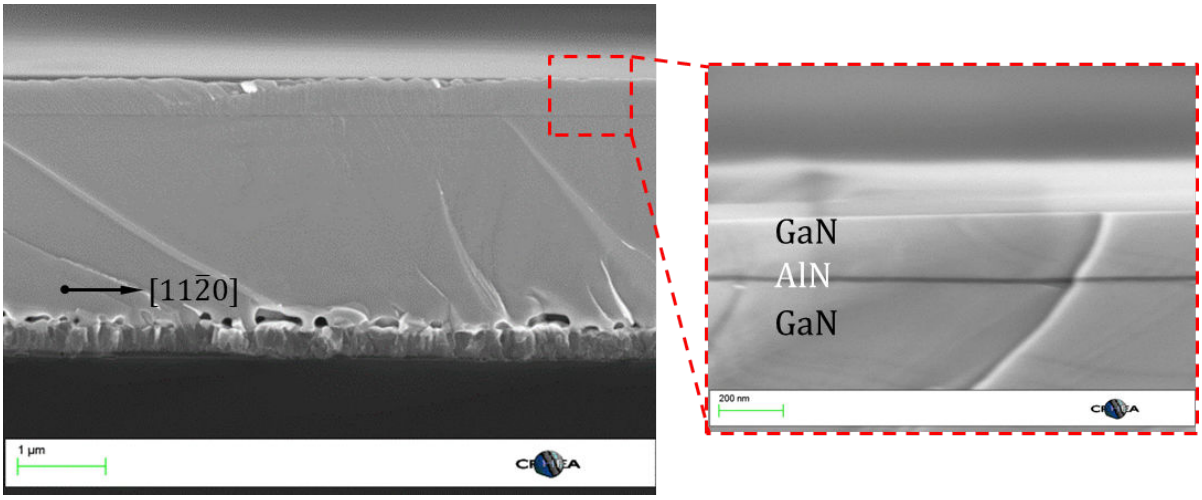

Figure 3.24 – Cross sectional SEM images showing the LT-AlN layer sandwiched between two GaN layers. Stripes do not appear as the image has been acquired with stripes parallel to the observation plane.

[12] Only the thickest 15 nm layer has been measured by SEM. For the rest, the values are extrapolated by assuming a linear growth rate.

In the plane-view CL panchromatic images acquired at 77 K shown in figure 3.25, the outcome as a function of the interlayer thickness in presented. A significant increase in TD and BSF densities is clearly observed, especially when the interlayer thickness increases (see figures 3.25 (b) and (c)). Indeed, the LT-AlN layers have also been tested before the coalescence of adjacent bands, and similar results have been observed.

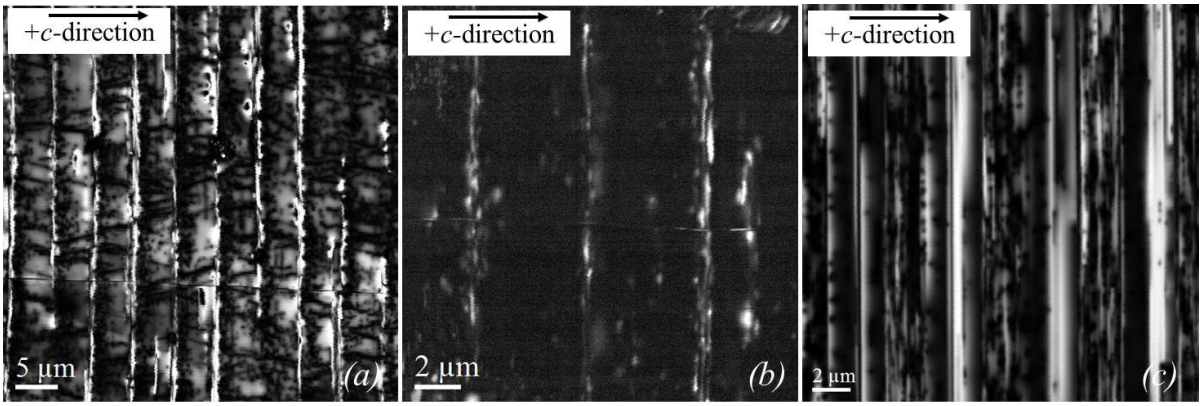

Figure 3.25 – Panchromatic CL images acquired at 77 K of a semipolar GaN layer with a LT-AlN interlayer grown for (a) 120 s (b) 300 s and (c) 600 s.

The obtained results may not be surprising since LT-AlN layers lead to lattice relaxation, typically via the formation of MDs at the GaN/LT-AlN interface. This could explain the elevated number of TDs after the interlayer insertion, as seen by the overall dark contrasts in figure 3.25. Wu *et al.* [152] reported on partial strain relaxation by BSF generation in InGaN MQWs grown on (10$\bar{1}$1). The results indicated that in high indium composition layers (40%), each I_1-type BSF is involved in the removal of a half basal plane, thus relaxing the compressive misfit strain in the InGaN layers. However, lower indium content layers (12%) exhibited no extended defect generation in the MQWs. The generation of more BSFs is therefore in coherence with what we observe in our samples. For the thin AlN interlayer, no significant change of defect generation is observed in comparison with a sample grown without an interlayer. However, upon increase in the interlayer's thickness, strain is further introduced and a promotion of BSF generation therefore becomes more likely.

Dadgar *et al.* [68] suggested that the observed BSF blocking is a result of misfit generation that preferably occurs at stacking faults and leads to their elimination *e.g.* by partial dislocations. The insertion of LT-AlN interlayers employed for BSF reduction may only be effective for low-inclination semipolar orientations *i.e.* 18° and 22° [94]. For higher inclination semipolar orientations (*i.e.* 61°), other approaches are therefore necessary.

3.3.2 SF_6 surface treatment

Seeing that LT-AlN interlayers are ineffective for reducing the density of structural defects in our semipolar layers, another approach involving an etching step has been investigated for the same purpose. In the following sections, all the substrate fabrication process will be introduced, the GaN growth will be described, and the material will be characterized structurally and optically. The layers' quality will be compared with the classical growth and previously reported state-of-the-art (10$\bar{1}$1) layers. The samples grown using this approach will be referred to as "surface-treated" samples.

3.3.2.1 AlN growth and post-processing steps

The following points list the fabrication steps of the silicon substrate prior to the GaN growth:

- Identical to the substrates used for the classical growth, patterned substrates with V-grooves and a single masked inclined facet are initially fabricated (see section 3.1 for details). The used period was 8.5 μm, and the inclined etched facets were ~ 5 μm large.

- Samples are then loaded into the MOVPE reactor and 100 nm of AlN at 1350°C is grown selectively on the Si ($\bar{1}\,\bar{1}$ 1) facets. Crystalline AlN is grown on the exposed facets, and polycrystalline AlN is deposited everywhere else above the dielectric mask due to the short diffusion length of aluminum (Figure 3.26 (a)). Until this point, nothing has changed from the classical fabrication and growth.

- Samples are then unloaded from the reactor and immersed in BOE. The SiO_2 mask (between the silicon substrate and the deposited poly-crystalline AlN) is then etched away and all the deposited poly-crystalline AlN on the mask is lifted-off (Figure 3.26 (b)). This results in exposing the previously masked silicon. The poly-cystalline AlN on the "opposite Si (111) facet" is not lifted-off after the SiO_2 etching. The AlN on the silicon facet and the poly-crystalline AlN form a continuous layer (indicated by the red circle in figure 3.26 (b)). This results in a void between the silicon facet and the poly-crystalline AlN after the SiO_2 is etched away. As we will see later, this inclined overhanging poly-crystalline AlN layer alone is not problematic. However, it is necessary to adjust the thickness of the grown AlN in order to avoid the sticking between the crystalline AlN and the polycrystalline AlN on the topmost surface. Otherwise, it has been seen that a thick AlN film results in forming a continuous layer hence making the lift-off impossible. This is shown in figure 3.27.

- The final step before the GaN growth involves using an RIE reactor, where samples are exposed to an SF_6 plasma by which they are isotropically etched (Figure 3.26 (c)). The SF_6 plasma effect

can be seen in the SEM figure where the silicon is clearly etched after 10 minutes. It is to be noted that the crystalline AlN is not influenced by the etching, or at least does not degrade the layer for the subsequent epitaxy.

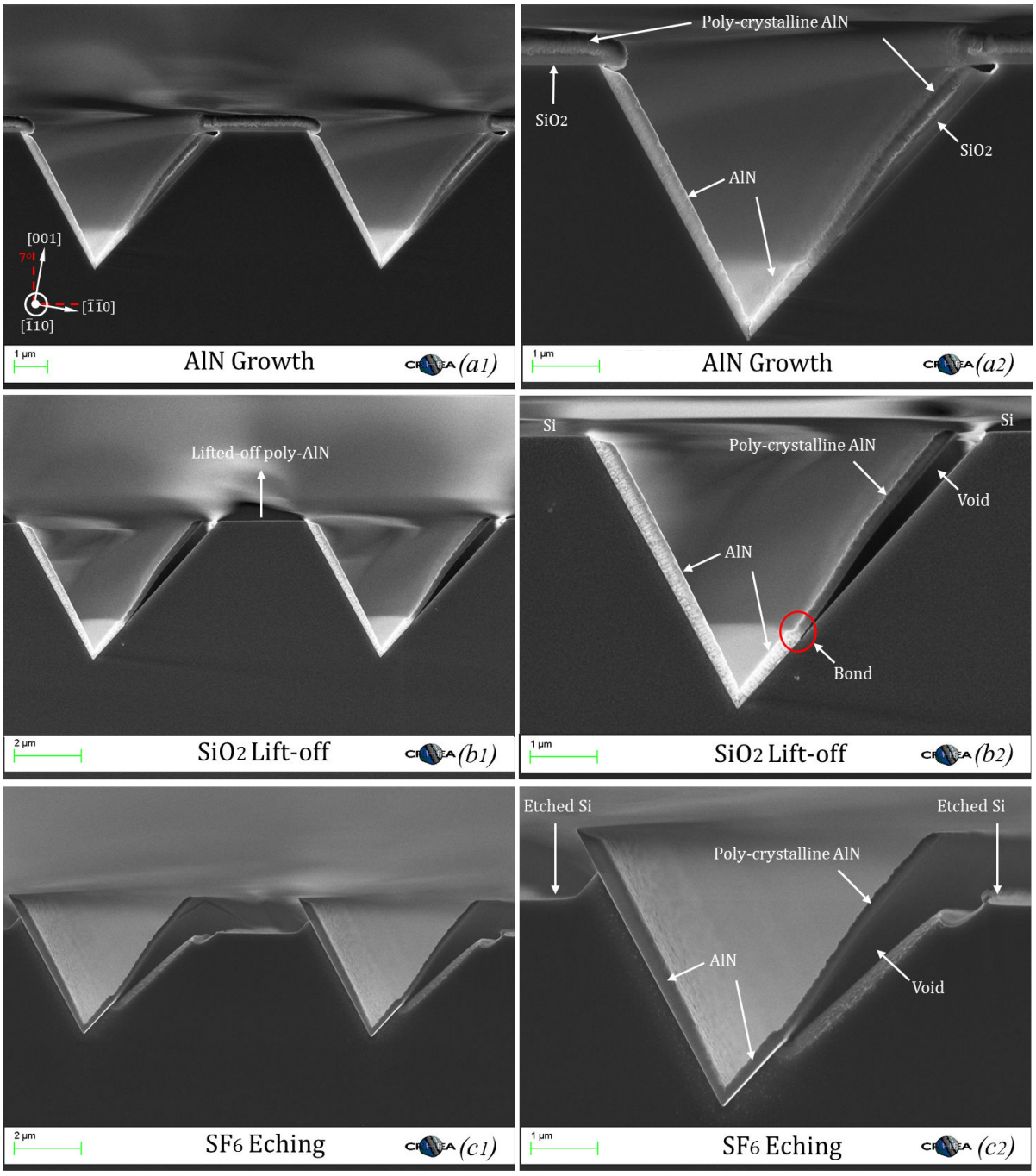

Figure 3.26 – Cross sectional SEM images of the (a) first fabrication step consisting of AlN growth on pre-etched V-grooves. (b) the second fabrication step consisting of the SiO_2 mask chemical etching with BOE, showing that the poly-crystalline AlN deposition is lifted-off from the topmost facet. Poly-crystalline AlN deposited on the inclined facet does not get lifted-off due to the bonding with the crystalline AlN as indicated with the red circle. (c)the third and last fabrication step before GaN growth consisting of 10 minutes of SF_6 reactive ion etching.

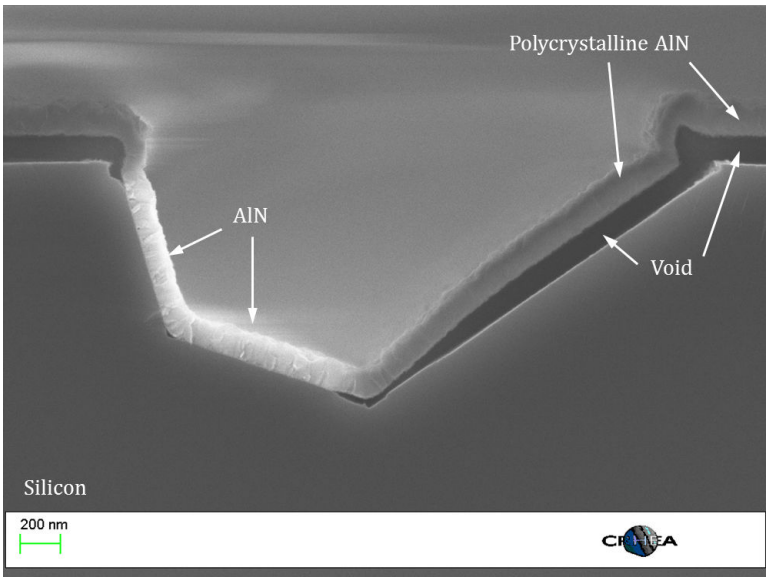

Figure 3.27 – Cross sectional SEM image after the growth of a thicker (compared to figure 3.26 (b)) AlN layer and subsequent BOE etching. The SiO_2 layer is indeed etched away, but no lift-off of the topmost poly-crystalline AlN occurs due to the bonding with the inclined AlN.

3.3.2.2 GaN growth

Once the SF_6 etching step was accomplished, samples were reloaded into the MOVPE reactor to launch the GaN growth. GaN growth was carried out at a temperature of 1210°C and a pressure of 300 mbar using TMGa and NH_3 as source precursors under a V/III ratio of 650 (*i.e.* same growth conditions as the one adopted for the single-step classical growth).

Figure 3.28 shows a cross sectional SEM image after the GaN growth on the fabricated sample prepared with 10 minutes of SF_6 etching. Figure 3.28 shows two striking features: first, the formation of a well-marked " dark line" that appears once GaN exceeds the upper limit of the AlN layer defined by the size of the initial silicon facet. Second, after the formation of this line, a kink is formed (see red arrow), creating a gap of ≈ 300 nm where GaN growth does not occur. We highlight here that the GaN growth has been done in one growth run without any interruptions, and without any change in parameters during growth. Moreover, it is remarkable to see that no growth or even deposition has occurred on the exposed silicon surfaces. More importantly, a significant reduction of meltback etching was remarked, and this even if the growth was performed under growth conditions where heavy meltback etching would have been observed if the SF_6 etching had not been done [13].

[13] We note here that we do not claim to eliminate meltback etching using this method. However, it has been noticed that the density of meltback etching was remarkably reduced in comparison with the classical growth under similar growth conditions.

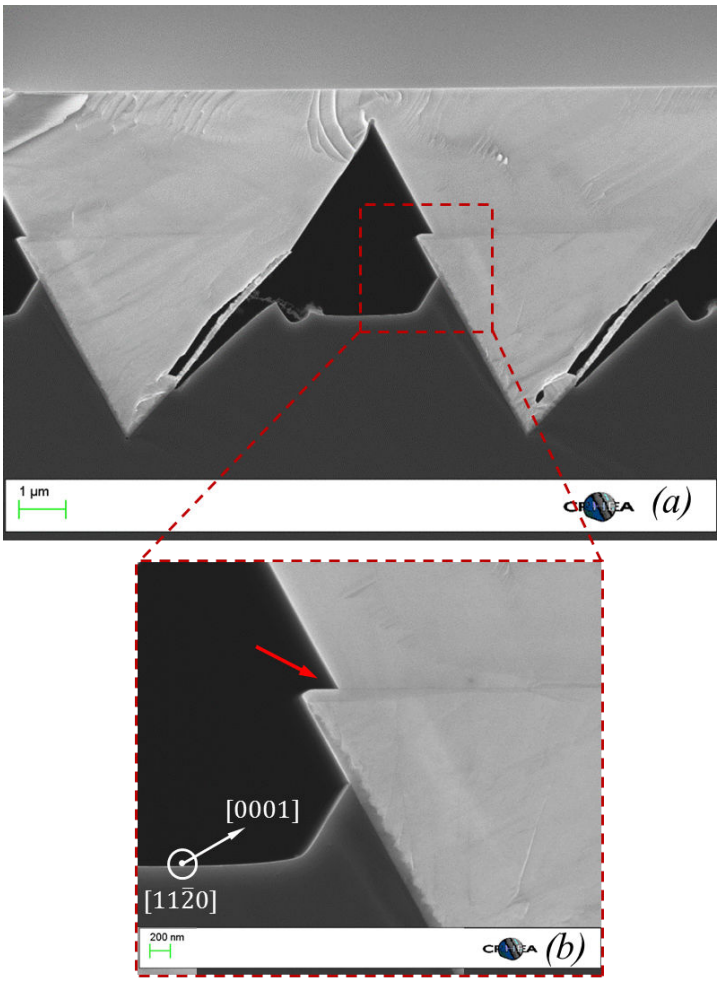

Figure 3.28 – (a) A cross-sectional SEM image after the growth of GaN and (b) a closeup on the crystal where the formation of the line and the kink are observed.

3.3.2.3 Micro-structural characterization by TEM and CL

To understand the effect of this treatment on the structural quality of the coalesced layer, detailed optical and structural characterization has been performed. Grown crystals' micro-structure was initially investigated by cross-sectional TEM and STEM. Bright-field multi-beam TEM/STEM (Figures 3.29 and 3.30) was performed along the [11$\bar{2}$0] zone axis; under imaging conditions permitting the observation of all *a*+*c*-type and two-thirds of the *a*-type TDs. In an identical manner as the previously discussed classical growth, TD nucleate at the Si/AlN/GaN interfaces, propagate in the +*c*-growth direction and then bend in the basal plane. However, in this case the formation of the thin layer blocks an important number of TDs from propagating any further towards the surface. TDs seem to be bent again and propagate in the plane containing this blocking layer. One can also see that the TD blocking is efficient in the beginning (*i.e.* close to the kink), but becomes less efficient gradually

as the distance from the kink increases. Furthermore, no BSFs were observed in any of the acquired TEM/STEM images, even in the *-c*-wings where BSFs were systematically observed when the classical single-step growth was adapted.

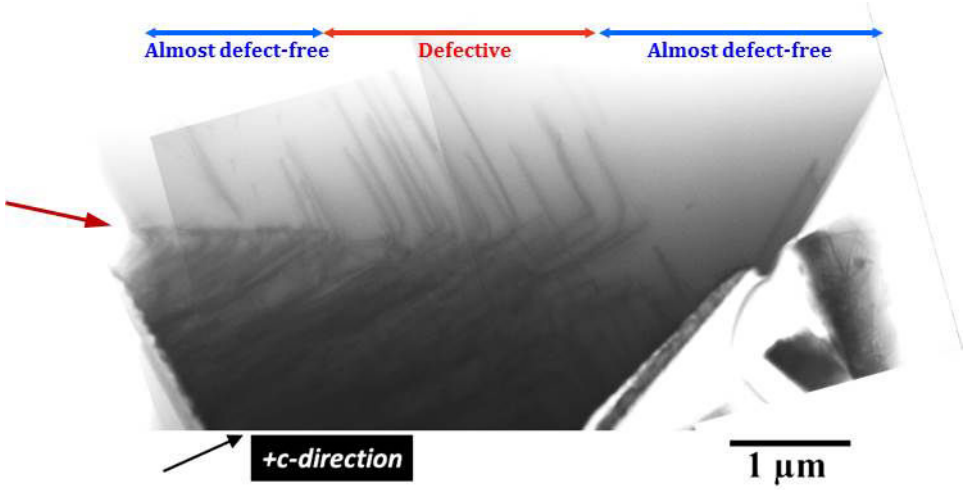

Figure 3.29 – BF-STEM image acquired in the [11$\bar{2}$0] zone axis. The red arrow indicates the position of the defect blocking layer. The crystal can also be divided into three zones indicating defected and defect-free areas.

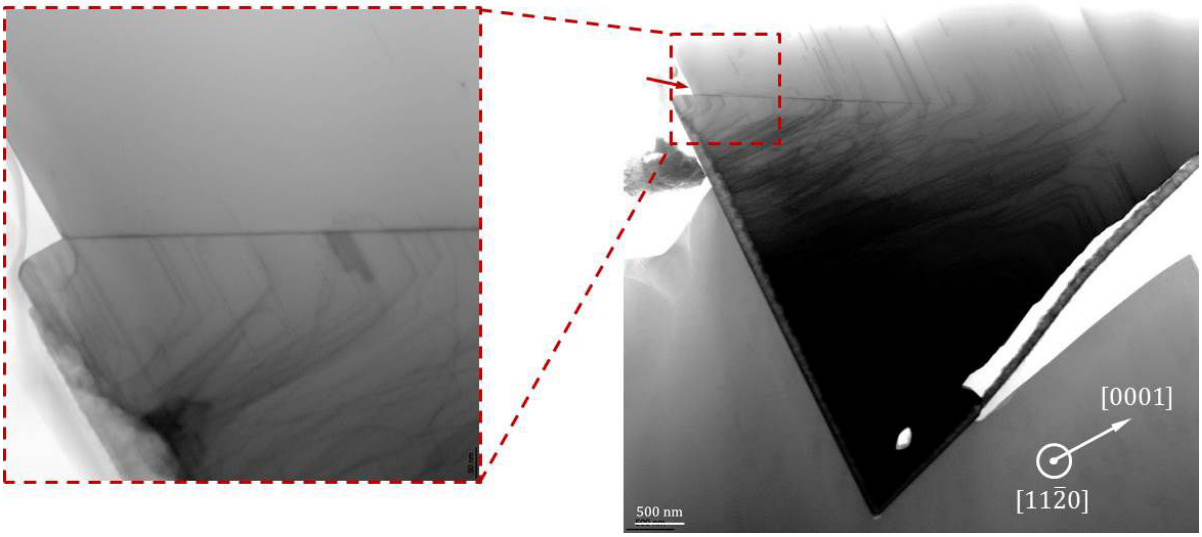

Figure 3.30 – BF-TEM image acquired in the [11$\bar{2}$0] zone axis of a single crystal (right). A higher resolution/magnification image better displaying the defect blocking layer, and the red arrow indicating its position (left).

To further understand the role of this blocking layer, samples were studied by low temperature plane-view CL in order to spatially resolve the defect distribution on the surface. The first remarkable feature is the significant reduction of black spots as shown in figure 3.31 (a) in comparison with the classical growth, which indeed confirms the effectiveness of the blocking layer. Moreover, and by correlating the panchromatic CL images with the previously discussed cross sectional TEM/STEM images, the spatial defect distribution can be divided into three main zones as shown in figures 3.29

and 3.31. The first blue zone, which is almost defect-free, corresponds to the area closest to the nucleation facet where the layer is highly effective in blocking TDs. The red zone, which is defective, corresponds to the part of the pyramidal crystal where TDs escape and propagate towards the surface. The presence of this defective region (marked in red) may be attributed to the formation of the blocking layer before a perfect pyramidal crystal is completed or that the blocking layer properties change in going from the kink to the opposite side of the band. This means that the dislocations that bend before the formation of the blocking layer are blocked, meanwhile, the subsequent extension of the crystal occurring after the formation of the blocking layer enables the dislocations that bend to propagate towards the surface. The second blue zone, which is also almost defect-free, corresponds to the area grown after the bending of all TDs is completed. For comparison, a classical sample grown under the same conditions and with the same period (8.5 μm) and facet size (~ 5 μm), exhibits a defective region with TDs covering ~ 68 % of the width of stripe, while the treated sample exhibits a less dense defective region covering ~ 33 % of the stripe's width.

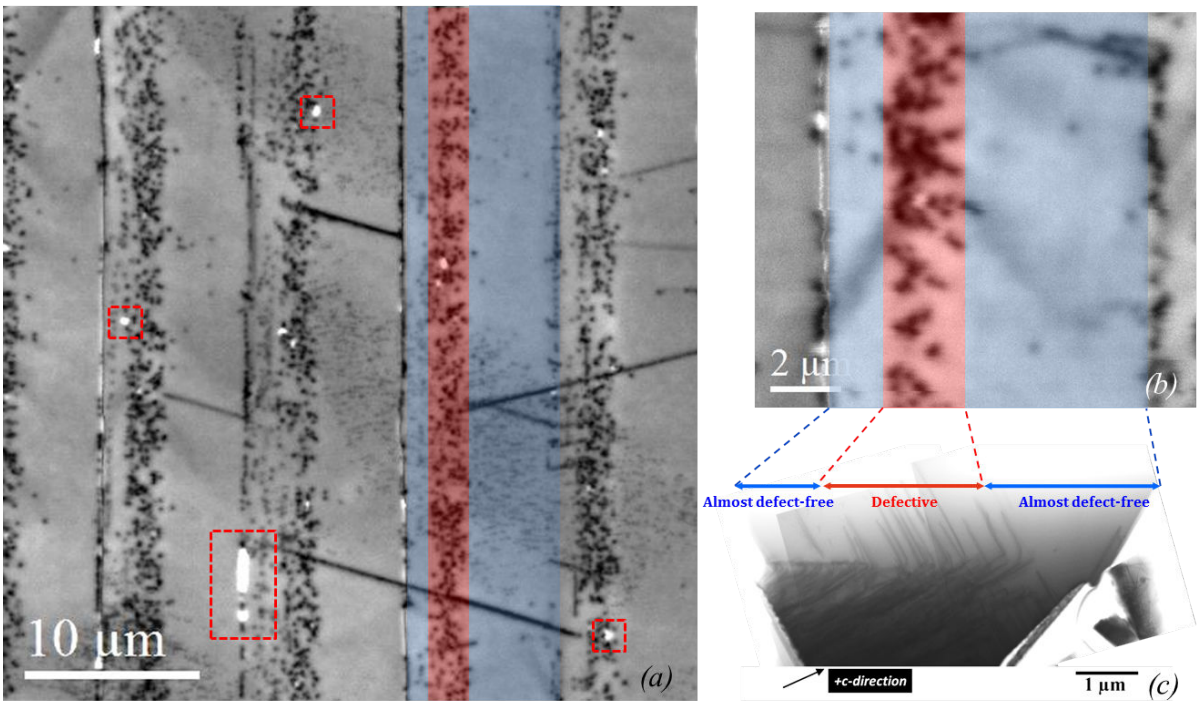

Figure 3.31 – (a) Plane-view panchromatic CL image of the treated sample's surface etched with SF_6 for 10 minutes and (b) a plane-view panchromatic CL image of a single stripe and (c) its corresponding cross sectional TEM image showing the alternation between defective and almost defect free zones. Dashed red squares indicate BSFs.

Quantitatively, by counting the black spots corresponding to TDs on panchromatic CL images, a total density of $2.7 \times 10^8\ cm^{-2}$ has been found. The total examined surface area was $\approx 300\ \mu m^2$ and 20%

of the total counted TDs has been added to the final sum in order to compensate for the uncounted TDs resulting from black spot overlapping. For comparison, Takami *et al.* [127] reported on a TD density of 1.2×10^8 cm^{-2} measured by CL of (10$\bar{1}$1) GaN grown on patterned sapphire substrates.

In what concerns BSFs, they have been seen to form in the -*c*-wing and then cluster along the length of the coalesced bands when the classical growth was adopted (see section 3.2.2.2). However, in the acquired panchromatic CL images of the treated samples, some BSFs were observed in the -*c*-wings, which does not correlate well with the cross sectional TEM/STEM study showing that BSFs do not exist in this area. It can therefore be suggested that these BSFs are created upon coalescence of adjacent cystals. Other BSFs, smaller in length and width, were also detected on the surface where normally only TDs are clustered. The exact origin of these BSFs is not well understood. The density of BSFs has shown to increase by a factor three, from 370 cm^{-1} before coalescence to 1.2×10^3 cm^{-1} after coalescence. Therefore, it can be assumed that BSFs are created when the coalescence of neighboring crystals occurs. BSFs are indicated by the red dashed square in figure 3.31 (a) and have been found to have an average width of 330 nm.

3.3.2.4 Distribution of defects and impurities

To further investigate the influence of the blocking layer on the grown GaN crystals before and after its formation, cross sectional CL experiments assessing the luminescence originating from defects and impurities are described below. Figure 3.32 shows a cross sectional SEM image of three coalesced bands and their corresponding CL mapping and spectra acquired at room temperature of the regions above and below the blocking layer (marked with a dashed red line for clarity).

Below the blocking layer (*i.e.* in the area close to the substrate), luminescence is dominated by a yellow-band emission at 2.175 eV (570 nm) having a FWHM of about 124 meV. Given that the grown GaN crystals are nominally undoped, this YL band is possibly related to a high concentration of impurities and/or point native defects introduced during the growth. Above the blocking layer (*i.e.* in the area close to the surface), the NBE emission is dominant and observed at 3.425 eV (362 nm)[14]. Remarkably, the YL band emission decreases above the blocking layer to an intensity lower than NBE by a factor 90. However, similar results have been observed when the single-step classical growth is performed (not shown). This suggests that the presence of the two zones having different optical properties is not related to the formed blocking layer.

A study performed by Cruz *et al.* [137] investigates carbon incorporation on different crystallographic planes. The study (Figure 3.33 (a)) shows that carbon incorporation on the (0001) plane is three orders of magnitude higher than on the (10$\bar{1}$1) plane, under growth conditions similar to the ones used in

[14] Recall that measurements here are acquired at RT to avoid confusion with transitions related to I_1-type BSFs acquired at low temperature.

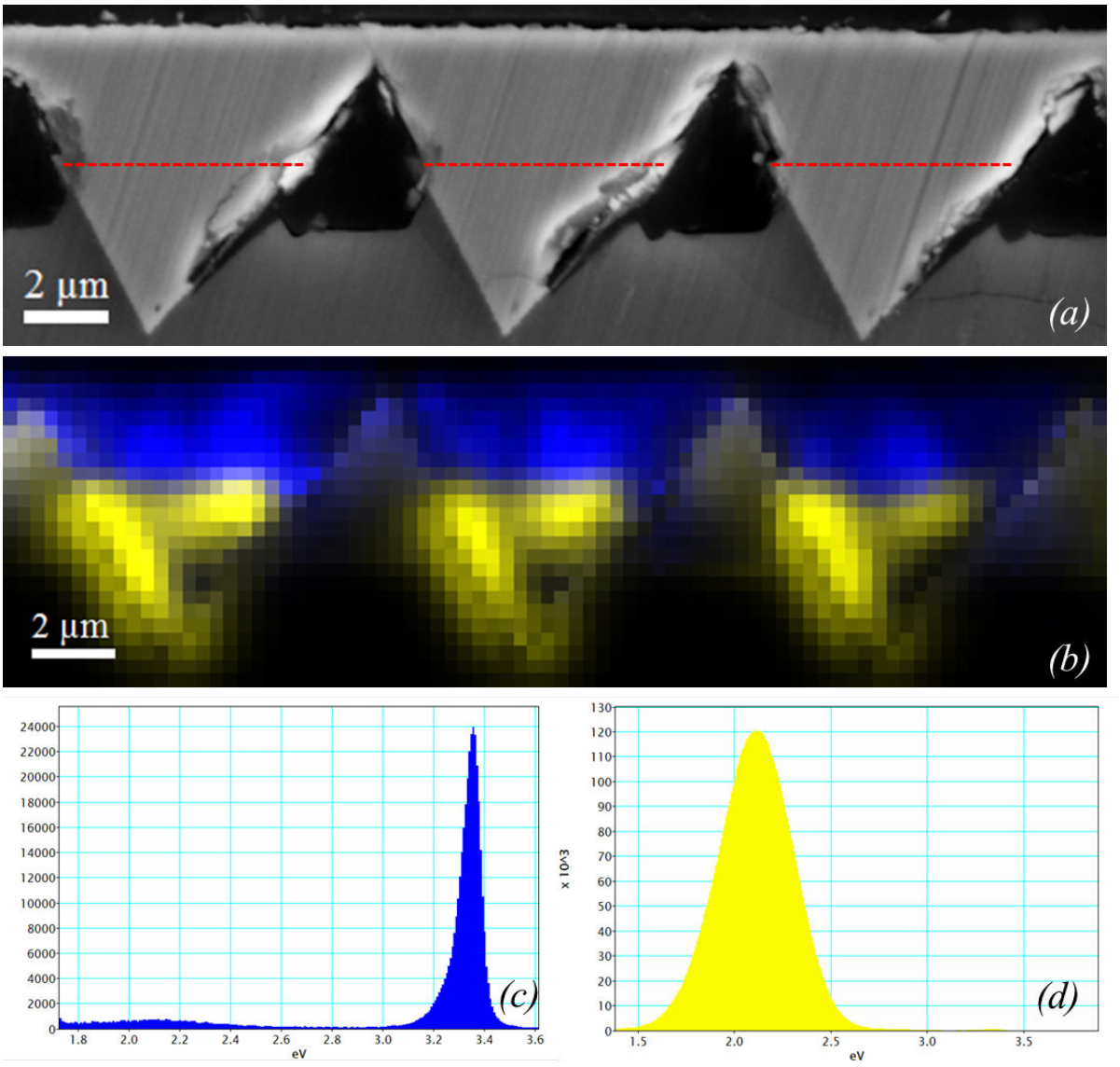

Figure 3.32 – (a) Cross sectional SEM image and its (b) corresponding CL mapping acquired at room temperature showing the two zones separated by the line. The upper blue zone corresponds to the NBE at 3.425 eV (362 nm) and the yellow zone indicates the yellow band emission at 2.175 eV (570 nm). RT CL spectra of (c) the zone above the blocking layer and (d) below the blocking layer.

our growths (1 slm of ammonia flow in our case). Figure 3.33 (b) shows a cross-sectional SEM image of the analyzed sample with dashed lines indicating the classical behavior of the progressive formation of a pyramid. Before a complete pyramid is formed, the crystal initially exhibits a large (0001) inclined facet that gradually decreases as the growth advances. The (0001) facet then disappears when a complete pyramid is created. Therefore, if the YL band is assumed to be a result of the excessive carbon incorporation and the plot in figure 3.33 (a) is taken into account, one can suggest that the presence of the two observed zones is related to the morphology evolution during the growth process. This means that carbon incorporates efficiently through the (0001) facet during the progressive

formation of a pyramid. The (0001) facet then ceases to exist when the pyramid is complete hence ending the excessive carbon incorporation and defining the lower zone dominated by YL shown in yellow in figures 3.32 (b) and (d). The upper zone (indicated in blue in figure 3.32 (b)) is then grown, while the gas flux is only exposed to the topmost (10$\bar{1}$1) facet, which has shown to have carbon concentration incorporation below detection limits resulting in luminescence dominated by NBE emission (figure 3.32 (c)). A similar cross-sectional CL study was also performed on a classical single-step grown sample, and the same two zones have been identified.

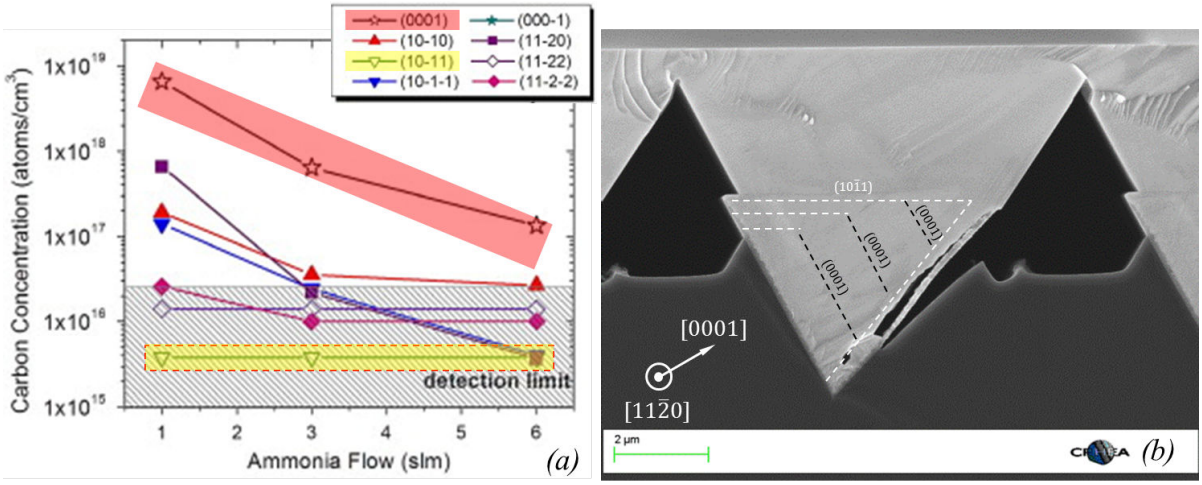

Figure 3.33 – (a) A plot showing the carbon concentration as a function of the ammonia flow for different crystallographic orientations ((0001) is highlighted in red and (10$\bar{1}$1) is highlighted in yellow) (Image source: [137]) and (b) cross sectional SEM image of the pyramid with marks showing the classical progressive formation of a complete pyramid.

Consistent with the results shown at RT, the upper zone exclusively exhibits an intense NBE emission at 3.446 eV, as shown in the mapping shown in figure 3.34 (b) and the spectrum in figure 3.35 (a). In the lower zone, two transitions that cannot be resolved at RT have been observed: one at 3.267 eV and another at 3.182 eV, and have been integrated together and plotted in the map shown in figure 3.34 (c) (figure 3.35 (b)).

If we assume that the GaN closer to the substrate is likely to be highly doped with silicon, the 3.267 eV transition can be associated to D^0A^0 originating from silicon-silicon pairs, due to Si amphoteric nature in GaN [153]. The 3.182 eV transition is often observed in samples with elevated densities of BSFs. However, BSFs are non-existent in the volume of the crystals (seen by TEM and STEM), but only appear in these samples at the coalescence boundaries. Thus, the origin of this transition is not yet understood.

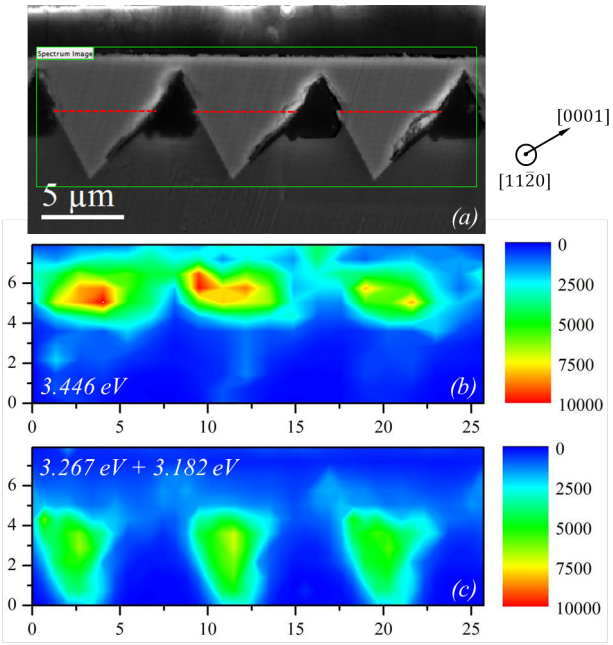

Figure 3.34 – (a) Cross sectional SEM image, with the red line indicating the position of the blocking layer and its corresponding CL mappings acquired at 77 K showing the energy resolved cartographies (b) at 3.446 eV and (c) 3.267 eV + 3.182 eV.

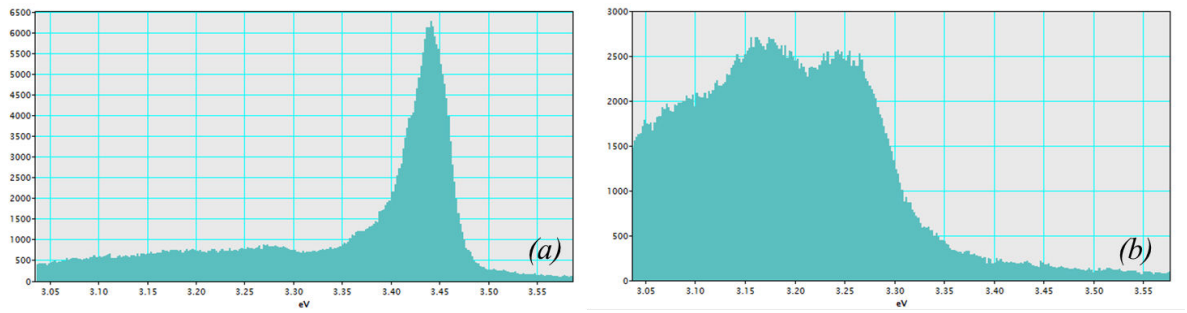

Figure 3.35 – CL spectra acquired at 77 K (a) in the upper zone with a peak at 3.446 eV corresponding to the D^0X transition and (b) in the lower zone with two transitions at 3.267 eV and 3.182 eV.

3.3.2.5 Overall layer quality assessment

In order to put things into perspective in terms of how these layers differ from the classical growth described in the first part of this chapter, the overall quality of the surface-treated samples has been investigated optically and structurally and compared to the classical growth samples.

Photoluminescence: Figure 3.36 displays PL spectra acquired at 10 K for a coalesced classical grown sample (in black) in comparison with a coalesced surface-treated sample (in red), both grown under identical growth conditions and have a thickness of almost ~ 1 μm.

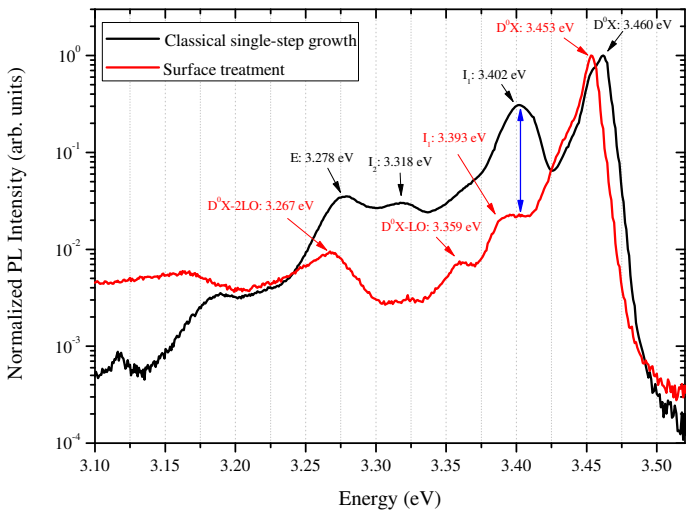

Figure 3.36 – PL spectra acquired at 10 K for a colaesced treated sample (in red) and a coalesced classical sample (in black). Both samples were grown under identical growth conditions and have the same thickness. The blue arrow shows the difference in the I_1-type BSFs between the two samples. In terms of overall intensity, both samples exhibited very similar features.

For the surface-treated sample, a D^0X transition at 3.453 eV indicates that the layer is under tensile strain. The linewidth of ~ 10 meV of the NBE transition is due to either stress gradients, or an n-doping which is often observed in GaN layers grown on silicon [154]. A transition at 3.393 eV is associated to I_1-type BSFs. The luminescence intensity of the I_1-type BSFs is ~ 100 times less intense than that of D^0X. Remarkably also, the I_1-type BSF intensity for the surface-treated sample is lower by a factor 20 in comparison with the I_1-type BSF intensity of the classical sample. This indicates a BSF reduction from the classical growth, and correlates well with the CL results that also showed a reduction in the BSF density on the surface [15].

Furthermore, surface-treated samples were compared to ones reported on sapphire of the same semipolar orientation. The PL intensity of samples grown on sapphire show a NBE:BSF ratio of 1:1 [72] indicating a comparable quality with our classical samples. Therefore, the surface-treated samples with SF_6 exhibit a superior quality than layers grown using the classical single-step method, on patterned silicon and sapphire alike.

[15] Indeed, no quantitative values precisely indicating the density of BSFs in the classical samples have been given. This is because of their high density along the -*c*-wings, which makes it impossible to individually resolve them.

X-ray diffraction: Symmetrical (10$\bar{1}$1) GaN X-ray rocking curves were used to assess the quality of the layers. Figure 3.37 plots the rocking curves' FWHM as a function of the azimuthal angle of the incident beam for a surface-treated sample (in red) and a the classical sample (in black), both grown under identical growth conditions and having a thickness of ~ 1 μm.

The FWHMs amount to a minima of 351 arcsec and maxima of 572 arcsec (average = 477 arcsec) for the surface-treated sample and 717 arcsec and 909 arcsec (average = 817 arcsec) for classical sample. Hence an improvement on the symmetrical scans by a factor 1.7 is obtained when the surface treatment method is applied. This may be associated to the reduction of TDs and BSFs in comparison with the classical single step growth. To compare with the published state-of-the-art results, GaN grown on sapphire of the same semipolar orientation in the azimuths parallel and perpendicular to the *c*-direction have been reported and amounted to 875 and 313 arcsec, respectively (average = 594 arcsec) [127].

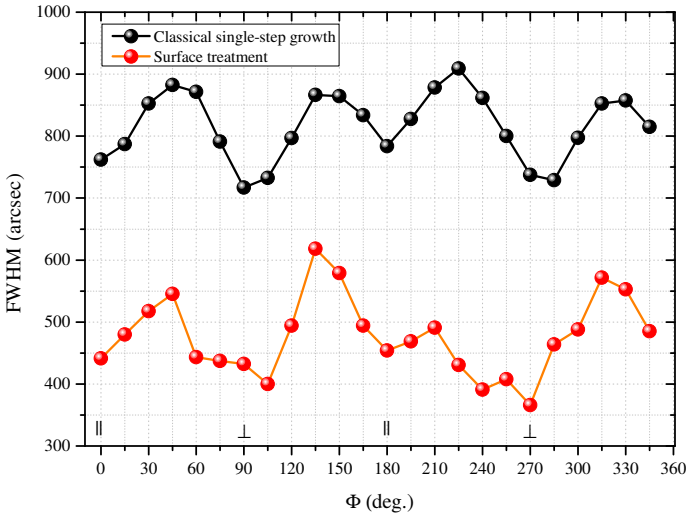

Figure 3.37 – X-ray rocking curve FWHMs on the symmetric (10$\bar{1}$1) GaN reflections by varying the azimuthal angle of the incident beam for a surface treated sample (in red) in comparison with a classical sample (in black). For $\Phi = 0° - 180°$ *the incident beam is parallel to the stripes and for* $\Phi = 90° - 270°$ *the incident beam is perpendicular to the stripes.*

3.3.2.6 What is the nature of this layer?

After introducing the surface-treatment process and discussing the results showing the positive effect of the formed blocking layer on the structural and optical quality of the subsequent GaN, the following section will describe the attempts to understand its nature and origin.

Figure 3.38 shows a HRSTEM-HAADF image acquired in the [11$\bar{2}$0] zone axis and its corresponding line profile measured perpendicular to the blocking layer. The layer is composed of 16 atomic planes that amount to a thickness of ≈ 4 nm.

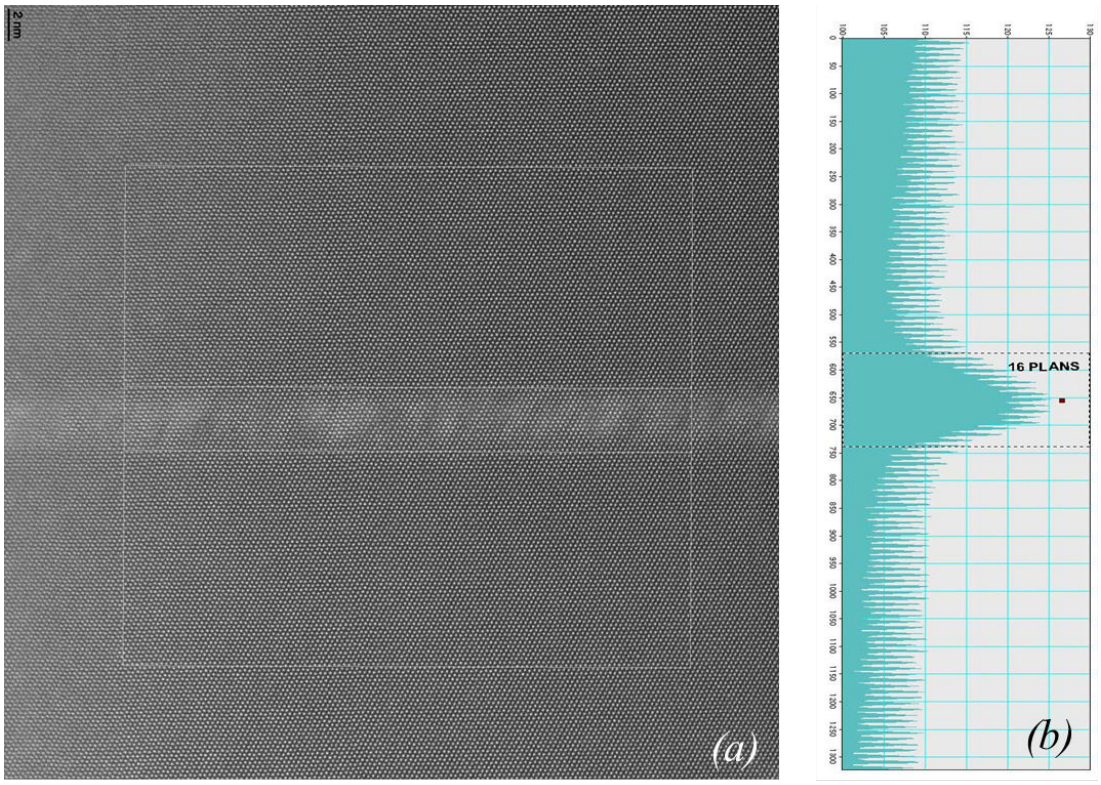

Figure 3.38 – (a) HRSTEM HAADF image acquired in the [11$\bar{2}$0] zone axis in the area where the blocking layer is positioned and (b) the corresponding line profile perpendicular to the blocking layer indicating a thickness of 16 atomic planes.

Figure 3.38 (a) shows a HR-HAADF image where the blocking layer is located. The blocking layer displays a brighter contrast, which corresponds to a higher atomic number compared to the GaN, above and below the blocking layer. In order to verify the chemical composition of the layer, EDX was performed within a TEM. Figure 3.39 (b) shows an STEM-EDX mapping of the area inside the red square (see figure 3.39 (a)) close to the kink and a line profile perpendicular to the blocking layer. No significant presence of any unexpected element was observed. However, 5% of silicon has been detected in the blocking layer.

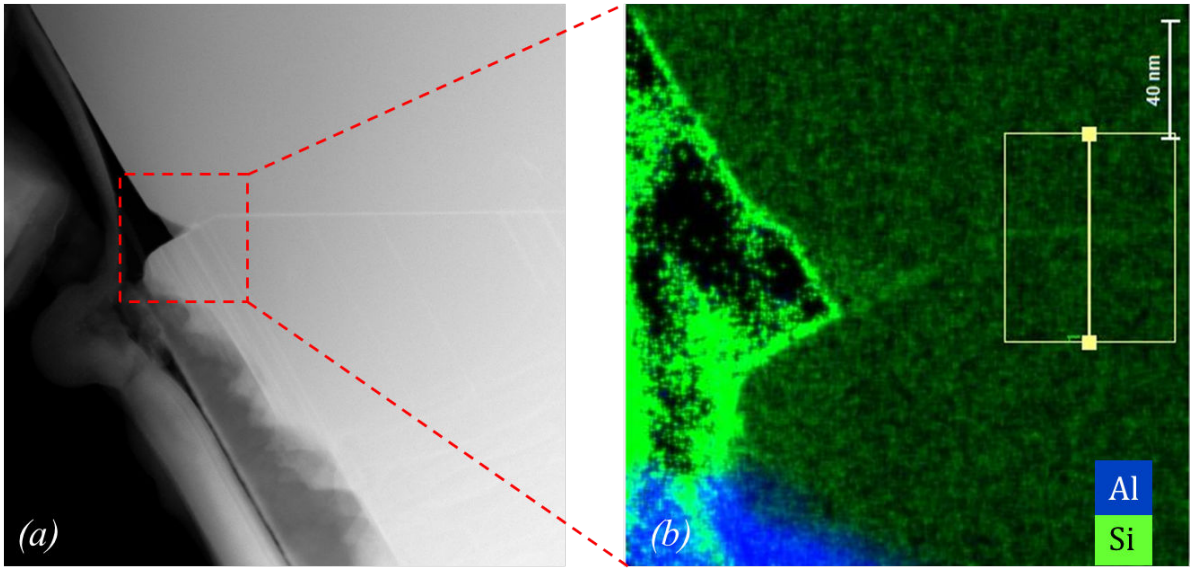

Figure 3.39 – (a) HAADF image in the area where the blocking layer is located and (b) the corresponding STEM-EDX image and line scan indicating the detection of 5% silicon. (Images credit: Vincent Delaye - CEA LETI (Grenoble, France))

Moreover, and since the GaN growth was performed right after the RIE SF_6 etching, the possibility of having SF_6 residues that contribute to the formation of the blocking layer was also investigated by X-ray photoelectron spectroscopy (XPS). The SF_6 etching recipe applied to the samples before the GaN growth was also applied on a bare Si(111) substrate. The etched Si(111) substrate was then analyzed by XPS that showed that no residual elements remain on the surface, namely sulfur and fluoride. A similar XPS study investigating silicon surfaces after SF_6 etching also reported that no sulfur remains on the surface after the etching [155]. Additionally, Electron energy loss spectroscopy (EELS) was also performed to analyze the atomic composition of the blocking layer, but no particular elements were found. Furthermore, in order to understand if the blocking layer has an effect on the strain state of the GaN grown above the layer, geometric phase analysis (GPA) [156] on the HR-STEM images was performed. Analysis along the (0002) and (10$\bar{1}$1) planes were done, and no detectable difference in the strain state above and below the blocking layer was observed.

3.3.2.7 Hypothesis

The characterization results described above are not conclusive enough. Besides the chemical composition, the formation mechanism of this layer must also be understood, and whether or not it influences the GaN growth mode after its formation is also necessary to be comprehended. Indeed, investigations are ongoing to understand the phenomenon. Still, a number of hypotheses can be advanced.

First, based on the discussed TEM and STEM images (see section 3.3.2.3) that show the bending of TDs upon intersection of the growing pyramid, we can assume that the growth starts in a similar manner as the classical growth: the progressive pyramidal formation with a topmost (10$\bar{1}$1) semipolar surface and a (0001) inclined surface that gradually decreases as the growth of the pyramid advances, as illustrated in figure 3.40 (a). It is worthwhile reminding the reader here that the GaN growth was done in a single growth run *without* any changes in growth parameters.

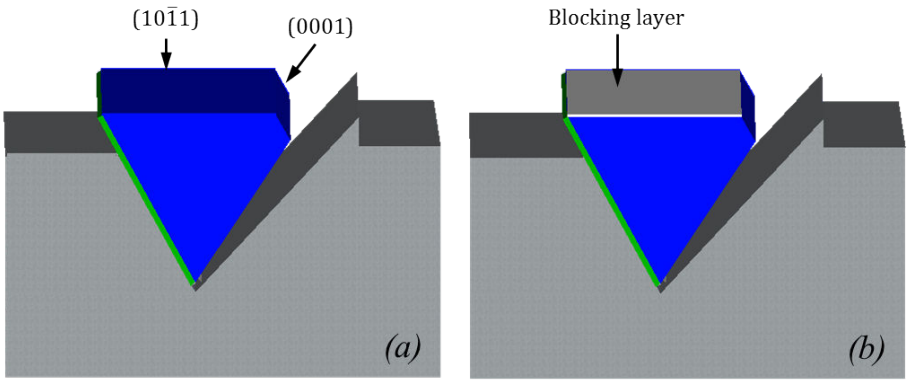

Figure 3.40 – Schematic illustration of the proposed hypothesis: (a) shows the growth of the pyramid with a topmost (10$\bar{1}$1) semipolar surface and an inclined c-facet and (b) shows the moment when the blocking layer is formed on the semipolar surface while the c-facet remains exposed.

Then, given that the location of the blocking layer is systematically observed right after the apex of the AlN layer, it may be suggested that its formation is a result of silicon migration from the etched substrate towards the GaN semipolar surface, as marked on the SEM image in figure 3.41. This migration results in forming a layer that is essentially constituted from silicon, gallium and nitrogen. Further, we suppose that the blocking layer is formed before a complete pyramid is created, and that it selectively only covers the topmost (10$\bar{1}$1) semipolar surface while the small inclined (0001) surface remains exposed, as depicted in figure 3.40 (b). Moreover, and based on the fact that the blocking layer is formed in one plane and exhibits a straight line from the cross section perspective, it is necessary to consider that its deposition occurs quasi-instantaneously and not continuously throughout the whole process of the progressive pyramidal formation. Otherwise, one would expect to see a step-like layer following the contour of the forming pyramid.

Assuming that the above hypothesis is true, one can thus suppose that the growth mode changes from its classical behavior after the formation of the blocking layer. Therefore, as figure 3.42 illustrates, we assume that the GaN nucleation restarts on the exposed inclined *c*-facet. The growth then proceeds laterally in the direction indicated by the yellow arrow until the surface is completely covered. During the lateral growth, TDs gradually bend into the plane containing the blocking layer. Also, BSFs are not created because the lateral growth does not proceed strictly along the [000$\bar{1}$] direction.

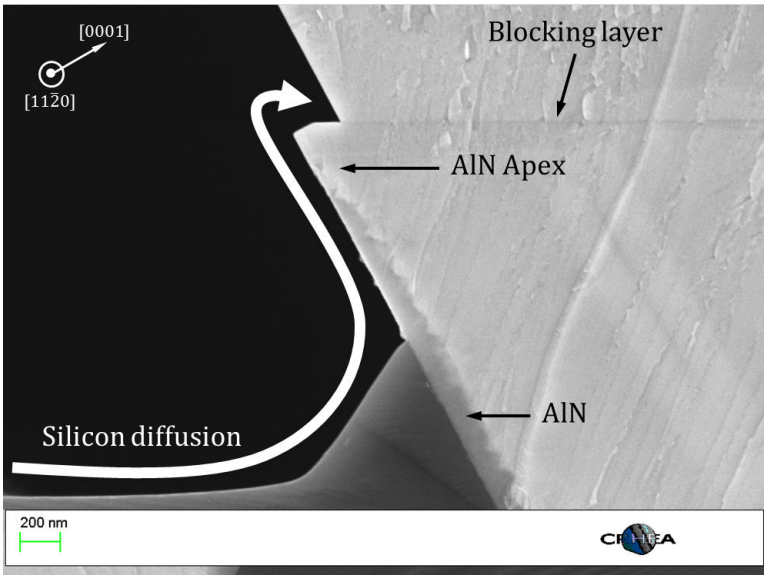

Figure 3.41 – Cross sectional SEM image of the edge of the pyramid showing the blocking layer. The silicon migration "route" from the substrate's surface to the GaN that may be the reason to form the layer is indicated by the curved white arrow.

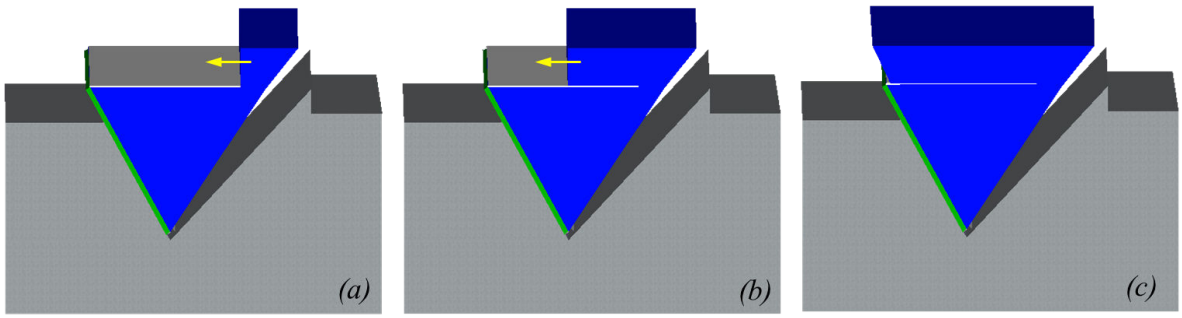

Figure 3.42 – Schematic illustration of the GaN growth after the formation of the blocking layer as per the formulated hypothesis: (a) shows the initial stages of the growth starting from the c-facet and (b) and (c) show how the crystal grows laterally above the blocking layer until a complete pyramid is created. The yellow arrows indicate the growth direction.

3.3.3 Si_xN_y interlayers

In order to investigate the proposed hypothesis, it was assumed that the blocking layer is formed by Si_xN_y. Therefore, to demonstrate the illustration presented in figures 3.40 and 3.42, an Si_xN_y interlayer was inserted close to the position where the blocking layer was systematically observed.

3.3.3.1 Selective growth

After growing 150 nm of an AlN buffer layer, GaN growth was carried out at a temperature of 1210°C, a pressure of 300 mbar and a V/III ratio of 650 for a duration of 3000 seconds. These parameters

permit controlling the growth before the formation of a complete pyramidal crystal is accomplished, thus maintaining a small (0001) inclined surface, as in figure 3.40 (a). Then, SiN was deposited on the structure using 10 slm of NH_3 and 100 sccm of SiH_4 for a duration of 70 seconds without changing the temperature and pressure. Afterwards, GaN growth was re-started for 600 seconds using the same growth conditions.

After the deposition of the SiN layer on the incomplete pyramidal band, GaN crystals selectively nucleate on the inclined (0001) surface in the form of isolated islands, while no nucleation takes place on the topmost (10$\bar{1}$1) surface, as shown in figure 3.43. This either suggests an enhanced selective deposition of SiN on the (10$\bar{1}$1) surface compared to the (0001) one, or the coverage of both surfaces by SiN where the formation of nuclei occurs at the intersection of the two facets where more free bonds are available. For simplicity, we will consider the former suggestion. The crystals growing from the (0001) surface (as indicated by the yellow arrow in figure 3.43 (b)) then extend laterally (*i.e.* perpendicular to the stripe as indicated by the blue arrow in figure 3.43 (b)), covering the topmost semipolar surface where the SiN is deposited. It may be interesting here to highlight that the lateral growth of the GaN crystals on the SiN masked stripe does not occur in the -*c*-direction, and therefore does not create any BSFs.

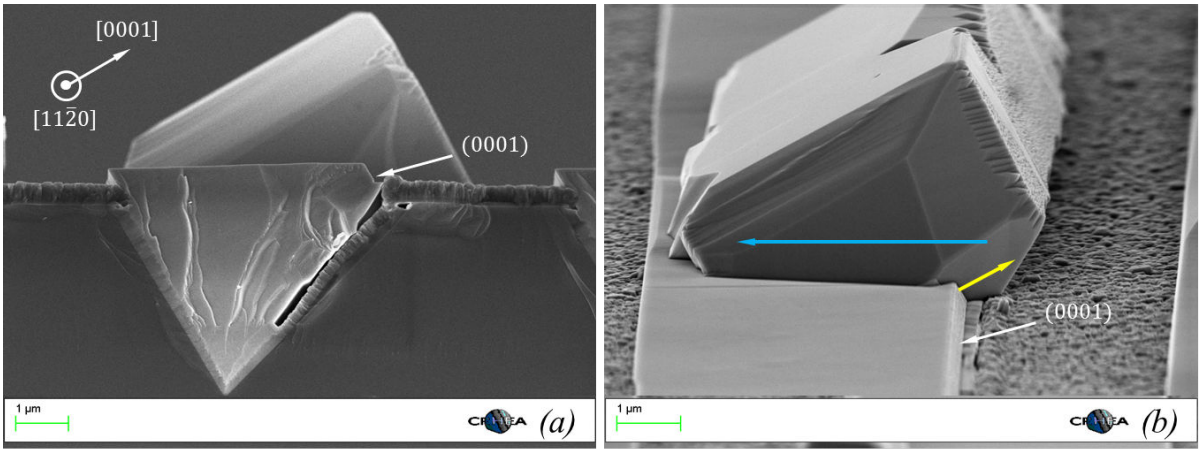

Figure 3.43 – (a) cross-sectional and (b) bird's-eye view SEM images of the crystals nucleating on the inclined c-facet after the SiN deposition. In (b) the yellow arrow indicates where the initial nucleation occurs and the blue arrow indicates the direction of the lateral growth.

3.3.3.2 Characterization by STEM and CL

To understand the consequence of the observed lateral growth, the micro-structure was investigated by STEM[16]. Figure 3.44 shows cross-sectional bright-field STEM images acquired in the [11$\bar{2}$0] zone axis at different magnifications of a crystal grown on the pyramid, and covering the whole width of the semipolar band. Indeed, TDs are almost completely blocked in the plane where the SiN layer is

[16]The sample was prepared using the focused ion beam (FIB) technique [157].

present. This suggests that TDs bend as the lateral growth advances and propagate in the topmost (10$\bar{1}$1) plane instead of threading towards the surface. Moreover, no BSFs in the overgrowing crystal have been found. The panchromatic CL image in figure 3.45 (b) confirms the STEM investigations, and shows that the overlapping crystal is almost free of any defects.

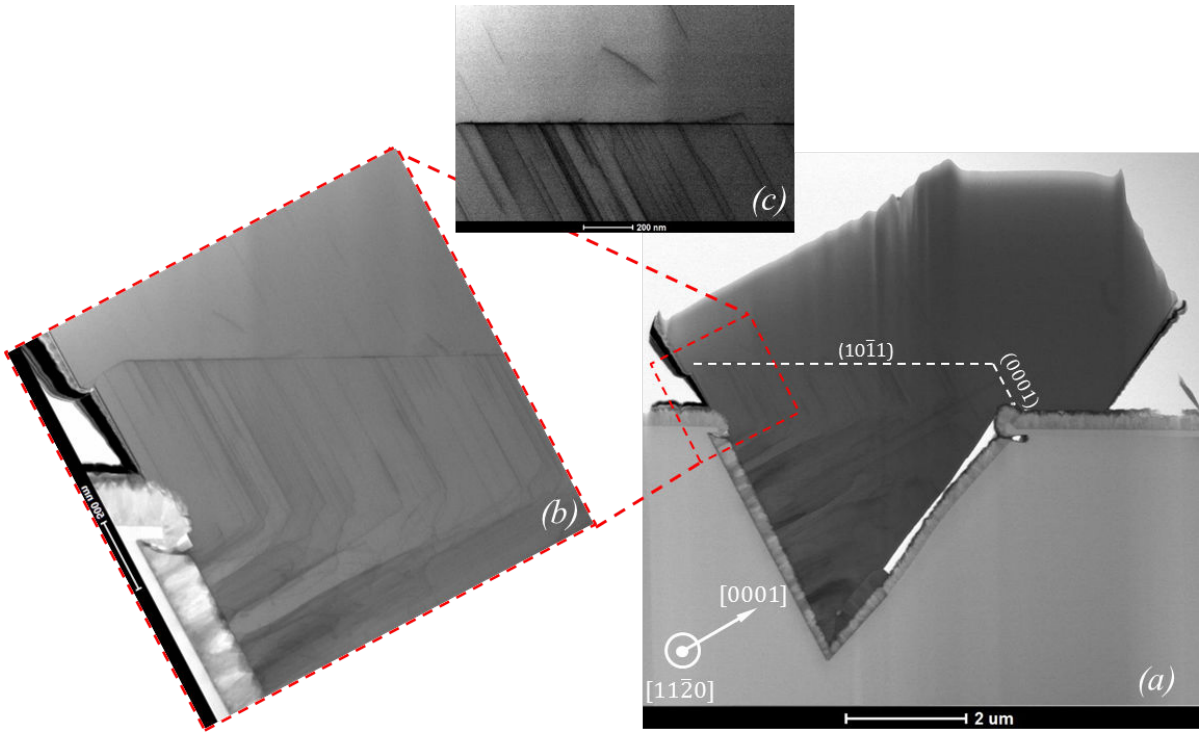

Figure 3.44 – Cross-sectional STEM images acquired in the [11$\bar{2}$0] zone axis at different magnifications clearly showing the TD blocking by the SiN layer (Images credit: Nicolas Mante - CEA LETI (Grenoble, France)).

Furthermore, figure 3.46 (a) shows a cross-sectional HAADF image acquired in the [11$\bar{2}$0] zone axis of the region where the SiN layer is deposited. The corresponding EDX maps of silicon and gallium are shown in figures 3.46 (b) and (c), respectively. As expected, the layer is dominated by the presence of silicon, which may be comparable to the EDX maps acquired on the blocking layer (for the SF_6 etched samples), as shown in figure 3.39. These results may therefore confirm the proposed hypothesis suggesting that silicon migration on the semipolar (10$\bar{1}$1) surface is behind the formation of the blocking layer.

Until now, the deposition of the SiN layer only produces isolated islands when the regrowth of GaN takes place, and not a continuous layer as the one demonstrated when the SF_6 surface treatment is applied. For this, further development should be carried out essentially to optimize the deposition duration of the SiN layer and to determine the optimum deposition stage, where its defect-reduction effect will be most effective.

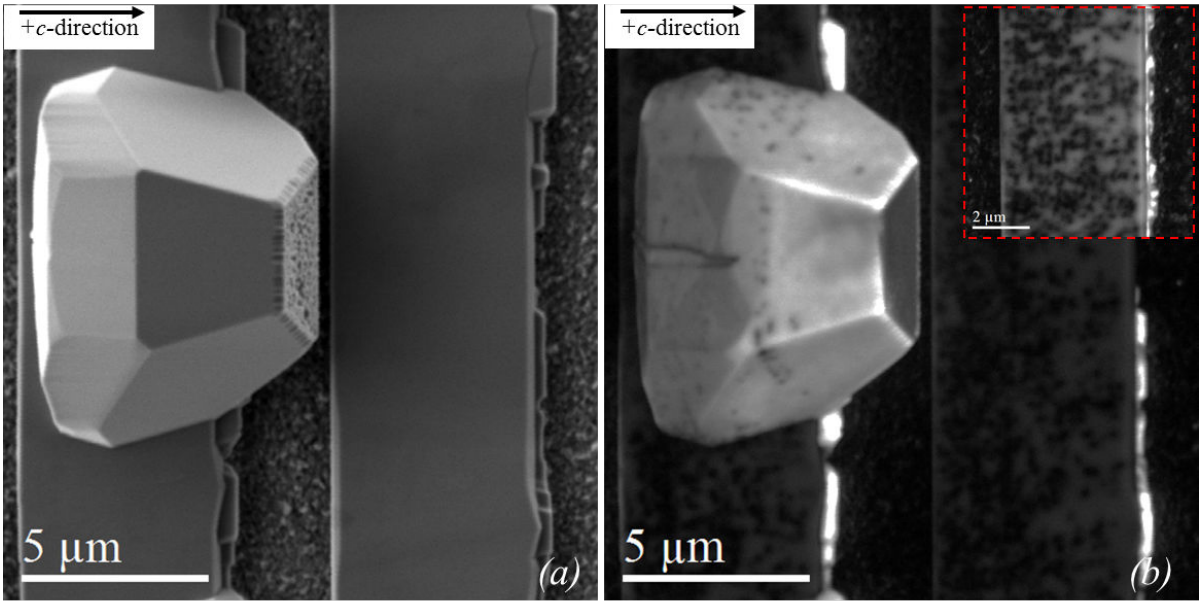

Figure 3.45 – (a) Plane-view SEM image of two bands, one of which is partially overlapped by the lateral growth and the (b) corresponding plane-view panchromatic CL image acquired at room temperature showing that the overlapping crystal is almost free of TDs. The inset better shows the elevated density of TDs on the band where no lateral overlapping occurs.

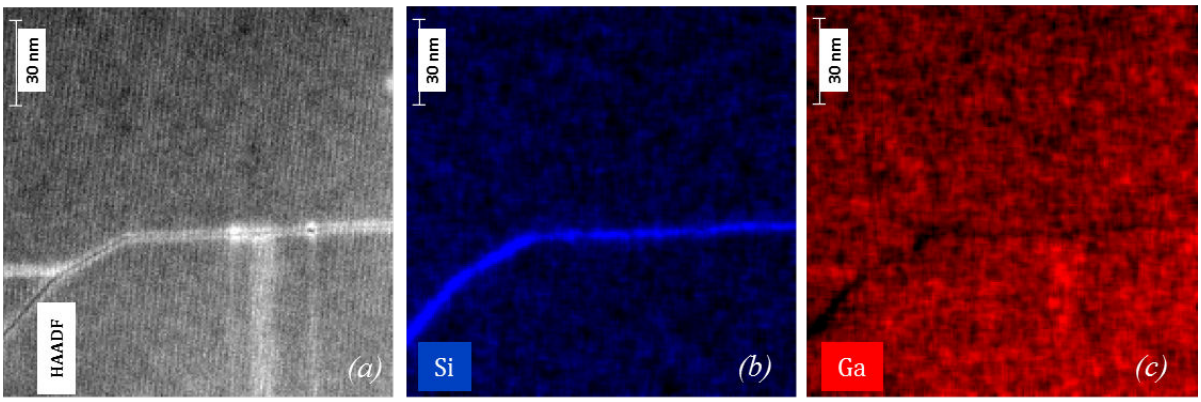

Figure 3.46 – (a) cross-sectional HAADF image acquired in the [11$\bar{2}$0] zone axis in the region where the SiN layer is deposited and the corresponding EDX mapping for (b) silicon and (c) gallium.

3.4 Conclusions

In the first part of this chapter, the fabrication process of the substrates was described. Then, the inclined growth of AlN and GaN on the processed substrates was investigated. A wide range of growth parameters was studied in order to understand the effect of growth conditions on the morphology of the grown GaN crystals. The results indicated that efficient in-situ defect blocking techniques that work well for the (11$\bar{2}$2) orientation, cannot be applied in our case for (10$\bar{1}$1). The single-step grown (10$\bar{1}$1) oriented GaN layers were characterized structurally and optically. Results have shown that the classical adapted growth has matched the state-of-the-art of film qualities reported in literature on the (10$\bar{1}$1) orientation, but indeed are not yet sufficient for optoelectronic device fabrication.

The second part of the chapter was aimed at developing a defect blocking method via interlayer insertion. We have introduced a surface treatment technique that blocks structural defects. Structural and optical characterization results indicate a considerable improvement from what has been presented in the classical single-step growth and undoubtedly surpassed the state-of-the-art reported on the (10$\bar{1}$1) orientation. Although full understanding of the defect blocking mechanism is not yet completed, and while further improvements must be achieved, the introduced method may be a cornerstone towards a fully in-situ process that enables blocking structural defects from reaching the surface.

4 GaN (20$\bar{2}$1) on Silicon (114)1°off

Since the first realizations of high quality LDs on homoepitaxially grown (20$\bar{2}$1) [56, 57, 58, 158], this orientation has drawn considerable attention as it has demonstrated highly reduced polarization effects, increased ability of indium uptake and elevated compositonal homogeneity [159]. These observations suggest that this crystallographic orientation might be more favorable than the conventional *c*-plane for the fabrication of long wavelength optoelectronic devices. Besides freestanding GaN, this orientation has been also demonstrated on (22$\bar{4}$3) patterned sapphire substrates [74, 147, 160], but not yet on silicon.

This chapter will be dedicated to discuss the findings on the (20$\bar{2}$1) semipolar GaN orientation grown on patterned silicon. The substrate fabrication, GaN growth and the subsequent optical and structural characterization will be discussed. However, since there are many features shared with the (10$\bar{1}$1) orientation, characterization descriptions will be brief and concise in order to avoid repetition.

4.1 Substrate selection

In order to obtain the (20$\bar{2}$1) GaN orientation on silicon, it is required to use a Si (114) substrate with an off-axis tilt of 1° around [$\bar{1}$10] towards [2$\bar{2}$1]. This allows to accommodate the difference between the (114) and ($\bar{1}$ $\bar{1}$1) Si (*i.e.* nucleation facet), that is 74.20° and the angle between GaN (20$\bar{2}$1) and (0001) at 74.85°. While the exact theoretical difference here is 0.65°, the substrate producer delivers substrates sliced at miscut increments of 1°. Moreover, the substrate slicing from the ingot as indicated by the fabricator comes with an error margin of ±0.20°. This may introduce a certain error on the exact orientation of the grown crystal, and may equally suggest that the usage of Si (114) on-axis is also feasible. The stereographic projection of Si (114) is shown in figure 4.1, and shows the crystallographic relationship between Si (114) and the four Si {111} facets.

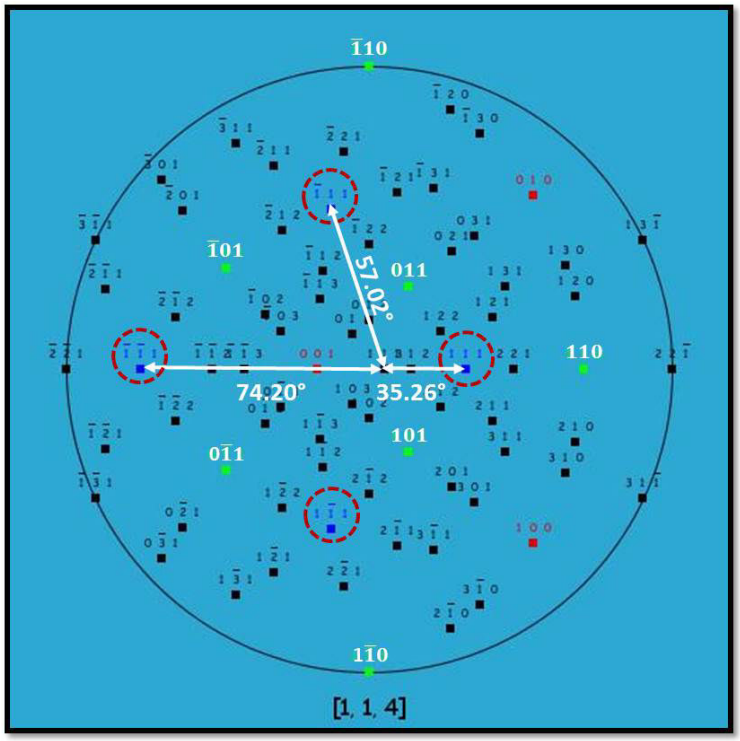

Figure 4.1 – Stereographic projection of Si (114) (Image source: [131]).

4.2 Substrate fabrication

In a similar manner as the fabrication process for the Si (001)7°off orientation, the processing steps for the Si (114)1°off substrates are listed below and are illustrated in figure 4.2:

- The first step is depositing a 100 nm thick SiO_2 film on the flat (114)1°off surface (Figure 4.2(a)). The substrate is then patterned using conventional photolithography with a striped mask having bands oriented parallel to the [1$\bar{1}$0] axis, as shown in figure 4.2(b). Two masks with different dimensions have been used. A mask having an 8.5 μm period (5 μm opening and 3.5 μm mask) and another having a 5 μm period (2.5 μm opening and 2.5 μm mask).

- The patterned substrate is then immersed in a stirred KOH solution where the mask openings are anisotropically etched. As a result, V-grooves with (111) and ($\bar{1}$ $\bar{1}$1) sidewall facets are obtained (Figure 4.2(c)).

- Then, in order to dictate the growth only on the adequate ($\bar{1}$ $\bar{1}$1) facet, inclined deposition of SiO_2 has been done using an IBS machine to mask the low inclination (111) sidewalls. Also as a result of the shadowing effect during the inclined deposition (see section 3.1), a small area on the bottom of the (111) facet remains unmasked as indicated in figure 4.2(d).

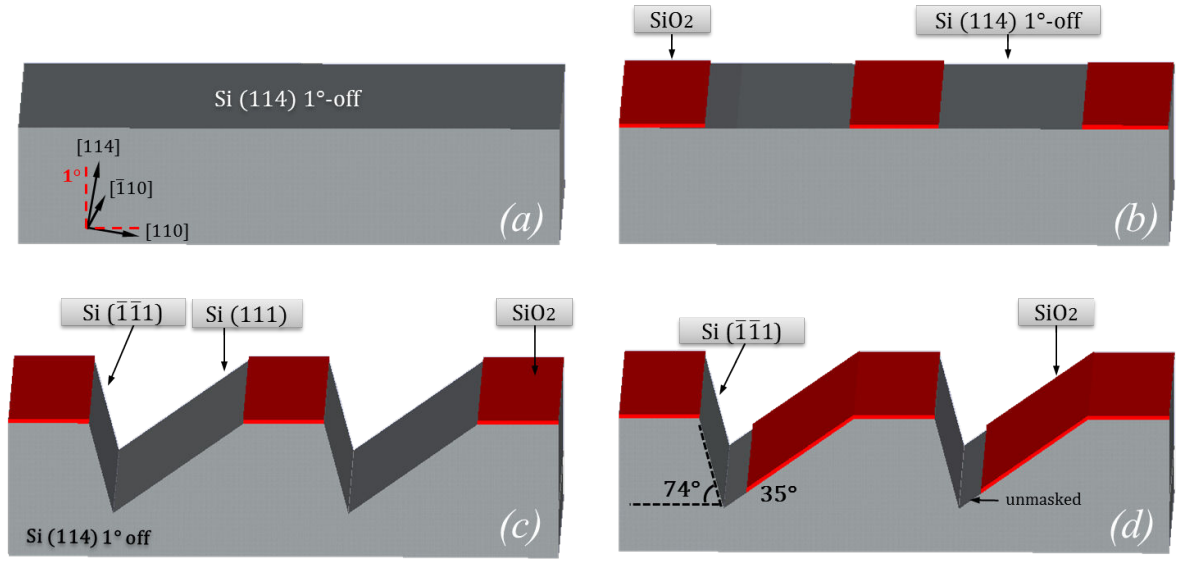

Figure 4.2 – Schematic of the processing steps for the fabrication of patterned silicon (114) 1° off substrates. Angles and directions are indicated on the figure.

4.3 Selective area epitaxy

After the substrates' patterning, the subsequent growth on the exposed facets has been studied. For reference, figure 4.3 illustrates the inclined growth of GaN on the patterned substrates indicating he necessary angles and directions. In the following section, the growth conditions used for the AlN buffer layer (not shown in figure 4.3) will be mentioned, and the subsequent growth of GaN under different growth conditions will be evaluated. Then, the coalescence modes of adjacent stripes will be shown and discussed.

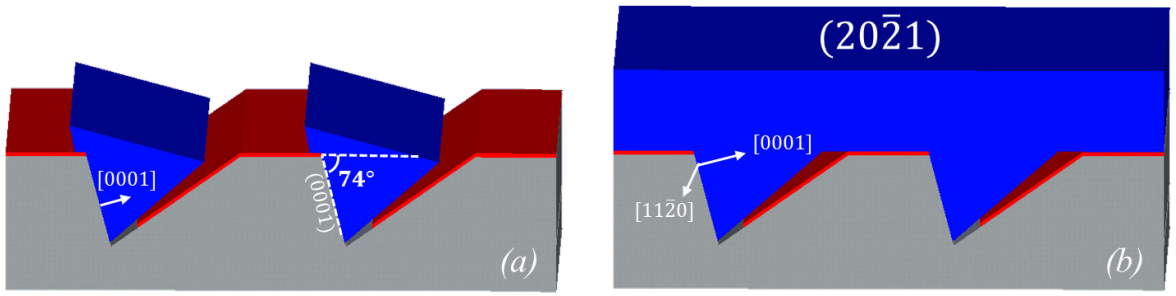

Figure 4.3 – Schematic of the inclined GaN growth (illustrated in blue) on the patterned substrates (a) before and (b) after coalescence. Angles and directions are indicated on the figure.

4.3.1 AlN buffer layer

An AlN buffer layer prior to the growth of GaN is epitaxially grown on the Si ($\bar{1}\,\bar{1}$1) facet. The thickness of the AlN layer is ≈ 150 nm grown at a temperature of 1250°C, and is set to a constant for all the growths discussed in this chapter.

4.3.2 Investigated GaN growth conditions

A wide range of growth conditions for growing GaN has been investigated in order to understand the effect on the morphology and structural quality on the crystals before proceeding to coalescence. In the following three sections, the effect of pressure, V/III ratio and temperature on the crystals will be detailed. For control purposes, each growth condition has been varied individually while keeping all other parameters constant.

4.3.2.1 GaN growth pressure

The outcomes of the pressure effect on the crystal behavior are shown in figure 4.4. All other growth parameters have been kept constant: T = 1210°C; V/III ratio = 3100; t = 2500 s. The results have shown that for any pressure, the growth mainly proceeds along the +c-direction, and a rather negligible growth occurs in the direction normal to the substrate's surface. However, the growth rate in the +c-direction is highly affected by the pressure, and decreases from 0.088 to 0.084 to 0.046 μ m/min upon the increase in pressure from 100 to 300 to 600 mbar, respectively. The growth rate is thus controlled by the reactor pressure [135].

Furthermore, at a pressure of 100 mbar, excessive polycrystalline GaN sticks on the dielectric mask where no growth is desired. The GaN surface morphology at 100 mbar, as seen by SEM, is rather rough and tends to form irregular hillocks on the topmost semipolar facet, as shown in figure 4.4(a). At 300 and 600 mbar, parasitic deposition and hillocks disappear and the surface exhibits smooth well-defined facets.

The slow growth rate at 600 mbar would require long growth runs and thus increase the probability of meltback etching. The excessive parasitic poly-crystalline deposition of GaN at 100 mbar is undesirable since it will disturb the growth of crystalline GaN. Thus, the choice of the GaN growth pressure for the initial growth stages is 300 mbar. Similar characteristics have been observed for the (10$\bar{1}$1) orientation upon pressure variation (see section 3.2.1.2 in the previous chapter).

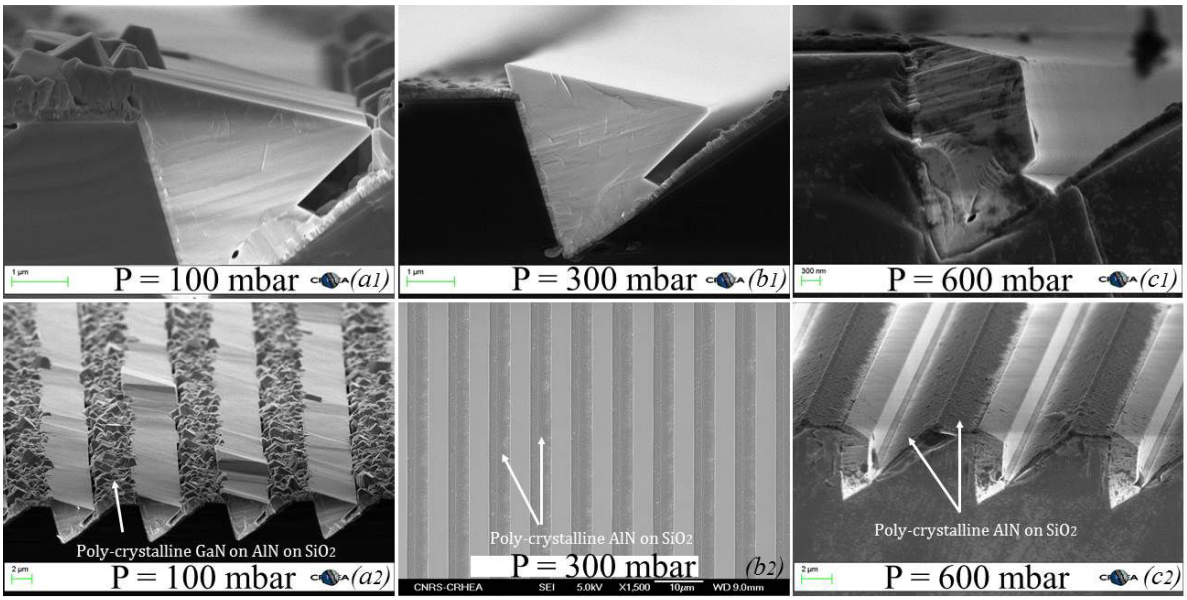

Figure 4.4 – cross sectional and bird's-eye view images showing the effect of pressure on the progress of the growth at (a) 100 mbar, (b) 300 mbar and (c) 600 mbar.

4.3.2.2 GaN V/III ratio

The V/III ratio has been investigated for the growth of GaN in the range from 220 to 4200 while keeping other parameters constant: T = 1210°C; P = 300 mbar; t = 2500 s. The results are displayed in figure 4.5.

Upon changing the V/III ratio, growth along different directions is observed. At low ratios (*i.e.* 220) the growth in the [0001] direction amounts to 0.140 μ m/min, which is faster than the growth rate at V/III ratios of 1550, or higher, by a factor 1.5. Similarly, for the growth direction normal to the surface, low V/III ratios exhibit a growth rate higher by a factor $\approx$ 2.5 in comparison to V/III in the range of 1550 or higher. Measured growth rates in the [0001], normal to the surface and [000$\bar{1}$] directions upon the variation of the V/III ratio are shown in table 4.1. The importance of growing in the direction normal to the surface in the initial growth stages lies in trying to avoid contact with the opposite (111) masked facet. This contact has shown to create additional defects as discussed in section 3.2.2.2.

Remarkably, XRD symmetrical (20$\bar{2}$1) $\omega-$scans on the azimuthal angles parallel (0° – 180°) and perpendicular (90° – 270°) to the stripes have indicated an improvement of the crystal quality upon the decrease in V/III ratio. The average FWHM for GaN grown at V/III ratio of 220 amounts to 750 arcsec and increases to 1300 arcsec for a V/III ratio of 1550 and above. The same structural behavior was observed by XRD for the (10$\bar{1}$1) orientation when crystals grown at low and high V/III ratios were compared (see section 3.2.1.2).

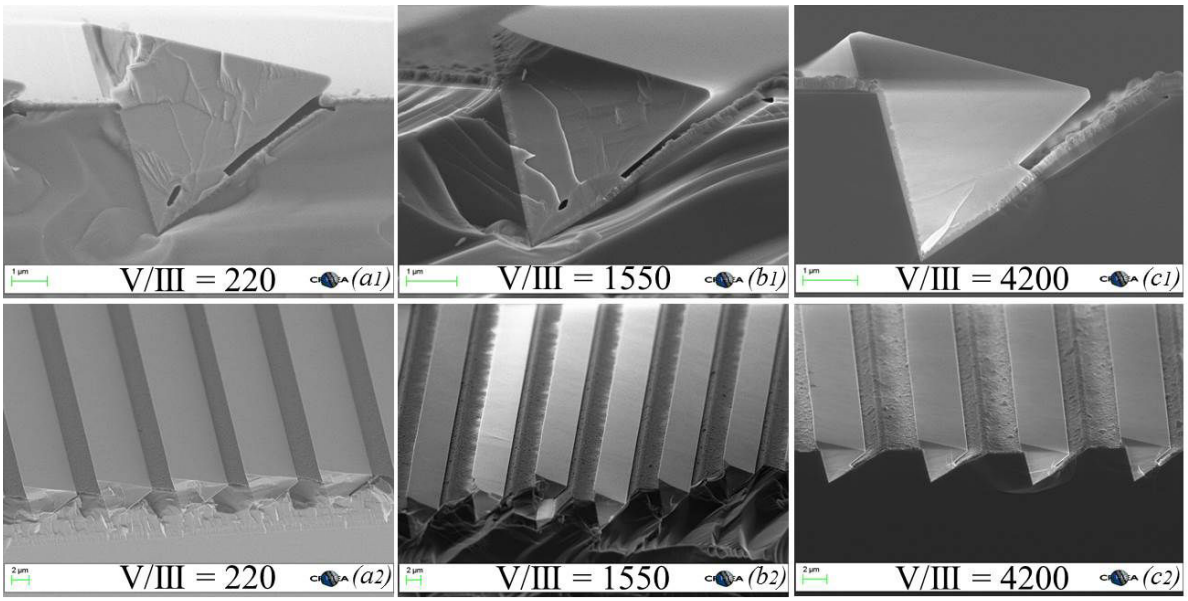

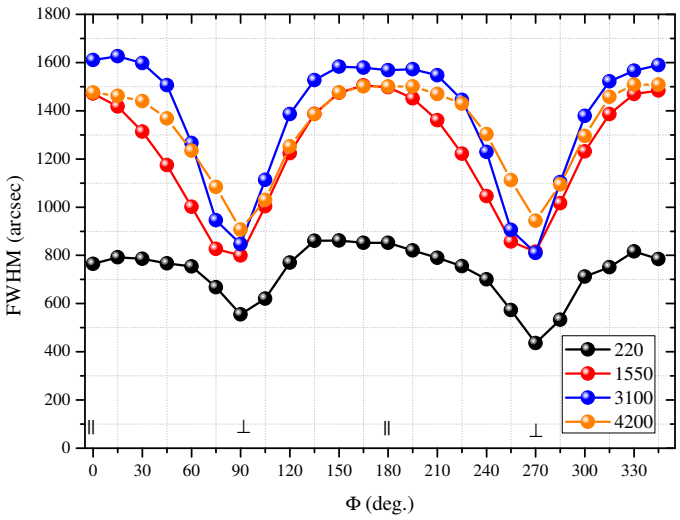

Figure 4.5 – SEM images showing the effect of the V/III ratio on the GaN crystals' morphology at (a) 220, (b) 1550 and (c) 4200. The plot shows the FWHM values of the acquired XRD symmetrical rocking curves on the azimuthal angles parallel and perpendicular to the stripes for each V/III ratio.

4.3.2.3 GaN growth temperature

In what concerns the temperature variation, similar results have been observed for the (10$\bar{1}$1) orientation. A window between 1150°C and 1270°C has been investigated. At low temperatures (*i.e.* 1150°C), irregular nucleation was dominant, and the formation of smooth facets was hindered. Higher temperatures (*i.e.* 1270°C) increased the density of meltback etching to points where no zones to char-

Growth direction	220	1550	3100	4200
[0001]	0.140	0.092	0.088	0.086
Normal to the surface	0.043	0.017	0.009	0.014
[000$\bar{1}$]	0.004	0.002	0.002	0.007

Table 4.1 – Growth rates (in $\mu m/min$) in the [0001], normal to the surface and [000$\bar{1}$] directions upon the variation of the V/III ratio.

acterize remained available. The optimal growth temperature forming smooth and regular surfaces, and limiting meltback etching, has been found to be 1210°C - same as the temperature used for the growth of (10$\bar{1}$1) GaN discussed in the previous chapter.

4.3.3 Initial growth stages

After presenting the studied growth conditions, one can immediately recognize a common striking feature, which is the consistent formation of a topmost surface inclined at 13° with respect to the horizontal substrate surface. This surface corresponds to the (10$\bar{1}$1) plane that forms instead of a flat horizontal (20$\bar{2}$1) surface (see Figure 4.6). This is attributed to the (20$\bar{2}$1) being an unnaturally occurring plane that is less thermodynamically favorable than the (10$\bar{1}$1) one. The results are consistent with recent theoretical calculations [161] and experimental observations carried out on (20$\bar{2}$1) GaN-on-sapphire [74, 147, 160].

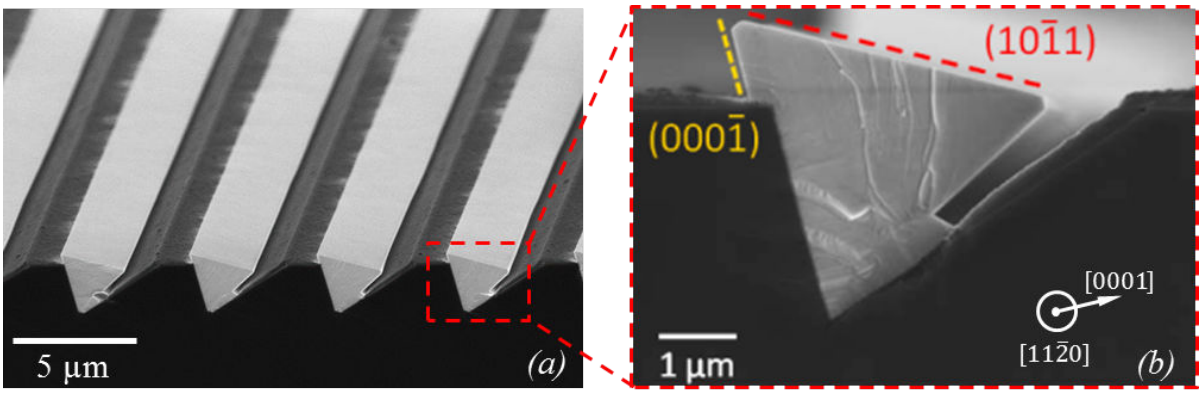

Figure 4.6 – Bird's-eye view SEM image of the (a) crystals in their initial growth stages and (b) the cross section of a single crystal.

4.3.4 Coalescence

As the growth proceeds further, adjacent crystals approach one another. However, different coalescence mechanisms have been observed upon changing the V/III ratio. When the GaN growth is performed at a V/III ratio of 220 (P = 300 mbar; T = 1210°C), coalescence does not occur. Instead, crystals grow in the direction normal to the surface at an increased growth rate in comparison to the

[0001] one. This creates the geometry shown in figure 4.7 (a) where each crystal is limited by (000$\bar{1}$), (10$\bar{1}$1) and (0001) surface planes. Coalescence not occurring may be due to the enhanced growth rate in the direction normal to the surface, which creates a gap between the (0001) and (000$\bar{1}$) planes of neighboring crystals as indicated by the white arrow in figure 4.7(a). This geometry may gradually reduce the likelihood of adatoms reaching the (0001) surface, and therefore stopping the growth from proceeding in this direction, thus rendering the coalescence to become unlikely to occur. This phenomena has also been observed by Okada *et al.* [74] where coalescence was not achieved even after 5 hours of growth.

By increasing the V/III ratio to 440 (keeping P = 300 mbar and T = 1210°*C*), the growth rate along the [0001] direction is slightly enhanced and the difference with the growth rate in the direction normal to the surface is reduced. Here coalescence occurs as shown in figure 4.7 (b). When coalescence occurs, the surface tends to facet and exposes more energetically favorable planes than (20$\bar{2}$1); indeed, the surface becomes dominated by alternating semipolar (10$\bar{1}$1) and nonpolar (10$\bar{1}$0) crystallographic facets. This is coherent with reports that describe the GaN {20$\bar{2}$1} surfaces to consist of nonpolar {10$\bar{1}$0} and semipolar {10$\bar{1}$1} nano-facets [161]. Similar coalescence properties have been experimentally observed on (20$\bar{2}$1) GaN on patterned sapphire [74, 160]. It should be noted that after a chemo-mechanical polishing step, this morphology can be flattened out to be used for potential epitaxial regrowth [147].

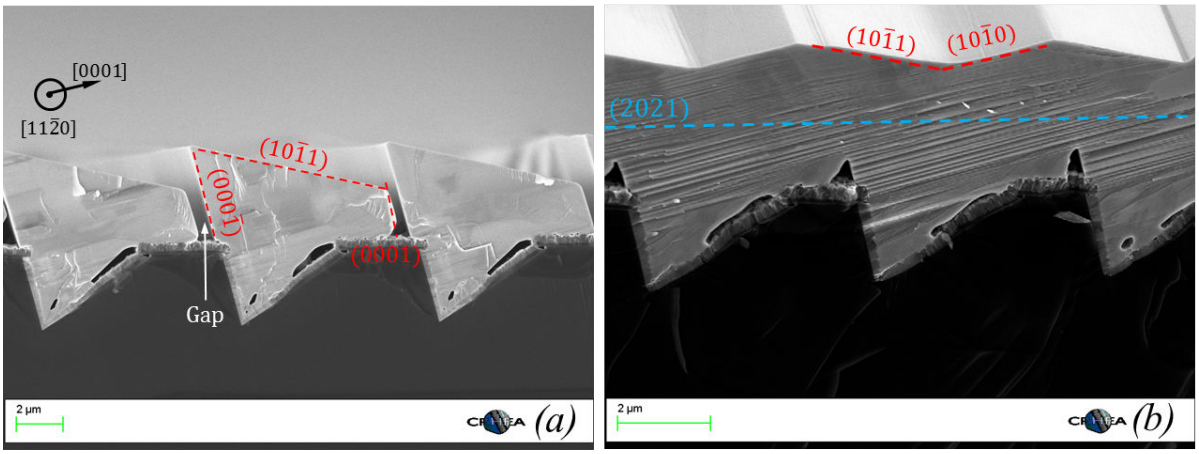

Figure 4.7 – Bird's-eye view SEM image of (a) non-coalesced crystals grown with a V/III ratio of 220 and (b) coalesced layer when grown at V/III ratio of 440 displaying the alternating micro-facets.

Furthermore, when the V/III ratio is further increased to 3100 (keeping P = 300 mbar and T = 1210°*C*), parasitic coalescence becomes dominant as shown in figure 4.8. Remarkably, coalescence occurs in bundles of two or three crystals at a time, forming an alternation of coalesced and uncoalesced bands. The coalesced bands form a combined single inclined (10$\bar{1}$1) surface, whereas the other crystals stop growing and do not coalesce. This behavior can be associated to the excessive transport

of growth species to the substrate where nucleation occurs parasitically on random sites. Then, as some bands coalesce, the bundle might become a preferential nucleation site for the subsequent adatoms reaching the surface.

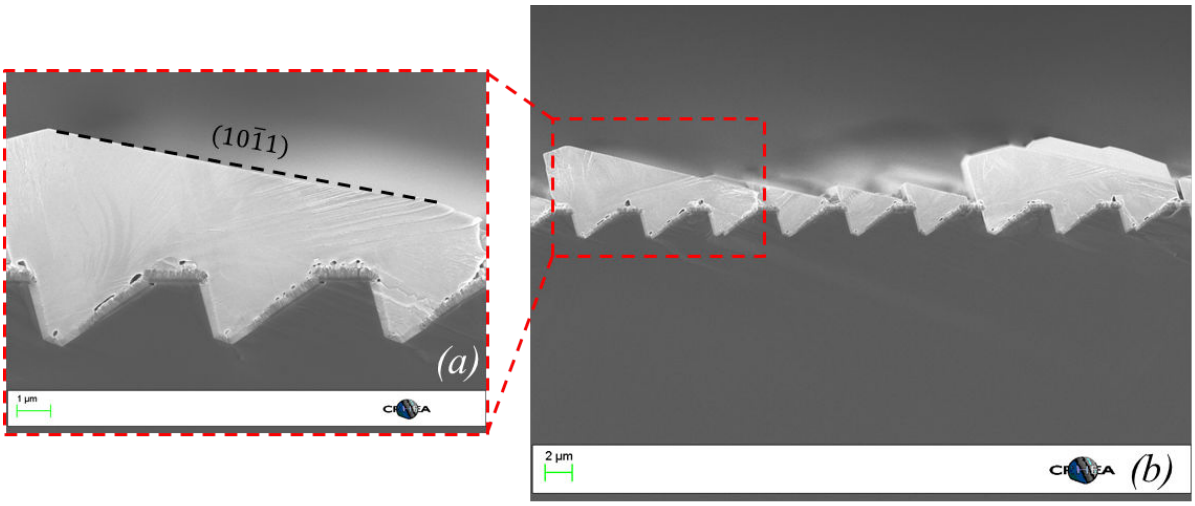

Figure 4.8 – Cross sectional view SEM image of a layer grown at 3100 V/III ratio displaying the coalescence of adjacent stripes in groups of three.

4.4 Defect behavior

The following sections describe the behavior of the crystalline defects present in the grown semipolar (20$\bar{2}$1) GaN layers.

4.4.1 Threading dislocations

The microstructure of the crystals was initially characterized by cross-section TEM. BF multi-beam TEM was performed along the [11$\bar{2}$0] zone axis, imaging conditions that permit the observation of all *a*+*c*-type and two-thirds of the *a*-type TDs. Figure 4.9 (a) and (b) show the bending of dislocations nucleated at the GaN/AlN/Si interfaces during the initial growth stages.

As observed for the (10$\bar{1}$1) orientation (see section 3.2.2), TDs propagate in the +*c*-growth direction and then bend mostly perpendicular to the +*c*-axis into the basal plane. TDs bending upwards thread towards the surface and are, therefore, concentrated in an area having a width equal to the side of the initial triangular shaped stripe. TDs bending downwards are blocked as they reach the bottom end of the crystal.

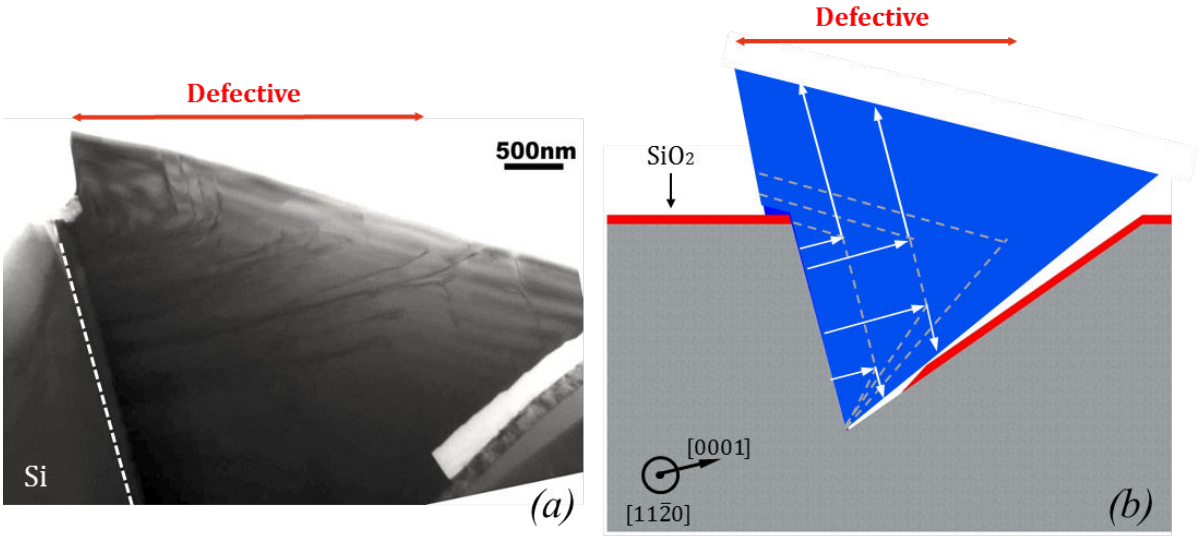

Figure 4.9 – (a) Cross-sectional TEM image showing the crystals in their initial growth stages displaying the bending of threading dislocations. The corresponding schematic (b) shows an illustration for enhanced clarity of TDs behavior (in white).

4.4.2 Basal stacking faults

When the topmost crystal surface arises above the (114)1°off masked silicon surface, growth proceeds in the opposite -*c*-direction as shown in figure 4.10. BF-TEM and HRTEM done in the -*c*-wing, shown in figures 4.11 (a) and (b), respectively, indicate that the micro-structure of the zone where the growth proceeds in the -*c*-direction is dominated by the presence of BSFs. Once these BSFs are created, they propagate all the way towards the surface thereby influencing the overall structural quality of the layer.

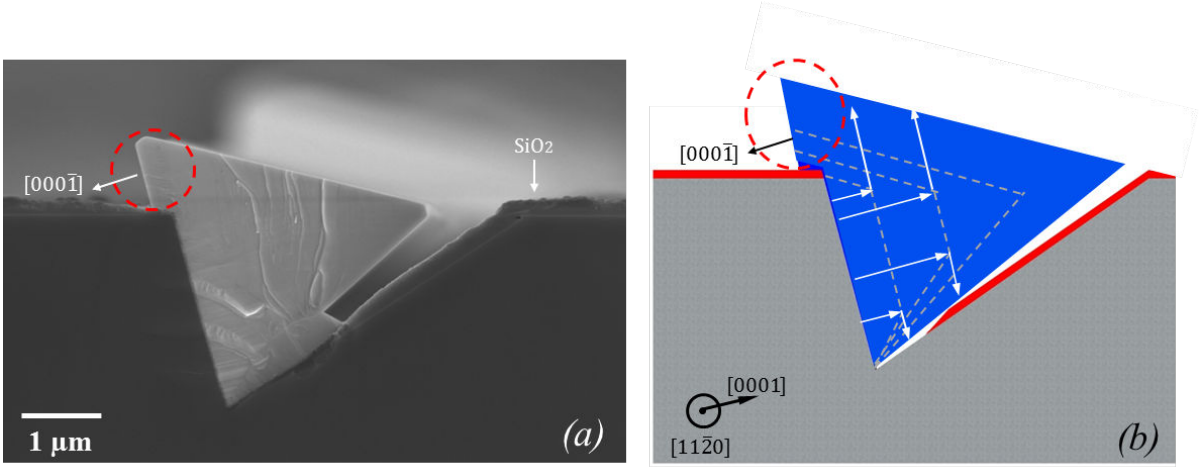

Figure 4.10 – (a) Cross-sectional SEM image and (b) its corresponding schematic showing the region (indicated by the dashed red circle) where the crystal grows in the [000$\bar{1}$] direction when its height exceeds the height of the mask.

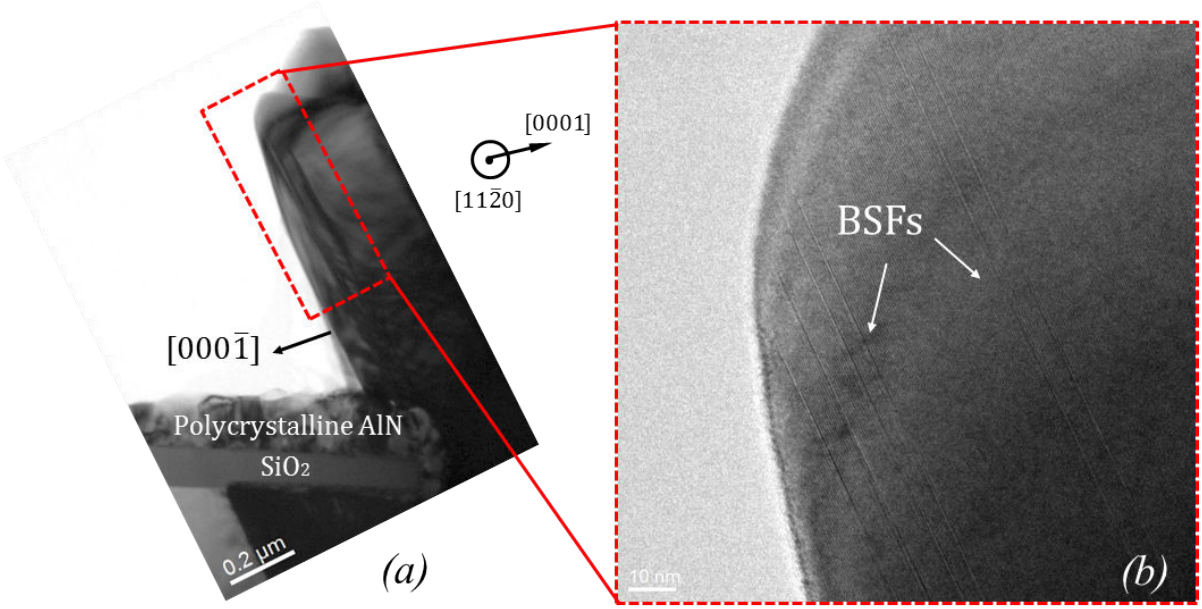

Figure 4.11 – (a) Bright-field TEM image of the BSFs created upon the growth in the –c-direction, and (b) HRTEM image of BSFs.

4.5 Spatial distribution of defects

To gain further insight into the behavior of observed crystalline defects and their spatial distribution, CL was used to investigate the layers' optical properties and correlate them with the TEM investigations illustrated in figure 4.9. In view of the TEM cross-section images, the coalesced layer can be divided into three different regions as indicated on the panchromatic image (Figure 4.12 *(a)*) and the monochromatic CL map (Figure 4.12 *(b)*).

Region A corresponds to the area where most TDs accumulate as a result of dislocation bending during the initial growth stages (see Figure 4.12 *(a)(b)*). This results in considerable intensity reduction due to the non-radiative nature of TDs. The exact TD density remains difficult to quantify due to black-spot overlapping, resulting in a final underestimation of the total density if CL is used as a measurement technique [118].

Region B corresponds to the –*c*-wings, which are dominated by bright elongated white lines due to the luminescence from BSFs. Well-defined I_1, I_2 and E features are detected (Figure 4.12 *(c)*). Studies on the (20$\bar{2}$1) orientation have only reported emission corresponding to the unique presence of I_1 BSFs [74, 147, 160]. Figure 4.12 *(b)* confirms the presence of BSFs only in this region, as represented by the red pixels corresponding to emission at 3.40 eV. Emissions related to I_2 at 3.33 eV and E at 3.28 eV have also been detected in this area (not shown in CL map). No further optically active defects were found in this region.

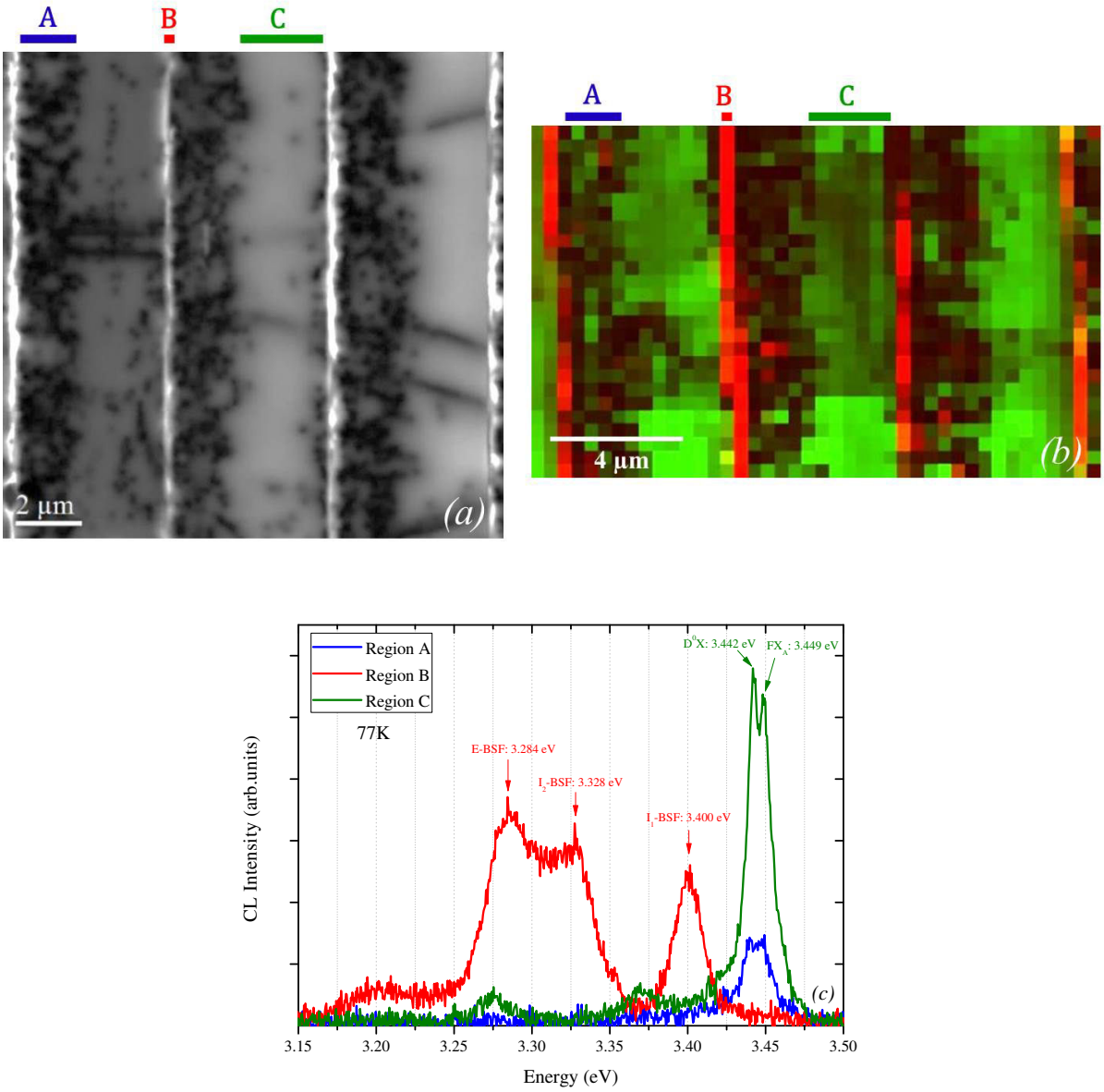

Figure 4.12 – (a) Plane-view panchromatic CL image acquired at 77 K displaying threading dislocations as black spots. (b) CL mapping displaying the NBE emission in green and I1 stacking faults at 3.42 eV in red. (c) The CL spectra in linear scale of the three different regions (same ordinate scales) of the layer marked on the panchromatic and monochromatic images.

Region C corresponds to the almost defect-free zone, with the luminescence being dominated by two excitonic transitions, at 3.442 eV and 3.449 eV, related to D^0X and FX_A, respectively. The CL map shows the regions dominated by the NBE emission in green implying that roughly 50% of the layer's total surface area is of relatively good optical quality and nearly defect-free.

4.6 Nucleation on the opposite Si (111) facet

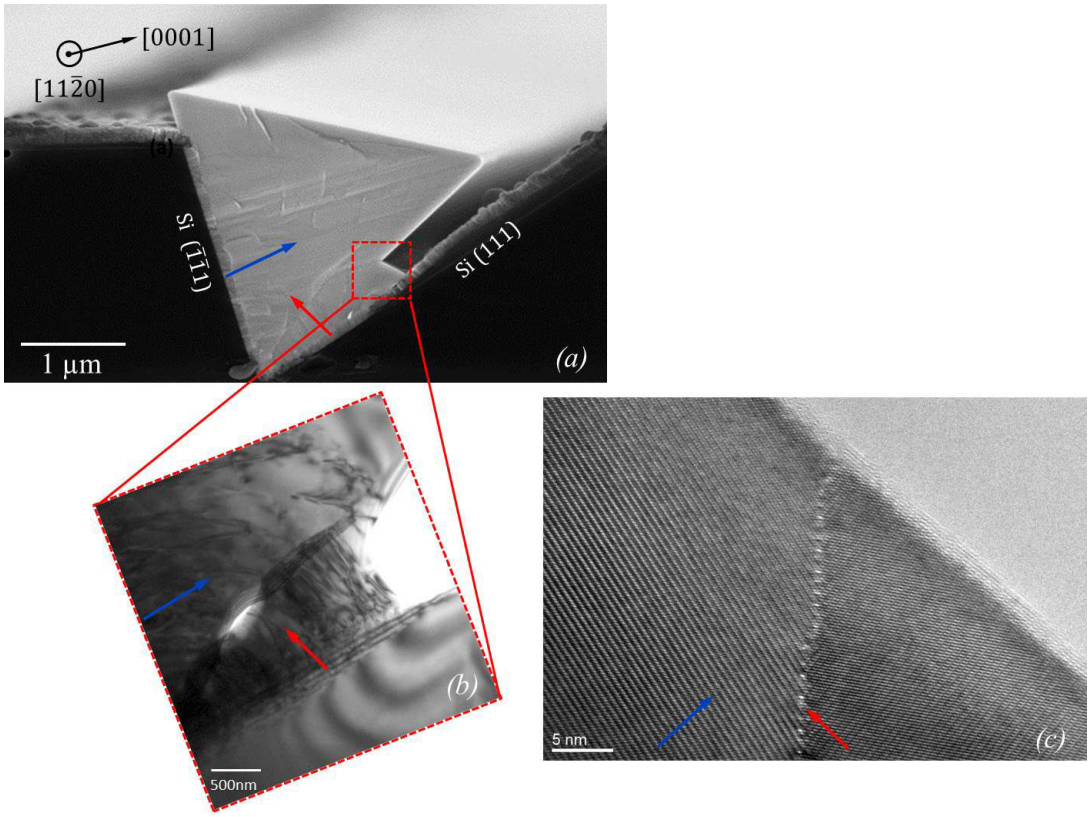

Figure 4.13 – (a) SEM image displaying crystals nucleating on Si (111) facets and whose c-directions are indicated by the arrows (b) Bright-field TEM image at the interface between the two crystals. (c) HRTEM image at the same interface. The blue arrows indicate the growth direction of the large crystal on the ($\bar{1}$ $\bar{1}$ 1) facet, and the red arrows indicate the growth direction of the small parasitic crystal grown on the unmasked part of the (111) facet.

During the inclined dielectric mask deposition, a shadowing effect by the adjacent trench prevents the SiO_2 from completely masking the inclined Si (111) sidewall where ideally no growth is wanted. This shadowing leaves an exposed region on the bottom end of the Si facet. Consequently, upon growth initiation crystalline GaN grows on the aforementioned facet opposing the primary crystal (Figure 4.13). BF TEM and HRTEM were performed at the contact interface of the two crystals as shown in Figure 4.13. According to the acquired images, after a short growth duration, the primary crystal overlaps the crystal growing on the "undesired" Si (111) facet, blocking its further extension. As evidenced by HRTEM, the overlap of the two *c*-oriented crystals, inclined with respect to each other by 71° (same angle as between adjacent 111 planes in Si) leads to the formation of a well-defined grain boundary. TEM indicates that the presence of this interface creates defects that remain in the plane of the grain boundary. These defects do not propagate towards the surface. Moreover, the grain boundary observed here does not exhibit a change in the crystallographic arrangement and remains

hexagonal. This is contrary to what has been observed when growing the (10$\bar{1}$1) orientation on Si (001)7°off (see section 3.2.5) where the opposite hexagonal grains become cubic at the boundary where they meet.

4.7 Orientation identification

The orientation of the GaN layer parallel to the substrate has been investigated through XRD. Figure 4.14 shows a symmetrical $2\theta - \omega$ scan profile that displays the substrate and a diffraction peak positioned at 70.5° corresponding to the intended (20$\bar{2}$1) GaN [162]. However, a third reflection positioned at 63.2° corresponding to GaN (10$\bar{1}$3) [162] has also been detected. This additional peak having an intensity one order of magnitude lower than the main peak, arises due to the small GaN crystal grown on the bottom part of the Si (111) facet as shown in figure 4.13. From the calculated intrinsic x-ray intensities, the diffraction intensity of (10$\bar{1}$3) GaN is twice higher than the one of (20$\bar{2}$1) [162]. This explains the comparable intensities of both peaks despite the larger volume of the (20$\bar{2}$1) oriented crystal.

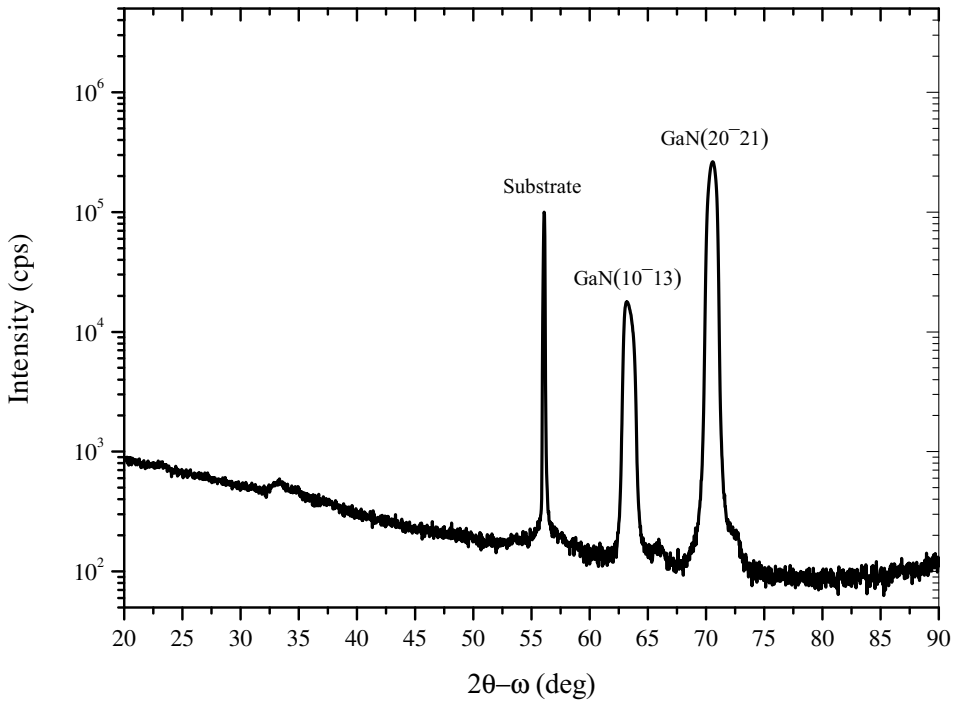

Figure 4.14 – XRD $2\theta - \omega$ scan displaying the peaks of the substrate and the two peaks of the primary and overlapped crystal.

4.8 Overall quality assessment

Optical and structural characterization was performed in order to determine the overall quality of the grown layers. A comparison between coalesced layers and non-coalesced bands will be discussed, in addition to a comparison with the current state-of-the-art reported values.

4.8.1 Photoluminescence

Low temperature PL was performed at 10 K in a sample with uncoalesced bands and in another with a coalesced layer having a 2 μm thickness, both grown under identical growth conditions (Figure 4.15). For the NBE transitions, one can notice that both samples experience a similar tensile stress with only 2 meV difference. This indicates that uncoalesced stripes experience the same average tensile strain as the coalesced layers, and are not completely relaxed via their free surfaces. In what concerns BSFs, an increase in density is observed after coalescence. By comparing the intensity ratios between the D^0X and the total intensity of all three BSF types combined, the ratio before coalescence decreases from a factor 10 to a factor 4 after coalescence. This suggests that BSFs are likely to be also generated at the coalescence boundaries of adjacent crystals, which is another source of BSFs besides the ones created in the -*c*-wings.

In comparison to PL spectra of coalesced (20$\bar{2}$1) layers on patterned sapphire, Okada *et al.* [74] and Leung *et al.* [147] report on similar PL spectra indicating a NBE intensity higher than I_1-type BSFs by a factor 3. Meisch *et al.* [160] also show PL spectra of their layers with NBE and I_1-type BSFs having equivalent intensities. In our layers, the NBE intensity was seen to be higher than I_1-type BSFs by a factor 10.

4.8.2 X-ray diffraction

The structural quality was assessed by measuring the XRD rocking curve FWHMs of the symmetrical (20$\bar{2}$1) reflections for uncoalesced and coalesced layers while varying the azimuthal angle of the incident beam (*i.e.* parallel ($\Phi = 0° - 180°$) and perpendicular ($\Phi = 90° - 270°$) to the stripes), as shown in figure 4.16. Both samples were grown under identical growth conditions and the coalesced sample had a thickness of ≈ 2 μm.

Before coalescence the average FWHM amounted to 720 arcsec with minima of 460 arcsec and maxima of 820 arcsec. After adjacent stripes coalesce, the average FWHM increases to 980 arcsec with minima of 710 arcsec and maxima of 1200 arcsec. The increase in the FWHM may be a consequence of the increase in the density of BSFs after coalescence occurs. Furthermore, it should be noted that the FWHM measured parallel to the stripes before and after coalescence is the same. The increase in

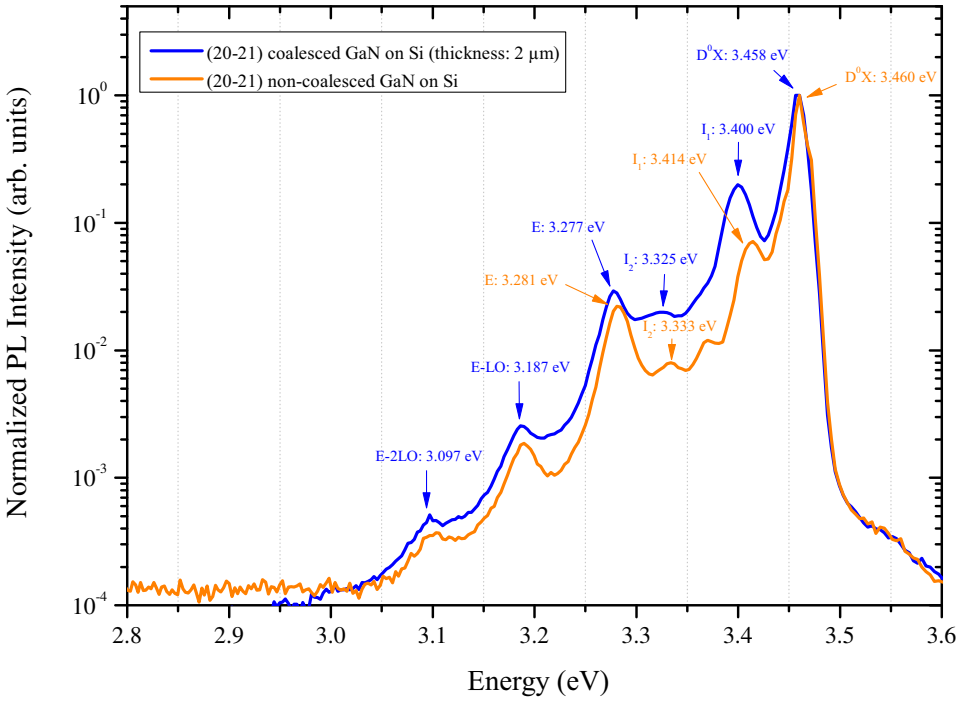

Figure 4.15 – PL spectra acquired at 10 K of a coalesced (in blue) and uncoalesced (in orange) sample of (20$\bar{2}$1) semipolar GaN on patterned silicon. Typically observed transitions are marked on the plot.

the BSF intensity is also shown in the PL spectra discussed earlier (see figure 4.15). According to the BSF extinction rules, diffraction occurs for I_1-type and I_2-type BSFs for the symmetrical (20$\bar{2}$1) scan when the projection of the x-ray beam is parallel to the projection of the *c*-axis [1].

In comparison with (20$\bar{2}$1) layers grown using the same inclined growth technique on sapphire, Leung *et al.* reported on an average FWHM of 259 arcsec for a layer thickness of ≈ 8 μm [147], Okada *et al.* reported on an average FWHM of 468 arcsec for a layer thickness of ≈ 5 μm [74], and Meisch *et al.* reported on an average FWHM of 1072 arcsec for a layer thickness of ≈ 2 μm [160]. These results indicate that if our layers behave as the ones grown on sapphire, the FWHM values should notably decrease with increasing thickness. This option however is tricky when growing on silicon, especially that long growth runs highly increase the probability of meltback etching.

[1] see section 2.4.2.2 for further details.

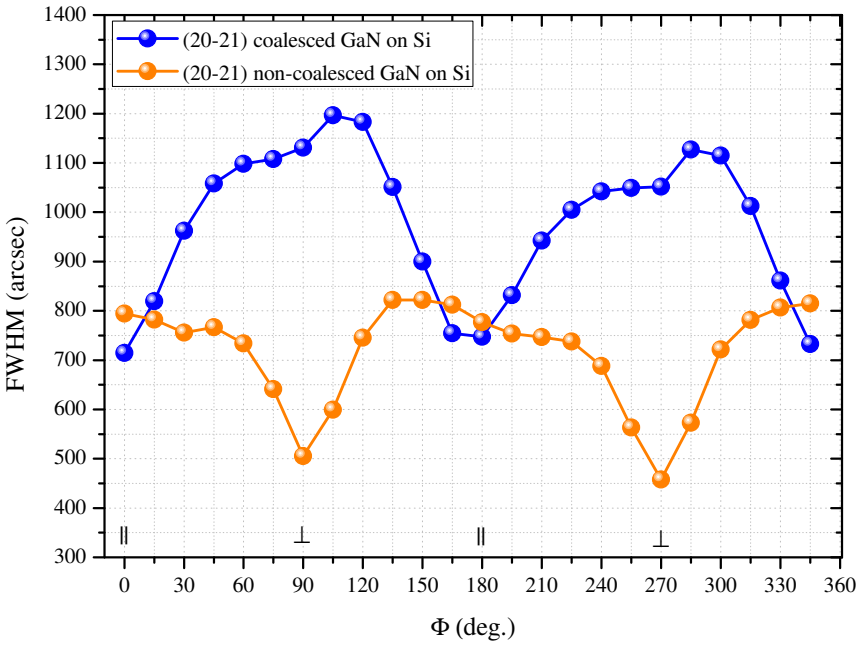

Figure 4.16 – X-ray rocking curve FWHMs on the symmetric (20$\bar{2}$1) GaN reflections by varying the azimuthal angle of the incident beam. For $\Phi = 0°$ *the incident beam is parallel to the stripes and for* $\Phi = 90°$ *the incident beam is perpendicular to the stripes. The orange plot shows the FWHM values of non-coalesced bands and the blue plot for the coalesced layers.*

4.9 Conclusions

In this chapter the growth of (20$\bar{2}$1) semipolar GaN has been achieved on patterned Si (114)1° off-axis substrates. The objective was to demonstrate the feasibility of growing the (20$\bar{2}$1) orientation on silicon for the first time and investigate the crystals' behavior under different growth conditions.

Indeed, numerous growth parameters have been investigated, and have shown that the formation of the inclined (10$\bar{1}$1) topmost surface in the initial growth stages is inevitable. This unavoidable formation of the (10$\bar{1}$1) surface inclined at 13° from the horizontal plane imposes a geometrical alignment where the height of the Ga-polar +*c*-wing always remains below the highly defected N-polar -*c*-wing. Such a geometry does not permit applying defect reduction strategies that enable the overgrowth of the defective region of one crystal by the defect-free region of the adjacent crystal.

Coalescence of adjacent crystals in a single-step process under optimized growth conditions was achieved. Coalesced layers show an alternating micro-facetted surface dominated by more energetically favorable nonpolar and semipolar crystallographic planes. Such layers therefore require a chemo-mechanical polishing step to flatten the surface if devices are to be fabricated thereon. Structural and optical characterization indicated that the overall quality of the layers grown on silicon is comparable to those grown on sapphire.

In principle, reducing the density of defects for the (20$\bar{2}$1) orientation may also be done by applying the interlayer defect blocking method that was demonstrated in the previous chapter.

5 Meltback Etching

This chapter will be dedicated to the so-called *"meltback etching"*: a major obstacle encountered during the course of this PhD. This deteriorating phenomenon occurring as a result of a chemical reaction between gallium and silicon is one of the challenging issues to be overcome when growing GaN-on-Si by MOVPE, especially when growth is performed on pre-patterned substrates. To our knowledge, meltback etching is not understood in detail, and clear routes to completely circumvent it remain scarce and not well established. In the following, to familiarize the reader with this phenomenon, meltback etching will be briefly introduced. Then, the different hypothesis predicting its origin in the grown samples will be presented, and meltback etched surfaces will be characterized. Moreover, and since the aim of this PhD is not to study meltback etching, but to avoid its presence, the last part presents the successful and failed attempts in suppressing meltback etching.

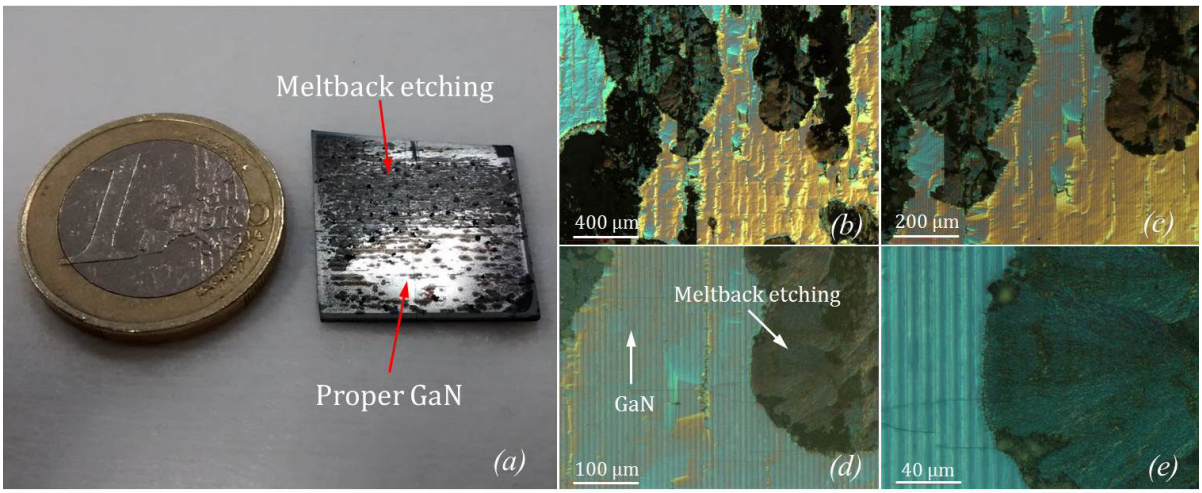

Figure 5.1 – Meltback etching (a) photograph as seen with the naked eye (b) 5 × (c) 10 × (d) 20 × (e) 50 × optical microscope images of a sample after the growth of GaN on the patterned silicon.

5.1 What is meltback etching?

Meltback etching is a chemical reaction occurring at typical GaN MOVPE growth conditions, namely at high temperatures, between silicon and gallium resulting in their inter-diffusion (*i.e.* silicon into gallium and vice-versa) and the violent outspread of matter. This reaction damages large areas on the wafer [80, 83, 93] as shown in the photo and optical microscope images in figure 5.1 (a) and figure 5.1 (b-e), respectively. The shown images display the reaction on patterned silicon substrates. In the early growth stages, typical meltback etched surfaces appear locally tainted and exhibit a rough texture as shown in figure 5.2 (a) and (b). Once the reaction is locally initiated, it cannot be stopped, so meltback etching gradually expands on the surface and in the volume as the growth duration increases. Heavily damaged samples typically exhibit deep hollow voids in the substrate (see figure 5.2 (c)), and parasitic deposition eventually dominates the surface in significant sizes and heights, commonly reaching 10 - 20 times the dimensions of the patterns, as shown in figure 5.2 (d). Meltback etching has also been observed for GaP layers on silicon substrates grown at low temperature (*i.e.* 440°*C*) by MBE [163] and MOVPE [164].

From the thermodynamic point of view, gallium forms a eutectic mixture (*i.e.* not completely soluble) with rather small quantities of silicon [165] at low temperatures as indicated by the Ga-Si phase diagram shown in figure 5.3. Gallium can also be found in liquid phase in a wide range of temperatures (from 29.77°*C* to 2237°*C*) [165, 166]. Liquid gallium can also be a solvent and catalyst synthesizing several crystals such as carbon nanotubes [167] and GaAs crystals [168], in addition to silicon [169]. The contact between gallium and silicon during growth must therefore be avoided if proper GaN surfaces have to be obtained.

To circumvent the occurrence of meltback etching when the growth of GaN-on-Si by MOVPE is carried out, an AlN layer covering the substrate prior to the growth of GaN is typically used [132, 87, 170, 171], and works well on planar substrates. However, AlN films may not always provide a perfect coverage, especially on patterned substrates. This may be due to fabrication errors and/or imperfect etched nucleation surfaces (*e.g.* macro-steps resulting from inaccurate mask alignment during photolithography, and/or fabrication residuals/contamination) that disturb the Al adatom surface diffusion and nucleation of AlN over the whole surface. Imperfections in the AlN buffer layer could therefore create diffusion channels forming a passage between Ga and Si, and thus induce meltback etching.

Diffusion channels may also be created by the formation of cracks. GaN layers grown on silicon experience a difference in the thermal expansion coefficients that put GaN layers under tensile stress. This mismatch causes the GaN layers to crack during the cool-down from growth to room temperatures [172]. However, Krost *et al.* [80] have also identified cracking that occurs during the growth

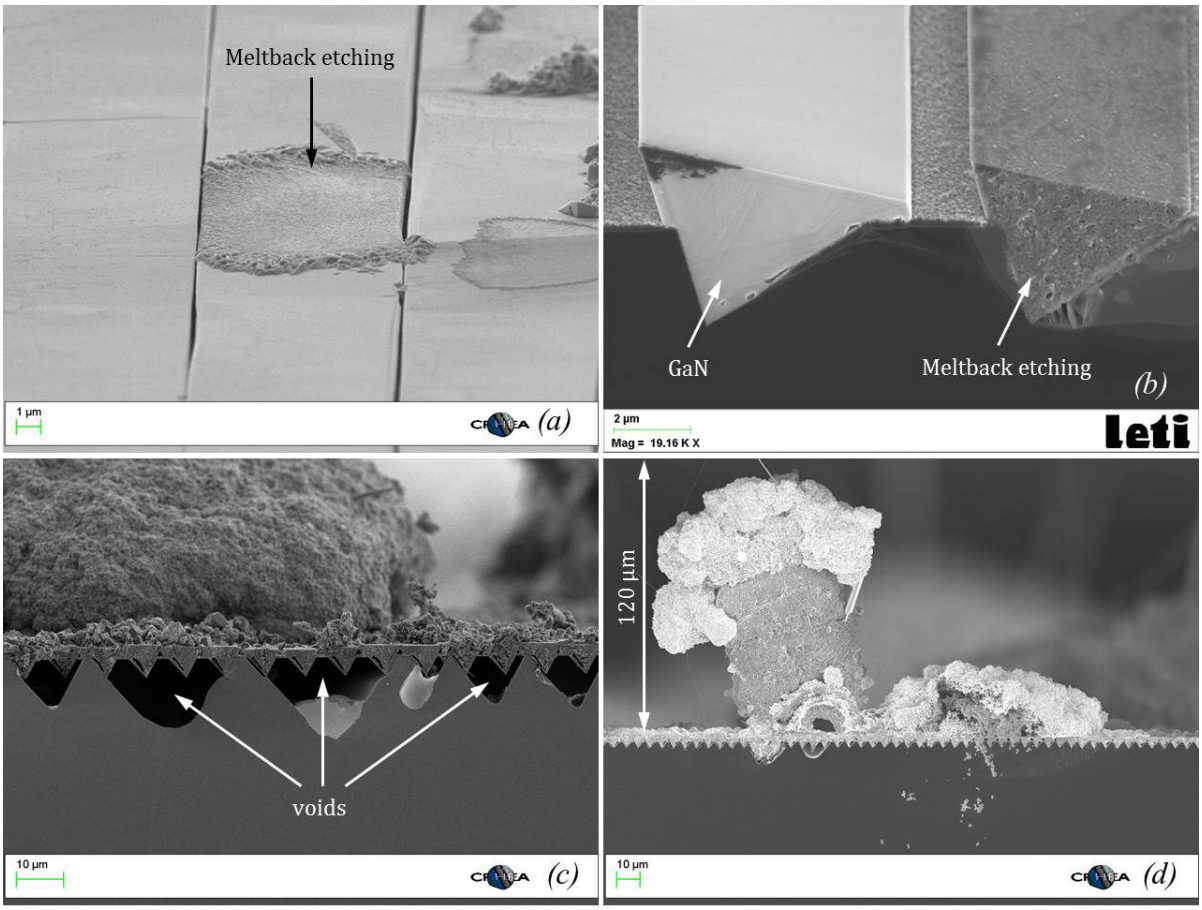

Figure 5.2 – SEM images showing examples from different samples of different observed stages of meltback etching (a, b) in its early stages and (c, d) after extended growth durations that lead to the creation of voids in the substrate and the formation of structures reaching heights exceeding 100 µm.

of GaN (on planar Si(111)), and were seen to extend deeply into the silicon substrate. Such cracks were distinguished from the ones forming during the cool-down by the formation of crystalline GaN facets at the vicinity of each crack. Similarly, Drechsel *et al.* [171] identified cracking of the AlN buffer layer on planar Si (111) when thicknesses exceeded 350 nm and concluded that the probability of meltback etching occurrence is a trade-off of improved protection due to increased thickness and the resultant higher chance of cracking. Therefore, when a GaN layer is grown on a cracked film, the crack may act as a diffusion channel between silicon and gallium, and further promote meltback etching. In our case, cracks occurring during the growth have not been observed, neither for GaN (no crystalline facetting has been identified at the vicinity of the observed cracks) nor for AlN.

5.2 Possible sources of meltback etching

In order to suppress meltback etching on patterned substrates, it is necessary to identify the origins by which Ga reacts with the Si during the growth. In the following, reasons causing meltback etching

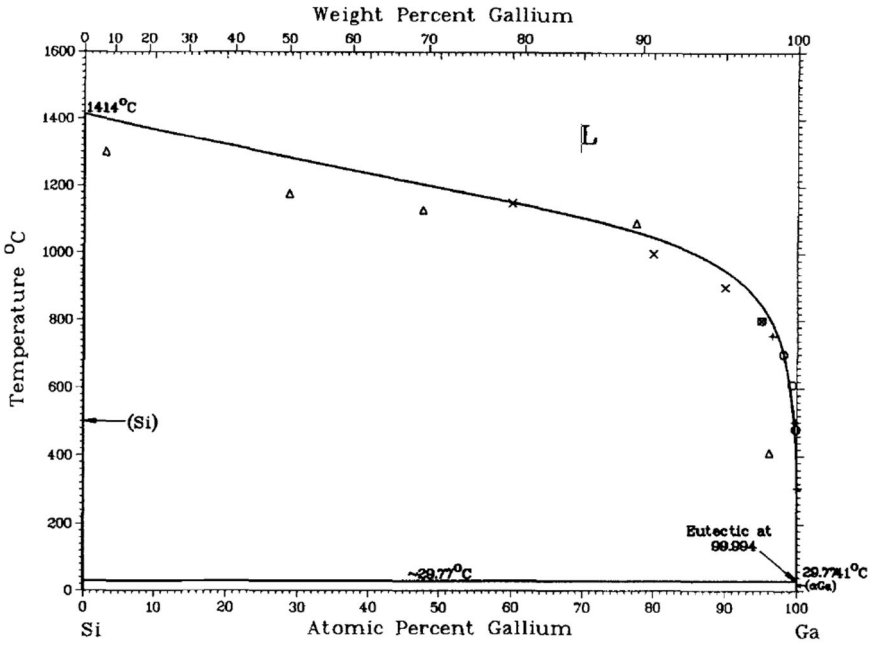

Figure 5.3 – The equilibrium phase diagram of the Si-Ga system including the eutectic transformation at a temperature very close to gallium's melting point (29.77°C) (Image source: [165]).

discussed in literature will be presented and compared to the samples investigated in this work. Other possible reasons, more specific to this work and that may be a source of meltback etching will be also discussed.

5.2.1 Gallium droplet formation

The formation of gallium droplets (*i.e.* in liquid phase) and their interaction with silicon in the early growth stages is the major reason causing meltback etching, as suggested by the current literature on the subject. Takemoto *et al.* [173] investigated the influence of the Ga partial pressure on the direct growth of LT-GaN (*i.e.* 600°C) on silicon by MOVPE. They demonstrated that using a partial pressure higher than the vapor pressure of metallic gallium results in the formation of Ga droplets on the silicon surface. Meanwhile, using a partial pressure lower than the vapor pressure of metallic gallium resulted in the formation of Ga vapor. Remarkably, after increasing the susceptor temperature on the same samples, meltback etching was induced on the surface where gallium droplets were present, while the surface without gallium droplets remained intact. Similar results were reported by Ishikawa *et al.* [174] for the growth of GaN-on-Si by MOVPE, where meltback etching was intentionally induced by depositing Ga droplets in the initial growth stages. Detz *et al.* [175] also recently reported on silicon deterioration in the presence of Ga droplets by MBE. Consistently, meltback etching was observed in GaP layers grown on Si by MOVPE at low temperatures, and has also been associated to the formation

of Ga droplets reacting with silicon [164]. These aforementioned results suggest that the amount of Ga deposited in the early growth stages has to be controlled to avoid the formation of gallium droplets, and consequently avoid meltback etching.

In this work, the GaN growth was performed on an AlN buffer layer grown on silicon, which, in principle, does not permit contact between the substrate and gallium. However, here we will temporarily assume that silicon is exposed, or partially exposed, to the gallium precursors in order to test the gallium droplet suggestion. In our case, the GaN growth was performed at $\sim 1000°C$ (*i.e.* higher than the growth temperatures reported in literature), which increases the vapor pressure of gallium to $\sim 4 \times 10^{-5}$ atm [176, 177]. Moreover, the partial pressure for the used growth conditions amounted to $\sim 4 \times 10^{-6}$ atm, one order of magnitude lower than the Ga vapor pressure at the same temperature. The partial pressure was calculated using the following equation:

$$P_{MO-Reactor} = \frac{P_{MO}(T_{Bubbler}) \times Q_B \times \frac{P_{Standard}}{P_{Bubbler}}}{Q_{Total} \times \frac{P_{Standard}}{P_{Reactor}}} \tag{5.1}$$

Where $P_{MO}(T_{Bubbler})$ is the equilibrium vapor pressure of the metalorganic component; Q_B is the carrier gas flux through the bubbler; $P_{Standard}$ is the standard atmospheric pressure (1013.25 mbar); $P_{Bubbler}$ is the regulated bubbler pressure; and Q_{Total} is the total gas flux.

These values indicate that gallium droplet formation is thermodynamically unfavorable under our used growth conditions and is, therefore, unlikely to occur. This also correlates well with the calculated GaN phase diagrams by Koukitu *et al.* [177], which indicate that the growth conditions used in our case satisfy the regime where GaN growth occurs, and never in the regime where the formation of gallium liquid droplets is favorable or where surface etching occurs. Thus, the origin of meltback etching observed in the samples investigated in this work is unlikely to be associated to gallium droplets reacting with silicon.

5.2.2 Pre-growth fabrication imperfections

Another suspect that may contribute to meltback etching is an imperfect substrate surface and pattern. During the substrate fabrication process, the mask and opening of each stripe is initially defined by the photo-lithography process that, in turn, defines the KOH etching boundaries. However, since

KOH is a chemical etchant, albeit anisotropic, under-etching is likely to occur. This results in the formation of the inclined facets slightly below the SiO_2 mask instead of forming at the exact edge. This creates an *over-hanging cap* of SiO_2 as shown in figure 5.4[1].

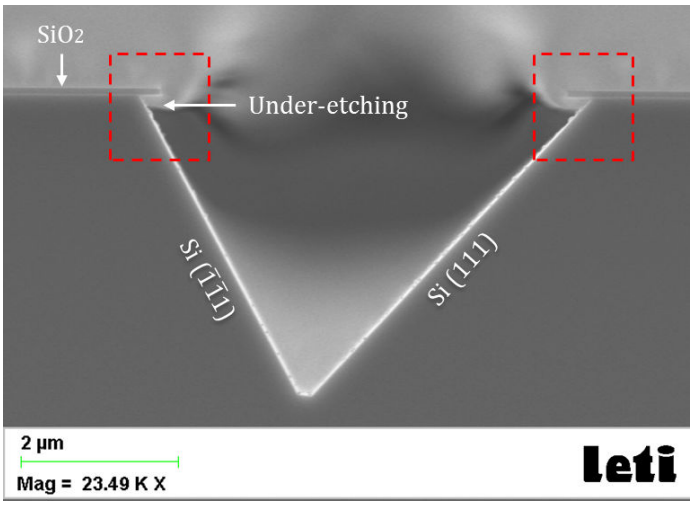

Figure 5.4 – Cross sectional SEM image of an etched V-groove showing the SiO_2 over-hanging cap as a result of KOH under-etching.

Consequently, when the growth is carried out, AlN does not nucleate in the corner below the over-hanging caps, as shown in figure 5.5. This results in the growth of a very thin, or sometimes null, AlN layer in this area, which keeps some silicon exposed to the subsequent growth of GaN that may induce the meltback reaction.

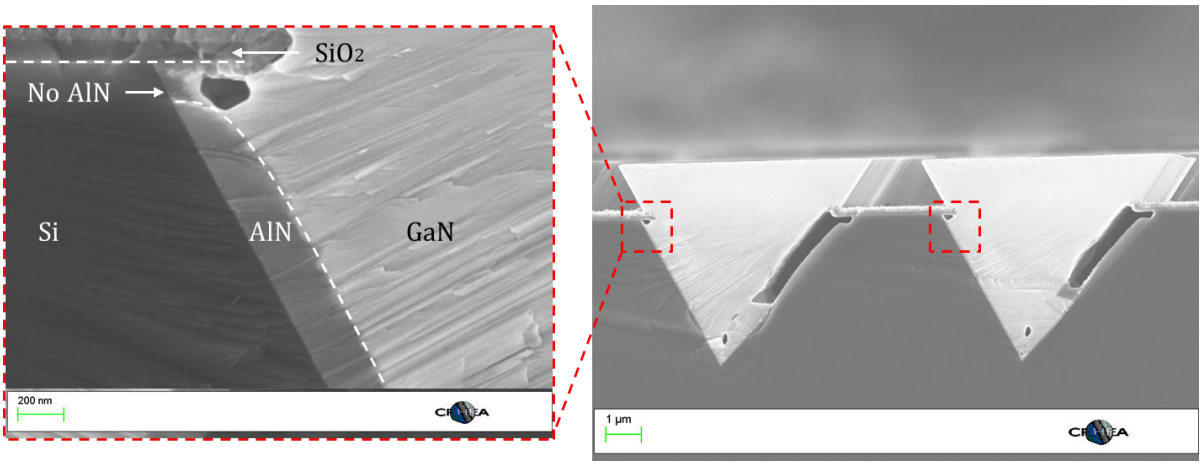

Figure 5.5 – Cross sectional SEM images of the GaN crystals grown on the substrate with SiO_2 over-hanging caps showing that no AlN reaches this region.

Besides the aforementioned issue, it is necessary to note that all pre-growth substrate fabrication was carried out through hand-held operations, and in machines run by multiple users and for multiple

[1] The removal of these caps has been attempted using ultra-sounds, which is expected to break them mechanically, but due to their rather small extension (*i.e.* around 200 nm), their breaking was not possible.

purposes. This may introduce the samples to unidentified environments that could lead to contaminated surfaces and fabrication defects in subsequent processing steps, and therefore contribute to meltback etching during growth. For comparison, some growth runs were performed on a patterned substrate and a planar Si(111) wafer loaded together in the reactor. The patterned substrates consistently showed major damaged regions as a result of meltback etching, while a few minor damaged spots were observed on the planar substrates. This supports the hypotheses suggesting surface imperfections and/or contamination to be contributors to meltback etching.

5.2.3 MOVPE reactor contamination

When meltback etching occurs, significant amounts of *fine black powder* resulting from the evaporated gallium and silicon cover the reactor walls, susceptor and shower-head. Indeed, after every performed GaN growth, the reactor is baked under hydrogen flow at temperatures typically higher than the GaN growth temperatures. This process serves to clean the reactor chamber from any reactant residuals deposited on the walls that may affect the subsequent growth run. However, ensuring a perfectly clean reactor chamber after the baking runs is not possible unless the shower-head, susceptor and other components are unmounted and cleaned individually. The presence of reactor residuals, despite the growth of an AlN buffer layer that serves to protect the Si surface, may disturb the complete coverage of this buffer layer and leave open channels. These open channels may contribute to further promote meltback etching when the growth of GaN is carried out. Residuals also influence the growth environment history on the layer growth (*i.e.* memory effects), and hence affect the run-to-run reproducibility.

5.3 Energy dispersive x-ray (EDX) spectroscopy and backscattered electron (BSE) imaging

To understand the chemical composition of the damaged surfaces and investigate the different stages of meltback etching, EDX analysis was performed and backscattered electrons SEM images were acquired. Three different samples were selected based on the severity of meltback etching, from low damage to high damage. Besides understanding how the chemical composition changes with the level of damage, these samples also give insight on how the morphology of the damaged layers evolves. In the following, two SEM figures of the same region will be shown. One image created by secondary electrons (*i.e.* surface-sensitive) used to display the morphology, and another image created by backscattered electrons that are sensitive to the atomic mass of the nuclei they scatter from. Consequently, heavier elements appear brighter than lighter elements in the backscattered electron image [178]. For reference, the atomic mass of gallium (Ga) is 69.723 amu and the atomic mass of silicon (Si) is 28.085 amu [179].

Low damage Figure 5.6 (a) and (b) show cross-sectional SEM images of secondary and backscattered electrons, respectively, of layers in the very early stages of meltback etching. A contrast difference between different regions in the silicon substrate is observed, which indicates a change in the chemical composition of the material. EDX spectra acquired on both areas on the substrate with different contrast were identical, and indicated the sole presence of silicon, as shown in figure 5.6 (c). This contrast change observed in BSE images but not detected by EDX may suggest a change in the chemical composition (*e.g.* diffusion of gallium into silicon and vice-versa) occurring at levels below detection limits, which is ~ 1 % in our case. The EDX spectrum acquired on the GaN crystals is shown in figure 5.6 (d). Gallium and Nitrogen have been detected with respective intensities of 3235 and 572 counts. These values represent what one can observe on a proper GaN layer, therefore indicating an intact material, which may also be confirmed by the seen morphology. The detected intensity counts and the respective intensity ratio (between gallium and nitrogen for GaN) will therefore serve as a reference for the regions investigated afterwards. The displayed EDX spectra have all been acquired under identical conditions (*i.e.* current, acceleration voltage and acquisition time).

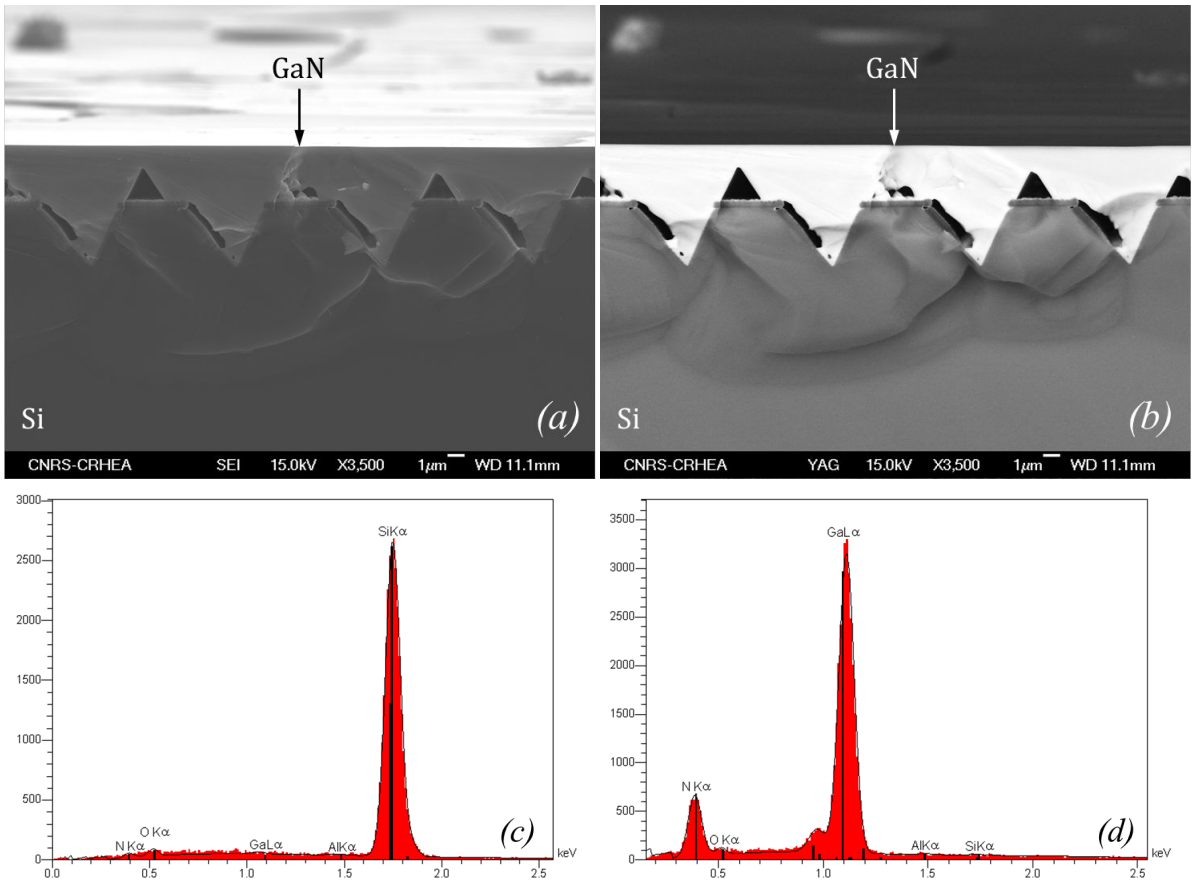

Figure 5.6 – Cross sectional SEM images of layers in the very early stages of meltback etching showing a contrast difference in the substrate: (a) secondary electrons and (b) backscattered electrons. The acquired EDX spectra (c) on the silicon substrate and (d) GaN crystals.

Intermediate damage At an intermediate stage of meltback etching, the substrate and the grown crystals exhibit changes in composition and morphology. Figure 5.7 shows cross-sectional SEM images ((a) secondary and (b) backscattered electrons) of layers in an advanced stage of meltback etching. From the figure, four different zones have been identified, and their corresponding EDX spectra are shown in the in figure 5.8. The plot in figure 5.9 shows the EDX peak intensity for each detected element in the intact GaN reference spectrum and all four zones:

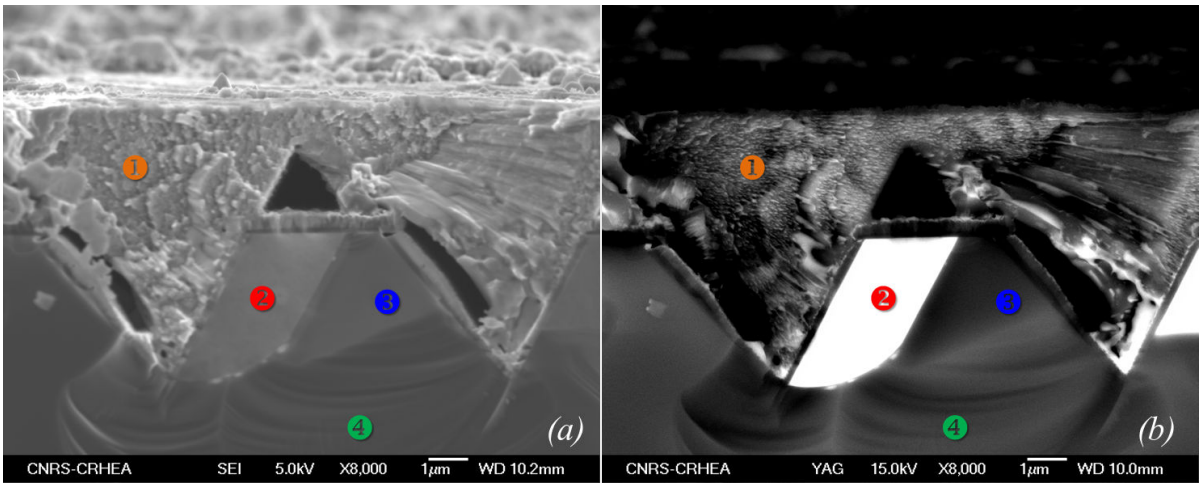

Figure 5.7 – Cross sectional SEM images of layers in advanced stages of meltback etching (a) secondary electrons and (b) backscattered electrons. Four different regions can be identified, and their EDX results are shown in figure 5.8

- **Zone 1** (•) corresponds to the meltback etched GaN crystal, which exhibits almost equivalent peak intensities of gallium, silicon and nitrogen with a minor presence of oxygen. In comparison with the reference EDX spectrum of the intact GaN crystal, the nitrogen intensity increases by almost a factor 1.9, while the gallium intensity decreases by a factor of 2.6.
- **Zone 2** (•) is the region in the substrate closest to the nucleation facet. It is almost dominated by the sole presence of gallium with a peak intensity comparable to the one seen on the intact reference GaN spectrum. Minor presence of silicon and oxygen was also detected in this region, while nitrogen was nonexistent.
- **Zone 3** (•) is the region in the substrate closest to the masked facet where no growth takes place, and exhibits a contrast different from the one of an intact silicon surface. Only silicon has been detected in this area.
- **Zone 4** (•) corresponds to the silicon substrate below the grooves, which in principle is not damaged. Only silicon is present in this zone.

From the shown zones, one can see that the previous GaN crystals become dominated by the presence of gallium, nitrogen and silicon, while the previous silicon substrate becomes dominated by

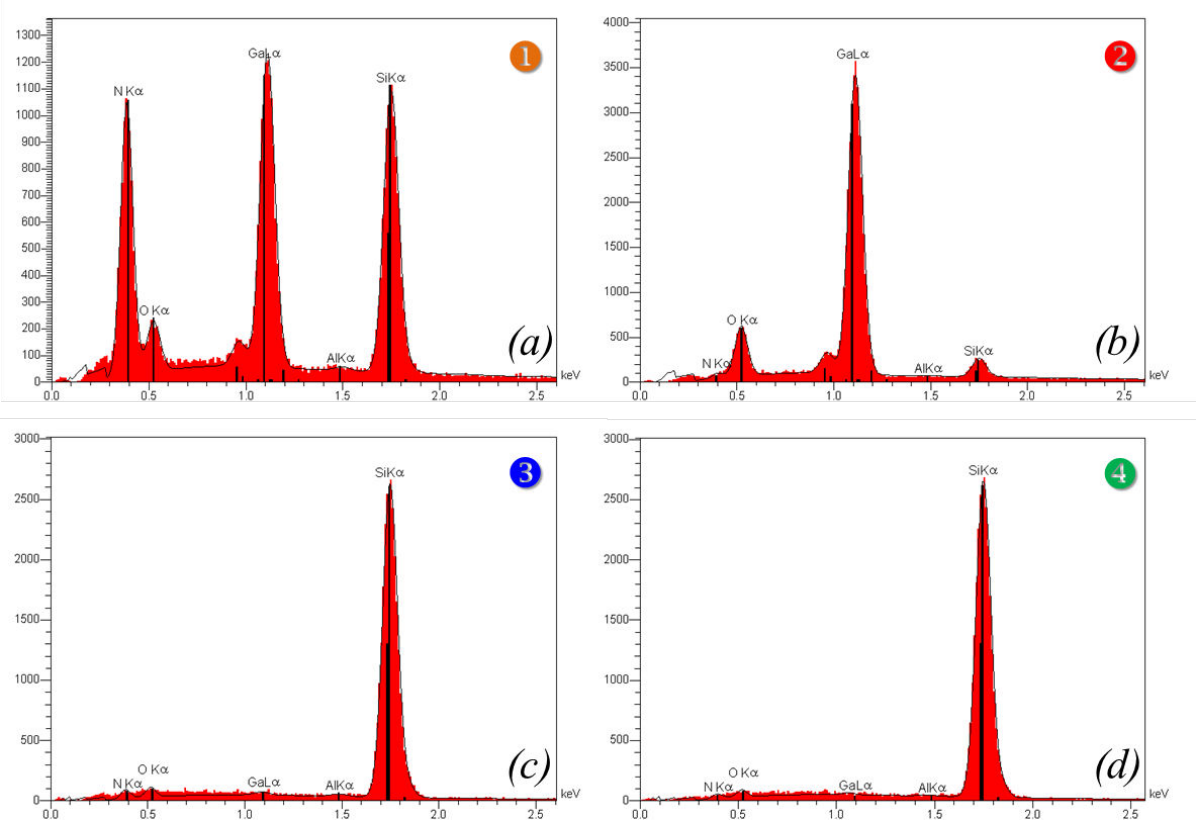

Figure 5.8 – EDX spectra of each of the four zones indicated in figure 5.7. The acquisition time is identical for all the spectra.

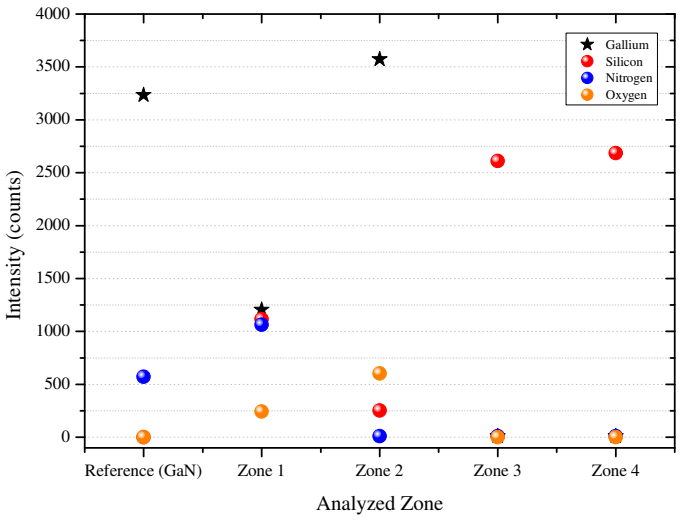

Figure 5.9 – Plot indicating the detected intensity counts for gallium, silicon, nitrogen and oxygen as a function of the GaN reference and each of the four zones shown in figure 5.7. The acquisition time and conditions is identical for all the spectra including the reference.

almost the sole presence of gallium. Moreover, only gallium being found in zone 2 indicates that nitrogen does not diffuse into the silicon substrate, only gallium does, which may explain the increase in the nitrogen EDX peak intensity and decrease of the gallium one in zone 1 (figure 5.8 (a)). This may also suggest that meltback etching induces localized inter-diffusion between gallium and silicon via the nucleation facet, where the inclined epitaxy of AlN and GaN initially takes place. The ASM Alloy Phase Diagram Database [180] shows that mutual solubility for the silicon-gallium-nitrogen system is unlikely, and only GaN and Si_3N_4 compounds can form, while no ternary compounds have been found.

High damage As meltback etching spreads further, the gallium found in the silicon substrate gradually vanishes. This creates large hollow voids in the substrate as shown in figure 5.10 ((a) secondary and (b) backscattered electrons). The size of these voids is sensitive to the growth temperature and duration, where longer growth runs and higher growth temperatures have shown to lead to larger voids [181]. Gallium has also been found to be present in the bottom of these voids. The EDX spectra acquired in these zones are comparable to the one shown in zone 2 (figure 5.7 and figure 5.8 (b)). This suggests that the gallium diffusing into the silicon substrate at intermediate stages, eventually evaporates as meltback etching further expands. Remarkably, the voids created in the substrate have systematically shown to shape-up in quasi-pyramidal forms that are limited by the boundaries of the Si {111} planes. This can be clearly seen in figure 5.10 where the sides of the triangular hollows are almost perfectly aligned parallel to the patterned Si (111) V-grooves. Similar behavior of meltback etching creating voids limited by Si (111) has also been observed for the growth of GaP-on-Si (100) [163] and GaN-on-Si (100) by MOVPE [182]. This may be attributed to the larger stability of the Si {111} planes compared to other silicon planes [183], and may suggest that the meltback reaction proceeds in a similar manner as etching of silicon with wet anisotropic etchants like KOH [184] and TMAH [185].

The surfaces of highly damaged samples display regions with two different compositions, as shown in the plane-view SEM images in figure 5.11. As the EDX results indicate, the first damaged surface, shown in figure 5.11 (a), consists of silicon, gallium and nitrogen. The detected peak intensities of these regions are comparable to the ones seen in Zone 1, as shown in figure 5.7. Another identified site with deposited artifacts, shown in 5.11 (b) consisted of only gallium as indicated by EDX. It is likely that this region forms at an advanced stage of meltback etching, where growth is continued on damaged surfaces. This results in growth precursors accumulating in parasitic bundles due to the lack of available nucleation sites.

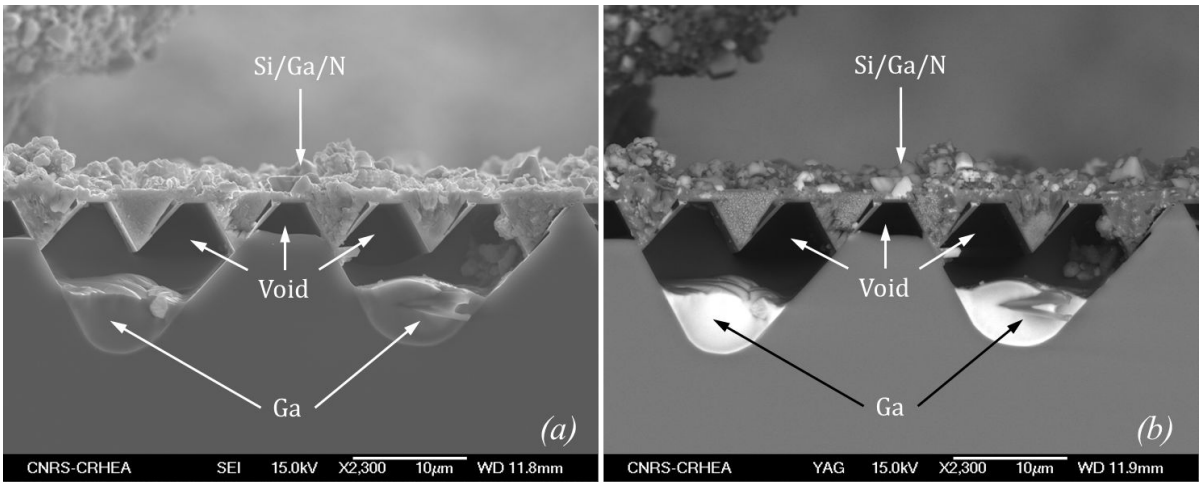

Figure 5.10 – Cross sectional SEM images (a) secondary electrons and (b) backscattered electrons of layers in the last stages of meltback etching where deep voids are observed.

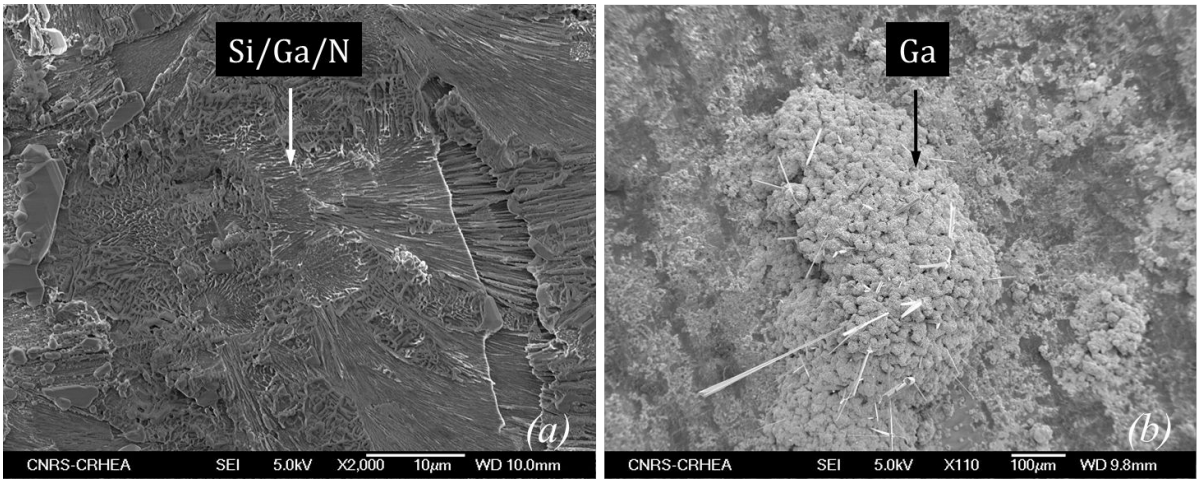

Figure 5.11 – Plane-view SEM images of the two observed meltback etching regions as detected by EDX: (a) when silicon was dominant and (b) when only gallium was found.

Figure 5.12 shows a plane-view SEM image of a partially meltback etched surface and its corresponding panchromatic CL image. As expected, damaged surfaces appear black due to the dominating presence of silicon, and luminescence is only collected from the regions with undamaged GaN.

5.4 Suppressing meltback etching

In principle AlN buffer layers providing a full coverage of the silicon are the key to avoid meltback etching under typical MOVPE growth conditions. However, AlN alone is often insufficient for this purpose, especially on patterned substrates. Alternative approaches must therefore be addressed in order to completely suppress meltback etching.

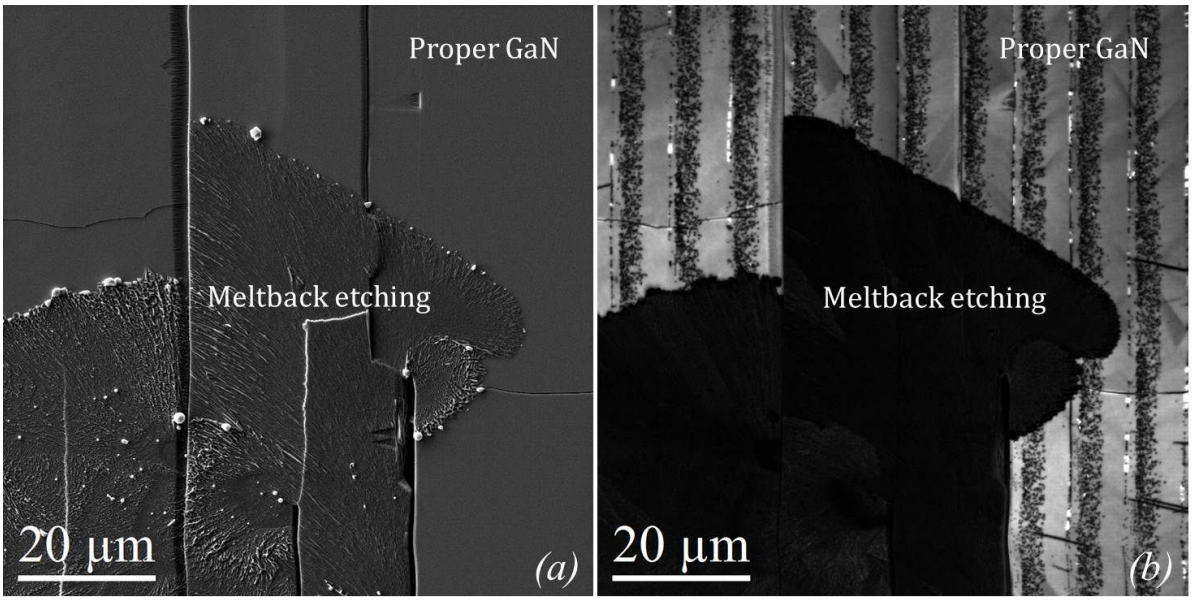

Figure 5.12 – (a) Plane view SEM image of a partially meltback etched zone and its (b) corresponding panchromatic CL image acquired at 77 K.

Indeed, claims to suppress meltback etching for semipolar GaN on patterned silicon just by changing the structure of the pattern from parallel bands to squared window patterns have been reported [186]. While this may be true, given the reduced surface area of the substrate exposed to the precursors, no explanation or images were provided to support this claim [186]. In the following sections, the experimented routes studied in the current work to suppress meltback etching will be presented. The advantages and disadvantages of each investigated approach will be described.

5.4.1 Growth of AlN before the inclined dielectric deposition

As described in section 5.2.2, one of the proposed origins of meltback etching in our case was the overhanging SiO_2 caps that prevented the complete coverage of the silicon nucleation facets with AlN.

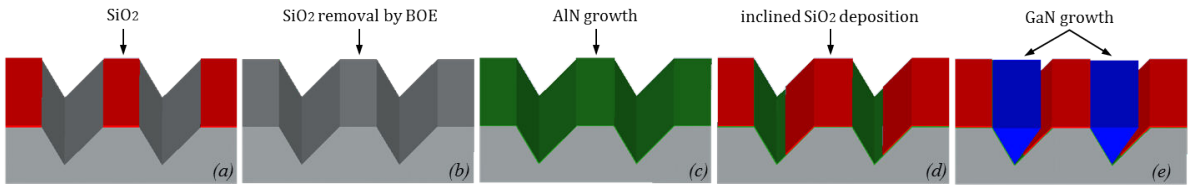

Figure 5.13 – Schematic illustration of the adapted process to eliminate the overhanging caps: (a) KOH etching of V-grooves after the classical photolithography step, (b) removal of the SiO_2 mask using BOE, (c) growth of AlN on the whole surface, (d) inclined deposition of SiO_2 to mask one inclined (111) facet and the topmost band and (e) the growth of GaN.

In order to investigate this hypothesis, a fabrication approach that eliminates the over-hanging caps was tested, and is illustrated in figure 5.13. Unlike the classical fabrication steps (see section 3.1), after the KOH etching that forms the V-grooves, the substrate was immersed in BOE, which removes the deposited SiO_2 mask that initially defines the stripes and that forms the over-hanging caps. 100 nm of AlN was then epitaxially grown by MOVPE at 1250°C on the whole substrate (*i.e.* both Si {111} inclined facets and the topmost horizontal surface). The final step was the inclined IBS deposition to masks one facet (It is to be noted here that the inclined IBS deposition masks both, the inclined Si(111) facet and the topmost horizontal silicon surface). The sample was then reloaded in the MOVPE reactor, and 50 nm of AlN was grown before the subsequent growth of GaN, as shown in figure 5.14 (a).

In principle, this approach enhances the silicon surface coverage with AlN (and SiO_2). However, no difference was remarked, and the destroyed surface areas were comparable to those observed when the classical technique was adapted, as shown in figure 5.14 (b). If a perfect coverage is assumed when using this approach, this indicates that the suspected over-hanging SiO_2 caps are not the only reason causing meltback etching, and suggests that different factors contribute to inducing this effect. Therefore, the imperfect coverage of silicon that causes meltback etching may be a result of low-quality AlN layers, or fabrication residuals (*i.e.* nano/micro particles, dust, etc.) on the growth facets that prevent the proper nucleation of AlN.

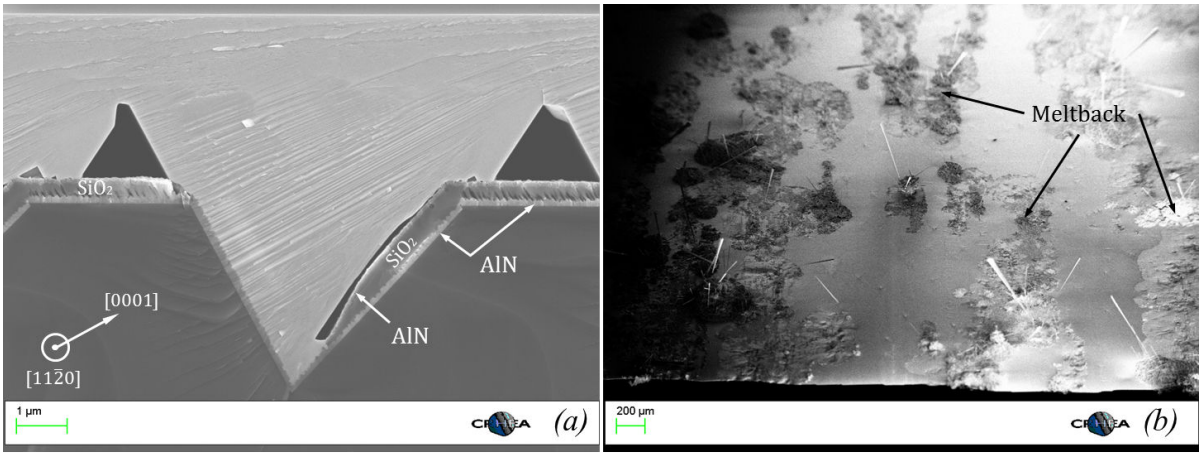

Figure 5.14 – (a) Cross sectional SEM image showing the SiO_2 layer sandwiched between two AlN layers and (b) a bird's eye view SEM image showing the result meltback etching after the GaN growth.

5.4.2 AlN growth temperature

Ravash *et al.* [150] address the meltback etching problem by using a LT-AlN layer prior to the growth of GaN. Therefore, in order to gain insight on how the growth temperature of the AlN buffer layer influences the presence of meltback etching on the subsequent GaN surfaces, the effect of the AlN

buffer layer growth temperature has been investigated on four samples. The layer thickness was fixed to 150 nm and the tested growth temperatures were: 1100°*C*, 1150°*C*, 1250°*C* and 1350°*C*. The subsequent growth of GaN was then done on all four samples using the same growth parameters (but not in the same growth run).

The samples with AlN buffer layers grown at 1250°*C* and 1350°*C* resulted in good structural quality GaN layers having smooth surfaces and well-defined facets. However, meltback etching was observed on both surfaces, and more pronounced on the sample grown at 1350°*C*. On the other hand, samples with an AlN buffer layer grown at 1100°*C* and 1150°*C* resulted in a poor morphology of the subsequent GaN layer translated into rough surfaces and irregular nucleation, as shown in figure 5.15. Moreover, symmetrical XRD rocking curves corresponding to the GaN layers grown on the LT-AlN, exhibited an average FWHM of 2000 arcsec (1100°*C*) and 1900 arcsec (1150°*C*), which is higher by a factor two from the FWHM observed for GaN layers grown on high-temperature AlN buffers.

Remarkably however, these layers had no meltback etching, which suggests an improved coverage of the silicon surface with LT-AlN. This may be due to the reduced adatom diffusion length at low growth temperatures, which increases the sticking of Al and results in adatoms nucleating at random sites. This random nucleation can arbitrarily improve the silicon coverage with AlN and therefore reduce meltback etching. Furthermore, the gradual temperature ramp for the growth of AlN from low temperatures (*i.e.* 1100°*C*, 1150°*C*) to high temperatures (*i.e.* 1250°*C*) has been also investigated. Similarly, the subsequent GaN layers grown thereon, exhibited a surface free of meltback etching, but again at the expense of a poor structural quality and irregular morphology. These results indicate that the AlN buffer layer growth temperature influences the presence of meltback etching, but by compromising the GaN layer quality. Similar results have been reported for GaN grown on Si (111) by MOVPE by varying AlN buffer layer temperatures [187].

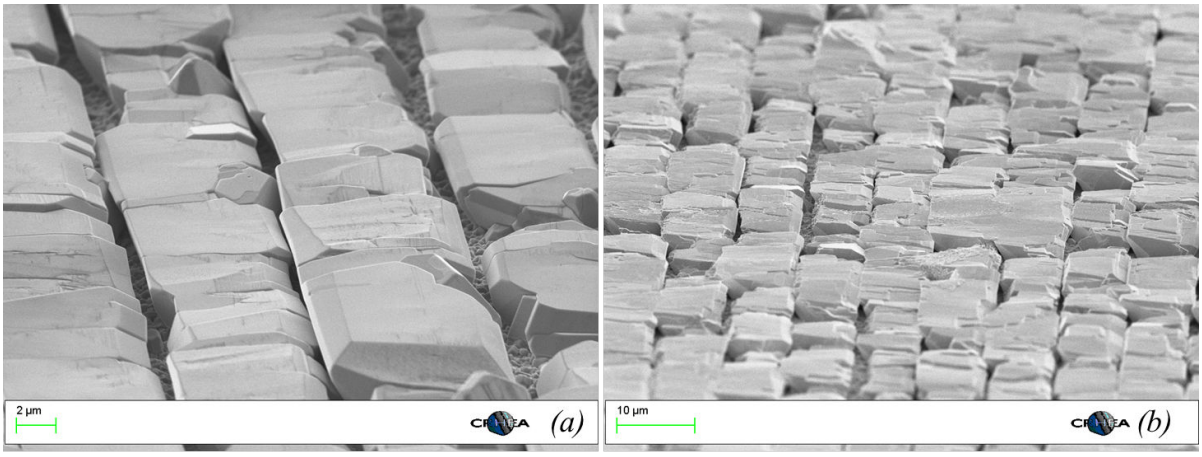

Figure 5.15 – (a) Bird's eye view SEM images showing the GaN bands on AlN buffer layers grown at (a) 1100°*C and (b)* 1150°*C*.

5.4.3 Carrier gas effect: N_2/H_2 ratio

In this section, the effect of the N_2/H_2 ratio has been investigated by using N_2 and H_2 together in different input mole ratios in order to examine the impact on the growth of GaN and the influence on meltback etching [2]. Six patterned substrates were investigated. A 150 nm thick AlN buffer layer grown at 1250°C was applied to all six samples alike. The subsequent GaN growth was performed on the samples, each with a different N_2/H_2 ratio: 100:0, 90:10, 70:30, 50:50, 30:70 and 10:90, while the total flow was fixed to 10 slm. The used GaN growth conditions were: T = 1210°C; V/III ratio = 220; P = 300 mbar; t = 2500 s.

By observing the growth results displayed in figure 5.16, the first striking issue is the excessive polycrystalline GaN deposition on the mask as the fraction of N_2 increases with respect to H_2. This may be attributed to the suggestion that samples grown under N_2 carrier gas typically exhibit low diffusion velocities of MO compounds and lower adsorbate surface mobility [188]. The parasitic deposition gradually decreases upon increasing the H_2 fraction in the total carrier gas flow until it almost disappears when 10% N_2 is used.

Furthermore, with these proportions (*i.e.* 10% N_2 and 90% H_2), significantly slower growth rates have been observed in comparison to growths performed under pure H_2 using the same growth parameters. In the +c-direction, the growth rate decreases by 54.3% from 0.138 μm/min to 0.063 μm/min . In the direction normal to the surface (*i.e.* [10$\bar{1}$1] direction) the growth rate decreases by 41.6%, from 0.024 μm/min to 0.014 μm/min.

This decrease in the growth rate, results in an increase of the density of defects in the grown layers, essentially BSFs. Besides the increase in the BSF density when nitrogen is used, CL has shown that BSFs are randomly distributed along the stripes, as shown in figure 5.17. This randomness is contrary to what has been discussed in section 3.2.2.2, where BSFs were spatially confined and only created in the -c-wings when pure hydrogen is used as carrier gas. This randomness impedes controlling the growth process for potential defect blocking strategies and is therefore unfavorable. The excessive formation of BSFs may be associated to the relatively slow growth rates and the lower surface mobility of adsorbates compared to growths done under pure H_2. This increases the probability of growth errors where adatoms have the tendency to bond to wrong sites [32] and thus increase the likelihood of creating BSFs. Moreover, slow growth rates (*i.e.* rates far from optimal growth conditions) may also result in higher incorporation of impurities, which may further contribute to increasing the probability of forming BSFs.

[2] All the discussed samples in the previous chapters have been grown under pure H_2 carrier gas to transport precursors to the reactor chamber.

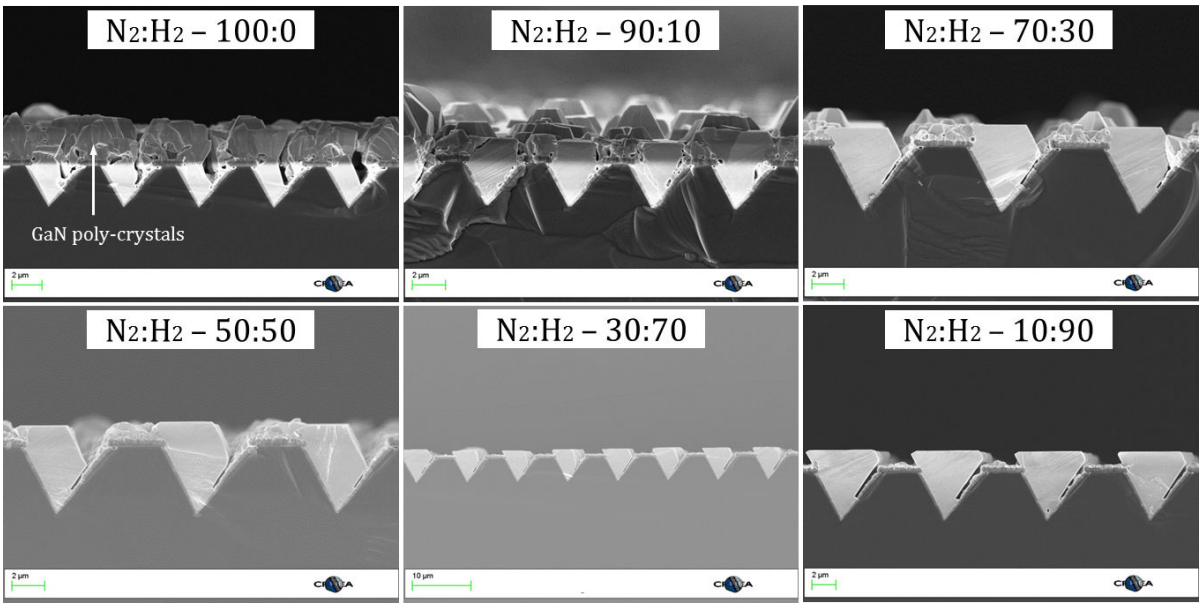

Figure 5.16 – Effect of carrier gas proportions between Hydrogen and Nitrogen on the progress of the growth (The SEM images do not have the same scale).

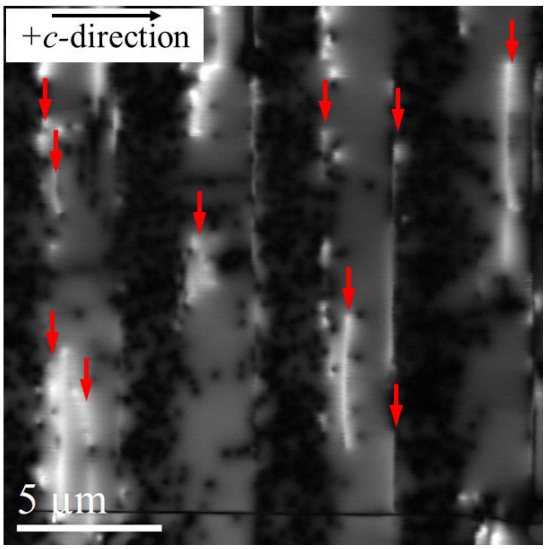

Figure 5.17 – Panchromatic CL image acquired at 77 K for a coalesced GaN layer grown with 10% N_2 and 90% H_2. BSFs show a random distribution and appear as white bright luminescent white lines indicated by the red arrows.

On the other hand, if the morphology and the optical quality of the layers grown with 10% N_2 and 90% H_2 are disregarded, the most interesting characteristic of using a fraction of N_2 in the carrier gas is the complete elimination of meltback etching, which is shown in figure 5.18. This has been also observed for any mole fraction combination between hydrogen and nitrogen. However, the mechanism by which meltback etching is eliminated upon changing the input mole fraction of the carrier gas is not well understood.

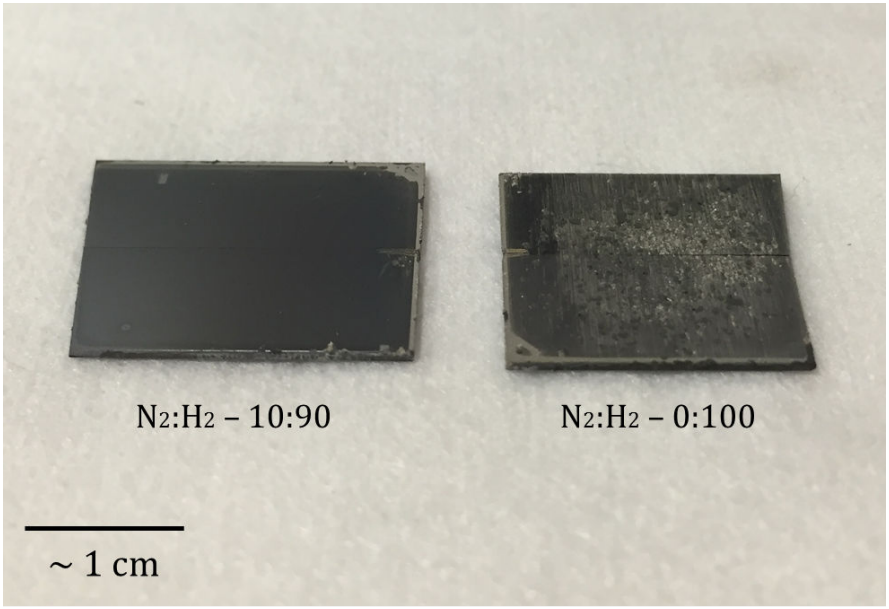

Figure 5.18 – Photo of the sample grown with a fraction of N_2 in the carrier gas (left) showing no meltback etching, and sample grown with pure H_2 carrier gas (right) showing the damaged surface. Except for the carrier gas, both samples were grown under identical growth conditions and for the same duration.

5.5 Conclusion

In this chapter meltback etching was introduced and its possible origins in the studied samples have been discussed. Damaged samples were characterized optically and chemically, and a model on the evolving stages of meltback etching was proposed.

The objective of this PhD was not to study meltback etching, but to eliminate its occurrence that damages the grown layers, so different experimented routes attempting to suppress meltback etching were presented. The results indicated that growth conditions have a significant effect on promoting or inhibiting meltback etching. Growing LT-AlN buffer layer or adding a fraction of N_2 to the carrier gas composition during the GaN growth have shown to stop meltback etching from occurring. Both processes however, under the growth conditions used in our case, compromise the layer quality either by creating a very poor morphology or by drastically increasing the density of structural defects.

Meltback etching therefore remains an important problem especially on patterned substrates, and its presence not only damages the surfaces, but also reduces the frame of manipulating growth conditions and limits the possibility of growing thick layers. Further development aiming to achieve meltback etching-free layers without compromising the layer quality are therefore necessary.

6 General Conclusions and Perspectives

This PhD was set out to investigate the MOVPE growth of semipolar GaN on patterned silicon substrates and to reduce the density of structural defects present in the layers. The presented work has been carried out between two labs in the framework of the Labex-GaNeX network and consisted of two stages: First, the silicon substrate fabrication, which was realized in the cleanrooms of CEA - LETI (Grenoble, France) and the subsequent MOVPE growth and characterization that took place in CNRS - CRHEA (Valbonne, France).

The first studied orientation was $(10\bar{1}1)$ GaN grown on patterned silicon (100)7°off. Adjacent pyramidal bands were brought to coalescence using a classical single-step growth approach. Structural and optical characterization have indicated the bending of threading dislocations and the formation of stacking faults in the *-c*-wings resulting in their concentration in stripe-like regions, and thus an elevated overall density of structural defects.

The second studied orientation was $(20\bar{2}1)$ GaN, which has been demonstrated for the first time in this PhD, based on silicon (114)1°off. The coalesced layers showed a micro-facetted surface dominated by more energetically stable crystallographic planes, unlike the coalesced $(10\bar{1}1)$ surface that exhibited a smoother morphology. Structural and optical characterization indicated a similar defect configuration to the one observed in the $(10\bar{1}1)$ layers. The attained structural and optical quality of the $(20\bar{2}1)$ GaN grown on silicon is comparable to the same orientation grown on sapphire and exhibits similar surface characteristics.

Since the primary objective is reducing the density of the present defects, a method comprising a surface treatment prior to the growth of GaN was introduced for the $(10\bar{1}1)$ orientation. The results indicated that the surface treatment triggers the formation of a thin layer situated in the semipolar GaN plane parallel to the substrate surface. This layer, that was assigned the name *defect blocking layer*, serves to efficiently block threading dislocations and to significantly reduce the presence of stacking faults. This was confirmed by detailed structural and optical characterization, and a hypoth-

esis explaining the defect blocking mechanism was proposed. Based on the presented hypothesis, and to simplify the aforementioned approach, an SiN layer was deposited in-situ on an incomplete GaN pyramidal band, whose geometry consisted of a topmost semipolar surface and an inclined polar one. This SiN layer has shown to induce a change in the growth mode, where the subsequently grown GaN either exclusively nucleates on the partially exposed inclined polar surface or at the intersection between the two facets. The growth then proceeds laterally in the direction perpendicular to the bands, extending above the SiN-covered semipolar surface. The structural and optical characterization of the laterally grown crystals indicated a high-quality material almost free of any defect.

These outcomes, albeit preliminary, point out a promising and efficient defect blocking design for the growth of high-quality semipolar GaN when the inclined growth on patterned substrates is adopted. It may be also assumed that this approach can be applicable to other semipolar orientations grown on silicon and sapphire substrates alike.

However, despite the presented results, a surface deteriorating obstacle known as meltback etching was encountered throughout the whole course of this work. Solutions have indeed been demonstrated in order to eliminate this effect from our patterned substrates, but the structural GaN quality had to be compromised. It is important to point out that the presence of meltback etching does not only hinder any device from being demonstrated. In fact, meltback etching also restrains the range in which growth conditions can be varied, in addition to limiting the possibility of increasing layer thicknesses that are often necessary for defect filtering.

From a broader perspective, indeed, the economic argument aiming at realizing low-cost optoelectronic devices is often used to justify the usage of silicon as a substrate for GaN. However, the inherent difficulties coupled with the usage of silicon impose the necessity of spending more efforts to eventually reach the same results reported, or that can be reported, on sapphire substrates. Additionally, and by seeing the significant decline of sapphire prices over the last few years, the question on whether or not adopting silicon does really present a profitable advantage remains a question to be answered.

Conclusion générale et perspectives

Cette thèse avait pour but d'étudier la croissance MOVPE du GaN semi-polaire sur des substrats de silicium structuré et de réduire la densité des défauts structuraux dans ces couches. Le travail présenté a été effectué au sein de deux laboratoires dans le cadre du projet Labex-GaNeX et consiste en deux parties: la fabrication des substrats de silicium, réalisée dans les salles blanches du CEA-LETI (Grenoble, France) etla croissance MOVPE ainsi que ses caractérisations, menées au CNRS-CRHEA (Valbonne, France).

Nous avons tout d'abord étudié les propriétés du GaN $(10\bar{1}1)$ épitaxié sur des substrats de silicium Si(100) désorienté de 7° et structuré. Les bandes pyramidales adjacentes ont été amenées à se coalescer en utilisant une étape de croissance classique. Les caractérisations structurales et optiques indiquent la flexion des défauts émergents et la formation de fautes d'empilement dans les ailes orientées c amenant à leur concentration dans des zones de bande, et ainsi à une densité de défauts structuraux élevés.

La deuxième orientation étudiée fut le GaN $(20\bar{2}1)$ dont la réalisation a été démontrée pour la première fois au cours de cette thèse. La croissance du GaN $(20\bar{2}1)$ a été effectuée sur du silicium Si(114) désorienté de 1°. Les couches coalescées présentent une surface micro-facettée dominée par les plans cristallographique les plus stables énergétiquement, contrairement à la surface $(10\bar{1}1)$ ayant une surface plus lisse. Les caractérisations structurales et optiques indiquent une configuration de défauts similaire a celle observée dans les couches $(10\bar{1}1)$. Les qualités structurale et optique du GaN $(20\bar{2}1)$ obtenu est comparable au GaN ayant la même orientation mais épitaxié sur saphir et présente également une morphologie de surface similaire.

Puisque l'objectif principal était de réduire la densité de défauts présents, une méthode comprenant un traitement de surface avant la croissance du GaN a été introduite pour l'orientation $(10\bar{1}1)$. Les résultats indiquent que la surface déclenche la formation d'une couche fine situé dans le plan du GaN semi-polaire parallèle à la surface du substrat. Cette couche, nommée "couche de blocage de défauts", sert à bloquer efficacement les dislocations et à réduire significativement la présence des fautes d'empilements. Ceci a été confirmé par une étude structurale et optique détaillée. Nous

proposons de plus une hypothèse pour expliquer le mécanisme de blocage des défauts. Afin de simplifier l'approche mentionnée précédemment et en prenant en compte notre hypothèse, nous avons adapter notre procédure. Une couche de SiN a ainsi été déposée in-situ sur des bandes pyramidales incomplètes de GaN dont la géométrie est la suivante: la surface plane du dessus est semi-polaire tandis que les surfaces inclinées sont polaires. La couche de SiN se dépose de manière sélective sur les facettes: les surfaces semi-polaires défectueuses sont complètement couvertes tandis que les surfaces polaires inclinées ne le sont que partiellement. Cette sélectivité montre qu'un changement du mode de croissance se produit. La nucléation du GaN épitaxié après dépôt du SiN se produit exclusivement sur la surface polaire incliné partiellement couverte. La croissance continue ensuite latéralement dans la direction perpendiculaire aux bandes, s'étendant au dessus de la surface semi-polaire couverte par le SiN. Les caractérisations structurales et optiques de la couche épitaxiée latéralement indiquent une haute qualité cristalline du matériau, presque sans aucun défaut.

Ces résultats, bien que préliminaires, démontrent une méthode efficace et prometteuse de blocage de défauts permettant la croissance d'une couche de GaN semi-polaire de haute qualité dès lors que la croissance inclinée sur des substrats structurés est adaptée. On peut également faire l'hypothèse que cette approche est applicable pour d'autres orientations semi-polaires lors de l'épitaxie sur des substrats silicium ou même saphir.

Malgré les résultats présentés, nous avons rencontré un obstacle. Il s'agit d'une forme de détérioration de la surface connue sous le nom de « gravure face arrière ». Des solutions ont été étudiées afin d'éliminer cet effet indésirable mais de manière générale, un compromis avec la qualité structurale du GaN est à faire. Il est important de noter que l'occurrence de la gravure face arrière entrave non seulement la réalisation d'un dispositif complet mais limite aussi le choix des conditions de croissance ainsi que l'épaisseur de la couche, deux facteurs qu'il est nécessaire d'ajuster pour le filtrage des défauts.

De manière plus générale, on évoque souvent un argument économique pour justifier la réalisation de dispositifs optoélectroniques sur silicium. Cependant, les difficultés inhérentes à l'utilisation de substrats silicium rendent nécessaires de fournir d'intenses efforts afin d'atteindre les résultats déjà obtenus sur substrats saphir. En outre, si l'on considère le déclin du prix des substrats de saphir ces dernières années, on peut se demander si l'adoption des substrats de silicium présente encore un réel avantage.

A Substrate Fabrication Details

The detailed substrate fabrication steps will be listed based on the developed process in the CEA - LETI cleanrooms.

1. The first step of the process involves substrate cleaning. In this work non-standard orientations were used, so substrate providers/manufacturers may deliver wafers with elevated levels of contamination (as seen by TXRF analysis in our case). Therefore, an organic/metallic chemical decontamination prior to fabrication is strongly advised as contaminated substrates could cause problems in later processing steps especially when chemical usage is involved.
   (a) Clean wafers with H_2SO_4 (98%):H_2O_2 (30%) (3:1) at 100°C for 15 minutes. Thin substrates should be immersed slowly to avoid thermal shock that may crack the wafer. Then, rinse with de-ionized water
   (b) Immerse wafers in BOE for 10 seconds, then rinse with de-ionized water.
2. Deposit a 100 nm thick SiO_2 layer by dry thermal oxidation (i.e. in pure oxygen gas atmosphere) using a Tempress6 oven at 1000°C.
3. Photo-lithography:
   (a) Bake substrate for 3 minutes at 115°C. This step permits the evaporation of any solvents that may be on the surface that prevent resist adhesion.
   (b) Deposit HMDS using a vapor oven at 90°C for 90 seconds.
   (c) Deposit S1818 resist using the Delta 80 GYRSET SUSS-MicroTec spin coater. For square substrates (36 mm × 36 mm) use 450 μl of resist and spin at 3000 rpm for 10 seconds. These parameters should result in a homogeneous resist spreading with a thickness of ~ 1.8 μm.
   (d) Bake substrate at 90°C for 60 seconds for resist solidification and adherence.

(e) With the GROOV striped mask (that's a custom name we gave it), expose the wafer with an energy of 140 mJ using a contact-less Micralign BetaSquared lithography system. Stripe alignment depends on each orientation. This is explained in the substrate fabrication section of each chapter.

(f) Develop the exposed wafer for 60 seconds using the M319 developer. Rinse every 15 seconds.

4. Apply a flash oxygen plasma for 30 seconds in the NE860 reactor. This step ensures that resist residuals from the developed areas are cleaned off, since any remaining resist residuals can block subsequent etching.

5. To create the openings, etch the exposed SiO_2 in the NE860 reactor using ICP mode with CHF_3:O_2 (50:1) ions to bombard the surface till the silicon is exposed. This recipe yields an etching rate of 100 nm/min. This step is critical since an extended etching duration can mask the silicon with a layer, thought to be a polymer. It is also very important to make sure that the substrate is in proper thermal contact with the susceptor, since temperature variations may influence homogeneity. Plasma etching was preferred over wet BOE etching for its enhanced reproduciblity. Wet etching may be another option, however, wet chemical usage may introduce lateral etching beneath the photo-resist resulting in heterogeneous dimension imperfections which will be pronounced in later processing steps.

6. Strip the resist using an acetone pressure gun. Then immerse the substrate in acetone for 10 minutes in an ultra-sound environment, and rinse with de-ionized water.

7. To etch the inclined facets, prepare a 10 wt% KOH solution by diluting solid pellets in de-ionized water, and heat up to $37°C$. These values were optimized for the structures used in this work, and have shown to yield the smoothest etched surfaces. Data on the etching rates for all three studied orientations are given in Appendix B. Etching duration depends on the desired depth and facet size. After etching, rinse samples with de-ionized water.

8. After KOH etching, small crystallites will often be observed at the surface [189] as shown in figure A.1 (a). To remove them, immerse the wafer in a 38 % HCl solution at room temperature and keep it overnight. The crystallites will then disappear as shown in figure A.1 (b).

9. Mask one of the inclined facets using the Oxford Ionfab300+ IBS tool. This machine is designed to process 200 mm wafers. Since in our case the substrates were in 36 mm × 36 mm square forms, sticking the sample on a 200 mm wafer dummy was necessary. Tilt the wafer at a 15° angle, turn off oscillations and rotation, and deposit 50 nm of SiO_2 (about 30 minutes). Ensure that the wafer is oriented correctly with respect to the ion beam. An illustration of the IBS mode of operation is shown in figure A.2.

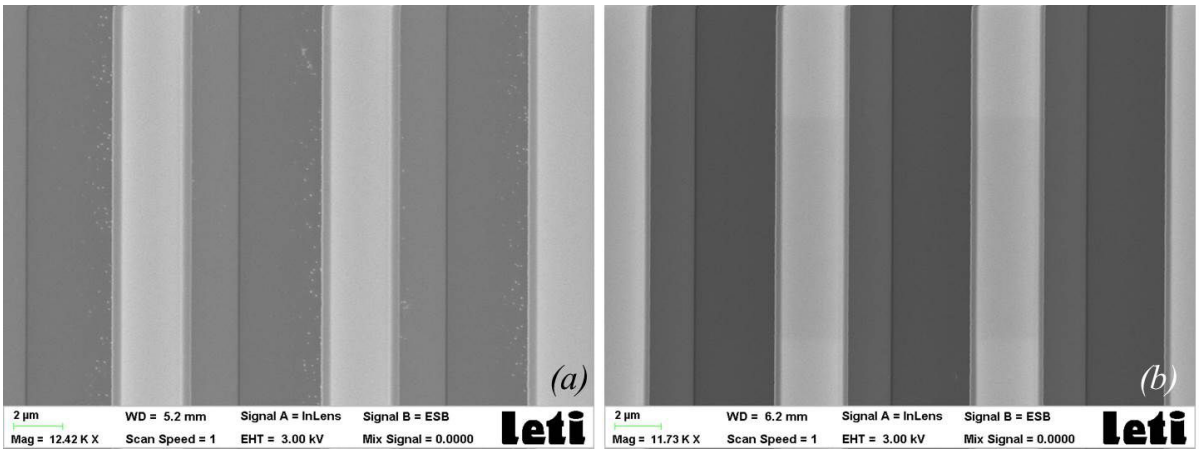

Figure A.1 – Plane-view SEM images of the etched V-grooves with KOH (a) before and (b) after the cleaning with HCl.

10. After the inclined deposition, a very thin layer of SiO_2 will also deposit on the hidden facet where growth will later take place. For that, immerse the wafer in BOE for 10 seconds.

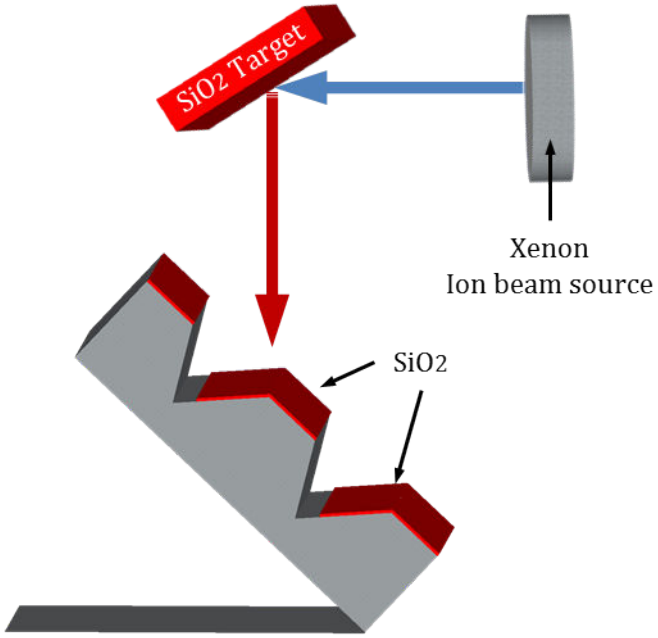

Figure A.2 – Schematic display of the IBS operating mode showing the ion beam source sputtering the SiO_2 target material, which then coats the substrate tilted towards the target with the sputtered SiO_2.

Confidential	CEA - LETI CNRS - CRHEA	GaNex	N° Experiment Plan - GaN Semipolar LEDs
Number of substrates			Comments
Nature	(100) 7° off		
Size	36mm x 36mm		
Step	**Recipe**	**Equipment**	**Comments**
Substrate Cleaning			
Cleaning contaminants	Piranha	Acid Workbench	H2SO4:H2O2 (3:1) for 15 minutes
Cleaning contaminants	BOE	Acid Workbench	BOE for 10 seconds
Hard Mask Deposition			
SiO_2	Dry Thermal Oxide	Tempress 6	100 nm thickness
Verify thickness		Filmetrics	Important for subsequent etching precision
Photolithography			
Pre-resist bake	115°C - 3 minutes	Delta80	To evaporate solvants that may affect resist adhesion
HMDS	90°C - 90 seconds	HMDS vapor	
Resist	450µl - 3000rpm - 10s	Delta80	Result thickness = 1.8 µm
Soft Bake	1 minute - 90°C	Delta80	To solidify the resist
Exposure	140mJ - BBB - Mask: GROOV	BetaSquared	Align parallel to the flat (tilt flat to the right)
Develop	1 minute w/ MF319	Dev Workbench	Rinse with developer at 45s - 30s - 15s
Resist residues cleaning			
Resist clean	FLASH - 2 minutes	NE860	Necessary to remove resist residuals that may block subsequent etching
Mask Openings			
Oxide Etching	SiO_2-A - 60 seconds	NE860	CHF3:O2 (50:1) - Etching rate = 100 nm/min
Resist Stripping			
Acetone pressure gun	10 seconds on vacuum holder	Solvent Workbench	
Acetone	10 minutes - Ultrasound Bath	Solvent Workbench	
Isopropanol and de-ionized water rinse	Rinse	Solvent Workbench	
Verify mask widths and openings	Optical Microscope	Olympus	
V-Groove Etching			
V- groove KOH etching	KOH: 37°C - 10 wt%	KOH Workbench	
Rinse	2 minutes	KOH Workbench	
Post-KOH Cleaning			
Removal of crystallites from surface	HCl solution - 15 hours	Acid Workbench	Keep sample in HCl overnight at room temperature
Observation/Imaging	SEM	Zeiss Ultra 55	Verify openings are correct. Verify surface decorations from KOH are gone.
Preparation for Angular Deposition			
Patch	Patch sample to 200mm dummy	Patch Workbench	Direction: rotate wafer to the right - very important to align accurately
Angular Deposition			
1 facet masking	15° - 0rpm - 30 minutes	Oxford IonFab 300+	Angle and deposition time may vary depending on the orientation and facet size.
Final Cleaning			
Diffused oxide removal from good facet	10 seconds Flash BOE	Acid Workbench	To remove any possibler deposition from the nucleation facet

Figure A.3 – Process steps adapted to the particular cleanroom and devices utilized.

B KOH etching rates

The KOH etching rate for each orientation as a function of KOH concentration and temperature are displayed in the following plots.

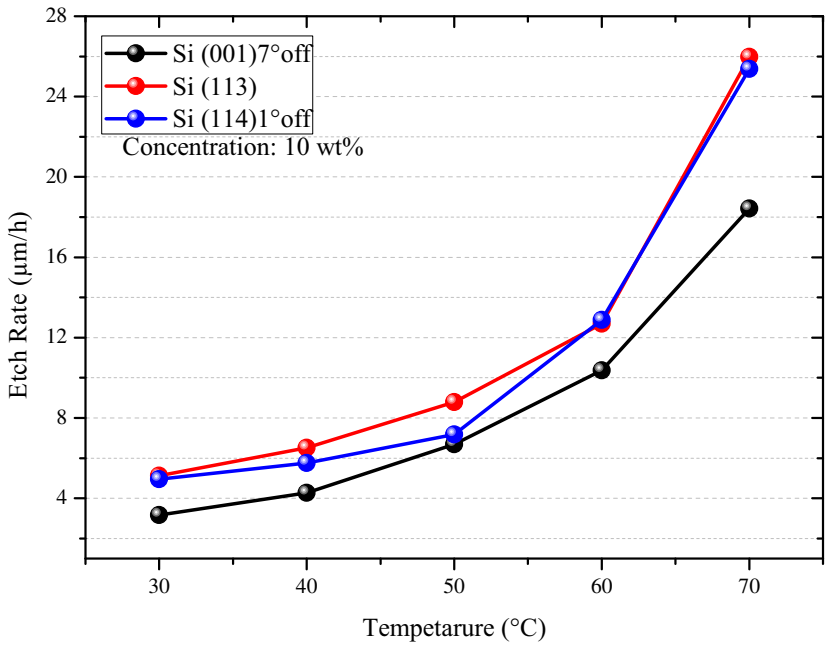

Figure B.1 – Etching rate as a function of the temperature of all studied orientations at a fixed KOH concentation.

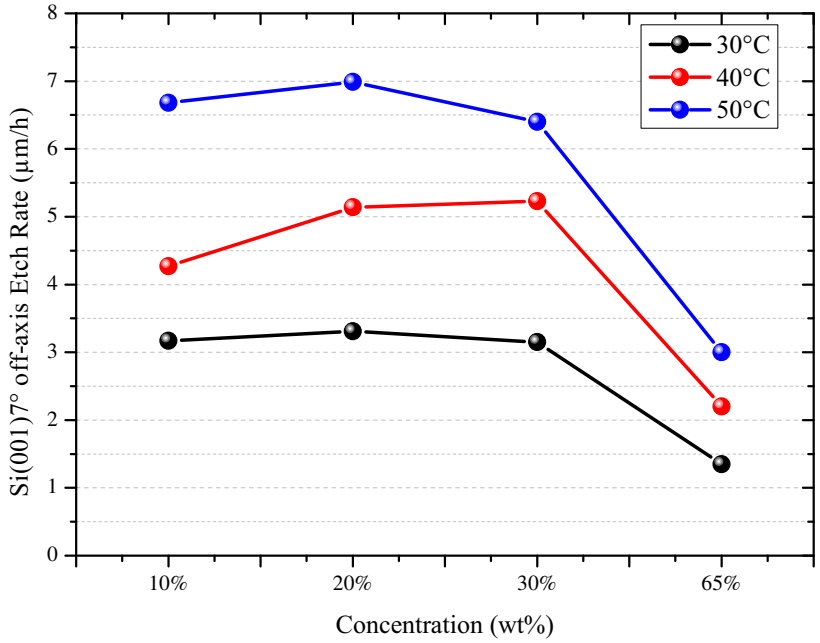

Figure B.2 – Etching rate of the Si (001)7° off as a function of the KOH concentration upon temperature variation.

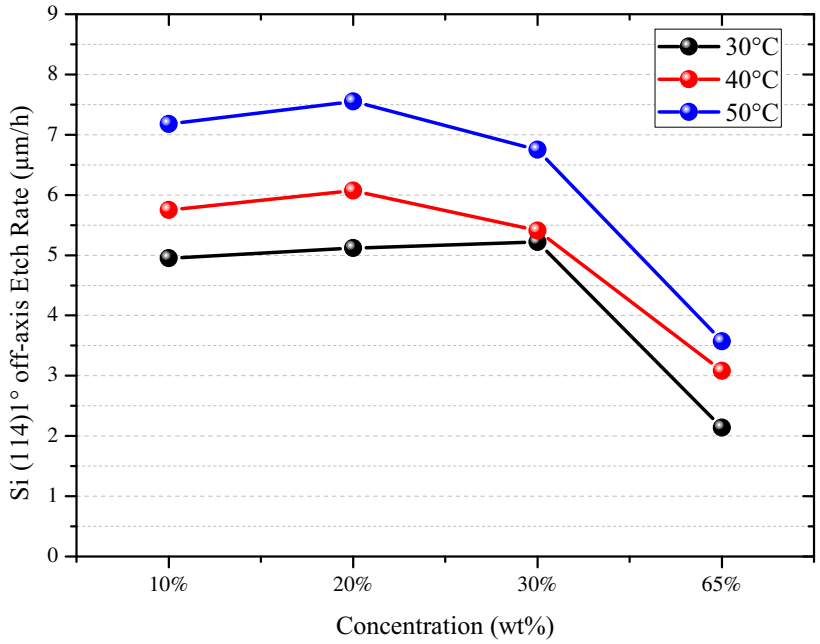

Figure B.3 – Etching rate of the Si (114)1° off as a function of the KOH concentration upon temperature variation.

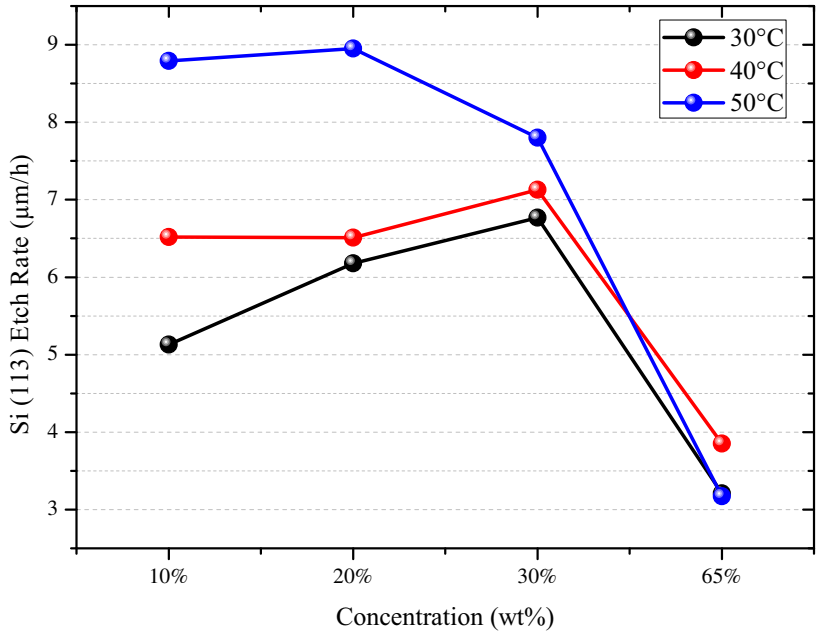

Figure B.4 – Etching rate of the Si (113) as a function of the KOH concentration upon temperature variation.

Bibliography

[1] E. F. Schubert et al. *Light emitting diodes*. Wiley Online Library (cited on pages 1, 16).

[2] H. P. Maruska et al. "The preparation and properties of Vapor-Deposited single-crystal-line GaN". *Applied Physics Letters* 15 (10) (1969), pp. 327–329. URL: http://dx.doi.org/10.1063/1.1652845 (cited on page 1).

[3] H. Amano et al. "Metalorganic vapor phase epitaxial growth of a high quality GaN film using an AlN buffer layer". *Applied Physics Letters* 48 (5) (1986), pp. 353–355. URL: http://dx.doi.org/10.1063/1.96549 (cited on page 1).

[4] H. Amano et al. "P-type conduction in Mg-doped GaN treated with low-energy electron beam irradiation (LEEBI)". *Japanese Journal of Applied Physics* 28 (12A) (1989), p. L2112. URL: http://iopscience.iop.org/article/10.1143/JJAP.28.L2112/meta (cited on page 1).

[5] S. Nakamura et al. "Thermal annealing effects on p-type Mg-doped GaN films". *Japanese Journal of Applied Physics* 31 (2B) (1992), p. L139. URL: http://iopscience.iop.org/article/10.1143/JJAP.31.L139/meta (cited on page 1).

[6] "The Nobel Prize in Physics" (2014). URL: http://www.nobelprize.org/nobel_prizes/physics/laureates/2014/ (cited on page 1).

[7] S. Nakamura et al. "High-power InGaN single-quantum-well-structure blue and violet light-emitting diodes". *Applied Physics Letters* 67 (13) (1995), pp. 1868–1870. URL: http://dx.doi.org/10.1063/1.114359 (cited on page 1).

[8] S. Nakamura et al. "Candela-class high-brightness InGaN/AlGaN double-heterostructure blue-light-emitting diodes". *Applied Physics Letters* 64 (13) (1994), pp. 1687–1689. URL: http://dx.doi.org/10.1063/1.111832 (cited on page 1).

[9] Y. Narukawa et al. "White light emitting diodes with super-high luminous efficacy". *Journal of physics D: Applied physics* 43 (35) (2010), p. 354002. URL: http://iopscience.iop.org/article/10.1088/0022-3727/43/35/354002/meta (cited on page 1).

[10] P. Waltereit et al. "Nitride semiconductors free of electrostatic fields for efficient white light-emitting diodes". *Nature* 406 (6798) (2000), pp. 865–868. URL: http://www.nature.com/nature/journal/v406/n6798/full/406865a0.html (cited on pages 1, 16, 17).

[11] A. E. Romanov et al. "Strain-induced polarization in wurtzite III-nitride semipolar layers". *Journal of Applied Physics* 100 (2) (2006), p. 023522. URL: http://scitation.aip.org/content/aip/journal/jap/100/2/10.1063/1.2218385 (cited on pages 2, 17, 18).

[12] K. Fujito et al. “High-quality nonpolar m-plane GaN substrates grown by HVPE”. *physica status solidi (a)* 205 (5) (2008), pp. 1056–1059. URL: http://onlinelibrary.wiley.com/doi/10.1002/pssa.200778709/abstract (cited on pages 2, 22).

[13] T. Hashimoto et al. “A GaN bulk crystal with improved structural quality grown by the ammonothermal method”. *Nature materials* 6 (8) (2007), pp. 568–571. URL: http://www.nature.com/nmat/journal/v6/n8/abs/nmat1955.html (cited on pages 2, 22).

[14] I Grzegory et al. “GaN substrates for molecular beam epitaxy growth of homoepitaxial structures”. *Thin Solid Films* 367 (1) (2000), pp. 281–289. URL: http://www.sciencedirect.com/science/article/pii/S0040609000006891 (cited on pages 2, 22).

[15] B. Gil. *III-nitride semiconductors and their modern devices*. Vol. 18. Oxford University Press, 2013 (cited on page 10).

[16] B Daudin et al. “Polarity determination of GaN films by ion channeling and convergent beam electron diffraction”. *Applied physics letters* 69 (17) (1996), pp. 2480–2482. URL: http://dx.doi.org/10.1063/1.117504 (cited on page 10).

[17] M Stutzmann et al. “Playing with polarity”. *physica status solidi (b)* 228 (2) (2001), pp. 505–512. URL: http://onlinelibrary.wiley.com/doi/10.1002/1521-3951(200111)228:2%3C505::AID-PSSB505%3E3.0.CO;2-U/abstract (cited on page 10).

[18] A. H. Cottrell. “Theory of crystal dislocations” (1964) (cited on page 11).

[19] M. Takeya et al. “Degradation in AlGaInN lasers”. *physica status solidi (c)* (7) (2003), pp. 2292–2295. URL: http://onlinelibrary.wiley.com/doi/10.1002/pssc.200303324/abstract (cited on page 12).

[20] C Mion et al. “Thermal conductivity, dislocation density and GaN device design”. *Superlattices and Microstructures* 40 (4) (2006), pp. 338–342. URL: http://www.sciencedirect.com/science/article/pii/S0749603606000954 (cited on page 12).

[21] K. Cheng et al. “High quality GaN grown on silicon (111) using a SixNy interlayer by metal-organic vapor phase epitaxy”. *Applied Physics Letters* 92 (19) (2008), p. 2111. URL: http://dx.doi.org/10.1063/1.2928224 (cited on page 12).

[22] X. Jinqiao et al. “Defect reduction in GaN epilayers grown by metal-organic chemical vapor deposition with in situ SiN {sub x} nanonetwork”. *Applied physics letters* 90 (26) (2007). URL: http://dx.doi.org/10.1063/1.2753096 (cited on page 12).

[23] M Ishida et al. “Drastic reduction of threading dislocation in GaN regrown on grooved stripe structure”. *Journal of crystal growth* 221 (1) (2000), pp. 345–349. URL: http://www.sciencedirect.com/science/article/pii/S0022024800007119 (cited on page 12).

[24] T Tanikawa et al. “Reduction of dislocations in a (112¯ 2) GaN grown by selective MOVPE on (113) Si”. *Journal of Crystal Growth* 311 (10) (2009), pp. 2879–2882. URL: http://www.sciencedirect.com/science/article/pii/S0022024809000578 (cited on pages 12, 34).

[25] T. J. Baker et al. “Characterization of planar semipolar gallium nitride films on sapphire substrates”. *Japanese Journal of Applied Physics* 45 (2L) (2006), p. L154. URL: http://iopscience.iop.org/1347-4065/45/2L/L154/ (cited on pages 12, 23).

[26] H Blank et al. “Fault structures in wurtzite”. *physica status solidi (b)* 7 (3) (1964), pp. 747–764. URL: http://onlinelibrary.wiley.com/doi/10.1002/pssb.19640070304/abstract (cited on page 12).

[27] J. Lähnemann et al. “Luminescence associated with stacking faults in GaN”. *Journal of Physics D: Applied Physics* 47 (42) (2014), p. 423001. URL: http://stacks.iop.org/0022-3727/47/i=42/a=423001 (cited on page 13).

[28] J. P. Hirth et al. “Theory of dislocations” (1982) (cited on page 13).

[29] C Stampfl et al. “Energetics and electronic structure of stacking faults in AlN, GaN, and InN”. *Physical Review B* 57 (24) (1998), R15052. URL: http://journals.aps.org/prb/abstract/10.1103/PhysRevB.57.R15052 (cited on pages 13, 43).

[30] C. Drum. “Intersecting faults on basal and prismatic planes in aluminium nitride”. *Philosophical Magazine* 11 (110) (1965), pp. 313–334 (cited on page 13).

[31] L Sugiura et al. “Effects of thermal treatment of low-temperature GaN buffer layers on the quality of subsequent GaN layers”. *Journal of applied physics* 82 (10) (1997), pp. 4877–4882. URL: http://dx.doi.org/10.1063/1.366350 (cited on page 13).

[32] F Ernst et al. “The formation mechanism of planar defects in compound semiconductors grown epitaxially on {100} silicon substrates”. *Journal of Materials Research* 4 (04) (1989), pp. 834–842. URL: http://dx.doi.org/10.1557/JMR.1989.0834 (cited on pages 13, 132).

[33] P. Vennéguès. “Propriétés structurales de films de semi-conducteurs wurtzite hetéroépitaxiés selon des orientations non- et semi-polaires”. *Habilitation à Diriger des Recherches* (2009) (cited on page 13).

[34] P Vennéguès et al. “On the origin of basal stacking faults in nonpolar wurtzite films epitaxially grown on sapphire substrates”. *Journal of Applied Physics* 112 (11) (2012), p. 113518. URL: http://dx.doi.org/10.1063/1.4768686 (cited on page 14).

[35] F. Wu et al. “Polarity determination of a-plane GaN on r-plane sapphire and its effects on lateral overgrowth and heteroepitaxy”. *Journal of applied physics* 94 (2) (2003). URL: http://dx.doi.org/10.1063/1.1578530 (cited on pages 14, 61).

[36] T Gühne et al. “Cathodoluminescence spectroscopy of epitaxial-lateral-overgrown nonpolar (11-20) and semipolar (11-22) GaN in relation to microstructural characterization”. *Journal of applied physics* 101 (11) (2007), p. 113101. URL: http://dx.doi.org/10.1063/1.2740361 (cited on pages 14, 61).

[37] T. Zywietz et al. “Adatom diffusion at GaN (0001) and (0001) surfaces”. *Applied physics letters* 73 (4) (1998), pp. 487–489. URL: http://dx.doi.org/10.1063/1.121909 (cited on page 14).

[38] Y. J. Sun et al. “Impact of nucleation conditions on the structural and optical properties of m-plane GaN (1100) grown on γ-LiAlO2”. *Journal of applied physics* 92 (10) (2002), pp. 5714–5719. URL: http://dx.doi.org/10.1063/1.1513874 (cited on page 14).

[39] K. H. Baik et al. “Effects of Basal Stacking Faults on Electrical Anisotropy of Nonpolar a-Plane () GaN Light-Emitting Diodes on Sapphire Substrate”. *Photonics Technology Letters, IEEE* 22 (9) (2010), pp. 595–597. URL: 10.1109/LPT.2010.2042950 (cited on pages 14, 22).

[40] F. Bernardini et al. “Spontaneous polarization and piezoelectric constants of III-V nitrides”. *Physical Review B* 56 (16) (1997), R10024. URL: http://journals.aps.org/prb/abstract/10.1103/PhysRevB.56.R10024 (cited on pages 14, 15).

[41] O Ambacher et al. “Role of Spontaneous and Piezoelectric Polarization Induced Effects in Group-III Nitride Based Heterostructures and Devices”. *physica status solidi (b)* 216 (1) (1999), pp. 381–389. URL: http://onlinelibrary.wiley.com/doi/10.1002/(SICI)1521-3951(199911)216:1%3C381::AID-PSSB381%3E3.0.CO;2-O/abstract (cited on page 14).

[42] C. Wood et al. *Polarization effects in semiconductors: from ab initio theory to device applications*. Springer Science & Business Media, 2007 (cited on page 14).

[43] T. Takeuchi et al. "Determination of piezoelectric fields in strained GaInN quantum wells using the quantum-confined Stark effect". *Applied physics letters* 73 (12) (1998), pp. 1691–1693. URL: http://scitation.aip.org/content/aip/journal/apl/73/12/10.1063/1.122247 (cited on page 15).

[44] T Gessmann et al. "Ohmic contacts to p-type GaN mediated by polarization fields in thin InxGa1- xN capping layers". *Applied physics letters* 80 (6) (2002), pp. 986–988. URL: http://dx.doi.org/10.1063/1.1445807 (cited on page 16).

[45] N. Grandjean et al. "Built-in electric-field effects in wurtzite AlGaN/GaN quantum wells". *Journal of applied physics* 86 (7) (1999), pp. 3714–3720. URL: http://scitation.aip.org/content/aip/journal/jap/86/7/10.1063/1.371241 (cited on page 16).

[46] R. Farrell et al. "Materials and growth issues for high-performance nonpolar and semipolar light-emitting devices". *Semiconductor Science and Technology* 27 (2) (2012), p. 024001. URL: http://iopscience.iop.org/0268-1242/27/2/024001 (cited on page 16).

[47] O Ambacher et al. "Two-dimensional electron gases induced by spontaneous and piezoelectric polarization charges in N-and Ga-face AlGaN/GaN heterostructures". *Journal of Applied Physics* 85 (6) (1999), p. 3222. URL: http://dx.doi.org/10.1063/1.369664 (cited on page 16).

[48] P. Bigenwald et al. "The calculation of semipolar orientations for wurtzitic semiconductor heterostructures: application to nitrides and oxides". *Semiconductor Science and Technology* 27 (2) (2012), p. 024009. URL: http://iopscience.iop.org/0268-1242/27/2/024009 (cited on page 17).

[49] D. F. Feezell et al. "Semipolar (20-2-1) InGaN/GaN light-emitting diodes for high-efficiency solid-state lighting". *Journal of Display Technology* 9 (4) (2013), pp. 190–198. URL: 10.1109/JDT.2012.2227682 (cited on page 19).

[50] J. E. Northrup et al. "Indium-induced changes in GaN (0001) surface morphology". *Physical Review B* 60 (12) (1999), R8473. URL: http://dx.doi.org/10.1103/PhysRevB.60.R8473 (cited on page 18).

[51] J. E. Northrup. "GaN and InGaN (112_2) surfaces: Group-III adlayers and indium incorporation". *Applied Physics Letters* 95 (13) (2009), pp. 133107–133107. URL: http://dx.doi.org/10.1063/1.3240401 (cited on page 19).

[52] H. Chen et al. "Surface structures and growth kinetics of InGaN (0001) grown by molecular beam epitaxy". *Journal of Vacuum Science & Technology B* 18 (4) (2000), pp. 2284–2289. URL: http://dx.doi.org/10.1116/1.1306296 (cited on page 19).

[53] Y. Zhao et al. "Indium incorporation and emission properties of nonpolar and semipolar InGaN quantum wells". *Applied Physics Letters* 100 (20) (2012), p. 201108. URL: http://dx.doi.org/10.1063/1.4719100 (cited on page 19).

[54] T. Wernicke et al. "Indium incorporation and emission wavelength of polar, nonpolar and semipolar InGaN quantum wells". *Semiconductor science and technology* 27 (2) (2012), p. 024014. URL: http://iopscience.iop.org/0268-1242/27/2/024014 (cited on pages 19, 20).

[55] N. Fellows et al. "Increased Polarization Ratio on Semipolar (1122) InGaN/GaN Light-Emitting Diodes with Increasing Indium Composition". *Japanese Journal of Applied Physics* 47 (10R) (2008), p. 7854. URL: http://iopscience.iop.org/1347-4065/47/10R/7854 (cited on page 20).

[56] Y. Enya et al. "531 nm green lasing of InGaN based laser diodes on semi-polar {2021} free-standing GaN substrates". *Applied Physics Express* 2 (8) (2009), p. 082101. URL: http://iopscience.iop.org/1882-0786/2/8/082101/ (cited on pages 20, 99).

[57] M. Adachi et al. “Low threshold current density InGaN based 520–530 nm green laser diodes on semi-polar {2021} free-standing GaN substrates”. *Applied physics express* 3 (12) (2010), p. 121001. URL: http://iopscience.iop.org/1882-0786/3/12/121001 (cited on pages 20, 99).

[58] Y. Yoshizumi et al. “Continuous-wave operation of 520 nm green InGaN-based laser diodes on semi-polar {2021} GaN substrates”. *Applied Physics Express* 2 (9) (2009), p. 092101. URL: http://iopscience.iop.org/1882-0786/2/9/092101 (cited on pages 20, 99).

[59] R. Bhat et al. “Experimental study of the orientation dependence of indium incorporation in GaInN”. *Journal of Crystal Growth* (2015). URL: http://www.sciencedirect.com/science/article/pii/S0022024815005898 (cited on page 20).

[60] J. Piprek. “Efficiency droop in nitride-based light-emitting diodes”. *physica status solidi (a)* 207 (10) (2010), pp. 2217–2225. URL: http://onlinelibrary.wiley.com/doi/10.1002/pssa.201026149/abstract (cited on page 21).

[61] E. Kioupakis et al. “Indirect Auger recombination as a cause of efficiency droop in nitride light-emitting diodes”. *Applied Physics Letters* 98 (16) (2011), p. 161107. URL: http://dx.doi.org/10.1063/1.3570656 (cited on page 21).

[62] J. Iveland et al. “Direct measurement of Auger electrons emitted from a semiconductor light-emitting diode under electrical injection: identification of the dominant mechanism for efficiency droop”. *Physical review letters* 110 (17) (2013), p. 177406. URL: http://dx.doi.org/10.1103/PhysRevLett.110.177406 (cited on page 21).

[63] M.-H. Kim et al. “Origin of efficiency droop in GaN-based light-emitting diodes”. *Applied Physics Letters* 91 (18) (2007), p. 183507. URL: http://dx.doi.org/10.1063/1.2800290 (cited on page 21).

[64] R. Dwiliński et al. “Excellent crystallinity of truly bulk ammonothermal GaN”. *Journal of Crystal Growth* 310 (17) (2008), pp. 3911–3916. URL: http://www.sciencedirect.com/science/article/pii/S002202480800451X (cited on page 22).

[65] S. Ploch et al. “Orientation control of GaN and grown on sapphire by metal-organic vapor phase epitaxy”. *Journal of Crystal Growth* 312 (15) (2010), pp. 2171–2174. URL: http://www.sciencedirect.com/science/article/pii/S002202481000299X (cited on page 23).

[66] R. Ravash et al. “Semipolar single component GaN on planar high index Si (11h) substrates”. *Applied Physics Letters* 97 (14) (2010), p. 142102. URL: http://dx.doi.org/10.1063/1.3492835 (cited on page 23).

[67] T. J. Baker et al. “Characterization of planar semipolar gallium nitride films on spinel substrates”. *Japanese journal of applied physics* 44 (7L) (2005), p. L920. URL: http://iopscience.iop.org/1347-4065/44/7L/L920 (cited on page 23).

[68] A Dadgar et al. “Eliminating stacking faults in semi-polar GaN by AlN interlayers”. *Applied Physics Letters* 99 (2) (2011), pp. 021905–021905. URL: http://dx.doi.org/10.1063/1.3610467 (cited on pages 24, 30, 77, 78).

[69] Z Bougrioua et al. “Reduction of stacking faults in (11-20) and (11-22) GaN films by ELO techniques and benefit on GaN wells emission”. *physica status solidi (a)* 204 (1) (2007), pp. 282–289. URL: http://onlinelibrary.wiley.com/doi/10.1002/pssa.200673585/abstract (cited on page 24).

[70] Y. Honda et al. “Growth of (1101) GaN on a 7-degree off-oriented (001) Si substrate by selective MOVPE”. *Journal of crystal growth* 242 (1) (2002), pp. 82–86. URL: http://www.sciencedirect.com/science/article/pii/S0022024802013532 (cited on pages 24, 26, 49).

[71] T. Tanikawa et al. “Growth of semi-polar (11-22) GaN on a (113) Si substrate by selective MOVPE”. *physica status solidi (c)* 5 (9) (2008), pp. 2966–2968. URL: http://onlinelibrary.wiley.com/doi/10.1002/pssc.200779236/abstract (cited on pages 24, 26, 32, 33, 76).

[72] S. Schwaiger et al. “Planar semipolar (10 1 1) GaN on (11 2 3) sapphire”. *Applied Physics Letters* 96 (23) (2010), pp. 231905–231905. URL: http://dx.doi.org/10.1063/1.3442484 (cited on pages 24, 26, 74, 89).

[73] N. Okada et al. “Growth of Semipolar (1122) GaN Layer by Controlling Anisotropic Growth Rates in r-Plane Patterned Sapphire Substrate”. *Applied physics express* 2 (9) (2009), p. 091001. URL: http://iopscience.iop.org/1882-0786/2/9/091001 (cited on pages 24, 26).

[74] N. Okada et al. “High-quality {20-21} GaN layers on patterned sapphire substrate with wide-terrace”. *Applied Physics Letters* 99 (24) (2011), p. 242103. URL: http://dx.doi.org/10.1063/1.3670046 (cited on pages 24, 26, 99, 105, 106, 109, 113, 114).

[75] D. T. Wei et al. “Ion beam sputtering”. *Thin Films for Optical Systems,](Flory, FR, ed.)* (1995), p. 133 (cited on pages 25, 51).

[76] M Khoury et al. “Growth of Semipolar (20 1) GaN Layers on Patterned Silicon (114) 1° off by Metal Organic Vapor Phase Epitaxy”. *Journal of Crystal Growth* (2015). URL: http://www.sciencedirect.com/science/article/pii/S0022024815001955 (cited on page 26).

[77] K. Hiramatsu et al. “Relaxation mechanism of thermal stresses in the heterostructure of GaN grown on sapphire by vapor phase epitaxy”. *Japanese journal of applied physics* 32 (4R) (1993), p. 1528. URL: http://iopscience.iop.org/article/10.1143/JJAP.32.1528/meta (cited on page 27).

[78] W Zulehner. “Czochralski growth of silicon”. *Journal of Crystal Growth* 65 (1) (1983), pp. 189–213. URL: http://www.sciencedirect.com/science/article/pii/0022024883900519 (cited on page 27).

[79] Z. Lu et al. “Growth of 450mm diameter semiconductor grade silicon crystals”. *Journal of Crystal Growth* 318 (1) (2011), pp. 193–195. URL: http://www.sciencedirect.com/science/article/pii/S0022024810008705 (cited on page 27).

[80] A. Krost et al. “GaN-based optoelectronics on silicon substrates”. *Materials Science and Engineering: B* 93 (1) (2002), pp. 77–84. URL: http://www.sciencedirect.com/science/article/pii/S0921510702000430 (cited on pages 28, 29, 118).

[81] S Zamir et al. “Thermal microcrack distribution control in GaN layers on Si substrates by lateral confined epitaxy”. *Applied Physics Letters* 78 (3) (2001), pp. 288–290. URL: http://dx.doi.org/10.1063/1.1338968 (cited on page 29).

[82] A. Dadgar. “Sixteen years GaN on Si”. *physica status solidi (b)* (2015). URL: http://onlinelibrary.wiley.com/doi/10.1002/pssb.201451656/full (cited on page 29).

[83] H. Ishikawa et al. “GaN on Si substrate with AlGaN/AlN intermediate layer”. *Japanese Journal of Applied Physics* 38 (5A) (1999), p. L492. URL: http://iopscience.iop.org/1347-4065/38/5A/L492 (cited on pages 29, 118).

[84] T. W. Weeks Jr et al. *Gallium nitride materials and methods*. US Patent 6,649,287. 2003 (cited on page 29).

[85] H. Marchand et al. “Metalorganic chemical vapor deposition of GaN on Si (111): Stress control and application to field-effect transistors”. *journal of Applied Physics* 89 (12) (2001), pp. 7846–7851. URL: http://dx.doi.org/10.1063/1.1372160 (cited on page 29).

[86] A Dadgar et al. “Thick, crack-free blue light-emitting diodes on Si (111) using low-temperature AlN interlayers and in situSixNy masking”. *Applied physics letters* 80 (20) (2002), pp. 3670–3672. URL: http://dx.doi.org/10.1063/1.1479455 (cited on page 29).

[87] E Feltin et al. “Crack-Free Thick GaN Layers on Silicon (111) by Metalorganic Vapor Phase Epitaxy”. *physica status solidi (a)* 188 (2) (2001), pp. 531–535. URL: doi/10.1002/1521-396X(200112)188:2<531::AID-PSSA531>3.0.CO;2-V/abstract (cited on pages 29, 118).

[88] H. Schenk et al. “Growth of thick, continuous GaN layers on 4-in. Si substrates by metalorganic chemical vapor deposition”. *Journal of Crystal Growth* 314 (1) (2011), pp. 85–91. URL: http://www.sciencedirect.com/science/article/pii/S0022024810009309 (cited on page 29).

[89] Y Honda et al. “Growth of GaN free from cracks on a (111) Si substrate by selective metalorganic vapor-phase epitaxy”. *Applied physics letters* 80 (2) (2002), pp. 222–224. URL: http://dx.doi.org/10.1063/1.1432764 (cited on page 29).

[90] A Dadgar et al. “Crack-Free InGaN/GaN Light Emitters on Si (111)”. *physica status solidi (a)* 188 (1) (2001), pp. 155–158. URL: http://onlinelibrary.wiley.com/doi/10.1002/1521-396X(200111)188:1%3C155::AID-PSSA155%3E3.0.CO;2-P/abstract (cited on page 29).

[91] S Zamir et al. “Reduction of cracks in GaN films grown on Si-on-insulator by lateral confined epitaxy”. *Journal of crystal growth* 243 (3) (2002), pp. 375–380. URL: http://www.sciencedirect.com/science/article/pii/S0022024802015786 (cited on page 29).

[92] A Dadgar et al. “Metalorganic chemical vapor phase epitaxy of gallium-nitride on silicon”. *physica status solidi (c)* (6) (2003), pp. 1583–1606. URL: http://onlinelibrary.wiley.com/doi/10.1002/pssc.200303122/abstract (cited on page 29).

[93] H. Ishikawa et al. “Thermal stability of GaN on (111) Si substrate”. *Journal of crystal growth* 189 (1998), pp. 178–182. URL: http://www.sciencedirect.com/science/article/pii/S0022024898002231 (cited on pages 29, 118).

[94] P. Vennéguès. “Defect reduction methods for III-nitride heteroepitaxial films grown along nonpolar and semipolar orientations”. *Semiconductor Science and Technology* 27 (2) (2012), p. 024004. URL: http://iopscience.iop.org/0268-1242/27/2/024004 (cited on pages 30, 78).

[95] J. Hollander et al. “Improvements in a-plane GaN crystal quality by a two-step growth process”. *Applied Physics Letters* 92 (10) (2008), p. 101104. URL: http://dx.doi.org/10.1063/1.2830023 (cited on page 30).

[96] A. Chakraborty et al. “Defect reduction in nonpolar a-plane GaN films using in situ SiN x nanomask”. *Applied physics letters* 89 (4) (2006), pp. 041903–041903. URL: http://dx.doi.org/10.1063/1.2234841 (cited on page 30).

[97] M. Moram et al. “Defect reduction in nonpolar and semipolar GaN using scandium nitride interlayers”. *Journal of Crystal Growth* 311 (12) (2009), pp. 3239–3242. URL: http://www.sciencedirect.com/science/article/pii/S0022024809003790 (cited on page 30).

[98] H Furuya et al. “Characterization of {11- 22} GaN grown using two-step growth technique on shallowly etched r-plane patterned sapphire substrates”. *Journal of Crystal Growth* 391 (2014), pp. 41–45. URL: http://www.sciencedirect.com/science/article/pii/S0022024813008907 (cited on page 30).

[99] T. S. Zheleva et al. “Dislocation density reduction via lateral epitaxy in selectively grown GaN structures”. *Applied physics letters* 71 (17) (1997), pp. 2472–2474. URL: http://dx.doi.org/10.1063/1.120091 (cited on page 31).

[100] P Vennégues et al. “Reduction mechanisms for defect densities in GaN using one-or two-step epitaxial lateral overgrowth methods”. *Journal of Applied Physics* 87 (9) (2000), pp. 4175–4181. URL: http://dx.doi.org/10.1063/1.373048 (cited on page 31).

[101] M Hao et al. “Configuration of dislocations in lateral overgrowth GaN films”. *Journal of applied physics* 85 (9) (1999), pp. 6497–6501. URL: http://dx.doi.org/10.1063/1.370110 (cited on page 31).

[102] S. Tanaka et al. “Defect structure in selective area growth GaN pyramid on (111) Si substrate”. *Applied Physics Letters* 76 (19) (2000), pp. 2701–2703. URL: http://dx.doi.org/10.1063/1.126448 (cited on page 31).

[103] S Gradečak et al. “Bending of dislocations in GaN during epitaxial lateral overgrowth”. *Applied physics letters* 85 (20) (2004), pp. 4648–4650. URL: http://dx.doi.org/10.1063/1.1823593 (cited on page 31).

[104] F. Tendille et al. “Defect reduction method in (11-22) semipolar GaN grown on patterned sapphire substrate by MOCVD: Toward heteroepitaxial semipolar GaN free of basal stacking faults”. *Journal of Crystal Growth* 404 (2014), pp. 177–183. URL: http://www.sciencedirect.com/science/article/pii/S0022024814005156 (cited on pages 33, 76).

[105] O. Takakuwa et al. “Optimizing the conditions for residual stress measurement using a two-dimensional XRD method with specimen oscillation” (2013). URL: http://file.scirp.org/Html/2-1510168_30322.htm (cited on page 35).

[106] J. Zuniga Perez. “Crystal growth and characterization of II-VI oxides thin films”. *PhD Thesis* (2005) (cited on page 36).

[107] M. Moram et al. “X-ray diffraction of III-nitrides”. *Reports on Progress in Physics* 72 (3) (2009), p. 036502. URL: http://iopscience.iop.org/0034-4885/72/3/036502 (cited on page 36).

[108] T Paskova et al. “High-quality bulk a-plane GaN sliced from boules in comparison to heteroepitaxially grown thick films on r-plane sapphire”. *Applied physics letters* 89 (5) (2006), pp. 051914–051914. URL: http://dx.doi.org/10.1063/1.2236901 (cited on page 36).

[109] M. B. McLaurin et al. “Basal plane stacking-fault related anisotropy in X-ray rocking curve widths of m-plane GaN”. *Japanese Journal of Applied Physics* 47 (7R) (2008), p. 5429. URL: http://iopscience.iop.org/1347-4065/47/7R/5429 (cited on page 36).

[110] C Roder et al. “Stress and wafer bending of a-plane GaN layers on r-plane sapphire substrates”. *Journal of Applied Physics* 100 (10) (2006), p. 103511. URL: http://dx.doi.org/10.1063/1.2386940 (cited on page 36).

[111] H. Wang et al. “Anisotropic structural characteristics of (1120) GaN templates and coalesced epitaxial lateral overgrown films deposited on (1012) sapphire”. *Applied physics letters* 84 (4) (2004), pp. 499–501. URL: http://dx.doi.org/10.1063/1.1644054 (cited on page 37).

[112] J. Serafińczuk et al. “Structural properties of bulk GaN substrates: Impact of structural anisotropy on non-polar and semi-polar crystals”. *Crystal Research and Technology* (2015). URL: http://onlinelibrary.wiley.com/doi/10.1002/crat.201500125/full (cited on page 37).

[113] D. B. Williams et al. “The Transmission electron microscope”. *Transmission Electron Microscopy*. Springer, 2009 (cited on pages 38, 39).

[114] B. Yacobi et al. “Cathodoluminescence scanning electron microscopy of semiconductors”. *Journal of applied physics* 59 (4) (1986), R1–R24 (cited on page 40).

[115] R. Martin et al. “Cathodoluminescence spectral mapping of III-nitride structures”. *PHYSICA STATUS SOLIDI A APPLIED RESEARCH* 201 (4) (2004), pp. 665–672. URL: http://onlinelibrary.wiley.com/doi/10.1002/pssa.200304089/abstract (cited on page 41).

[116] D Drouin. “CASINO a powerful simulation tool for cathodoluminescence applications”. *Microscopy and Microanalysis* 12 (S02) (2006), pp. 1512–1513. URL: http://dx.doi.org/10.1017/S1431927606069686 (cited on page 41).

[117] F. Ponce et al. “Spatial distribution of the luminescence in GaN thin films”. *Applied physics letters* 68 (1) (1996), pp. 57–59. URL: http://dx.doi.org/10.1063/1.116756 (cited on page 41).

[118] M. Khoury et al. “Imaging and counting threading dislocations in c-oriented epitaxial GaN layers”. *Semiconductor Science and Technology* 28 (3) (2013), p. 035006. URL: http://stacks.iop.org/0268-1242/28/i=3/a=035006 (cited on pages 42, 73, 109).

[119] Y. Rebane et al. “Stacking faults as quantum wells for excitons in wurtzite GaN”. *Physica status solidi (a)* 164 (1) (1997), pp. 141–144. URL: http://onlinelibrary.wiley.com/doi/10.1002/1521-396X(199711)164:1%3C141::AID-PSSA141%3E3.0.CO;2-G/abstract (cited on page 43).

[120] M Albrecht et al. “Luminescence related to stacking faults in heterepitaxially grown wurtzite GaN”. *MRS Proceedings*. Vol. 468. Cambridge Univ Press. 1997, p. 293 (cited on page 43).

[121] R Liu et al. “Luminescence from stacking faults in gallium nitride”. *Applied Physics Letters* 86 (2) (2005), p. 1908. URL: http://dx.doi.org/10.1063/1.1852085 (cited on page 45).

[122] M. A. Reshchikov et al. “Luminescence properties of defects in GaN”. *Journal of applied physics* 97 (6) (2005), p. 061301. URL: http://scitation.aip.org/content/aip/journal/jap/97/6/10.1063/1.1868059 (cited on page 45).

[123] P. Paskov et al. “Emission properties of a-plane GaN grown by metal-organic chemical-vapor deposition”. *Journal of applied physics* 98 (9) (2005), pp. 093519–093519. URL: http://scitation.aip.org/content/aip/journal/jap/98/9/10.1063/1.2128496 (cited on pages 45, 64).

[124] M. Leroux et al. “From relaxed to highly tensily strained GaN grown on 6H-SiC and Si (111): Optical characterization”. *Materials Science Forum*. Vol. 353. Trans Tech Publ. 2001, pp. 795–798 (cited on page 45).

[125] H. Lahrèche et al. “Buffer free direct growth of GaN on 6H–SiC by metalorganic vapor phase epitaxy”. *Journal of Applied Physics* 87 (1) (2000), pp. 577–583. URL: http://dx.doi.org/10.1063/1.371902 (cited on page 45).

[126] G. Binnig et al. “Atomic Force Microscope”. *Phys. Rev. Lett.* 56 (1986), pp. 930–933. URL: http://link.aps.org/doi/10.1103/PhysRevLett.56.930 (cited on page 46).

[127] M. Takami et al. “Growth of semipolar (10-11) GaN from c-plane-like sapphire sidewall of patterned n-plane sapphire substrate”. *physica status solidi (c)* 8 (7-8) (2011), pp. 2101–2103. URL: http://onlinelibrary.wiley.com/doi/10.1002/pssc.201001095/abstract (cited on pages 46, 49, 75, 85, 90).

[128] I. Horcas et al. “WSXM: a software for scanning probe microscopy and a tool for nanotechnology”. *Review of Scientific Instruments* 78 (1) (2007), p. 013705. URL: http://dx.doi.org/10.1063/1.2432410 (cited on page 47).

[129] M. Kushimoto et al. “Optically pumped lasing properties of (10-11) InGaN/GaN stripe multiquantum wells with ridge cavity structure on patterned (001) Si substrates”. *Applied Physics Express* 8 (2) (2015), p. 022702. URL: http://iopscience.iop.org/article/10.7567/APEX.8.022702/meta (cited on page 49).

[130] T Hikosaka et al. "Fabrication and properties of semi-polar (1-101) and (11-22) InGaN/GaN light emitting diodes on patterned Si substrates". *physica status solidi (c)* 5 (6) (2008), pp. 2234–2237. URL: http://onlinelibrary.wiley.com/doi/10.1002/pssc.200778642/abstract (cited on page 49).

[131] P Stadelmann. "JEMS JAVA electron microscopy software". *Version* 2 (2004), W2005 (cited on pages 50, 100).

[132] H Lahreche et al. "Optimisation of AlN and GaN growth by metalorganic vapour-phase epitaxy (MOVPE) on Si (111)". *Journal of crystal growth* 217 (1) (2000), pp. 13–25. URL: http://www.sciencedirect.com/science/article/pii/S0022024800004784 (cited on pages 53, 118).

[133] E. Frayssinet et al. "Growth of thick GaN layers on 4-in. and 6-in. silicon(111) by metal-organic vapor phase epitaxy". *Physica Status Solidi. C: Current Topics in Solid State Physics* 8 (5) (2011), pp. 1479–1482. URL: http://onlinelibrary.wiley.com/doi/10.1002/pssc.201000885/abstract (cited on pages 53, 72).

[134] Q. Sun et al. "Understanding nonpolar GaN growth through kinetic Wulff plots". *Journal of Applied Physics* 104 (9) (2008), p. 093523. URL: http://dx.doi.org/10.1063/1.3009969 (cited on page 53).

[135] G. B. Stringfellow. *Organometallic vapor-phase epitaxy: theory and practice*. Academic Press, 1999 (cited on pages 54, 102).

[136] M. Aoki et al. "Influence of 3d-transition-metal additives on single crystal growth of GaN by the Na flux method". *Japanese journal of applied physics* 42 (9R) (2003), p. 5445. URL: http://iopscience.iop.org/article/10.1143/JJAP.42.5445/meta (cited on page 58).

[137] S. C. Cruz et al. "Crystallographic orientation dependence of dopant and impurity incorporation in GaN films grown by metalorganic chemical vapor deposition". *Journal of crystal growth* 311 (15) (2009), pp. 3817–3823. URL: http://www.sciencedirect.com/science/article/pii/S0022024809005739 (cited on pages 62, 85, 87).

[138] P. Corfdir et al. "Low-temperature time-resolved cathodoluminescence study of exciton dynamics involving basal stacking faults in a-plane GaN". *Applied Physics Letters* 94 (LOEQ-ARTICLE-2009-006) (2009), p. 201115. URL: http://dx.doi.org/10.1063/1.3142396 (cited on page 64).

[139] M Häberlen et al. "Low temperature photoluminescence and cathodoluminescence studies of nonpolar GaN grown using epitaxial lateral overgrowth". *Journal of Applied Physics* 108 (3) (2010), p. 033523. URL: http://dx.doi.org/10.1063/1.3460641 (cited on page 64).

[140] N Okada et al. "Generation of dislocation clusters by glide m-planes in semipolar GaN layers". *physica status solidi (a)* 211 (4) (2014), pp. 736–739. URL: http://onlinelibrary.wiley.com/doi/10.1002/pssa.201300465/full (cited on page 64).

[141] J. Matthews et al. "Defects in epitaxial multilayers: I. Misfit dislocations". *Journal of Crystal Growth* 27 (1974), pp. 118–125. URL: http://www.sciencedirect.com/science/article/pii/S0022024874800552 (cited on page 66).

[142] A. Tyagi et al. "Partial strain relaxation via misfit dislocation generation at heterointerfaces in (Al, In) GaN epitaxial layers grown on semipolar (112xAF2) GaN free standing substrates". *Applied Physics Letters* 95 (25) (2009), p. 1905. URL: http://dx.doi.org/10.1063/1.3275717 (cited on page 66).

[143] A. E. Romanov et al. "Basal plane misfit dislocations and stress relaxation in III-nitride semipolar heteroepitaxy". *Journal of Applied Physics* 109 (10) (2011), p. 103522. URL: http://dx.doi.org/10.1063/1.3590141 (cited on page 66).

[144] S Srinivasan et al. "Slip systems and misfit dislocations in InGaN epilayers". *Applied physics letters* 83 (25) (2003), pp. 5187–5189. URL: http://dx.doi.org/10.1063/1.1633029 (cited on page 66).

[145] J. Laconte et al. *Micromachined thin-film sensors for SOI-CMOS co-integration*. Springer Science & Business Media, 2006 (cited on page 70).

[146] M Madou. "Etch-Stop Techniques". *Fundamentals of Microfabrication, CRC Press, New York* (1997), pp. 193–199 (cited on page 70).

[147] B. Leung et al. "Semipolar (20-21) GaN and InGaN quantum wells on sapphire substrates". *Applied Physics Letters* 104 (26) (2014), p. 262105. URL: http://dx.doi.org/10.1063/1.4886578 (cited on pages 72, 99, 105, 106, 109, 113, 114).

[148] N. Grandjean. "private communication" (2015) (cited on page 72).

[149] C. Bayram et al. "Cubic Phase GaN on Nano-grooved Si (100) via Maskless Selective Area Epitaxy". *Advanced Functional Materials* 24 (28) (2014), pp. 4492–4496. URL: http://onlinelibrary.wiley.com/doi/10.1002/adfm.201304062/full (cited on pages 74, 75).

[150] R. Ravash et al. "Growth and stacking fault reduction in semi-polar GaN films on planar Si (112) and Si (113)". *physica status solidi (c)* 9 (3-4) (2012), pp. 507–510. URL: http://onlinelibrary.wiley.com/doi/10.1002/pssc.201100532/abstract (cited on pages 77, 130).

[151] T Mitsunari et al. "Single-crystalline semipolar GaN on Si (001) using a directional sputtered AlN intermediate layer". *Journal of Crystal Growth* (2015). URL: http://www.sciencedirect.com/science/article/pii/S0022024815005448 (cited on page 77).

[152] Z. Wu et al. "Partial strain relaxation by stacking fault generation in InGaN multiple quantum wells grown on (10-11) semipolar GaN". *Applied Physics Letters* 98 (5) (2011), p. 1902. URL: http://dx.doi.org/10.1063/1.3549561 (cited on page 78).

[153] J Jayapalan et al. "Optical spectroscopy of Si-related donor and acceptor levels in Si-doped GaN grown by hydride vapor phase epitaxy". *Applied physics letters* 73 (9) (1998), pp. 1188–1190. URL: http://dx.doi.org/10.1063/1.122123 (cited on page 87).

[154] M Leroux et al. "Luminescence and reflectivity studies of undoped, n-and p-doped GaN on (0001) sapphire". *Materials Science and Engineering: B* 50 (1) (1997), pp. 97–104. URL: http://www.sciencedirect.com/science/article/pii/S0921510797001438 (cited on page 89).

[155] K. Eisele. "SF 6, a Preferable Etchant for Plasma Etching Silicon". *Journal of The Electrochemical Society* 128 (1) (1981), pp. 123–126. URL: http://jes.ecsdl.org/content/128/1/123.short (cited on page 92).

[156] M. Hÿtch. "Geometric phase analysis of high resolution electron microscope images". *Scanning Microscopy* 11 (1997), pp. 53–66 (cited on page 92).

[157] L. Giannuzzi et al. "A review of focused ion beam milling techniques for TEM specimen preparation". *Micron* 30 (3) (1999), pp. 197–204. URL: http://www.sciencedirect.com/science/article/pii/S0968432899000050 (cited on page 95).

[158] Y.-D. Lin et al. "High quality InGaN/AlGaN multiple quantum wells for semipolar InGaN green laser diodes". *Applied Physics Express* 3 (8) (2010), p. 082001. URL: http://iopscience.iop.org/1882-0786/3/8/082001 (cited on page 99).

[159] M. Funato et al. "Weak Carrier/Exciton Localization in InGaN Quantum Wells for Green Laser Diodes Fabricated on Semi-Polar {2021} GaN Substrates". *Applied physics express* 3 (2) (2010), p. 021002. URL: http://iopscience.iop.org/1882-0786/3/2/021002 (cited on page 99).

[160] T. Meisch et al. "(20-21) MOVPE and HVPE GaN grown on 2 in. patterned sapphire substrates". *physica status solidi (c)* 11 (3-4) (2014), pp. 537–540. URL: http://onlinelibrary.wiley.com/doi/10.1002/pssc.201300396/abstract (cited on pages 99, 105, 106, 109, 113, 114).

[161] P Mutombo et al. "Ab initio density functional theory study of non-polar (101 {sup¯} 0),(112 {sup¯} 0) and semipolar (202 {sup¯} 1) GaN surfaces". *Journal of Applied Physics* 115 (20) (2014). URL: http://dx.doi.org/10.1063/1.4879675 (cited on pages 105, 106).

[162] C Boudias et al. "Software CaRine Crystallography". *CaRine Crystallography, Senlis, France* (1998) (cited on page 112).

[163] K. Yamane et al. "Growth of pit-free GaP on Si by suppression of a surface reaction at an initial growth stage". *Journal of Crystal Growth* 311 (3) (2009), pp. 794–797. URL: http://www.sciencedirect.com/science/article/pii/S0022024808009366 (cited on pages 118, 127).

[164] K. Volz et al. "GaP-nucleation on exact Si (001) substrates for III/V device integration". *Journal of Crystal Growth* 315 (1) (2011), pp. 37–47. URL: http://www.sciencedirect.com/science/article/pii/S0022024810007669 (cited on pages 118, 121).

[165] R. W. Olesinski et al. "The Ga- Si (Gallium-Silicon) system". *Journal of Phase Equilibria* 6 (4) (1985), pp. 362–364. URL: http://link.springer.com/article/10.1007%2FBF02880523?LI=true (cited on pages 118, 120).

[166] R. Moskalyk. "Gallium: the backbone of the electronics industry". *Minerals Engineering* 16 (10) (2003), pp. 921–929. URL: http://www.sciencedirect.com/science/article/pii/S0892687503002759 (cited on page 118).

[167] Z. W. Pan et al. "Gallium-mediated growth of multiwall carbon nanotubes". *Applied physics letters* 82 (12) (2003), pp. 1947–1949. URL: http://dx.doi.org/10.1063/1.1563727 (cited on page 118).

[168] P. Knoll et al. "Method for preparation of thin, oriented GaAs crystals". *Journal of Applied Physics* 37 (13) (1966), pp. 5006–5007. URL: http://dx.doi.org/10.1063/1.1708191 (cited on page 118).

[169] M. K. Sunkara et al. "Bulk synthesis of silicon nanowires using a low-temperature vapor–liquid–solid method". *Applied Physics Letters* 79 (10) (2001), pp. 1546–1548. URL: http://dx.doi.org/10.1063/1.1401089 (cited on page 118).

[170] R Liu et al. "Atomic arrangement at the AlN/Si (111) interface". *Applied physics letters* 83 (5) (2003), pp. 860–862. URL: http://dx.doi.org/10.1063/1.1597749 (cited on page 118).

[171] P. Drechsel et al. "Impact of buffer growth on crystalline quality of GaN grown on Si (111) substrates". *physica status solidi (a)* 209 (3) (2012), pp. 427–430. URL: http://onlinelibrary.wiley.com/doi/10.1002/pssa.201100477/full (cited on pages 118, 119).

[172] J.-M. Bethoux et al. "Growth of high quality crack-free AlGaN films on GaN templates using plastic relaxation through buried cracks". *Journal of applied physics* 94 (10) (2003), pp. 6499–6507. URL: http://dx.doi.org/10.1063/1.1622993 (cited on page 118).

[173] K. Takemoto et al. "Growth of GaN directly on Si (111) substrate by controlling atomic configuration of Si surface by metalorganic vapor phase epitaxy". *Japanese journal of applied physics* 45 (5L) (2006), p. L478. URL: http://dx.doi.org/10.1143/JJAP.45.L478 (cited on page 120).

[174] H. Ishikawa et al. "Reduction of threading dislocations in GaN on in-situ meltback-etched Si substrates". *Journal of Crystal Growth* 315 (1) (2011), pp. 196–199. URL: http://www.sciencedirect.com/science/article/pii/S0022024810006913 (cited on page 120).

[175] H Detz et al. “Nucleation of Ga droplets on Si and SiOx surfaces”. *Nanotechnology* 26 (31) (2015), p. 315601. URL: http://iopscience.iop.org/article/10.1088/0957-4484/26/31/315601/meta (cited on page 120).

[176] R. Honig et al. “Vapor Pressure Curves of the Elements”. *RCA Laboratories* (1968) (cited on page 121).

[177] A. Koukitu et al. “Thermodynamic study on metalorganic vapor-phase epitaxial growth of group III nitrides”. *Japanese journal of applied physics* 36 (9A) (1997), p. L1136. URL: http://iopscience.iop.org/article/10.1143/JJAP.36.L1136/meta (cited on page 121).

[178] G. E. Lloyd. “Atomic number and crystallographic contrast images with the SEM: a review of backscattered electron techniques”. *Mineralogical Magazine* 51 (359) (1987), pp. 3–19. URL: http://www.minersoc.org/pages/Archive-MM/Volume_51/51-359-3.pdf (cited on page 123).

[179] D. R. Lide. *CRC handbook of chemistry and physics*. CRC press, 2004 (cited on page 123).

[180] “ASM Alloy Phase Diagram Database” (). URL: http://www1.asminternational.org/asmenterprise/apd/ (cited on page 127).

[181] X. F. Li et al. “Size-temperature phase diagram of gallium”. *EPL (Europhysics Letters)* 94 (1) (2011), p. 16001. URL: http://iopscience.iop.org/article/10.1209/0295-5075/94/16001/meta (cited on page 127).

[182] K Werner et al. “Structural characteristics of gallium metal deposited on Si (001) by MOCVD”. *Journal of Crystal Growth* 405 (2014), pp. 102–109. URL: http://www.sciencedirect.com/science/article/pii/S0022024814005478 (cited on page 127).

[183] N. Bartelt et al. “Orientational stability of silicon surfaces”. *Journal of Vacuum Science & Technology A* 7 (3) (1989), pp. 1898–1905. URL: http://dx.doi.org/10.1116/1.576025 (cited on page 127).

[184] O. Tabata et al. “Anisotropic etching of silicon in TMAH solutions”. *Sensors and Actuators A: Physical* 34 (1) (1992), pp. 51–57. URL: http://www.sciencedirect.com/science/article/pii/092442479280139T (cited on page 127).

[185] H Seidel et al. “Anisotropic etching of crystalline silicon in alkaline solutions I. Orientation dependence and behavior of passivation layers”. *Journal of the electrochemical society* 137 (11) (1990), pp. 3612–3626. URL: http://jes.ecsdl.org/content/137/11/3612.short (cited on page 127).

[186] J Bai et al. “Growth and characterization of semi-polar (11-22) GaN on patterned (113) Si substrates”. *Semiconductor Science and Technology* 30 (6) (2015), p. 065012. URL: http://iopscience.iop.org/article/10.1088/0268-1242/30/6/065012/meta (cited on page 129).

[187] Y. Lu et al. “Influence of the growth temperature of the high-temperature AlN buffer on the properties of GaN grown on Si (111) substrate”. *Journal of crystal growth* 263 (1) (2004), pp. 4–11. URL: http://www.sciencedirect.com/science/article/pii/S0022024803019948 (cited on page 131).

[188] O Schön et al. “Comparison of hydrogen and nitrogen as carrier gas for MOVPE growth of GaN”. *Journal of crystal growth* 189 (1998), pp. 335–339. URL: http://www.sciencedirect.com/science/article/pii/S0022024898002875 (cited on page 132).

[189] C. B. Nielsen et al. “Particle precipitation in connection with KOH etching of silicon”. *Journal of The Electrochemical Society* 151 (5) (2004), G338–G342. URL: http://jes.ecsdl.org/content/151/5/G338.short (cited on page 142).